

Study of Charm and Beauty Production at HERA/H1 using Dilepton Events

Dissertation

zur Erlangung des Doktorgrades
des Fachbereichs Physik
der Universität Hamburg

vorgelegt von

Martin Göttlich

aus Sögel

Hamburg
2007

Gutachter der Dissertation:	Prof. Dr. B. Naroska Dr. A. Geiser
Gutachter der Disputation:	Prof. Dr. R.-D. Heuer Dr. A. Geiser
Datum der Disputation:	27.03.2007
Vorsitzende/Vorsitzender des Prüfungsausschusses:	Prof. Dr. Peter Schleper
Vorsitzender des Promotionsausschusses:	Prof. Dr. G. Huber
Dekan der Fakultät Mathematik, Informatik, Naturwissenschaften:	Prof. Dr. A. Frühwald

Abstract

A measurement is presented which investigates the production of charm and beauty quarks in ep collisions at a centre-of-mass energy of 318 GeV. Data taken by the H1 detector at the HERA collider in the years 1999, 2000, 2004 and 2005 are analysed. The collected data correspond to an integrated luminosity of 221.6 pb⁻¹. This is the first measurement of charm and beauty cross sections using HERA II data. Events with two or more jets of transverse momentum $p_t > 5(4)$ GeV in the polar angular range $20^\circ < \theta < 160^\circ$ together with two leptons of transverse momentum $p_t > 2(1)$ GeV in the polar angular ranges $30^\circ < \theta_1 < 130^\circ$ and $20^\circ < \theta_2 < 150^\circ$, respectively, are selected. The first lepton is a muon, the second either a muon or an electron. Cross sections are measured in photoproduction, i.e. at photon virtualities $Q^2 < 1$ GeV², and for inelasticities $0.1 < y < 0.7$. The relative transverse momentum p_t^{rel} of the leptons with respect to the jet they are associated to and the charge and angle correlation of the leptons are exploited to extract the fractions of charm and beauty events on a statistical basis. For the first time at H1, visible charm and beauty cross sections for the production of dijet and dilepton events are determined:

$$\sigma(ep \rightarrow ec\bar{c}X \rightarrow ejj\mu eX') = 4.6 \pm 1.0(stat.) \pm 0.5(sys.) \text{ pb}$$

$$\sigma(ep \rightarrow ec\bar{c}X \rightarrow ejj\mu\mu X') = 2.7 \pm 0.9(stat.) \pm 0.3(sys.) \text{ pb}$$

$$\sigma(ep \rightarrow eb\bar{b}X \rightarrow ejj\mu eX') = 9.4 \pm 1.2(stat.) \pm 0.9(sys.) \text{ pb}$$

$$\sigma(ep \rightarrow eb\bar{b}X \rightarrow ejj\mu\mu X') = 10.4 \pm 1.5(stat.) \pm 1.0(sys.) \text{ pb}$$

To gain a deeper understanding of dilepton correlations in beauty events, differential dilepton cross sections are determined using the observable p_t^{rel} alone. The invariant mass $m(\mu l)$, the transverse momentum $p_t(\mu l)$, the polar angle $\theta(\mu l)$ and the charge and angle correlation $|\Delta\phi(\mu_1, l_2)| \times Q(\mu_1) \times Q(l_2)$ of the dilepton system are investigated. In addition, differential jet cross sections are determined. The measurements are compared with leading order QCD calculations, supplemented with parton showers. The charm cross sections are consistent with the predictions, while the predicted beauty cross sections are somewhat lower than the measurement. The predicted differential beauty cross sections describe the shape of the measurements.

Kurzfassung

Ziel dieser Analyse ist die Untersuchung der Produktionsmechanismen für Charm- und Beauty-Quarks in ep Kollisionen bei einer Schwerpunktsenergie von 318 GeV. Die Analyse basiert auf Daten, die in den Jahren 1999, 2000, 2004 und 2005 vom H1 Detektor bei HERA aufgenommen wurden. Die zur Verfügung stehende integrierte Luminosität beträgt 221.6 pb^{-1} . Dies ist die erste Messung von Wirkungsquerschnitten für die Produktion von Charm- und Beauty-Quarks, in der auch HERA II Daten verwendet werden. Selektiert werden Ereignisse mit mindestens zwei Jets im zentralen Polarwinkelbereich $20^\circ < \theta < 160^\circ$ und den Transversalimpulsen $p_t > 5(4) \text{ GeV}$. Zusätzlich werden zwei Leptonen mit den Transversalimpulsen $p_t > 2(1) \text{ GeV}$ in den Polarwinkelbereichen $30^\circ < \theta_1 < 130^\circ$ und $20^\circ < \theta_2 < 150^\circ$ verlangt. Bei dem ersten Lepton handelt es sich um ein Myon. Das zweite Lepton kann entweder ein Myon oder ein Elektron sein. Untersucht werden Photoproduktionsereignisse mit einer Photonvirtualität von $Q^2 < 1 \text{ GeV}^2$ und einer Inelastizität von $0.1 < y < 0.7$. Der relative Transversalimpuls p_t^{rel} der Leptonen bezogen auf den Jet, dem sie zugeordnet sind, und die Ladungs- und Winkelkorrelationen zwischen den Leptonen werden ausgenutzt, um den Anteil an Charm- und Beauty-Ereignissen zu bestimmen. Zum ersten Mal werden bei H1 sichtbare Charm- und Beauty-Wirkungsquerschnitte für die Produktion von Zwei-Jet und Zwei-Lepton Ereignissen bestimmt:

$$\sigma(ep \rightarrow ec\bar{c}X \rightarrow ejj\mu eX') = 4.6 \pm 1.0(stat.) \pm 0.5(sys.) \text{ pb}$$

$$\sigma(ep \rightarrow ec\bar{c}X \rightarrow ejj\mu\mu X') = 2.7 \pm 0.9(stat.) \pm 0.3(sys.) \text{ pb}$$

$$\sigma(ep \rightarrow eb\bar{b}X \rightarrow ejj\mu eX') = 9.4 \pm 1.2(stat.) \pm 0.9(sys.) \text{ pb}$$

$$\sigma(ep \rightarrow eb\bar{b}X \rightarrow ejj\mu\mu X') = 10.4 \pm 1.5(stat.) \pm 1.0(sys.) \text{ pb}$$

Um einen tieferen Einblick in die Leptonkorrelationen zu erhalten, werden differentielle Wirkungsquerschnitte als Funktion der invarianten Masse $m(\mu l)$, des Transversalimpulses $p_t(\mu l)$, des Polarwinkels $\theta(\mu l)$ und der Ladungs- und Winkelkorrelation $|\Delta\phi(\mu_1, l_2)| \times Q(\mu_1) \times Q(l_2)$ des Leptonensystems bestimmt. Für die Untersuchung der Leptonkorrelationen wird nur die Observable p_t^{rel} verwendet, um den Beauty-Anteil zu bestimmen. Zusätzlich werden differentielle Wirkungsquerschnitte als Funktion des Transversalimpulses und des Polarwinkels der Jets und der Leptonen bestimmt. Die Messungen werden mit QCD Rechnungen in führender Ordnung mit Partonschauern verglichen. Der vorhergesagte Charm-Wirkungsquerschnitt stimmt mit den Messungen überein, während der gemessene Beauty-Wirkungsquerschnitt höher als der theoretisch vorhergesagte Wert ist. Die differentiellen Verteilungen werden in ihrem Verlauf zufriedenstellend beschrieben.

Contents

1	Introduction	1
2	Theoretical Overview	3
2.1	Inelastic Electron-Proton Scattering at HERA	3
2.1.1	Kinematics	4
2.1.2	Inclusive ep Cross Section and Structure Functions	4
2.1.3	Higher Order Corrections	5
2.1.4	Factorisation and Parton Evolution	6
2.1.5	Photoproduction at HERA	7
2.2	Production of Heavy Quarks at HERA	9
2.3	Hadronisation	10
2.4	Monte Carlo Event Generators	12
2.5	Jets and Jet Algorithms	14
2.6	Dijet and Dilepton Events from Open Heavy Flavour	15
2.6.1	Dilepton Charge and Angle Correlation	15
2.6.2	Relative Transverse Momentum p_t^{rel}	19
2.6.3	Contributions from Direct and Resolved Processes	20
2.7	Other Sources of Lepton Pairs at HERA	22
3	The H1 Experiment	24
3.1	HERA	24
3.2	The H1 Detector	25
3.2.1	Central Tracking System	27
3.2.2	Calorimeters	30
3.2.3	Central Muon Detector	31
3.2.4	Trigger System and Data Acquisition	34
3.3	Previous Measurements of Charm and Beauty Production	35
3.3.1	Charm Production	35
3.3.2	Beauty Production	36

3.3.3	Experimental Context of the Present Analysis	38
4	Lepton Identification	40
4.1	Identification of Electrons	40
4.1.1	Electron Identification in the Calorimeter	41
4.1.2	Electron Identification by KALEP	41
4.1.3	Discriminating Variables	42
4.1.4	The Fisher Discriminant Method	45
4.1.5	Electron Identification Efficiency	46
4.2	Muon Identification	54
4.2.1	Muons in the Instrumented Iron	54
4.2.2	Muon Identification in the Calorimeter	55
4.2.3	Muon Identification Efficiency	57
5	Data Selection	66
5.1	Run Selection	67
5.2	Jet Selection	67
5.2.1	The HFS algorithm	67
5.3	Lepton Selection	69
5.3.1	Dimuon Selection	69
5.3.2	Electron Selection	70
5.4	Trigger Selection	72
5.5	Selection of Photoproduction Events	79
5.6	Background Studies	79
5.6.1	Unlike Sign Muons from J/ψ decays	79
5.6.2	Electrons from Photon Conversion Processes	80
5.6.3	DIS Background	80
5.7	Summary of the Selection Cuts	84
5.8	Comparison of Data and Simulation	84
6	Determination of the Charm and Beauty Fractions	97
6.1	Discriminating Variables	97
6.2	Contributions to the Event Samples and Fit Strategies	98
6.3	The Fit Procedure	100
6.4	Charm and Beauty Fractions from Muon-Electron Events	102
6.4.1	One-Dimensional Fit	103
6.4.2	The Two-Dimensional Fit	106
6.4.3	Charm Fraction from Muon-Electron Events	107
6.5	Charm and Beauty Fractions from Dimuon Events	107

7	Total Cross Sections	112
7.1	Cross Section Definition	112
7.2	Systematic Uncertainties	114
7.3	Visible Charm and Beauty Cross Sections	116
8	Differential Cross-Sections	123
8.1	Determination of Differential Cross Sections	123
8.2	Single Lepton, Dilepton and Jet Cross Sections	124
8.3	Differential Cross Sections in x_γ^{obs}	130
9	Summary, Conclusions and Outlook	131
A	Monte Carlo Data Sets	134
B	Measured Differential Cross Sections	136
B.1	Muon-Electron Events	136
B.2	Dimuon Events	139

CHAPTER 1

INTRODUCTION

At HERA, electrons¹ are collided head-on with protons at a centre-of-mass energy of 318 GeV. The electrons can be regarded as a source of high energetic virtual photons which penetrate the proton and resolve its substructure. HERA offers thus a unique opportunity to probe the proton structure. Due to the large energy transfer, the proton usually breaks up, producing a complex multiparticle state of high invariant mass allowing to study the interactions between elementary particles in detail.

The processes observed at HERA can be described very successfully by the Standard Model (SM) of particle physics. In this model, the fundamental constituents of matter are fermions, i.e. leptons and quarks, and their antiparticles. There are three generations of leptons and quarks (see table 1.1). The particles interact via the exchange of gauge bosons. The electromagnetic force is mediated by virtual photons γ , the weak force by the Z^0 and W^\pm bosons and in the case of the strong interaction gluons g_i ($i = 1, \dots, 8$) are exchanged. The electromagnetic and the weak interaction are successfully described by the unified electroweak model. The strong interaction is well described by quantum chromodynamics (QCD). A characteristic feature of QCD is the so-called 'asymptotic freedom' which means that the strong coupling constant α_s becomes smaller with increasing energy, i.e. decreasing distance, leading to quasi free particles. The matrix elements which enter the cross section formula are calculated using perturbative QCD (pQCD). This means that the matrix element is obtained by a perturbative expansion in the strong coupling constant. In the presence of a hard scale α_s is small which leads to a fast convergence of the perturbative expansion. A hard scale can be provided for example by the mass of the produced quarks. Heavy flavour physics is thus well suited to test QCD. The main production mechanism for heavy quarks in the photoproduction regime, i.e. when the virtuality of the exchanged photon is small, is the photon-gluon fusion process (PGF): $\gamma g \rightarrow Q\bar{Q}$, with $Q = c, b$.

In the present analysis, events with two jets and two leptons, i.e. two muons or a muon and an electron, are selected. The jets allow to reconstruct the kinematics of the outgoing partons and the leptons serve as heavy flavour tag. The transverse momentum p_t^{rel} of the leptons relative to the jets they are associated to and the charge and azimuthal angle correlation of the leptons are used to extract the fraction of charm and beauty events in the data samples by a

¹HERA can be operated with both electrons and positrons. Throughout this thesis no distinction is made between particles and their anti-particles.

fit. Cross sections for charm and beauty photoproduction are determined. The measurements are compared to leading order QCD calculations supplemented with parton showers.

	Leptons			Quarks		
	Lepton	Charge	Mass in MeV	Flavour	Charge	Mass in MeV
First generation	e	-1	0.51	u	2/3	1.5 to 4
	ν_e	0	$< 3 \cdot 10^{-6}$	d	-1/3	4 to 8
Second generation	μ	-1	105.7	c	2/3	1150 to 1350
	ν_μ	0	< 0.19	s	-1/3	80 to 130
Third generation	τ	-1	1777	t	2/3	174300
	ν_τ	0	< 18.2	b	-1/3	4100 to 4400

Table 1.1: *The fundamental fermions of the Standard Model (spin $\frac{1}{2}$). The charge is given in units of the proton charge.*

The outline of the thesis is as follows: In the second chapter a short introduction to the theoretical aspects of ep scattering is given. The emphasis is on heavy quark production and on the properties of dijet and dilepton events. In the third chapter an overview of the H1 Experiment is given. The HERA collider and the H1 detector are briefly described. The detector parts that are most relevant for this analysis, namely the central tracking system, the liquid argon calorimeter and the central muon system are described in more detail. The fourth chapter is dedicated to the identification of muons and electrons with the H1 detector. The new electron finder which was developed in the course of this analysis is presented. The identification efficiencies for electrons and muons are extracted from data using the leptonic decay of elastically produced J/ψ mesons. The results are compared with the predictions from a Monte Carlo simulation and correction factors as a function of the transverse momentum and the polar angle are determined where necessary. The data selection is described in chapter five. The selection cuts for the dimuon and the muon-electron sample are discussed. In the sixth chapter, the method used to determine the fraction of events from charm and beauty quarks is explained and the results for both dilepton samples are presented. The fitted fractions are used in chapter seven where the charm and beauty cross sections for the photoproduction of two leptons and two jets are determined. Differential beauty cross sections are investigated in chapter eight. The emphasis is on differential dilepton cross sections. A summary of the present analysis, a discussion of the results and an outlook is given in chapter nine.

A Note on Units

Throughout this thesis a system of natural units is used whereby $\hbar = c = 1$.

CHAPTER 2

THEORETICAL OVERVIEW

This chapter gives a brief overview of the theoretical description of deep inelastic electron-proton scattering and the production of heavy quarks at HERA. The emphasis is on the production mechanisms of lepton pairs and dilepton charge and angle correlations.

2.1 Inelastic Electron-Proton Scattering at HERA

Protons and electrons interact either electromagnetically via the exchange of a virtual photon γ or weakly via the exchange of a Z^0 or W^\pm gauge boson. Figure 2.1 shows the Feynman diagrams in leading order for the neutral (γ , Z^0) and charged current (W^\pm) processes, respectively. The weak interaction is relevant only at large momentum transfers and is negligible in the framework of the present analysis which addresses photoproduction, $Q^2 < 1 \text{ GeV}^2$. In inelastic electron-proton scattering $ep \rightarrow eY$ the proton breaks up and forms the hadronic final state Y .

The exchanged virtual photon can be used to probe the internal structure of the proton.

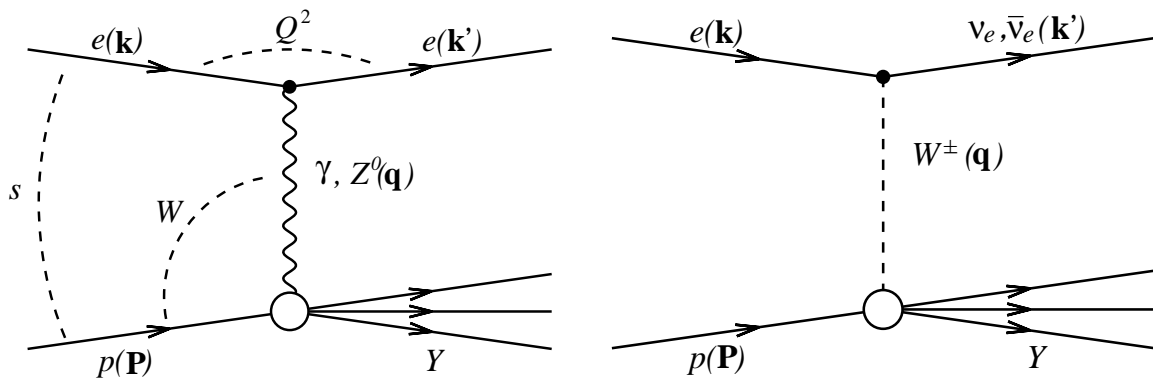


Figure 2.1: Basic Feynman diagrams in leading order for inelastic electron proton scattering. The electron interacts with the proton via the exchange of a virtual photon γ or Z boson (neutral current, left) or via the exchange of a W boson (charged current, right).

2.1.1 Kinematics

At HERA, protons with an energy of $E_p = 920$ GeV collide head on with $E_e = 27.6$ GeV electrons. In order to describe the kinematics of the deep inelastic electron proton scattering process, the following Lorentz invariant quantities are defined, using the four-momenta of the incoming proton \mathbf{P} , the incoming electron \mathbf{k} and the scattered lepton \mathbf{k}' , respectively:

$$s = (\mathbf{k} + \mathbf{P})^2 \quad (2.1)$$

$$Q^2 = -q^2 = -(\mathbf{k} - \mathbf{k}')^2 \quad (2.2)$$

$$x = \frac{Q^2}{2\mathbf{P} \cdot \mathbf{q}} \quad (2.3)$$

$$y = \frac{\mathbf{P} \cdot \mathbf{q}}{\mathbf{P} \cdot \mathbf{k}} \quad (2.4)$$

Here $\sqrt{s} \approx \sqrt{4E_e E_p} \approx 320$ GeV is the centre-of-mass energy of the electron proton system and Q^2 is the virtuality of the exchanged boson. In the quark parton model the Bjorken scaling variable x corresponds to the momentum fraction carried by the struck quark. The inelasticity y is the fractional energy loss of the electron in the proton rest frame. Neglecting the masses of the electron and the proton the following relation holds:

$$Q^2 = x \cdot y \cdot s. \quad (2.5)$$

Since the centre-of-mass energy is constant at HERA two quantities are sufficient to completely describe the kinematics for unpolarised beams.

If the energy E'_e and the polar angle θ_e of the scattered electron are measured, the kinematic variables are given by the following equations:

$$Q^2 = 4E_e E'_e \cos^2 \frac{\theta_e}{2} \quad (2.6)$$

$$y = 1 - \frac{E'_e}{E_e} \sin^2 \frac{\theta_e}{2} \quad (2.7)$$

Alternatively, the kinematics can be reconstructed using the hadronic final state Y , i.e. all particles in the final state except for the scattered electron:

$$Q^2 = \frac{\left(\sum_{h,i} p_{th,i}\right)^2}{1 - y_h} \quad (2.8)$$

$$y = \sum_{h,i} \frac{E_{h,i} - p_{zh,i}}{2E_e} \quad (2.9)$$

$E_{h,i}$, $p_{th,i}$ and $p_{zh,i}$ are the energy, the transverse momentum and the longitudinal momentum of the i -th hadronic final state particle.

2.1.2 Inclusive ep Cross Section and Structure Functions

Neglecting the weak interaction which is relevant only at large momentum transfers the inclusive double differential cross section as a function of x and Q^2 is given by the following formula (see

for example [1]):

$$\frac{d^2\sigma}{dx dQ^2} = \frac{4\pi\alpha^2}{xQ^4} \cdot [y^2 x F_1(x, Q^2) + (1-y) F_2(x, Q^2)] \quad (2.10)$$

The structure functions F_1 and F_2 serve to parametrise our ignorance of the proton structure and details of the interaction at the photon-proton vertex.

Virtual photons can either be longitudinally or transversely polarised, whereas real photons are always transversely polarised. The longitudinal structure function $F_L(x, Q^2)$ can be expressed in terms of the structure functions $F_1(x, Q^2)$ and $F_2(x, Q^2)$:

$$F_L(x, Q^2) = F_2(x, Q^2) - 2x F_1(x, Q^2) \quad (2.11)$$

Using this relation equation 2.10 can be rewritten as follows:

$$\frac{d^2\sigma}{dx dQ^2} = \frac{2\pi\alpha^2}{xQ^4} \cdot [(1 + (1-y)^2) \cdot F_2(x, Q^2) - y^2 \cdot F_L(x, Q^2)] \quad (2.12)$$

The contribution from longitudinally polarised virtual photons is only relevant at high y and only at high Q^2 and is negligible in the kinematic regime of this analysis.

At sufficiently high virtualities $Q^2 \gtrsim 1 \text{ GeV}^2$, i.e. short wavelengths of the exchanged photon, the substructure of the proton is resolved and the photon interacts with a single point-like constituent of the proton which essentially behaves as if it was free since the interaction takes place over a short time. In this simple picture the structure functions F_1 and F_2 depend on x alone. The dependence on Q^2 vanishes since the constituents of the proton, the partons, do not have a substructure. This behaviour is known as 'scaling of the structure functions'. Assuming partons which carry the spin $\frac{1}{2}$ the so-called Callan-Gross relation holds:

$$2x F_1(x) = F_2(x) \quad (2.13)$$

Within the quark parton model (QPM), the structure function F_2 is given by the following formula:

$$F_2(x) = x \sum_i q_i^2 f_i(x) \quad (2.14)$$

$f_i(x)$ are the parton density functions (PDF) of the quarks inside the proton and q_i are the corresponding charges. Gluons are not considered in this simple model. The scaling behaviour of the structure functions is experimentally confirmed for $x \gtrsim 0.1$. This can be regarded as an evidence for the partonic structure of the proton and the existence of quarks.

2.1.3 Higher Order Corrections

At low x a strong rise of the structure function $F_2(x, Q^2)$ towards high Q^2 is observed ('scaling violation'). The observation of scaling violations shows that QCD effects have to be included to describe the data in all regions of phase space. Figure 2.2 shows the Feynman diagrams for the QCD corrections in leading order of the strong coupling constant α_s , the QCD Compton (QCDC) and the boson-gluon fusion (BGF) process. Another observation is that at fixed Q^2 the inclusive deep inelastic scattering (DIS) cross section increases as x becomes smaller. The reason for this behaviour is the increase of the gluon density towards smaller x giving rise to a higher rate of boson-gluon fusion (BGF) events.

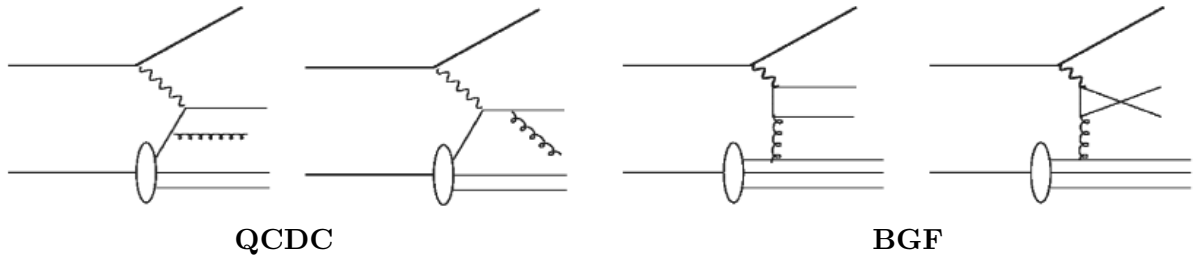


Figure 2.2: Feynman diagrams for the QCD Compton (QCDC) and the boson-gluon fusion (BGF) processes in leading order α_s .

2.1.4 Factorisation and Parton Evolution

As described above, the QPM has to be extended to account for QCD effects. The first step is to calculate the matrix elements for the QCDC and BGF processes applying perturbative QCD (pQCD). Since pQCD calculations can only be safely performed if a hard scale is present, the matrix elements are calculated using a lower cut-off scale, the factorisation scale μ_F , which is large enough to allow for reliable QCD calculations. The non-perturbative part is absorbed into the proton parton density functions $f_{i/p}(x, \mu_0^2)$, where μ_0 is the starting scale and the subscript i denotes the parton type. The parton density functions at the starting scale have to be determined experimentally. They can be evolved to any other scale $\mu_F > \mu_0$ using the parton evolution schemes DGLAP [2, 3, 4, 5], CCFM [6, 7, 8, 9] or BFKL [10, 11, 12]. To evolve the parton density functions processes like gluon splitting and gluon radiation are considered. Such processes may occur several times leading to a gluon ladder as depicted in figure 2.3. All evolution schemes calculate the gluon ladder up to an arbitrary number of gluon radiations but they use different approximations. The DGLAP approach describes the parton evolution in Q^2 and is able to describe the scaling violations of the structure function F_2 observed at HERA down to the smallest accessible x (see figure 2.4). The principle of the approach to factorise the scattering process, as described above, is illustrated in figure 2.5. σ_i denotes the cross section of the hard process.

The validity of this factorisation approach is proven in the QCD factorisation theorem (see for example [13]). The only constraint is the presence of a hard scale. A hard scale can be provided, for example, by the Q^2 of the event, the transverse momentum of the outgoing partons or in the case of heavy flavour production by the mass of the heavy quarks. Applying the factorisation theorem the ep cross section can be decomposed as follows:

$$d\sigma(ep \rightarrow eY) = \sum_{i \in p} \int_0^1 f_{i/p}(x, \mu_F^2) \cdot d\hat{\sigma}_i(\hat{s}, \alpha_s(\mu_R^2), \mu_R, \mu_F) dx \quad (2.15)$$

The cross section for the hard process $\hat{\sigma}_i$ depends on the centre-of-mass energy of the partonic system $\sqrt{\hat{s}}$, the factorisation scale μ_F , the strong coupling constant $\alpha_s(\mu_R^2)$ and the renormalisation scale $\mu_R \gg \Lambda_{QCD} \approx 200$ MeV. The renormalisation scale μ_R is introduced to remove the ultra violet divergences which occur when virtual corrections are taken into account in the calculation of the matrix element. These divergencies are absorbed into the running of the strong coupling constant $\alpha_s(\mu_R^2)$.

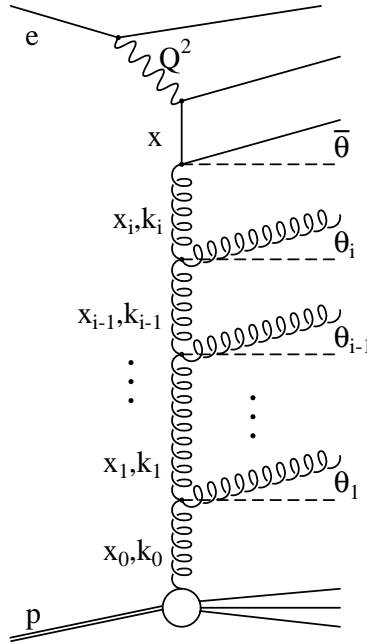


Figure 2.3: A number of subsequently emitted gluons form a gluon ladder with an arbitrary number of intermediate partons with momentum fraction x_i and virtualities k_i^2 . θ_i are the emission angles.

The proton parton density functions $f_{i/p}$ are universal, i.e. they are independent of the process and can be used in $p\bar{p}$ interactions at the Tevatron or in pp interactions at the LHC.

2.1.5 Photoproduction at HERA

The total rate of ep events at HERA is dominated by photoproduction events in which the virtuality Q^2 of the exchanged photon is small ($Q^2 \rightarrow 0$), i.e. the exchanged photon is quasi real. The reason for this behaviour is that the photon propagator leads to a factor $1/Q^4$ in the ep cross section (cf. equation 2.10). In the H1 experiment the boundary between the photoproduction and the DIS regime is experimentally defined at H1 by the acceptance of the backward calorimeter. For $Q^2 < 1 \text{ GeV}^2$ the electron is scattered under such a small angle that it escapes detection in the main part of the H1 detector. This kinematic range thus defines the photoproduction regime. For polar angles of the scattered electron close to 180° the kinematic variable y is given to a good approximation by

$$y = 1 - \frac{E'_e}{E_e} \quad (2.16)$$

The photon-proton centre-of-mass energy $W_{\gamma p}$ is related to y via the following equation:

$$W = \sqrt{ys - Q^2} \approx \sqrt{ys} \quad (2.17)$$

The quasi real photon can either directly enter the hard interaction or it can split into a $q\bar{q}$ pair which is subject to gluon splitting and gluon radiation before one of the partons from the

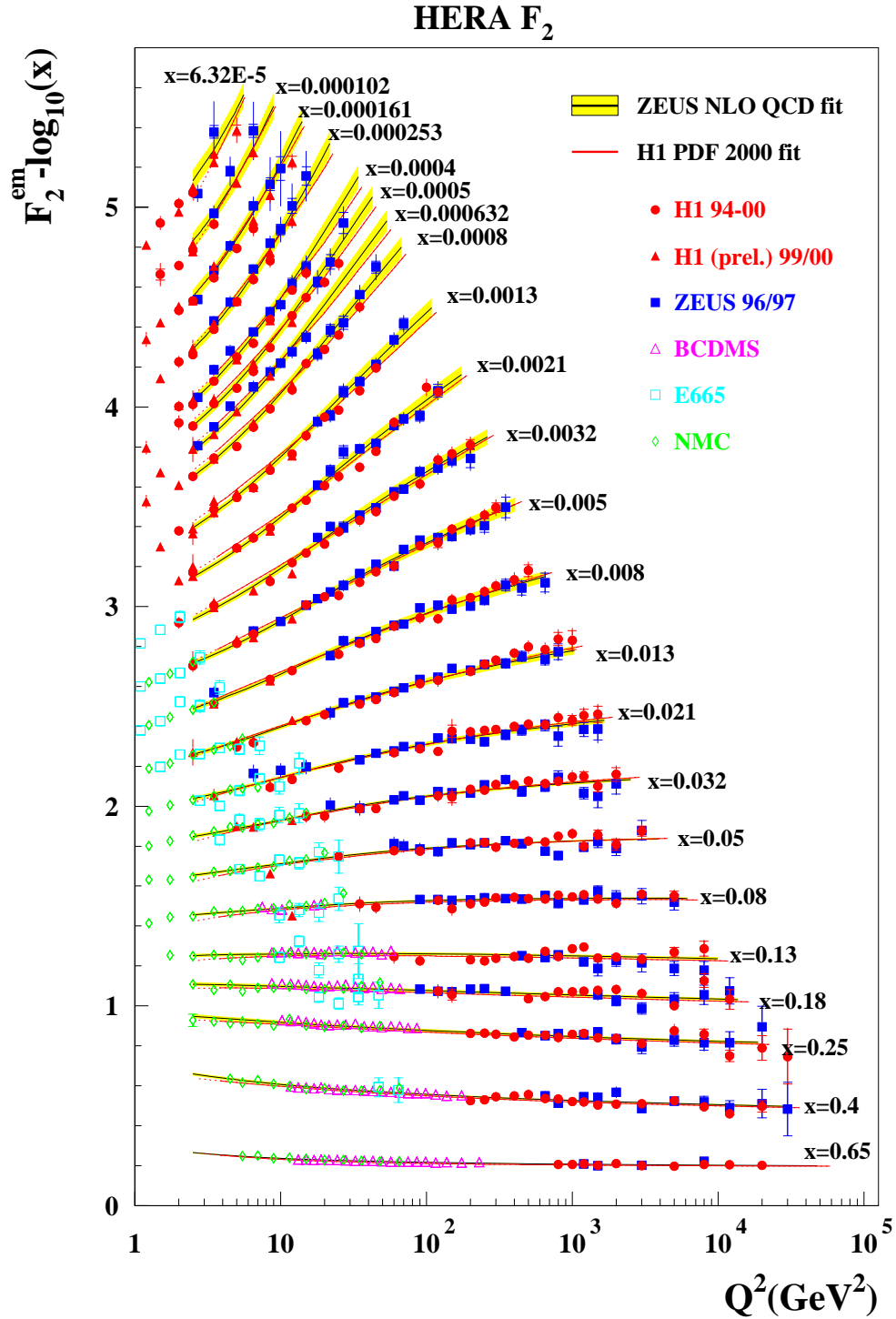


Figure 2.4: Measurements of the proton structure function F_2 as a function of Q^2 in bins of x by H1, ZEUS and fixed target experiments. The results of the QCD fits using the DGLAP evolution equations performed by H1 and ZEUS are shown as lines.

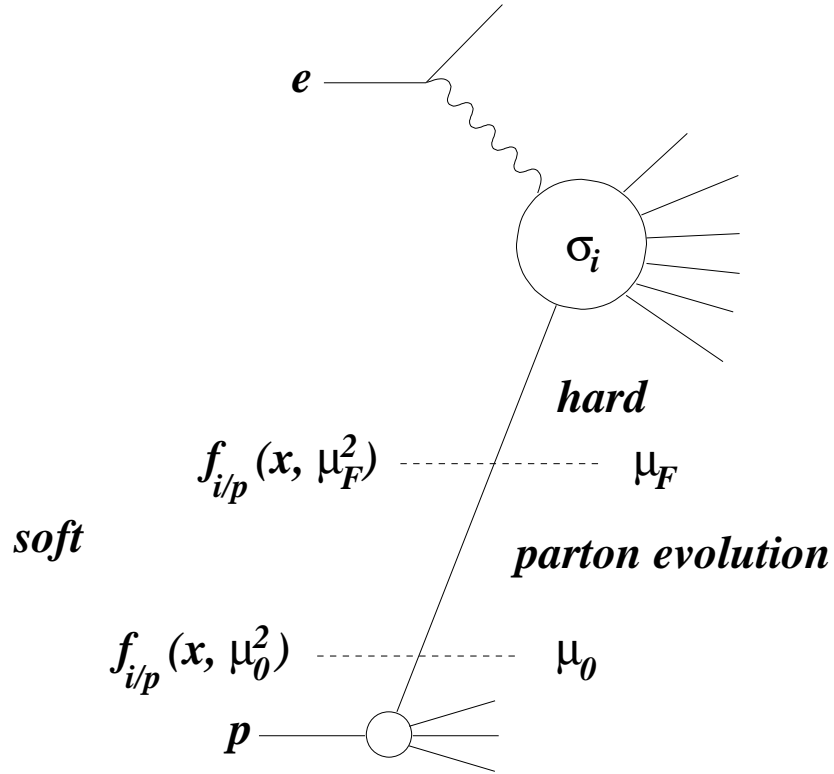


Figure 2.5: *Illustration of the principle of factorisation in QCD.*

cascade enters the hard interaction. The latter processes, referred to as resolved processes, are only relevant in the photoproduction regime since the virtuality Q^2 of the exchanged photon does not provide a hard scale anymore. The soft QCD processes are factorised and absorbed into the structure function of the photon $f_{j/\gamma}(x_\gamma, \nu_F^2)$. x_γ is the fraction of the photon momentum carried by the parton which enters the hard interaction and ν_F^2 is the factorisation scale. Taking into account resolved processes the cross section is given by the following expression:

$$d\sigma = \sum_{i \in p} \sum_{j \in \gamma} \int_0^1 \int_0^1 f_{i/p}(x_p, \mu_F^2) \cdot f_{j/\gamma}(x_\gamma, \nu_F^2) \cdot d\hat{\sigma}_{ij}(\hat{s}, \alpha_s(\mu_R^2), \mu_R, \mu_F, \nu_F) dx_p dx_\gamma \quad (2.18)$$

Here $\hat{\sigma}_{ij}$ is the partonic cross section. For direct processes x_γ is one and the parton j in the photon is the photon itself.

2.2 Production of Heavy Quarks at HERA

The main production mechanism for charm and beauty quarks at HERA is the photon-gluon fusion process. The production of heavy quarks during the fragmentation process via gluon splitting $g \rightarrow Q\bar{Q}$ is strongly suppressed at HERA due to the high quark masses. Top quarks are not produced in pairs since the centre-of-mass energy at HERA is not high enough and the single top quark production mechanism has a very low cross section.

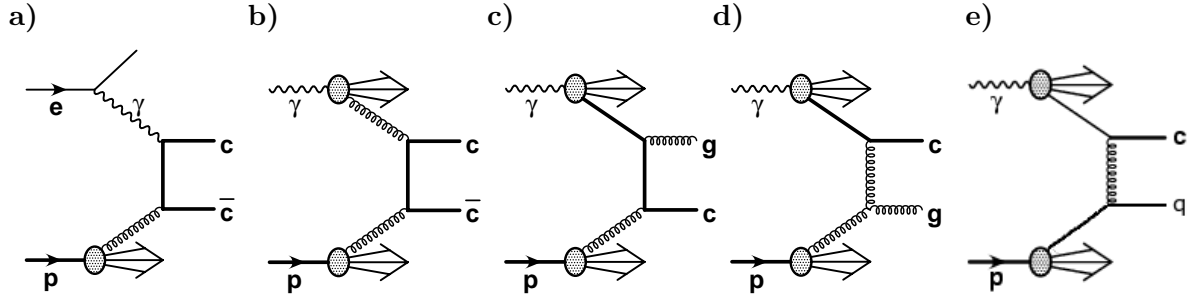


Figure 2.6: Photon-gluon fusion in leading order pQCD: a) direct process, b) normal resolved process, c)-e) excitation processes.

Figure 2.6 shows examples of the Feynman diagrams for charm production via photon-gluon fusion in leading order pQCD. The same diagrams apply to beauty production. Shown are the diagrams for the direct 2.6 a) and the resolved processes 2.6 b)-e). Among the resolved processes the normal resolved process and the excitation processes in which a heavy quark enters the hard interaction from the photon side can be distinguished. Since the heavy quark masses always provide a hard scale $m_{c,b} \gg \Lambda_{QCD}$ perturbative QCD calculations are possible down to very low virtualities Q^2 and transverse momenta p_t of the outgoing quarks. The study of heavy quark production is thus an ideal testing ground for perturbative QCD. Furthermore the gluon density in the proton can be probed measuring heavy flavour cross sections.

The direct photon-gluon fusion (PGF) cross section in leading order pQCD is given by [14]

$$\hat{\sigma}_{\gamma g \rightarrow Q\bar{Q}}(\hat{s}, Q^2) = \frac{\pi q_Q^2 \alpha \alpha_s}{\hat{s}} \left[(2 + 2\omega - \omega^2) \ln \frac{1 + \chi}{1 - \chi} - 2\chi(1 + \chi) \right] \quad (2.19)$$

where

$$\omega = \frac{2m_Q^2}{\hat{s}} \quad \text{and} \quad \chi = \sqrt{1 - \omega}$$

$\hat{s} = (p_Q + p_{\bar{Q}})^2$ is the squared centre-of-mass energy of the $Q\bar{Q}$ pair, q_Q the electric charge of the heavy quarks in unit of the proton charge and m_Q is the heavy quark mass. The cross section for beauty production is about two orders of magnitude smaller than the cross section for charm production since the mass of the beauty quark ($m_b \approx 4.75$ GeV) is much larger compared to the mass of the charm quark ($m_c \approx 1.5$ GeV). In addition the beauty cross section is suppressed due the smaller charge: $|q_b| = 1/3$ vs. $|q_c| = 2/3$.

2.3 Hadronisation

The long life-time of charm and beauty quarks allows them to form hadrons which can be experimentally observed. The transition from partons to colourless hadrons is called hadronisation. The hadronisation process cannot be described using perturbative QCD but phenomenological models have to be applied. Starting point are the partons from the perturbatively calculable final state, e.g. the parton configuration after the final state parton showering in leading order calculations. It is assumed that the full process can be factorised into a hard, perturbatively

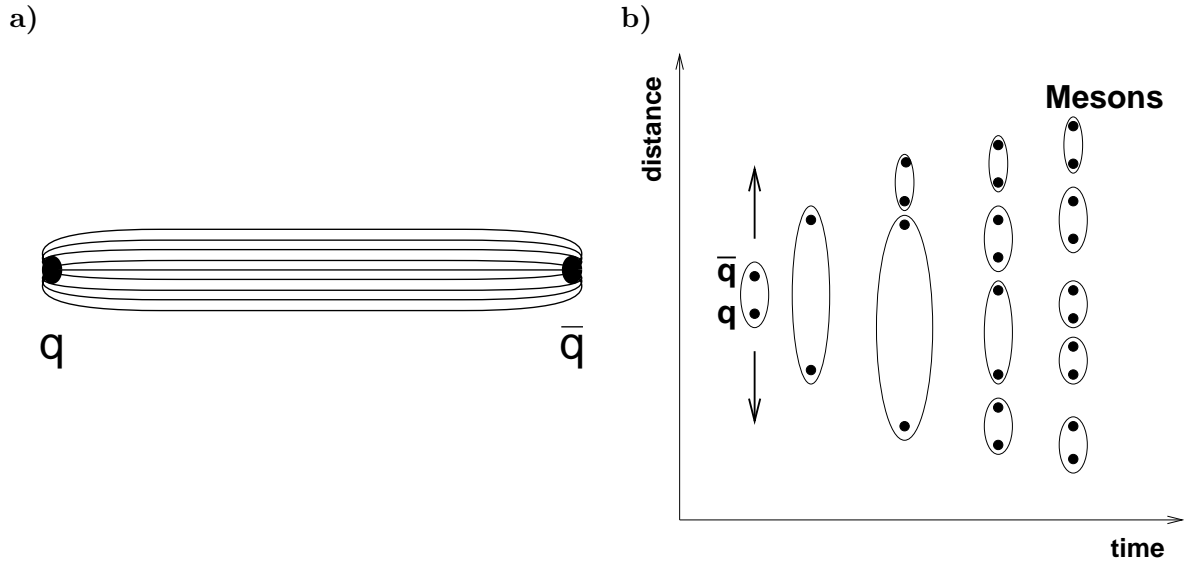


Figure 2.7: Illustration of the Lund string hadronisation model. a) The tube-like colour field between a quark and an anti-quark according to the QCD potential (cf. equation 2.20). b) Formation of colourless hadrons according to the Lund fragmentation model.

calculable and a soft, non-perturbative part and that the hadronisation is independent of the hard scattering process, i.e. the models and their parameters measured at one experiment, e.g. at the e^+e^- collider LEP, can be used at any other experiment.

One of the most successful hadronisation models is the Lund string model [15]. The colour field between two quarks is squeezed into a tube-like region, a colour string, as depicted in figure 2.7 a). The colour field is given by the QCD potential

$$V(r) = -\frac{4\alpha_s}{3r} + \kappa r. \quad (2.20)$$

Here the second term κr accounts for the QCD colour confinement which causes the colour interaction to become stronger when the quarks separate. Since κ is of the order 1 GeV/fm, the second term dominates at large distances r , leading to the tube-like shape of the colour field. The string breaks up if the energy is large enough to produce a $q\bar{q}$ pair which then may produce a cascade of additional quark pairs until the energy is exhausted and bound quark states are produced. This process is illustrated in figure 2.7 b). Within this model baryons are created via the production of diquark pairs $qq\bar{q}\bar{q}$.

While the transverse momentum spectrum of the produced hadrons is assumed to be Gaussian, the longitudinal momentum is derived from fragmentation functions $f(z)$. The fragmentation functions describe the probability for a Hadron H , which originates from a quark Q , to carry the fraction $z = (E + p_{\parallel})_H / (E + p)_{Q}$ of the quark's longitudinal momentum. Different fragmentation functions can be used within the Lund string model. In the following the two fragmentation function used in this analysis are presented. The Lund fragmentation function is defined as follows:

$$D_Q^H(z) = N \frac{(1-z)^a}{z} \exp \left[\frac{-bm_{\perp}^2}{z} \right] \quad (2.21)$$

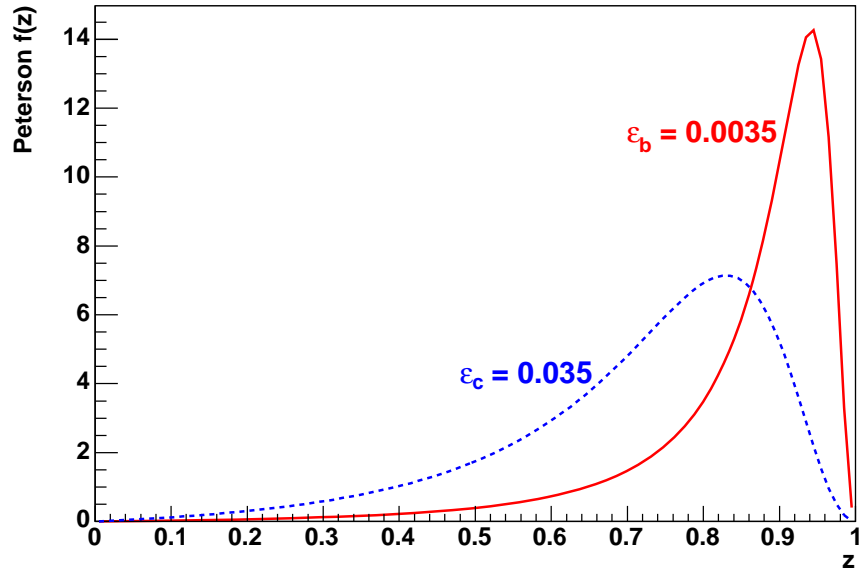


Figure 2.8: Peterson fragmentation functions for charm and beauty (next-to-leading order parameters for ϵ_c and ϵ_b are used).

Where $m_{\perp}^2 = E^2 - p_z^2$ is the transverse mass of the hadron H and a and b are parameters which have to be adjusted to data.

For heavy flavour production the Peterson fragmentation function $D_Q^H(z)$ [16] is preferentially used, since it provides a harder fragmentation which is needed to describe charm and beauty data:

$$D_Q^H(z) = \frac{N}{z} \left(1 - \frac{1}{z} - \frac{\epsilon_Q}{1-z} \right)^{-2} \quad (2.22)$$

The Peterson parameter ϵ_Q has to be adjusted to the data. It scales between flavours like $\epsilon_Q \propto \frac{1}{m_Q}$. At leading order a common choice for the parameter ϵ_Q is $\epsilon_c \approx 0.058$ for charm and $\epsilon_b \approx 0.0069$ for beauty hadrons. According to [17] the common choice at next-to-leading order is $\epsilon_c \approx 0.035$ and $\epsilon_b \approx 0.0033$. In figure 2.8 the Peterson fragmentation functions for the latter case are depicted. The fragmentation is harder for beauty quarks due to their larger mass. At next-to-leading order the fragmentation parameters are smaller because the possibility of gluon radiation is already included in the matrix element. An additional parametrisation is the Kartvelishvili fragmentation function [18].

2.4 Monte Carlo Event Generators

Monte Carlo event generators are used in high energy physics to model events as detailed as could be observed by a perfect detector. Since the process of event generation is too complex to be performed in one go, it is subdivided into several parts. This is illustrated in figure 2.9 for the example of a photon-gluon fusion event at HERA and a leading order plus parton shower event generator. The emission of virtual photons by the electron can be described using QED. In the photoproduction regime the photon flux $f_{\gamma/e}(y, Q^2)$ is given by the Weizsäcker-Williams

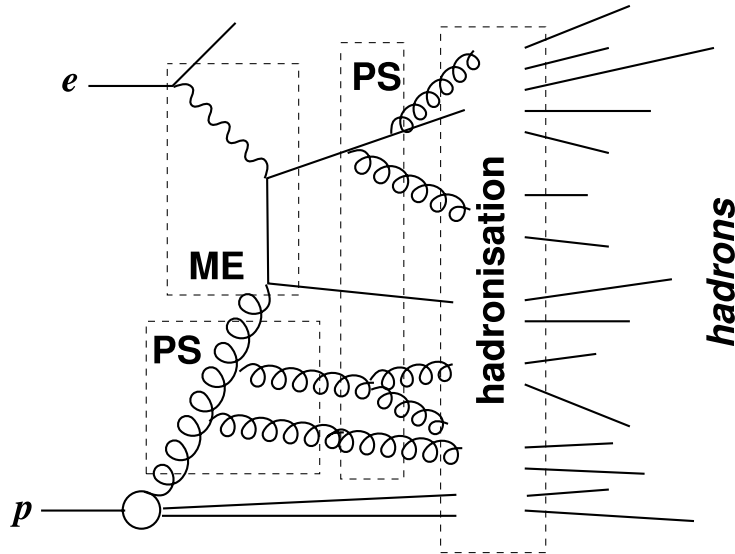


Figure 2.9: Principle layout of an event generator with initial and final state parton shower (PS), leading order matrix element (ME) and hadronisation.

approximation [19, 20]. The proton parton density function defines the flavour and the energy of the particle which takes part in the interaction from the proton side. To obtain the parton density function at the appropriate scale, parton evolution schemes, e.g. DGLAP or CCFM, are used. The parton from the proton starts off a sequence of branchings, such as $g \rightarrow gg$, leading to an initial state parton shower (PS). The photon and a parton from the initial state parton shower enter the $2 \rightarrow 2$ hard process. The matrix element (ME) of this process is calculated in leading order. The outgoing partons from the hard process are subject to final state parton showers. The main properties of an event are determined by the LO matrix element and the parton showers effectively approximate higher order effects. The outgoing partons from the parton showers enter the hadronisation step, which is based on phenomenological models.

The event generator PYTHIA [21] is used in this analysis to model signal as well as background events. PYTHIA is a leading order plus parton shower event generator which uses the collinear factorisation scheme, i.e. the DGLAP parton evolution and on-shell matrix elements. For the Monte Carlo data sets used in this analysis PYTHIA is run in the 'full inclusive' mode (MSTP(14)=30). Direct and resolved photon processes are considered using massless matrix elements for all flavours. The resolved photon processes include the normal resolved and the charm and beauty excitation processes (cf. figure 2.6). The Lund string model using the Peterson fragmentation function is used for the hadronisation step but Monte Carlo data sets using the Lund fragmentation function are generated as well to allow for systematic checks. The PYTHIA Monte Carlo is used to model the signal and the background distributions.

The cross sections obtained in this analysis are also compared to the predictions of the CASCADE event generator [22, 23]. CASCADE is based on the CCFM evolution equation and uses unintegrated parton density functions. Matrix elements are calculated off-shell. Resolved processes are not produced separately, but k_t factorisation effectively includes the excitation component.

The generated events are passed through a detailed simulation of the detector response based on the GEANT program [24]. For the reconstruction the same software is used as for data. The reconstructed PYTHIA Monte Carlo events are used to determine the reconstruction and the trigger efficiency.

Table A.1 in appendix A gives an overview of the Monte Carlo data sets used in the present analysis. The proton and the photon parton density functions, the fragmentation functions and the heavy quark masses which are used are quoted. In addition the main selection cuts are given.

2.5 Jets and Jet Algorithms

A jet is a collimated bunch of particles flying in the same direction. Jets are defined by jet algorithms which unambiguously allow to build jets from a set of input particles. These input particles can either be partons, hadrons or objects measured on detector level. The jet algorithm should be infrared and collinear safe. This means that the result of the algorithm for a given event must not be affected by processes like soft gluon radiation or collinear splitting, i.e. processes where a parton splits into two other partons with only a very small opening angle. A good jet algorithm also possesses a good correlation between jets on parton and jets on hadron level. This allows to identify jets on detector level with jets on parton level, e.g. heavy quarks produced via the BGF process.

The inclusive k_t algorithm [25, 26, 27], which is used in this analysis, fulfils the criteria listed above. It is a clustering algorithm which iteratively combines objects, the protojets, to jets until all input objects are merged. The algorithm is invariant under Lorentz boosts along the z -axis. In this analysis the ΔR -resolution and the p_t -weighted recombination scheme is used and the jet algorithm is applied in the laboratory frame.

The algorithm starts with a list of protojets, i.e. the input particles, and an empty list of jets. The iterative procedure to build jets is as follows:

1. For each protojet i and each pair of protojets ij the following distances are defined:

$$d_i = p_{t,i}^2 \quad (2.23)$$

$$d_{ij} = \min(p_{t,i}^2, p_{t,j}^2) \cdot \Delta R_{ij}^2 / R_0^2 \quad \text{with} \quad \Delta R_{ij}^2 = \Delta \eta_{ij}^2 + \Delta \phi_{ij}^2 \quad (2.24)$$

ϕ is the azimuthal angle and $\eta = -\ln \tan \frac{\theta}{2}$ is the pseudorapidity of the protojet. R_0 is a separation parameter and is chosen to be 1 in this analysis.

2. Find the smallest distances $d_{i,min}$ and $d_{ij,min}$.
3. If $d_{i,min} < d_{ij,min}$ the protojet i is removed from the list of protojets and added to the list of final jets. Otherwise, the protojets i and j with the smallest distance are merged using the p_t -weighted recombination scheme to form a new protojet:

$$p_{t,k} = p_{t,i} + p_{t,j} \quad (2.25)$$

$$\eta_k = \frac{p_{t,i} \cdot \eta_i + p_{t,j} \cdot \eta_j}{p_{t,k}} \quad (2.26)$$

$$\phi_k = \frac{p_{t,i} \cdot \phi_i + p_{t,j} \cdot \phi_j}{p_{t,k}} \quad (2.27)$$

4. Go to step 1 until there are no protojets left in the list.

The final jets found by this algorithm are massless and ordered with increasing p_t . In this analysis the two leading jets, i.e. the two jets with the highest transverse momentum p_t , are selected.

2.6 Dijet and Dilepton Events from Open Heavy Flavour

In open heavy flavour production the heavy quarks, which are produced via the BGF process, hadronise independently and form jets, whereas in hidden charm or beauty production, the heavy quarks form a bound state, e.g. a J/ψ ($c\bar{c}$) or Υ ($b\bar{b}$) meson. In the present analysis, the open charm and beauty production is studied using events with two leptons and two jets in the final state. For experimental reasons, which will be described later, only dimuon and muon-electron events are investigated. The jets and the leptons are used as a heavy flavour tag and to determine the fraction of charm and beauty events in the data samples. To determine the fraction of beauty events, the transverse momentum of the leptons with respect to the axis of the jet the lepton is associated to via the jet algorithm p_t^{rel} is used. In addition the charge and azimuthal angle correlation of the leptons

$$|\Delta\phi(\mu_1, l_2)| \times Q(\mu_1) \times Q(l_2)$$

is exploited to determine both the charm and the beauty fraction. Here, $Q(\mu_1)$ and $Q(l_2)$ are the charges of the (first) muon and the second lepton in units of the proton charge and $|\Delta\phi(\mu_1, l_2)|$ is the azimuthal difference between the leptons. In the following the properties of events with two leptons and two jets from open heavy flavour production are investigated. The aim is to bring out the different experimental signatures one expects for charm and beauty events and to investigate the production mechanisms in detail.

To study dilepton and dijet ($\mu l j j$) events from charm and beauty the PYTHIA Monte Carlo is used. All distributions which are shown in this section are on generator level, i.e. before the detector simulation and event reconstruction but after the parton showering and hadronisation. They are normalised to one to allow for shape comparisons. Beauty events are defined by requiring that there be at least one beauty quark in the list of outgoing hard partons. Charm events are separated from beauty events by requiring that there be at least one charm quark but no beauty quark in the list of outgoing hard partons. The selection cuts listed in table 2.1 are applied. In addition it is required that both leptons are associated to one of the selected jets via the jet algorithm. 94 % of all charm events fulfil this requirement. For beauty the fraction is considerably smaller and amounts to 67 %. This is a consequence of the larger contribution from excitation processes in beauty events as will be described in detail later. Leptons are selected if they originate from a direct or indirect decay of a charm or beauty hadron.

2.6.1 Dilepton Charge and Angle Correlation

According to the leading order picture of the BGF process in photoproduction, the outgoing heavy quarks of the hard interaction are back-to-back in the $r\phi$ -plane of the laboratory frame.

Event Selection Cuts	
Photoproduction	$Q^2 < 1 \text{ GeV}^2$ $0.1 < y_h < 0.7$
First Lepton (Muon)	$p_t > 2.0 \text{ GeV}$ $30^\circ < \theta < 130^\circ$
Second Lepton (Electron or Muon)	$p_t > 1.0 \text{ GeV}$ $20^\circ < \theta < 150^\circ$
Jets (inclusive k_t -algorithm)	$p_t > 5(4) \text{ GeV}$ $20^\circ < \theta < 160^\circ$

Table 2.1: Summary of the event selection cuts (generator level).

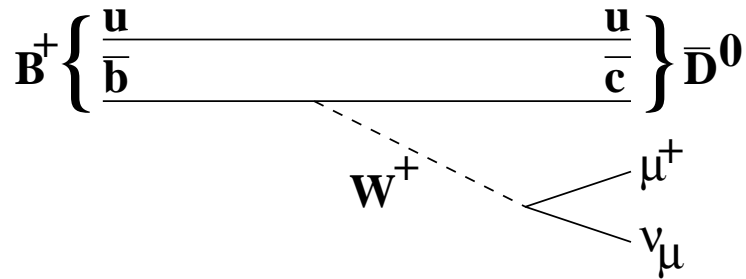


Figure 2.10: The decay $B^+ \rightarrow \bar{D}^0 \mu^+ \nu_\mu$ in the spectator model.

The heavy quarks hadronise independently and form heavy hadrons, which decay into lighter particles. The decay lengths $c\tau$ are of the order of a few hundred μm . In this analysis heavy hadrons are tagged via their decay into high p_t leptons. The leptonic decay can be explained within the spectator model where the heavy quark as a constituent of the hadron decays semileptonically without being influenced by the accompanying quarks. This is illustrated in figure 2.10, which shows the decay of a B^+ meson into a \bar{D}^0 meson, an antimuon and a muon-neutrino in the spectator model. The probability for the leptonic decay of a W boson is [28]:

$$\mathcal{P}(W^+ \rightarrow l^+ \nu) = (10.68 \pm 0.12)\% \quad (2.28)$$

l indicates either an electron, a muon or a tau-lepton. The b quark decays predominantly into a c quark. The direct decay of a b quark into a u quark is strongly suppressed since the magnitude of the V_{ub} matrix element of the Cabibbo-Kobayashi-Maskawa-Matrix (CKM-matrix), which is related to the transition probability $b \rightarrow u$, is very small ($|V_{ub}| \approx 0.004$). The charm quark may decay semileptonically as well, yielding a high p_t lepton. The charm quark predominantly decays into a strange quark. Other decays are suppressed according to the CKM-matrix.

Open charm production yields only unlike sign lepton pairs with a large opening angle $\Delta\phi \approx 180^\circ$. This is shown in figure 2.11 for the example of muon pair production in PGF. In open beauty production more configurations are possible. This is due to cascade decays such as shown in figure 2.12. The b quark decays into a c quark which then decays into an s quark. Both decays can be semileptonic or purely hadronic. The following four configurations are possible in the case of open beauty production:

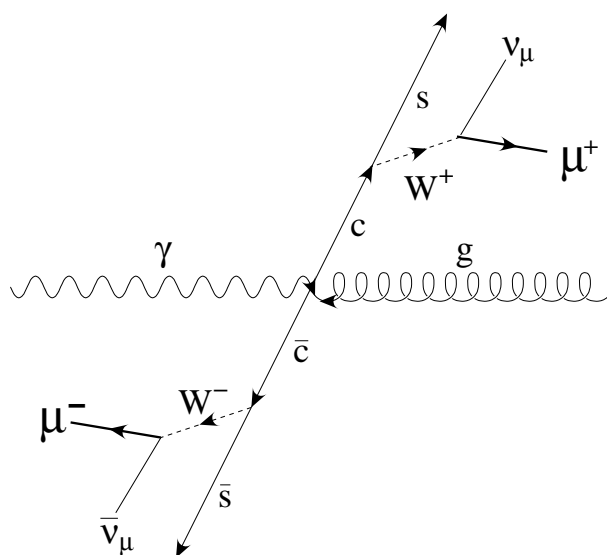


Figure 2.11: Production of an unlike sign muon pair in photon-gluon fusion.

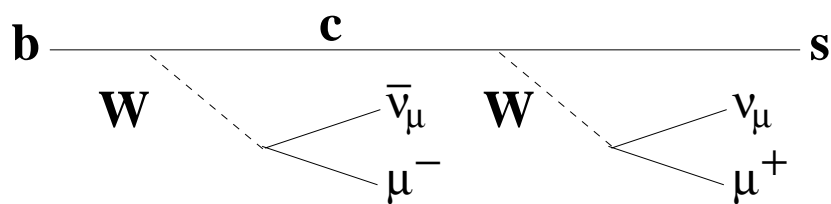


Figure 2.12: Cascade decay of a beauty quark.

	$\Delta\phi \approx 180^\circ$	$\Delta\phi \approx 0^\circ$
unlike sign (+-)	charm and beauty $\mu^- \bar{s} \leftarrow \bar{c} c \rightarrow s \mu^+$ $\mu^+ \bar{c} \leftarrow \bar{b} b \rightarrow c \mu^-$ $\bar{s} \mu^- \leftarrow \bar{c} \leftarrow \bar{b} b \rightarrow c \rightarrow \mu^+ s$	beauty $\mathbf{b} \rightarrow \mu^- c \rightarrow \mu^- \mu^+ s$ $\bar{\mathbf{b}} \rightarrow \mu^+ \bar{c} \rightarrow \mu^+ \mu^- \bar{s}$
like sign (++, --)	beauty $\mu^+ \bar{c} \leftarrow \bar{b} b \rightarrow c \rightarrow \mu^+ s$ $\bar{s} \mu^- \leftarrow \bar{c} \leftarrow \bar{b} b \rightarrow c \mu^-$	—

Table 2.2: Possible lepton charge and azimuthal angle correlations in open charm and beauty production. $\Delta\phi$ is the azimuthal difference between the leptons. Note that only quarks and leptons are considered. The neutrinos are omitted.

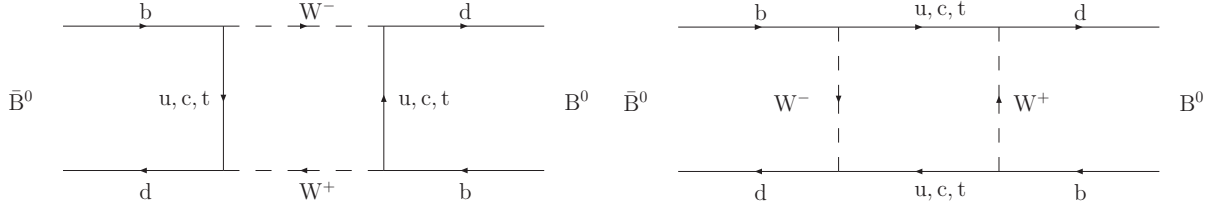


Figure 2.13: Feynman diagrams for $B^0 - \bar{B}^0$ mixing.

1. Both leptons originate from a direct b decay, yielding an unlike sign (+-) lepton pair with a large opening angle $\Delta\phi \approx 180^\circ$. This configuration is also allowed for open charm production.
2. One lepton originates from a direct b decay while the other lepton is from a decay of a c quark which was produced in the cascade decay of the other beauty quark. This process is a source of like sign (++, --) lepton pairs with a large opening angle $\Delta\phi \approx 180^\circ$.
3. Both leptons come from a c decay (in a cascade) yielding unlike sign (+-) leptons with a large opening angle $\Delta\phi \approx 180^\circ$.
4. The leptons originate from the cascade decay of the same b . Here unlike sign (+-) leptons with a small opening angle $\Delta\phi \approx 0^\circ$ are expected.

All the possible dilepton charge and azimuthal angle correlations, which are observed for open charm and beauty production, are summarised in table 2.2. Due to $B_q^0 - \bar{B}_q^0$ mixing ($q = d, s$) deviations from this simple picture arise, e.g. a like sign lepton pair with a large opening angle $\Delta\phi \approx 180^\circ$ is produced if both B mesons decay directly producing a lepton but one of the two mesons oscillates before it decays. The Feynman diagrams for $B^0 - \bar{B}^0$ mixing are depicted in figure 2.13. The flavour of the heavy quark is changed by the weak interaction.

Figure 2.14 shows the dilepton charge and angle correlation

$$|\Delta\phi| \times Q(\mu) \times Q(e) \quad (2.29)$$

for muon-electron events in open charm and beauty production as predicted by the PYTHIA Monte Carlo. The events fulfil the selection cuts listed in table 2.1. Here Q_μ and Q_e refer to

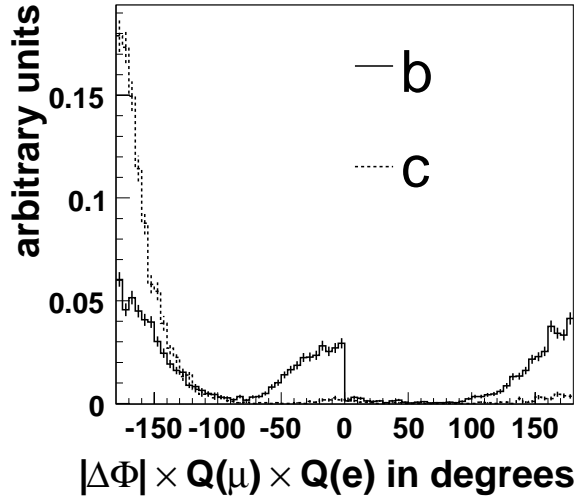


Figure 2.14: The charge and angle correlation of the muon and the electron according to the PYTHIA Monte Carlo.

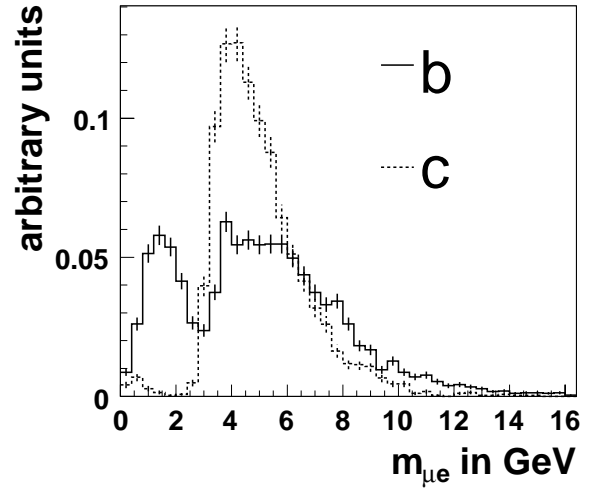


Figure 2.15: The invariant mass $m_{\mu e}$ of the muon-electron system according to the PYTHIA Monte Carlo.

the muon and electron charge in units of the proton charge and $\Delta\phi$ is the azimuthal difference between the leptons. The distributions show the expected behaviour (cf. table 2.2). The distribution of the azimuthal difference between the leptons tends to be broader for beauty events. This is a consequence of the much larger beauty quark mass. The $|\Delta\phi| \times Q(\mu) \times Q(e)$ distribution is exploited in this analysis to distinguish between charm and beauty events.

Figure 2.15 shows the distribution of the invariant mass $m_{\mu e}$ of the muon-electron system. The invariant mass is strongly correlated with the azimuthal difference $\Delta\phi$ between the leptons. For charm events one expects $\Delta\phi \approx 180^\circ$ which leads to large invariant masses $m_{\mu e} \gtrsim 3$ GeV. In the case of beauty events there are contributions where the opening angle between the leptons is small giving rise to events with small invariant masses. For large opening angles the invariant mass $m_{\mu e}$ tends to be larger for beauty events compared to charm events. This is again a consequence of the larger beauty quark mass.

2.6.2 Relative Transverse Momentum p_t^{rel}

Leptons from b quark decays tend to have a much larger transverse momentum with respect to the direction of flight of the parent quark than leptons from charm decays. This is due to the considerably larger mass of beauty quarks in comparison to charm quarks. Using the axis of the jet the decay lepton is associated to via the jet algorithm as an estimator for the quark direction, the observable p_t^{rel} is defined as the transverse momentum of the lepton with respect to the jet axis (cf. figure 2.16):

$$p_t^{rel} = \frac{|\vec{p}_{lep} \times (\vec{p}_{jet} - \vec{p}_{lep})|}{|\vec{p}_{jet} - \vec{p}_{lep}|} \quad (2.30)$$

Figure 2.17 shows the p_t^{rel} spectra for the muon and the electron. The distributions for both charm and beauty are investigated. The p_t^{rel} spectra for beauty events are much harder compared

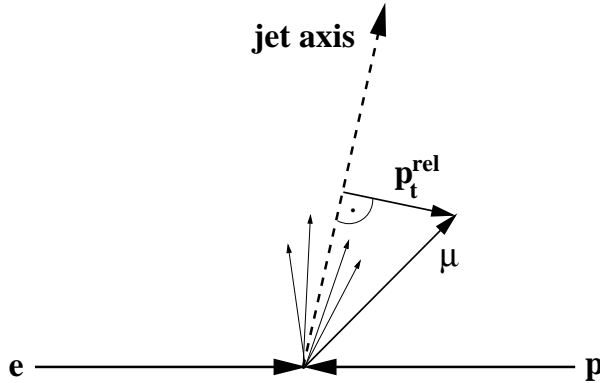


Figure 2.16: The definition of the observable p_t^{rel} .

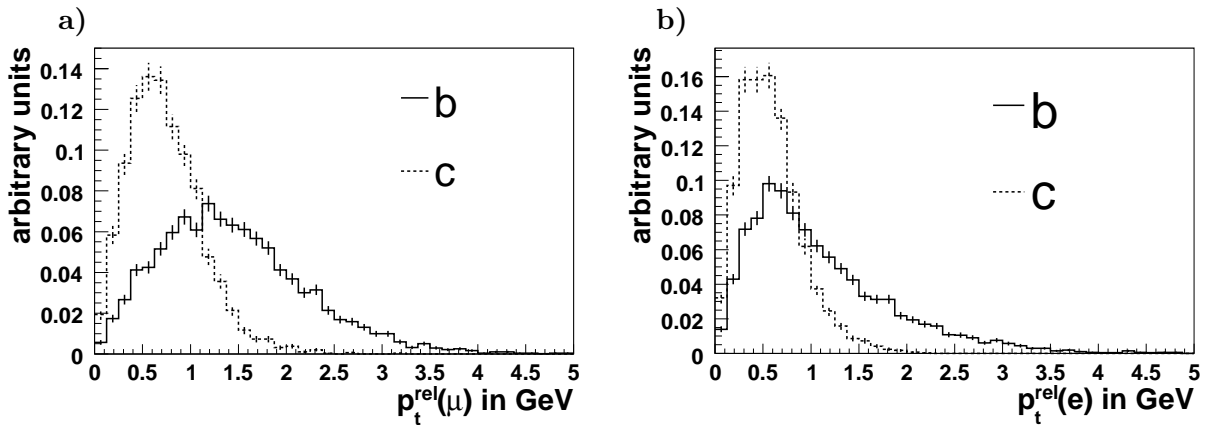


Figure 2.17: p_t^{rel} distributions for the muon (a) and the electron (b) according to the PYTHIA Monte Carlo (generator level).

to the spectra in charm events. This is exploited to separate events with a muon from a semileptonic b quark decay from charm and light quark events.

2.6.3 Contributions from Direct and Resolved Processes

The observable x_γ^{obs} is related to the fraction of the photon energy x_γ entering the hard interaction. It is obtained from the two selected jets and the hadronic final state according to the following formula

$$x_\gamma^{\text{obs}} = \frac{\sum_{\text{Jet } 1}(E - p_z) + \sum_{\text{Jet } 2}(E - p_z)}{\sum_{\text{HFS}}(E - p_z)} \quad (2.31)$$

where the sums in the nominator run over all particles associated with the two leading jets and that in the denominator over all detected particles of the hadronic final state. In the leading order picture, x_γ^{obs} approaches unity for the direct process, since the hadronic final state consists of only two hard jets and the proton remnant in the forward region which contributes little to $\sum_{\text{HFS}}(E - p_z)$. For resolved processes x_γ^{obs} tends to be smaller.

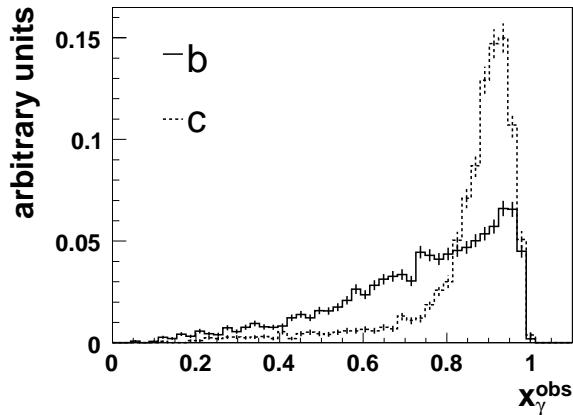


Figure 2.18: x_γ^{obs} for charm and beauty events as predicted by the PYTHIA Monte Carlo (muon-electron events).

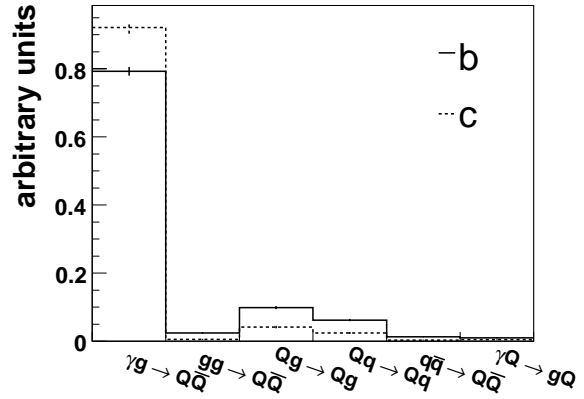


Figure 2.19: $2 \rightarrow 2$ hard subprocesses contributing to the muon-electron sample according to the PYTHIA Monte Carlo.

Figure 2.18 shows the x_γ^{obs} distributions for charm and beauty events according to the PYTHIA Monte Carlo. The contribution from resolved processes is smaller for charm events compared to beauty events. This is also shown in figure 2.19 where the contributions from the different $2 \rightarrow 2$ hard subprocesses are investigated for charm and beauty events. The contribution from direct processes ($\gamma g \rightarrow Q\bar{Q}$) is dominating. According to the PYTHIA Monte Carlo the direct contribution amounts to about 80% for beauty and about 90% for charm events. Among the resolved processes the heavy quark excitation processes $Qg \rightarrow Qg$ (plus charge conjugate) and $Qq \rightarrow Qq$ (plus charge conjugate) are the most important ones. The normal resolved component ($gg \rightarrow Q\bar{Q}$) and the resolved process with a light quark from the photon and the proton side ($q\bar{q} \rightarrow Q\bar{Q}$ plus conjugate) are negligible. The contribution from direct processes with a heavy quark entering the hard interaction from the proton side ($\gamma Q \rightarrow gQ$ plus conjugate) are negligible as well.

Processes with only one outgoing heavy quark are suppressed in the present analysis due to the requirement of two high p_t leptons. This effect is much larger for charm than for beauty. This has mainly two reasons. Firstly, in contrast to a c quark a b quark can decay via a cascade producing two leptons, which fulfil the selection cuts. Secondly, in beauty excitation events a beauty quark in the photon remnant may decay producing a high p_t lepton which can be detected in the central part of the H1 detector. This is unlikely for charm quarks since their mass is considerably smaller. Beauty excitation events which fulfil the dilepton selection cuts are likely to be rejected by the requirement that both leptons are associated to one of the selected jets, since it is likely that the selected high p_t jets are produced by the two outgoing partons from the hard subprocess. According to the PYTHIA Monte Carlo about 50 % of the events from beauty excitation are lost due to the requirement that the leptons are associated to the jets. For direct events the loss amounts only to 27 %. This is still significantly larger in comparison to charm events where only 6 % of the events are lost. Figure 2.20 shows the lepton charge and angle correlation $|\Delta\phi| \times Q(\mu) \times Q(e)$ for resolved (mainly excitation) and direct beauty events with and without the requirement that both leptons are associated to a jet. In events from beauty excitation the contribution from events with leptons from a cascade decay of a B hadron is much larger than in direct events. As described above, this is a consequence of the dilepton

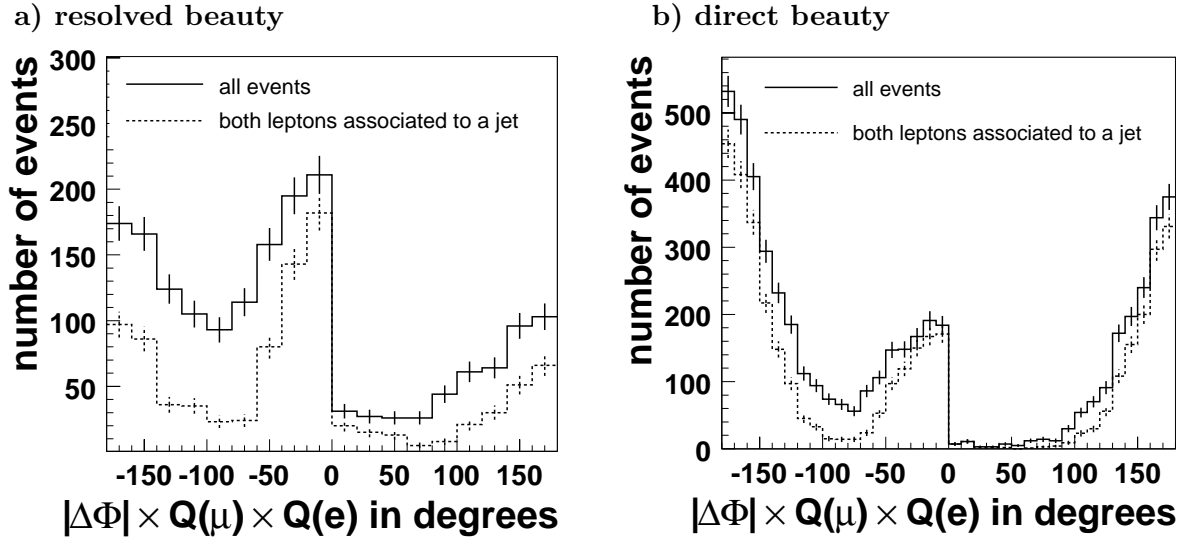


Figure 2.20: Charge and angle correlation of leptons from resolved (a) and direct (b) processes according to the PYTHIA Monte Carlo (beauty).

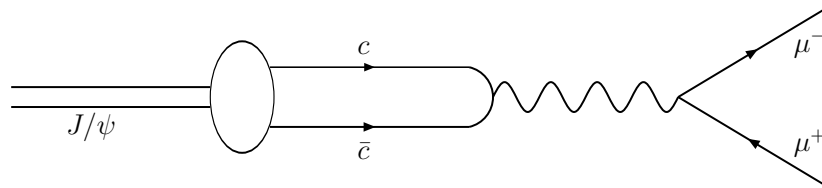


Figure 2.21: Diagram for the decay of a J/ψ meson into two unlike sign muons.

selection. This effect is much larger if the leptons are required to be associated to one of the selected jets.

2.7 Other Sources of Lepton Pairs at HERA

In contrast to muon-electron events there are several production mechanisms for muon pairs in ep collisions. The most important sources of muon pairs which are considered as background in this analysis are:

1. Quarkonium decays

Bound $q\bar{q}$ states are a source of unlike sign muon and electron pairs. The invariant mass of the decay leptons is equal to the mass of the bound state thus leptons from this source can be identified by peaks in the invariant mass distribution. This resonant background can be easily removed from the dimuon sample by excluding the mass regions where $q\bar{q}$ states contribute. Another possibility is to require that the selected muons are not isolated since leptons from open heavy flavour decays are accompanied by hadronic activity while leptons from quarkonia tend to be isolated. Only promptly produced quarkonia are considered

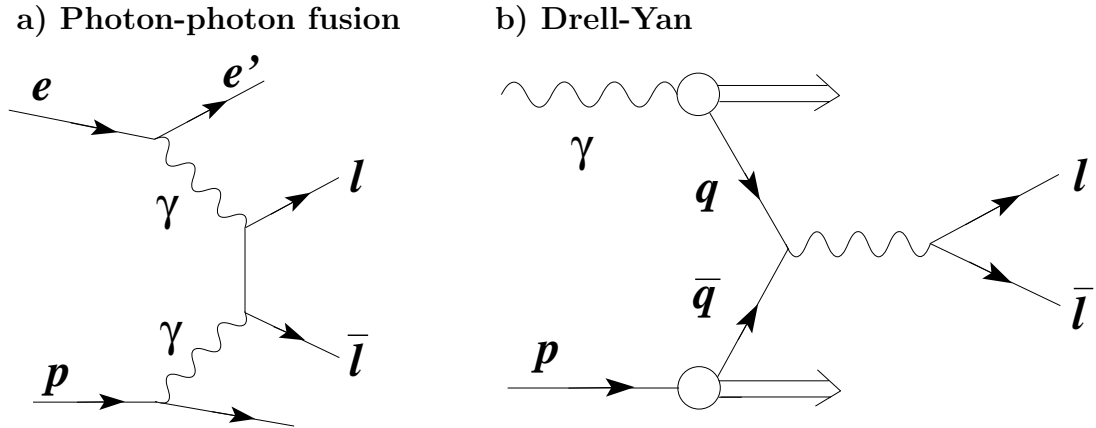


Figure 2.22: Production of unlike sign lepton pairs in photon-photon fusion (a) and Drell-Yan (b) processes.

as background. J/ψ mesons from the decay of a B-hadron for example are considered as signal.

Contributions from light meson decays, e.g. ϕ -, ρ^0 -, ω -, η - and η' -mesons, to the dimuon sample are negligible due to the small branching fractions for the decay into two leptons and due to the relatively high momentum cuts which are imposed on the muons.

Bound states of two charm (J/ψ and ψ' mesons) or two beauty quarks (Υ) from hidden charm and beauty production are the most important sources of resonant background in this analysis. The largest contribution arises from inelastically produced J/ψ mesons. Again this contribution is suppressed due to the relatively high momentum cuts on the muons. The schematic Feynman diagram for the muonic decay of a J/ψ meson is depicted in figure 2.21.

2. Photon-Photon Fusion and Drell-Yan processes

Figure 2.22 shows the leading order Feynman diagrams for the photon-photon fusion and the Drell-Yan process. Both processes are sources of unlike sign lepton pairs. Due to the requirement of two jets in the final state the contributions from photon-photon fusion and Drell-Yan processes to the dimuon sample are negligible.

Except for inelastic J/ψ production all background processes discussed here are negligible in this analysis.

CHAPTER 3

THE H1 EXPERIMENT AT HERA

The data used in this analysis were taken by the H1 detector at the electron proton storage ring HERA. In this chapter the H1 detector and the HERA machine are described. First an overview of the collider is given. In the subsequent section the H1 detector is described. The focus is on the detector components most relevant for this analysis namely the central tracking system, the calorimeters and the muon system. In the last section of this chapter the experimental methods used to study the production of charm and beauty quarks are discussed and some recent results from the HERA experiments H1 and ZEUS are presented.

3.1 HERA

The electron proton storage ring HERA¹ is located at the DESY² laboratory in Hamburg, Germany. The storage ring measures 6.3 km in circumference and consists of two independent accelerators for electrons and protons, respectively. Electrons are accelerated to energies of 27.6 GeV and protons to energies of 920 GeV (820 GeV before 1998) yielding a centre-of-mass energy of about $\sqrt{s} = 320$ GeV at the two interaction regions where the multi-purpose detectors H1 and ZEUS are located (cf. figure 3.1). The protons are accelerated to 40 GeV before they are injected. To guide the proton beam superconducting dipole magnets at 4.68 T are used. The proton ring was designed to accelerate and store up to 210 proton bunches. The design current is 760 μA per bunch. The electron ring is equipped with a warm magnet system at 0.165 T to guide the electron beam. Electrons are injected at 12 GeV. The design current for electrons is 290 μA per bunch. HERA can be operated with both electrons and positrons. For positrons a longer beam lifetime at high currents is obtained. Electron and proton bunches collide every 96 ns. In the year 2000 an average luminosity of $\langle L \rangle = 6.47 \times 10^{30} \text{ cm}^{-2}\text{s}^{-1}$ was reached. The average current was $\langle I_p \rangle = 86.77$ mA for protons and $\langle I_e \rangle = 25.12$ mA for electrons. Since the HERA upgrade the luminosity is considerably larger. In the year 2005 HERA delivered in average a luminosity of $\langle L \rangle = 17.20 \times 10^{30} \text{ cm}^{-2}\text{s}^{-1}$. This was achieved by increasing in the specific luminosity with the help of additional focussing magnets which were installed close to the interaction points. The average currents in 2005 were similar to the currents in the year 2000.

¹Hadron-Elektron-Ring-Anlage

²Deutsches Elektronen Synchrotron

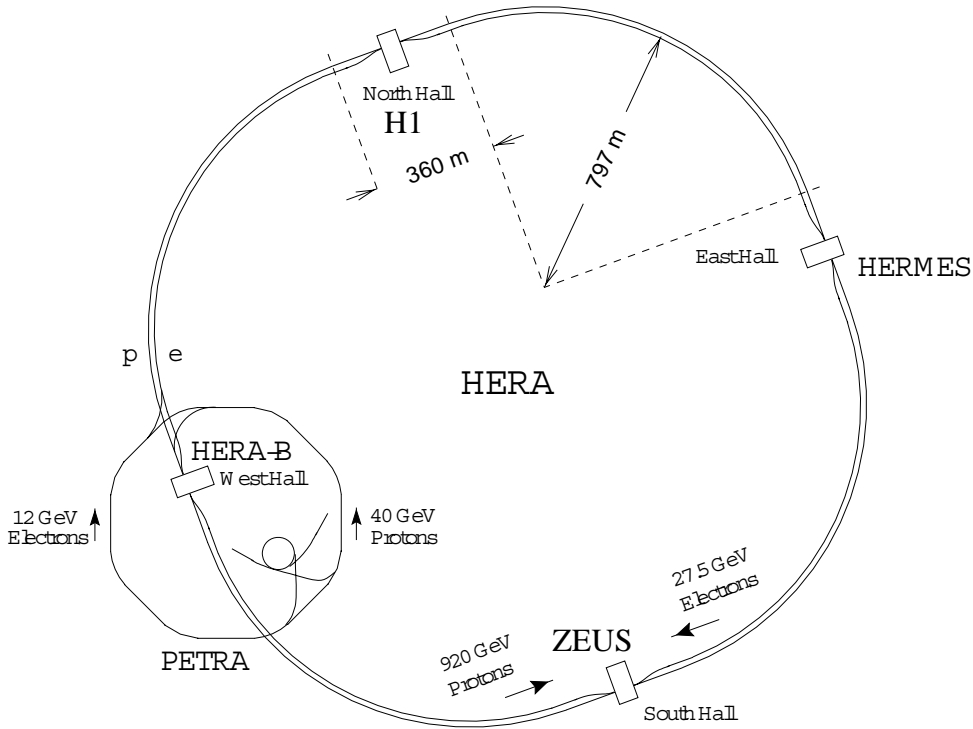


Figure 3.1: The electron proton storage ring HERA and the location of the experiments.

3.2 The H1 Detector

The H1 detector is described in detail in [29] and [30]. Here just a brief overview with emphasis on the detector components most relevant for this analysis is given. Figure 3.2 shows a longitudinal cut through the H1 detector along the beam line. The directions of flight of the electron and proton beam are indicated. Also shown is the reference frame commonly used at the H1 experiment. The right-handed Cartesian coordinate system has its origin in the nominal interaction point. The positive z -axis points in the direction of the proton beam, also called the forward direction. The x -axis is horizontal, pointing to the centre of the HERA rings. The polar angle θ is the angle with respect to the z -axis. The azimuthal angle ϕ is measured relative to the x -axis in the xy -plane. The detector was designed to cover almost the full solid angle around the nominal interaction region. This is necessary for energy flow measurements as well as missing energy detection. Since the energy of the proton beam is considerably larger than the energy of the electron beam, the centre of mass is boosted along the proton direction ($\gamma_{cm} = 2.86$). For this reason the H1 detector is more massive and highly segmented in the forward region.

The innermost part of the detector consists of the forward and the central tracking system. The tracking system allows to reconstruct the four momenta of charged particles and to identify particles by measuring their specific energy loss due to ionisation dE/dx . A superconducting solenoid surrounding both the tracking system and the calorimeter provides an almost uniform magnetic field of 1.15 T parallel to the HERA beams necessary for the momentum measurement. The coil is located outside the calorimeter to reduce the amount of dead material in front of the main detector components. The iron yoke which returns the magnetic flux of the solenoid

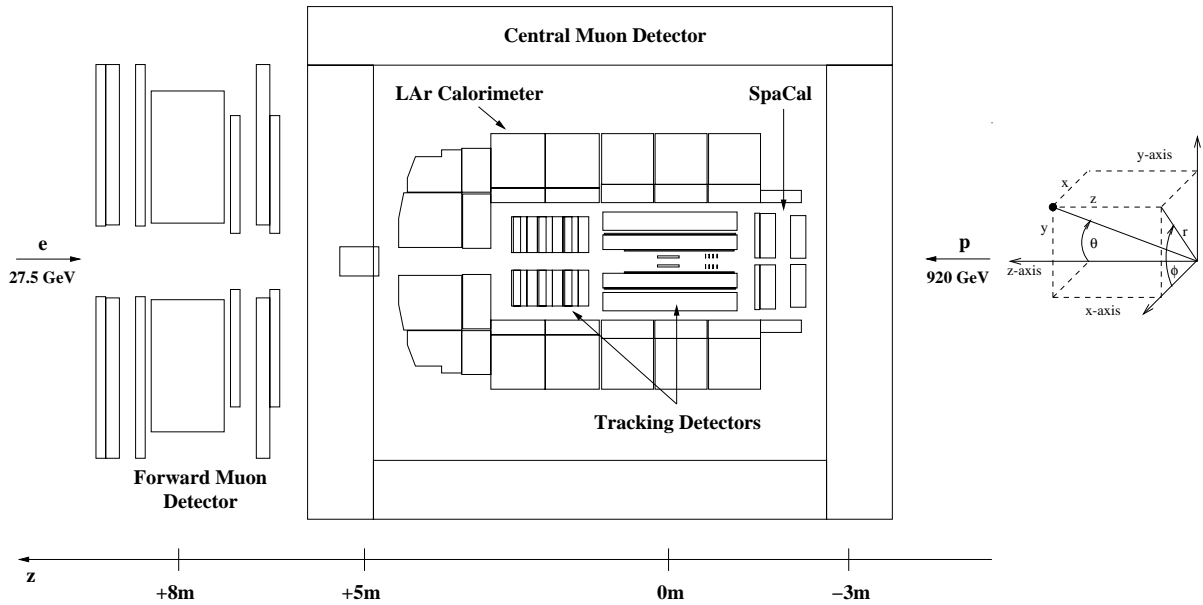


Figure 3.2: Schematic side view of the H1 detector at HERA. Also shown is the coordinate system with the z -axis along the direction of flight of the proton beam. The size of the detector is about $12 \times 15 \times 10 \text{ m}^3$ and the mass amounts to approximately 2800 t .

is instrumented with limited streamer tubes and is used as muon detector. The liquid argon calorimeter consists of an electromagnetic and a hadronic part. It is used for the reconstruction of the hadronic final state and to detect the scattered electron for virtualities Q^2 above 100 GeV^2 . The spaghetti calorimeter, SpaCal, detects the scattered electron under smaller electron scattering angles and covers the polar angular range $153^\circ < \theta < 177^\circ$ which corresponds to photon virtualities between 2 GeV^2 (4 GeV^2 after the detector upgrade) and 100 GeV^2 .

The forward region of the detector is equipped with a muon spectrometer which allows to detect muons with momenta above 5 GeV within the polar angular range $3^\circ < \theta < 17^\circ$. The forward muon detector (FMD) consists of a toroid magnet between three double layers of drift chambers at both sides. The drift chambers allow to measure the muon track before and after the magnet. The momentum can be deduced from the deflection of the muon trajectory in the magnetic field of the toroid.

To tag the proton remnant the PLUG calorimeter was installed in the very forward region. It covers the polar angular range between 0.6° and 4° .

The rate of Bethe-Heitler bremsstrahlung processes $ep \rightarrow e\gamma p$ is used to measure the luminosity at the H1 experiment. For the offline luminosity measurement the radiated photon is detected in a calorimeter at $z = -102.9 \text{ m}$. During the detector upgrade the HERA I photodetector made of KRS (Kristallschmelze) crystals was replaced by a quartz-fibre/tungsten Čerenkov sampling calorimeter suitable for high radiation level environments. The photon detector is located close to the beam pipe since the angular distribution for the photons is strongly peaked in the direction of the incident electron beam. For the online luminosity measurement in the HERA I running phase the electron and the photon from the Bethe-Heitler process were detected in coincidence using the photon detector and an electron tagger at $z = -33.4 \text{ m}$. In the HERA II running phase only the photon detector is used for the online luminosity measurement. The integrated

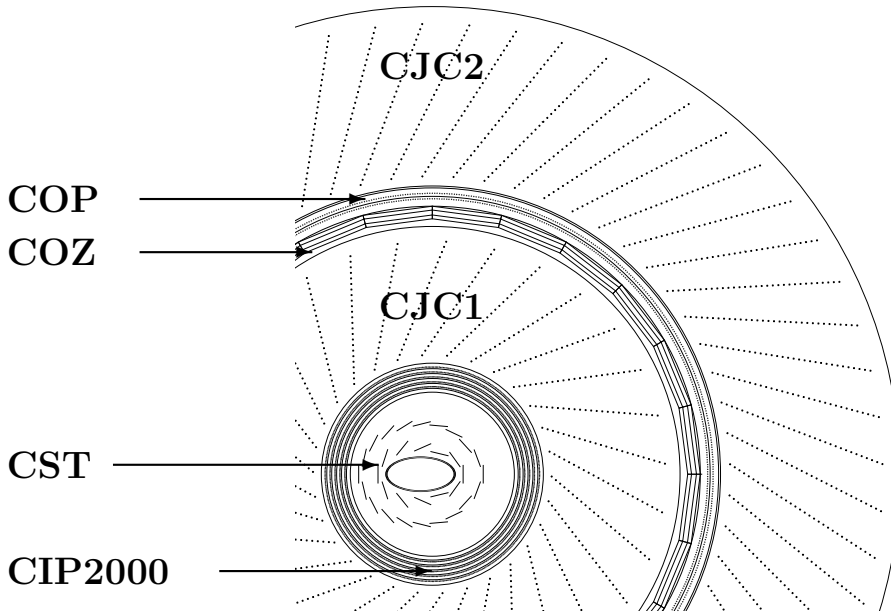


Figure 3.3: Cross section of the central tracking system perpendicular to the beam axis. Shown is the configuration after the detector upgrade in the year 2001 (HERA II).

luminosity can be determined to a precision of 1.5%. The electron tagger is also used to detect the electron in photoproduction events where the electron is scattered under a very small angle ('tagged photoproduction').

In the following the central tracking detectors, the calorimeters, the muon detector and the trigger and the data acquisition system are described in more detail.

3.2.1 Central Tracking System

Figure 3.3 shows a cross section of the central tracking system after the detector upgrade in the year 2001.

The main tracking devices are the two gas-filled coaxial cylindrical central jet chambers, the CJC1 and CJC2. The inner jet chamber, the CJC1, consists of 30 drift cells with 24 sense wires each and covers the polar angle range of $11^\circ < \theta < 169^\circ$. The outer jet chamber, the CJC2, comprises 60 drift cells with 32 sense wires each and covers the polar angle range $26^\circ < \theta < 154^\circ$. The sense wires are strung parallel to the beam axis to allow for a precise measurement in the $r - \phi$ plane. They are read out at both ends. The drift cells are tilted by about 30° with respect to the radial direction. This ensures that particles from the interaction vertex traverse more than one drift cell which solves drift ambiguities caused by mirror track segments. In addition the tilt makes the electrons which are liberated by a charged particle through ionisation drift approximately perpendicular to the direction of flight of the particle. This almost cancels the effect of the magnetic field which causes that the drift direction of the electrons and the direction of the electric field are different (Lorentz angle). In the $r - \phi$ plane a resolution of $\sigma_{r\phi} = 130 \mu\text{m}$ is achieved. The resolution in z amounts to $\sigma_z = 22 \text{ mm}$. The z resolution is worse since the z -position is determined by charge division.

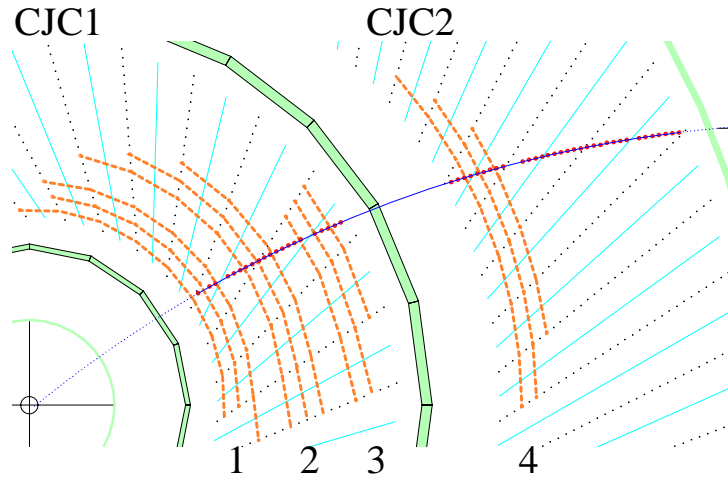


Figure 3.4: r - ϕ view of the central drift chambers. The four trigger layers used by the FTT are indicated. In each trigger layer track segments are fitted and then linked together to give a track candidate as indicated in this figure.

The first central jet chamber trigger which was in operation until the year 2005, the so-called DCRPh Trigger [31], used seven wire layers in the CJC1 and three layers in the CJC2 to find tracks in the $r - \phi$ -plane. This was done by comparing the hit patterns in those layers with predefined track masks. By this method a rough estimate of track momenta could be performed on the first trigger level. Only tracks which have a distance of closest approach to the nominal beam line of less than 2 cm are considered to suppress beam-wall events as well as synchrotron radiation background.

In the year 2005 the DCRPh Trigger was replaced by the Fast Track Trigger (FTT) [32] which uses information from the central jet chambers obtained from four groups of three wire layers each, three of them in CJC1 and one in CJC2 as depicted in figure 3.4. In a first step track segments are reconstructed in each trigger layer. These track segments are linked in a second step to give track candidates. On the second trigger level the p_t resolution is about a factor four worse compared to the offline reconstruction. On trigger level one track multiplicities for eight different p_t thresholds are available. This fine binning in the transverse momentum is only possible because of the good momentum resolution that can already be achieved here. This is one of the advantages over the DCRPh Trigger.

To achieve a better resolution in z , additional chambers, the central inner and the central outer z -chambers (CIZ and COZ), were installed. The sense wires of the CIZ are tilted by 45° with respect to the beam axis while the sense wires of the COZ are perpendicular to the beam axis. An accuracy in z of about $350 \mu\text{m}$ is reached with the help of these chambers.

Two multiwire proportional chambers, the central inner proportional chamber (CIP) and the central outer proportional chamber (COP), were built to deliver a fast timing signal as well as information on the position of the interaction vertex along the z -axis to the central trigger. Both cylindrical chambers consist of two layers of wires and pad cathodes which are segmented in z and in the azimuthal angle ϕ . Track candidates are defined by a four-fold coincidence of pads of both double layer chambers. Hits in the different proportional chambers are connected by straight lines which point to the z -axis. A region of about 88 cm along the z -axis around

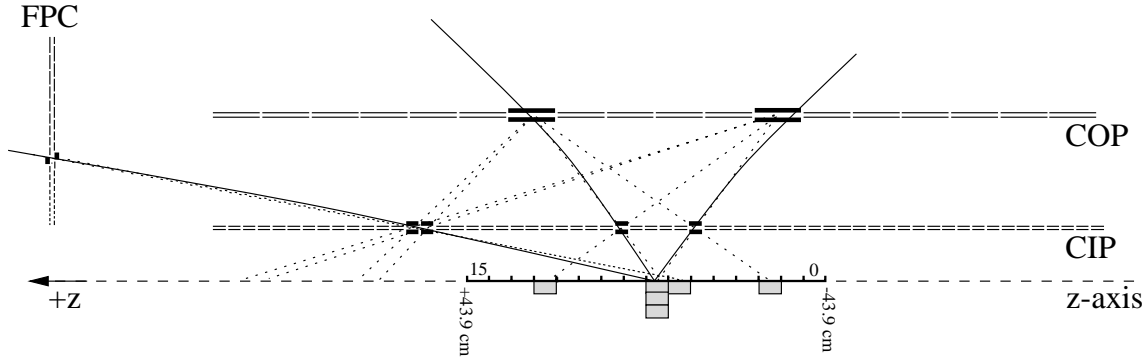


Figure 3.5: Principle of the z -Vertex Trigger which was in operation in the HERA I running period. The dotted lines correspond to all possible track candidates.

the nominal interaction point is divided into 16 bins. Depending on where a given ray intersects the z -axis in this region the corresponding bin in the so called z -vertex histogram gets an entry. Figure 3.5 illustrates this procedure. In addition to both central proportional chambers also the first layer of the forward proportional chamber is used. Tracks from an ep interaction point to the same bin and cause a peak while the combinatorial background may lead to contributions in any bin. To decide whether there is a significant peak in the z -vertex histogram or not the following quantity is evaluated:

$$\sigma = \frac{P - B}{\sqrt{P}} \quad (3.1)$$

P is the number of entries in the peak bin and B is the average background. Three different threshold values for the significance are defined. The trigger element $zVtx_sig$ which consists of two bits delivers the information which threshold was passed to the central trigger logic. A detailed description of the trigger can be found in [33] and [34].

During the detector upgrade the CIP and the CIZ were replaced by the CIP 2000 chamber [35] (cf. figure 3.3), a multiwire proportional chamber consisting of 5 cylindrical layers which are 120-fold segmented in z and 16-fold in the azimuthal angle ϕ . The spatial resolution of the CIP 2000 chamber in z amounts to about 1.5 cm. Since the chambers are 2 m long the CIP 2000 has a much larger polar acceptance compared to the HERA I CIP. This allows to reject proton induced background with a true or apparent vertex position outside the H1 detector at -150 to -200 cm. In addition the acceptance for heavy quark and jet physics is increased. The trigger decision is based on track segments which are reconstructed using the five layers of the CIP 2000 as depicted in figure 3.6. Information on the event timing, the track multiplicity and the significance of the event vertex are delivered to the central trigger logic.

The innermost tracking device is the central silicon tracker (CST). A detailed description of this detector can be found in [36]. In [37] the upgraded CST is described. The CST comprises two 36 cm long layers of silicon strip detectors. This results in a polar angular coverage of $30^\circ < \theta < 150^\circ$. The inner layer consists of 12 and the outer layer of 20 ladders. Each ladder consists of six double sided silicon strip sensors which are read out by two hybrids at either end of the ladder. Before the detector upgrade both layers were cylindrical and they surrounded the beam pipe at radii of 57.5 mm and 97 mm from the beam axis. During the upgrade the

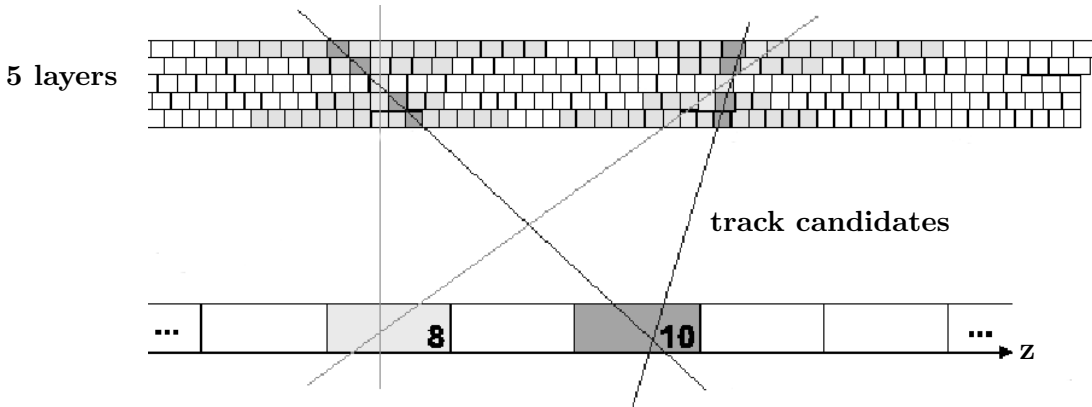


Figure 3.6: Principle of the track segment reconstruction using the five layers of the CIP 2000 (HERA II).

cylindrical beam pipe was replaced by an elliptical one and the ladders were re-arranged (see figure 3.3). A resolution of $12 \mu\text{m}$ in the $r - \phi$ -plane and of $25 \mu\text{m}$ in z is achieved. To profit from this very good spacial resolution the inner layer is installed as close to the interaction point as possible. The distance of closest approach d_{ca} of a track to the nominal interaction vertex in the $r - \phi$ -plane can be measured with a precision of $\sigma_{dca} \approx 33 \mu\text{m} \oplus 90 \mu\text{m}/p_t[\text{GeV}]$ if the track is reconstructed in the central tracking system with hits in both CST layers (HERA I). The first term arises from the intrinsic resolution and the second term from multiple scattering in the beam pipe and the CST itself. In the year 2006 a d_{ca} resolution of $28 \mu\text{m}$ in the limit of high p_t is achieved.

3.2.2 Calorimeters

Here, only the calorimeters which are important for the present analysis are described in detail. Both calorimeters the SpaCal and the liquid argon calorimeter (LAr) are used for the reconstruction of the hadronic final state and the detection of the scattered electron. In addition the liquid argon calorimeter is used to identify muons and electrons e.g. from semileptonic decays of heavy quarks.

3.2.2.1 Liquid Argon Calorimeter

The liquid argon calorimeter [38] is a non-compensating sampling calorimeter. It encloses the forward and the central part of the detector with a polar angular coverage of $4^\circ < \theta < 154^\circ$. As shown in figure 3.7 the liquid argon calorimeter is divided into 8 wheels along the z -axis. The six central wheels consist of an inner electromagnetic and an outer hadronic part. In the electromagnetic part lead is used as absorber material whereas in the hadronic part stainless steel is used. In the case of the central wheels the absorber plates are parallel to the beam axis. For the other wheels the absorber plates are oriented perpendicular to the beam axis. Depending on the calorimeter wheel the thickness of the electromagnetic part varies between 20 and 30 radiation length X_0 and between 4.7 and 8 nuclear interaction lengths λ for the hadronic part. Each wheel comprises 8 octants as it is shown in figure 3.8 for the wheel CB2. The space

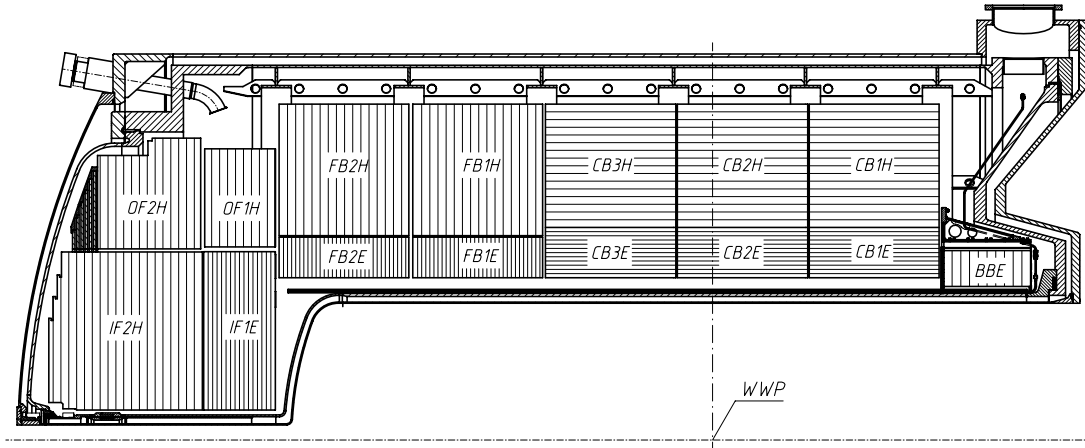


Figure 3.7: *The upper half of the liquid argon calorimeter ($r-z$ -view). Shown are the different wheels and the orientation of the absorber plates.*

between the octants and the wheels is not instrumented. As active material liquid argon is used which is cooled down to -183° Celsius. The smallest unit consisting of absorber and active material which is read out is called calorimeter cell.

The electromagnetic part is highly segmented with a total number of about 31,000 readout channels and has a good energy resolution of $\sigma(E)/E = 12\%/\sqrt{E[\text{GeV}]} \oplus 1.0\%$. In the hadronic part the granularity is much coarser with a total number of 13,500 readout cells. An energy resolution of $\sigma(E)/E = 50\%/\sqrt{E[\text{GeV}]} \oplus 2.0\%$ is achieved in the hadronic part of the calorimeter.

3.2.2.2 Spaghetti Calorimeter

The backward region of the H1 detector is equipped with the spaghetti calorimeter (SpaCal), a lead-scintillating fibre calorimeter with an electromagnetic and a hadronic section [39]. The SpaCal covers the angular range of $153^\circ < \theta < 178^\circ$. It allows to measure the energy and the impact position of the scattered electron with high accuracy. The energy resolution in the electromagnetic section of the SpaCal amounts to $\sigma(E)/E = 7.1\%/\sqrt{E[\text{GeV}]} \oplus 1.0\%$. Before the luminosity upgrade the acceptance in the SpaCal corresponded to photon virtualities of $2 < Q^2 < 100 \text{ GeV}^2$. During the upgrade a number of inner SpaCal cells were removed which reduced the polar angular coverage to $153^\circ < \theta < 173^\circ$ [40]. As a consequence the acceptance in Q^2 is reduced as well: $4 < Q^2 < 100 \text{ GeV}^2$.

The SpaCal electron trigger makes use of the good time resolution of the SpaCal. The trigger is only active in a time window in which particles from an ep interaction around the nominal vertex are expected to reach the SpaCal. This strongly suppresses proton background.

3.2.3 Central Muon Detector

High energetic muons mainly lose their energy due to ionisation, leading to a very high penetration depth compared to hadrons, electrons and photons. Electrons and photons produce electromagnetic showers and are stopped in the electromagnetic part of the calorimeter while

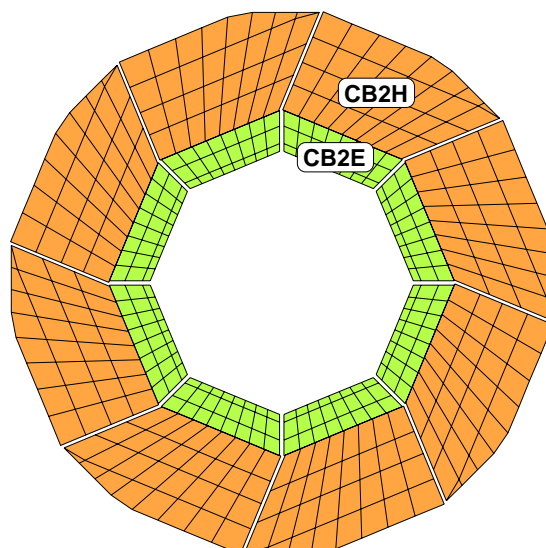


Figure 3.8: $r - \phi$ -view of the calorimeter wheel CB2. The wheel is divided into 8 octants and consists of an inner electromagnetic and an outer hadronic section.

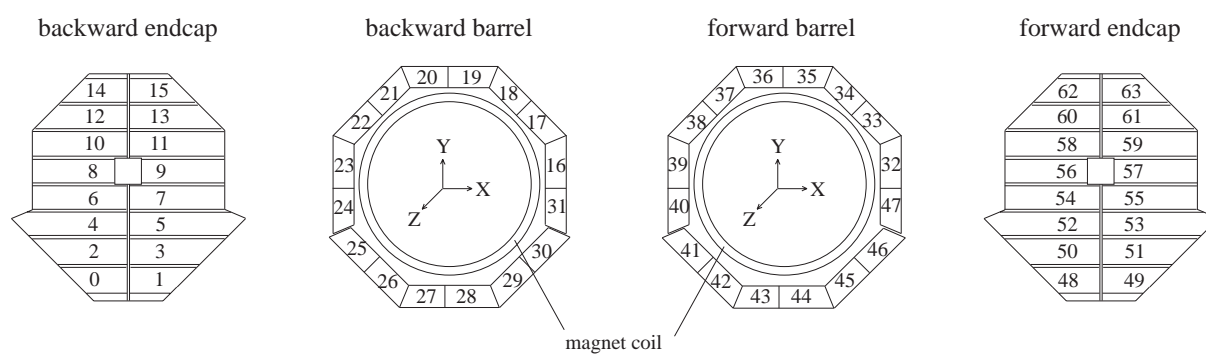


Figure 3.9: The central muon detector is divided into four parts. Each part consists of sixteen instrumented iron modules. In total the detector comprises 64 modules.

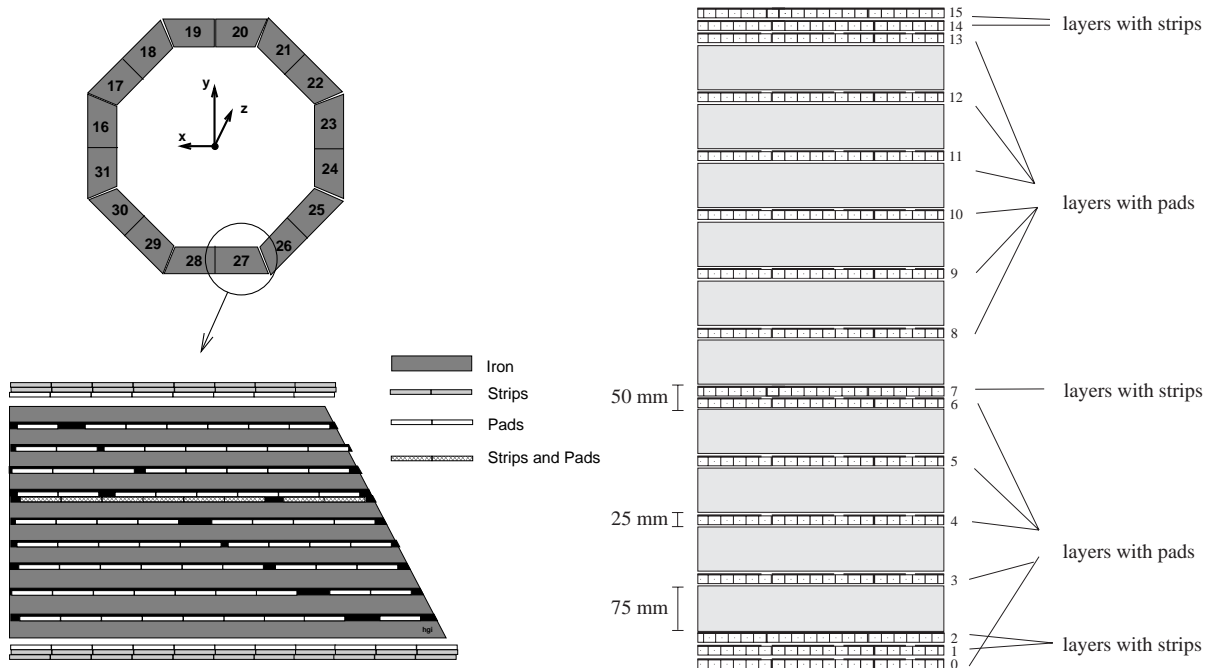


Figure 3.10: *Cross section view of an instrumented iron module.*

hadrons interact strongly and deposit their energy mainly in the hadronic section. To take advantage of this characteristic behaviour muon detectors are usually located outside the calorimeter. In the H1 detector the iron return yoke of the solenoid is laminated and instrumented with limited streamer tubes to measure muon tracks. The central muon detector (CMD) comprises four parts: the backward endcap, the backward barrel, the forward barrel and the forward endcap. Each part consist of sixteen instrumented iron modules (see figure 3.9). In total the CMD consists 64 modules. The two barrel parts cover an angular range of $35^\circ < \theta < 135^\circ$. The whole muon detector has an angular acceptance of $5^\circ < \theta < 175^\circ$.

As shown in figure 3.10, an instrumented iron module consist of ten 75 mm thick iron plates and sixteen layers of limited streamer tube elements. Three layers of streamer chambers, the so-called muon-boxes, are installed in front and behind of the iron plates. The other layers are located between the iron plates. The chambers consist of streamer tubes which have a cross section of $1 \times 1 \text{ cm}^2$ with sense wires strung parallel (barrel) or perpendicular (endcap) to the beam axis. The wire chambers are either equipped with strips or with pads to provide a two-dimensional measurement. While the layers with strips are used to reconstruct muon tracks, the layers with pads are mainly used to resolve track ambiguities and to detect hadronic energy leaking out of the calorimeter. The streamer chamber layers 3, 4, 5, 8 and 12 are also used by the instrumented iron muon trigger. In the barrel part two out of the innermost four trigger layers are required in order to fire the corresponding trigger element (MU_Bar).

The momentum resolution achieved in the barrel part of the muon system amounts to about 30%. Since this is not sufficient, muon tracks reconstructed in the instrumented iron ('iron tracks') are linked to tracks reconstructed by the tracking detectors ('inner tracks'). In this analysis only muon candidates with an inner track link are used. In this case the muon system is used to identify muons while the momentum measurement is provided by the tracking system.

3.2.4 Trigger System and Data Acquisition

The task of the trigger system is to quickly decide whether an event originates from an ep interaction of physics interest or not. While the bunch crossing rate is 10.4 MHz, the rate of ep interactions is much smaller. The probability for an ep interaction per bunch crossing is of the order 10^{-3} . For tagged photoproduction the cross section amounts to about $1.6 \mu\text{b}$ (according to [29]). This leads to a rate of about 25 Hz assuming a luminosity of $\mathcal{L} = 1.5 \times 10^{31} \text{ cm}^{-2}\text{s}^{-1}$. For W production ($\sigma \approx 0.4 \text{ pb}$) the rate is 0.5 d^{-1} . These numbers have to be compared with the rate of background events. Beam gas interactions contribute with a rate of 50 kHz and cosmic muons in the barrel part of the muon system occur at a rate of 4 kHz. The background rate is several orders of magnitudes larger than the rate of interesting ep events. To cope with this challenging situation the H1 detector is equipped with a trigger system consisting of several trigger levels:

Trigger level L1: Most subdetectors provide information, so-called trigger elements, which are used by the central trigger logic. The decision time of some subdetectors is larger than the bunch crossing interval of 96 ns. In the central drift chambers, for example, the largest drift times are about $1 \mu\text{s}$. The entire detector information is thus stored temporarily in pipelines for $2.5 \mu\text{s}$. Within this time the L1 trigger decision is made. Since the L1 input rate amounts to 100 kHz a pipeline length of $2.5 \mu\text{s}$ is sufficient.

Trigger elements from different subdetectors are logically combined to form so-called subtriggers. If one of the subtriggers fires the pipeline is stopped and the event read out is started. Since the level two input rate is limited to 1 kHz a subtrigger that delivers a rate which is too high is prescaled to get an acceptable output rate. A prescale factor of n means that the subtrigger has to fire n times to be accepted.

Trigger level L2: Neural networks and topological triggers are used on trigger level two to reduce the input rate of 1 kHz down to 50 Hz, the maximum input rate for the fourth trigger level. The decision whether to start the detector read out or to reject the event and to restart the pipelines is taken within $20 \mu\text{s}$.

Trigger level L3: The third trigger level was implemented during the year 2006. Tracks reconstructed by the fast track trigger are used to search for exclusive final states, e.g. D^* mesons via the most suitable decay channel (the so-called golden channel) $D^* \rightarrow D^0 \pi_s \rightarrow K \pi \pi_s$. Before this upgrade events with D^* mesons were collected mainly by triggers which require a scattered electron, a muon in the instrumented iron or jets. The FTT allows to implement a pure track-based trigger to collect D^* mesons which results in a much larger event yield. It is expected that about 20,000 D^* mesons will be collected until the HERA shut-down.

Trigger level L4/5: On this trigger level a full event reconstruction is performed by a multi-processor farm. Since this is done using an asynchronous event buffer the computing time does not contribute to the dead time of the experiment. If the decisions taken on the previous trigger levels are verified it is decided to which physics classes the event belongs to. The most important classes in view of heavy flavour physics are the classes for exclusive final states like D^* or J/ψ mesons and the class for hard scale physics. An event belongs to the latter class if it contains a

track with a momentum above 1 GeV or a scattered electron at a sufficiently large Q^2 . Events which belong to at least one physics class are kept, all others are downscaled. The L4/5 output rate is limited to about 20 Hz. The data is permanently stored on tape (physics output tape, POT). The data relevant for physics analyses is in addition stored on disc (data summary tape, DST).

In the HERA I running phase a fast online event reconstruction was performed on trigger level four and a decision was taken if the event should be kept for permanent recording or not. The full event reconstruction was done offline on trigger level five. During the detector upgrade both trigger levels were merged.

3.3 Previous Measurements of Charm and Beauty Production

Previous measurements of charm and beauty quark production are briefly reviewed. The emphasis is on recent results from the HERA experiments H1 and ZEUS and on the experimental methods which are used to tag heavy quarks. The production of charm quarks is addressed first followed by the discussion of beauty production. The aim is to bring out the experimental context and the open question which are addressed in the analysis presented in this thesis.

3.3.1 Charm Production

The charm quark was simultaneously discovered in November 1974 at the Stanford Linear Accelerator Center (SLAC) and at the Brookhaven National Laboratory (BNL) [41, 42]. The experimental signature at both experiments was a narrow resonance at 3.1 GeV, interpreted as a $c\bar{c}$ bound state which was later named J/ψ meson.

In the scope of this thesis only a few results on charm production can be discussed. The emphasis is on recent measurements which are compared to the results of the present analysis. Other results, such as measurements of the gluon density in the proton, are not discussed, although they are important for the understanding of the proton structure. A compilation of all charm results at HERA can be found for example in [43] and [44].

Charm quarks from open charm production are tagged via the full reconstruction of decays of charm hadrons into charged particles. The most suitable choice is the D^* meson which is reconstructed via the 'golden' decay channel: $D^{*+} \rightarrow D^0\pi_s^+ \rightarrow (K^-\pi^+)\pi_s^+$. The mass difference between the D^* and the D^0 meson is only a few MeV above the pion mass. This leads to an excellent signal to background ratio as the phase space for combinatorial background is suppressed. In order to extract the number of D^* mesons the observable $\Delta m = m(K^-\pi^+\pi_s^+) - m(K^-\pi^+)$ is used which provides a good mass resolution since the track errors of the kaon and the pion largely cancel. The charm cross section obtained in the present analysis is compared to a recent H1 analysis in which the photoproduction of D^* mesons is studied [45]. In addition to D^* , D^* -jet and D^* -dijet photoproduction cross sections, differential cross sections were determined and D^* -jet correlations were studied in the mentioned publication. The results are compared to next-to-leading order calculations in the massive (FMNR [46, 47]) and in the massless scheme (zero-mass variable-flavour-number scheme, ZMVFNS [48, 49]) and to a matched scheme (general-mass variable-flavour-number scheme, GMVFNS [50, 51]). While the charm photoproduction is in general reasonably understood, none of the calculations describe all details of the

differential measurements.

Using a lifetime tag, i.e. exploiting the long lifetime of D mesons, which leads to a displaced secondary vertex, suppresses the light flavour background and allows to reconstruct also other D mesons apart from D^* mesons. In [52] the inclusive production of D^+ , D^0 , D_s^+ and D^{*+} mesons in deep inelastic scattering was studied by reconstructing a displaced secondary vertex. The results support the approach to factorise the hard scattering process and the hadronisation process, which is assumed to be universal.

In [53] charm and beauty dijet cross sections in photoproduction are presented. The fractions of events containing charm and beauty quarks are determined using a method based on the impact parameter of all tracks with respect to the primary vertex. The charm cross sections are consistent with pQCD calculations in next-to-leading order (NLO), while the predicted cross sections for beauty production are somewhat lower than the measurement. The results of this analysis are also compared with the measurements of the present analysis.

Another analysis at H1 exploits the charge and angle correlation between a D^* meson and a muon to distinguish between events with charm and beauty quarks [54]. The muon serves as a second heavy flavour tag. The visible charm cross section is found to be in agreement with next-to-leading order calculations while the beauty cross section is higher. The $D^*\mu$ analysis is in principle quite similar to the analysis presented here since it is also a 'double tag' analysis but it uses about a factor four less luminosity. The results of both analyses are compared.

In summary, it can be concluded that charm production at HERA is reasonably well described by next-to-leading order calculations, but there are indications in some analyses that not all differential measurements are understood which motivates further studies.

3.3.2 Beauty Production

The beauty quark was discovered via the Υ resonance at 9.5 GeV in 1977 at the Fermi National Accelerator Laboratory (FERMILAB) [53]. Since then the production of beauty quarks has been studied for example in $p\bar{p}$ collisions at the $Spp\bar{p}S$, in photon-photon interactions at LEP, in pp collisions at the Tevatron collider and in ep collisions at HERA.

From the experimental point of view, two properties of the b quark are exploited to tag beauty quarks: the large mass and the long lifetime. The relatively large mass of the beauty quark gives rise to large transverse momenta of leptons from a semileptonic decay relative to the direction of flight of the B hadron. In order to exploit this characteristic behaviour the observable p_t^{rel} , i.e. the transverse momentum of the decay lepton with respect to the associated jet, is used. The long lifetime of B hadrons leads to a displaced secondary vertex. With the help of silicon vertex detectors, which provide the necessary spatial resolution, secondary vertices are reconstructed, or methods based on the impact parameter δ are applied. The impact parameter δ is the distance of closest approach in the transverse plane of tracks, e.g. leptons from semileptonic b decays, to the primary vertex.

Measurements at LEP and early measurements at the Tevatron show large discrepancies between the data and NLO calculations compared to the charm sector (see for example the CDF publication [55]). However, these discrepancies were not expected since the mass of the b quark provides a hard scale and pQCD calculations are expected to give reliable results. Recent publications of the Tevatron experiments D0 and CDF show a better agreement of the NLO calculations and

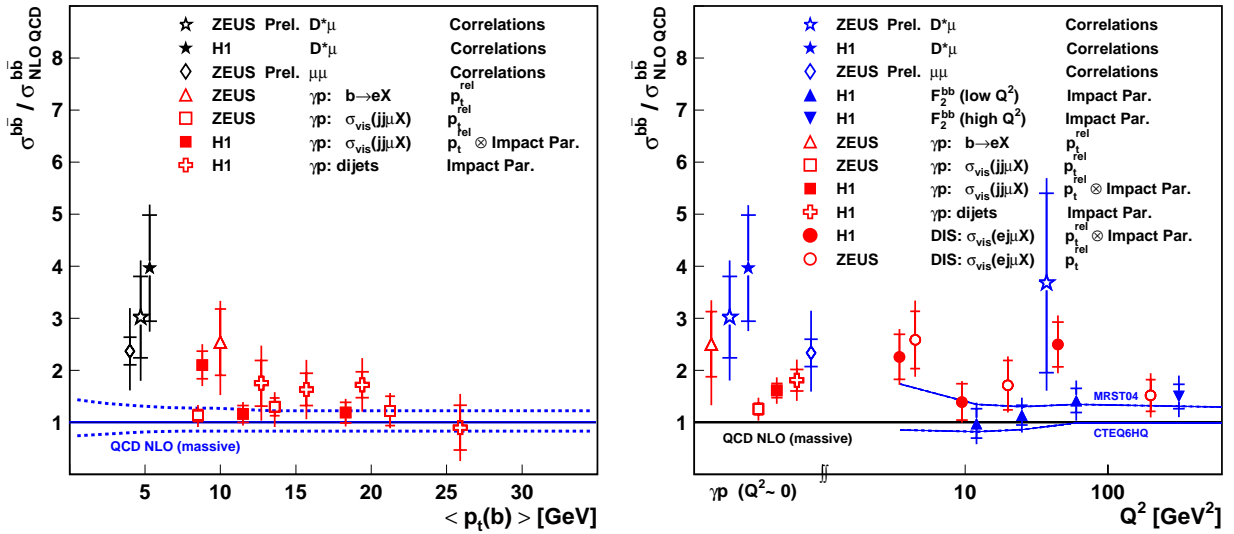


Figure 3.11: Summary of previous beauty measurements at HERA. The ratio between the measured cross sections and the corresponding predictions from NLO calculations are shown as a function of the mean transverse momentum of the b quark $\langle p_t(b) \rangle$ (left) and the photon virtuality Q^2 (right).

the data. This was achieved by improvements on the experimental and the theoretical side. In a very recent measurement from the CDF experiment a good agreement between data and theory is observed [56]. The theoretical predictions are based on the fixed order and next to leading log scheme (FONLL) [57].

Figure 3.11 summarises previous measurements of beauty production at HERA. The ratios between the measured cross sections and the theoretical predictions from fixed order massive NLO calculations are shown as a function of the mean transverse momentum of the b quark $\langle p_t(b) \rangle$ and as a function of the photon virtuality Q^2 . The final states which are investigated and the methods used to extract the beauty cross sections are indicated as well. The phase space covered by the individual measurements can differ considerably. The data tend to be somewhat higher than the predictions but are still in agreement taking into account the experimental and the theoretical uncertainties. The deviations from the measurements seem to increase towards lower mean transverse momenta of the beauty quark and lower photon virtualities. In the following some recent measurements performed by H1 and ZEUS are discussed in more detail. The beauty cross sections obtained in the present analysis are compared to these measurements.

In [58] beauty production is studied at H1 in photoproduction and in DIS using events with muons and jets in the final state. For the photoproduction analysis at least two jets were required ($jj\mu$) while for the DIS analysis at least one jet and a scattered electron were required ($ej\mu$). The fraction of beauty events was determined by a likelihood fit to the two-dimensional distribution of the impact parameter δ and the relative transverse momentum p_t^{rel} . The combination of both observables resulted in a significant improvement of the statistical precision. The results of this analysis are shown in figure 3.11 as full squares (photoproduction) and full circles (electroproduction). From differential measurements it was concluded that the excess is observed mainly at small muon and jet transverse momenta while at large momenta a reasonable

description is obtained. A similar analysis in a comparable phase space region was performed by the ZEUS experiment using the observable p_t^{rel} alone [59]. A good agreement between the measurement and the prediction is found (see figure 3.11, open squares). In contrast to the H1 measurement no excess at low jet transverse momenta is observed.

At H1 and ZEUS beauty production was measured using events with a D^* meson and a muon in the final state. The charge and angle correlation was exploited to distinguish between charm and beauty events [54, 60]. The mean transverse momenta of the b quarks $\langle p_t(b) \rangle$ reached in the $D^*\mu$ analyses are considerably smaller compared to the p_t^{rel} analyses discussed above since no jets are required (cf. figure 3.11, full and open stars). Even lower $\langle p_t(b) \rangle$ values are reached in the ZEUS dimuon analysis presented in [61] (cf. figure 3.11, open rhombus). The ZEUS dimuon event sample is enriched with beauty events. The background from other processes is strongly suppressed. Due to the low transverse momentum thresholds for muon identification and the large solid angle coverage of the ZEUS muon system the total beauty cross section can be determined with almost no extrapolation. For the determination of the number of beauty events it is assumed that for the light flavour background the like sign and the unlike sign dimuon distributions are almost equal. The difference between the like sign and the unlike sign distributions is thus essentially free from light flavour background. The remaining background contributions, e.g. from charm and heavy quarkonia, are subtracted using normalised Monte Carlo samples which are used to model the background. The normalisation of the charm background is estimated using an external constraint from the ZEUS $D^*\mu$ analysis. The extrapolation to the number of like sign and unlike sign dimuon events from beauty is performed using beauty Monte Carlo.

3.3.3 Experimental Context of the Present Analysis

The present dilepton and dijet analysis addresses photoproduction and, according to the PYTHIA Monte Carlo, a mean transverse momentum of the tagged beauty quarks of $\langle p_t(b) \rangle \approx 10$ GeV. In this respect the present analysis is similar the $jj\mu$ analyses from H1 and ZEUS discussed above. At low mean transverse momenta of the beauty quarks and in photoproduction the largest deviations between the data and the NLO calculations are observed (cf. figure 3.11). Providing an additional measurement in this region of phase space is thus a helpful step towards understanding the observed discrepancies. In addition the cuts on the transverse momenta of the leptons and the jets are considerably lower compared to the $jj\mu$ analyses. This allows to study the discrepancies between the data and the prediction at low lepton and jet transverse momenta as observed by H1 but not by ZEUS. In the following the advantages and the drawbacks of the present analysis are discussed.

The observable p_t^{rel} and the charge and azimuthal angle correlation of the leptons can be both used separately to determine the beauty fraction. This allows on the one hand to cross check both results and on the other hand both methods can be combined to reduce the statistical and the systematic uncertainties.

Two different data samples, a dimuon and a muon-electron sample, are investigated in the present analysis. This allows for comparisons and cross checks at each step of the analysis and combining both results increases the statistical precision.

Mainly due to the jet requirement the extrapolations to the total $b\bar{b}$ cross section are expected to be considerably larger compared to the ZEUS dimuon analysis. On the other hand the charm

contribution can be determined from the data samples and no external constraints are necessary. In addition other background processes as prompt J/ψ production and lepton pairs from photon-photon fusion processes are negligible in the dimuon sample or just do not occur for the muon-electron sample. The lepton correlation can be studied using the observable p_t^{rel} providing a measurement applying a different method in a different kinematic regime. Furthermore, the requirement of two jets allows to study the contributions of direct and resolved processes via the observable x_γ^{obs} and to reconstruct the kinematics of the outgoing partons from the hard subprocess.

CHAPTER 4

LEPTON IDENTIFICATION

The production of charm and beauty quarks is studied using dimuon and muon-electron events. In order to identify leptons, information from the central tracking system, the liquid argon calorimeter and, in the case of muons, the muon system are combined. The central tracks provide the momentum measurement and are used to match energy depositions in the calorimeter to a given particle. A software package, KALEP [62], is implemented in the standard H1 event reconstruction software to search for electron and muon signatures in the calorimeter. In this analysis muons found by KALEP or identified in the muon system are selected. KALEP is not used for electrons since the misidentification probability is too high. An algorithm with a lower misidentification probability but with a similar efficiency for finding electrons was developed. The estimators which are used to separate electrons from hadrons, the new algorithm and its properties are explained in the first section of this chapter. Then the muon identification is investigated. For both leptons it is studied if the calorimeter estimators are well described by the Monte Carlo simulation. In particular the description of some KALEP estimators which are used to identify muons in the calorimeter is quite poor. This results in significant corrections to the efficiency retrieved from the simulation.

4.1 Identification of Electrons

As already mentioned, the KALEP software package was developed to search for muon and electron signatures in the liquid argon calorimeter. Selecting electron candidates with the highest KALEP quality the contribution from beauty events to the total sample is too low for a meaningful analysis. In particular at low momenta the probability for a hadron to be misidentified as an electron is unsatisfactory. A new method for electron identification is thus developed. It is based on four discriminating variables: The ratio of the energy deposited in the electromagnetic part of the liquid argon calorimeter and the momentum measured in the jet chambers, the energy in the hadronic part of the calorimeter and two estimators which are related to the shower shape in the calorimeter. To motivate the definitions of these discriminators, the differences in the way hadrons and electrons interact with matter will be briefly described in the following. Then, after a brief discussion of the KALEP algorithm, the four variables that are used in this analysis for the electron identification are presented in detail. To separate electrons from hadrons, the Fisher discriminant method is applied. Finally, the reconstruction efficiencies and

the misidentification probabilities are investigated and compared to the KALEP output. The misidentification probability is reduced such that the cut on the transverse momentum can be lowered significantly to 1.0 GeV without being overwhelmed by background. At the same time the reconstruction efficiency is fully compatible to that from the KALEP algorithm. Special care is taken that the estimators are well described by the Monte Carlo simulation.

4.1.1 Electron Identification in the Calorimeter

Electrons typically deposit their entire energy in the electromagnetic part of the liquid argon calorimeter. They produce electromagnetic showers which are quite narrow and homogeneous. Hadrons, in contrast, deposit a smaller fraction of their energy in the electromagnetic part of the calorimeter than electrons and depending on their energy their showers extend into the hadronic part of the calorimeter or may even leak into the tail catcher and the instrumented iron where they may fake muons ('punch through'). In addition, the calorimeter of the H1 detector does not compensate for energy losses in hadronic showers. Energy is lost for calorimetry, for example, due to the excitation of atomic nuclei or if muons or neutrinos are produced during the development of a hadronic shower. For all these reasons, for hadrons, the energy deposited in the electromagnetic part of the calorimeter is expected to be significantly smaller than the energy deduced from the momentum measurement in the tracking chambers but about the same for electrons. Therefore the ratio between the energy deposited in the calorimeter and the momentum of a track E/p can be used to separate electrons from hadrons. Of course the E/p measurement is deteriorated to a certain extent if a particle is not well isolated and showers from different particles are overlapping in the calorimeter. For this reason also other variables like the total energy around the extrapolated track in the hadronic and the electromagnetic part of the calorimeter respectively are taken into account to obtain a more efficient separation. Also variables that are related to the shower shape in the calorimeter have proven to be very helpful in this respect, as will be demonstrated in this chapter.

4.1.2 Electron Identification by KALEP

The KALEP electron finder uses the following four estimators:

1. The sum of the energy e_i deposited in all calorimeter cells in the electromagnetic part of the liquid argon calorimeter with a distance of closest approach to the extrapolated track smaller than $R_a = 15$ cm:

$$E_{em} = \sum_{\text{em cells}} e_i.$$

2. The electromagnetic energy divided by the track momentum:

$$E_{em}/p.$$

3. The hadronic energy ($R_b = 30$ cm):

$$E_{had} = \sum_{\text{hadronic cells}} e_i.$$

4. The distance l_i along the extrapolated track from the calorimeter surface to each cell in the electromagnetic calorimeter within $R_a = 15$ cm is multiplied with the cell energy e_i . Then all energy weighted distances are summed up:

$$L_{em} = \sum_{\text{em cells}} l_i e_i.$$

The cell energy referred to here is the energy on the electromagnetic scale after applying corrections for energy loss due to dead material. Only tracks with a transverse momentum greater than 0.8 GeV are considered. No sharp cuts on the four discriminators are imposed but deviations from the limits defined for each variable are summed up. According to the outcome three different qualities are defined:

- weak electron quality: $Q = 1$
- medium electron quality: $Q = 2$
- good electron quality: $Q = 3$

Electrons will be selected in this analysis by a different algorithm but for cross checks a sample with KALEP electrons is investigated as well. Only calorimeter electrons with the highest KALEP quality are considered. Properties of this algorithm regarding the reconstruction efficiencies and the misidentification probabilities are discussed later when a comparison with the method used in this analysis is performed.

4.1.3 Discriminating Variables

In this analysis only electron candidates with a transverse momentum larger than 1.0 GeV and within the polar angular range $20^\circ < \theta < 150^\circ$ are considered. A minimum transverse momentum is required to suppress fake electrons, i.e. misidentified hadrons. The restriction on the polar angle is given by the acceptance of the central tracking system and the electromagnetic calorimeter. Only primary vertex fitted tracks are selected to suppress background from photon conversion processes.

For an efficient electron identification, measurements of the central tracking system and calorimeter information have to be combined. As in the KALEP program package, calorimeter information on cell level is used. In order to suppress noise a minimum cell energy is required:

$$|e_{cell}| > 0.02 \text{ GeV} \quad (4.1)$$

e_{cell} is the energy on the electromagnetic scale after dead material corrections. Tracks are extrapolated as a helix into the calorimeter. Each cell that lies along an extrapolated track is associated to it and the distance of closest approach d_{ca} is calculated. The energy of each cell is then weighted by the following function:

$$h(d_{ca}) = \begin{cases} 1 & d_{ca} \leq R \\ \frac{2}{1 + \exp\left[\frac{d_{ca} - R}{2}\right]} & d_{ca} > R \end{cases} \quad (4.2)$$

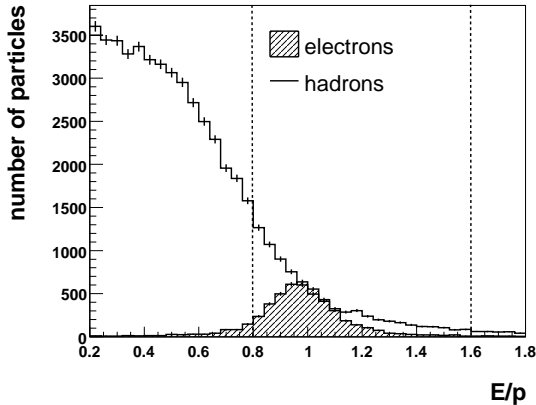


Figure 4.1: E/p for electrons and hadrons according to the beauty Monte Carlo simulation. The distribution for electrons peaks at one while hadrons tend to values significantly lower than one. The dotted lines indicate the preselection cuts.

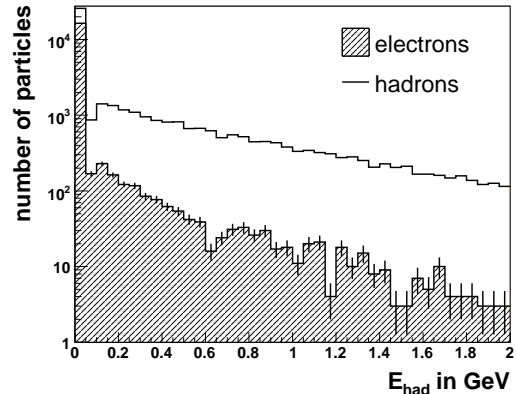


Figure 4.2: Energy in the hadronic part of the liquid argon calorimeter E_{had} for electrons and hadrons passing the track selection and the cut on E/p according to the beauty Monte Carlo.

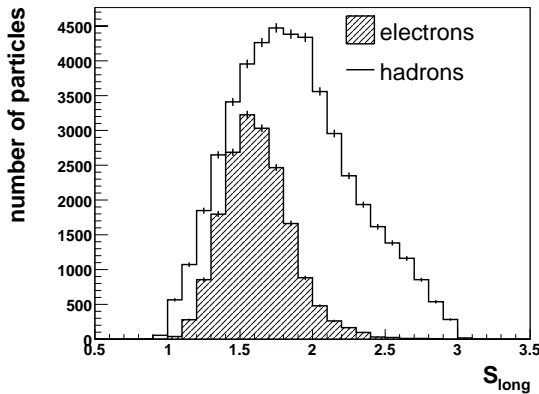


Figure 4.3: Longitudinal shower spread S_{long} (beauty Monte Carlo) for electrons and hadrons passing the track selection and the cut on E/p .

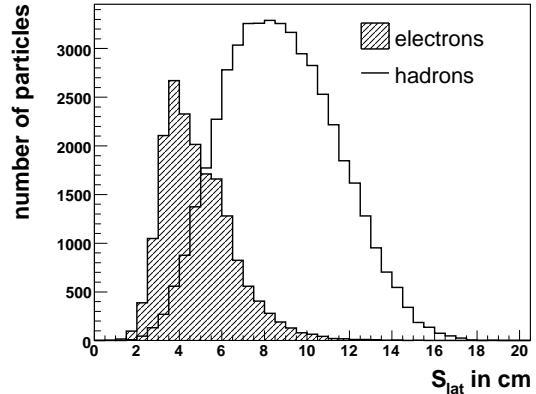


Figure 4.4: Lateral shower spread S_{lat} for electrons and hadrons passing the track selection and the cut on E/p . Both distributions are well separated.

A cell is assigned a weight of one if it lies within a cylinder of radius R around the helix trajectory. Beyond R the function is steeply falling but ensures a smooth transition in contrast to a rectangle function. This method is supposed to give more stable results in the case of detector problems like inaccurate geometrical calibration for instance. The parameter R is chosen to be $R_a = 15$ cm or $R_b = 30$ cm depending on whether the energy of an electromagnetic or of a hadronic shower is to be reconstructed.

Four discriminators are used in this analysis to distinguish between electrons and hadrons. All

four variables enter the Fisher discriminant function. The first quantity is E/p , which is defined according to the following formula:

$$\frac{E}{p} = \frac{E_{em}}{p} \quad \text{with} \quad E_{em} = \sum_{\text{em cells}} e_i \cdot h(d_{ca,i}) \quad (4.3)$$

The sum includes all cells in the electromagnetic part of the liquid argon calorimeter that are matched to the track applying the procedure described above. As distance parameter $R = 15$ cm is chosen to collect all the energy of an electromagnetic shower but only a part of a hadronic shower. p is the momentum measured in the central tracking system. The E/p distributions for electrons and hadrons are depicted in figure 4.1. A simulated sample of events with beauty quarks is used for this investigation. Only the electron candidate with the largest transverse momentum is considered. The vast majority of hadrons are rejected by a cut on this quantity. As will be shown later, the E/p distribution is well modelled by the Monte Carlo simulation. It should be stressed that the contribution from fake electrons is of course significantly higher for an inclusive data sample which is not enriched with electrons from semileptonic b quark decays.

Electrons tend to deposit their whole energy in the electromagnetic part of the calorimeter while hadrons in general reach the hadronic part. This behaviour is reflected in the distributions of the hadronic energy E_{had} for electrons and hadrons as depicted in figure 4.2. Only particles passing the preselection, namely the track selection and the cut on E/p ($0.8 < E/p < 1.6$, cf. figure 4.1), are shown. The distribution for electrons is falling steeply towards increasing energy in the hadronic section while the distribution of hadrons reaches much higher values of E_{had} .

To allow for a more efficient separation of electrons and hadrons two additional discriminators related to the lateral and the longitudinal shower spread are used. As a measure for the longitudinal shower extension the following variable is defined:

$$S_{long} = \frac{\sum_{i=1}^{\#em \text{ layers}} i \cdot E_i}{\sum_{i=1}^{\#em \text{ layers}} E_i} \quad (4.4)$$

E_i is the energy in the i -th electromagnetic layer:

$$E_i = \sum_{\text{cells}} e_j h(d_{ca,j}) \quad (4.5)$$

In comparison to electrons, larger values of S_{long} are expected for hadrons, since hadrons typically penetrate the calorimeter much deeper due to the fact that the hadronic interaction length is significantly larger than the radiation length. This can be seen in figure 4.3 where the S_{long} distribution for hadrons peaks at a larger value.

As a measure for the lateral shower spread the following variable is defined:

$$S_{lat} = \sqrt{\frac{\sum_{\text{cells}} d_{ca,i}^2 \cdot e_i \cdot h(d_{ca,i})}{\sum_{\text{cells}} e_i}} \quad (4.6)$$

The distance of closest approach d_{ca} enters the quantity quadratically and is weighted by the cell energy. Therefore cells with a significant energy that are more distant to the extrapolated track give rise to large terms in the expression above. To cancel the energy dependence, the expression is divided by the sum of all cell energies. By design S_{lat} is large for hadrons and small

for electrons. The distributions of S_{lat} for electrons and hadrons passing the track selection and the E/p cut is depicted in figure 4.4. Electrons and hadrons are well separated. Together with E/p this quantity provides the highest separation power. A drawback is the long tail in the electron distribution.

4.1.4 The Fisher Discriminant Method

The Fisher Discriminant Method [63] is a standard method to derive a single test statistic t out of a set of discriminating variables. For the test statistic a linear approach is made:

$$t(x) = \sum_{i=1}^n a_i x_i \quad (4.7)$$

The sum is carried out over the n discriminating variables x_i . The coefficients a_i can be extracted from a signal and a background sample using the Fisher algorithm:

$$a_i = \sum_k (V^{-1})_{ik} (\bar{x}_k^{(1)} - \bar{x}_k^{(2)}) \quad (4.8)$$

$\bar{x}_k^{(1)}$ and $\bar{x}_k^{(2)}$ are the mean values of the signal and background distributions respectively and V is the joint covariance matrix:

$$V = \frac{1}{2} (V^{(1)} + V^{(2)}) \quad (4.9)$$

$V^{(1)}$ and $V^{(2)}$ are the covariance matrices for the signal and the background sample, respectively. It can be shown that for variables coming from a multi-normal distribution the test statistic t calculated using the Fisher algorithm encapsulates all the discrimination information. Even when the input variables are not of this form the Fisher variable is still useful.

As already mentioned, the four discriminating variables described above enter the Fisher test statistics that is used in this analysis to distinguish between the electron and the hadron hypothesis for a given particle. The input particles have to fulfil the preselection cuts, namely the track selection cuts (primary vertex fitted tracks, $p_t > 1.0$ GeV, $20^\circ < \theta < 150^\circ$) and the cut on E/p ($0.8 < E_{em}/p < 1.6$), to be considered. For electron candidates passing the preselection cuts, the most significant variable is S_{lat} but also the other variables contribute to the discriminating power. Leaving out one of the variables the discriminating power of the test statistics decreases. To calculate the coefficients in equation 4.7 a signal and a background sample is needed. Here the samples are taken from the beauty Monte Carlo. Figure 4.5 shows the distribution of the test statistic for hadrons and electrons. Both distributions are normalised to one. It can be seen that the distributions are well separated. It should be stressed that only electrons and hadrons after the preselection, i.e. the E/p cut, are considered here.

To investigate the selection efficiency, the distributions in figure 4.5 are integrated. The result is depicted in figure 4.6. From this plot one can read off the selection efficiencies for different cuts on the test statistic t . The cut can be adjusted easily according to the needs of a specific analysis. In this analysis $t > -8.0$ is required for an electron candidate to be selected. This yields a selection efficiency of about 83% for electrons passing the preselection. On the other hand 90% of the hadrons are rejected.

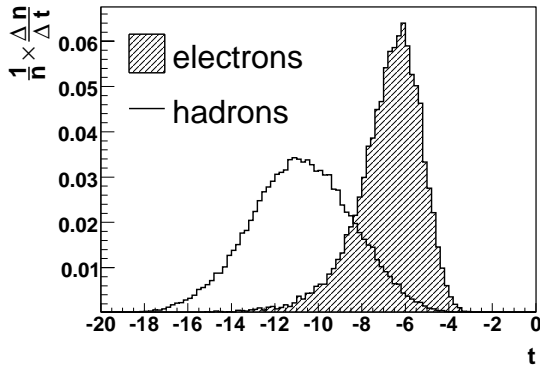


Figure 4.5: Distribution of the Fisher test statistics t for electrons and hadrons passing the preselection, i.e. the track selection and the E/p cut. Both distributions are normalised to one.

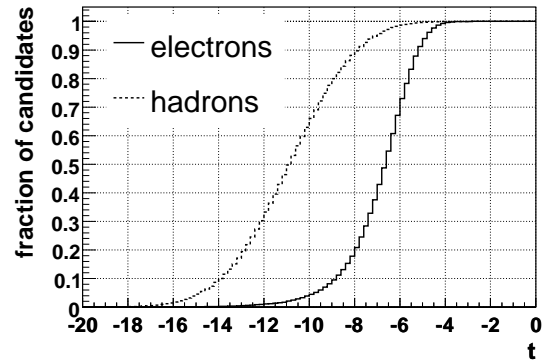


Figure 4.6: Efficiency and fake suppression depending on the Fisher test statistics t . This figure is obtained by integrating the distributions depicted in figure 4.5. Requiring t to be larger than -8 90% of the hadrons that pass the preselection are rejected but about 83% of the electrons survive the cut.

In table 4.1 the reconstruction efficiencies and the misidentification probabilities for different electron selection algorithms are listed. The numbers are extracted from the beauty Monte Carlo and they refer to electron candidates passing the track selection criteria and the kinematic cuts that are also given in table 4.1. The scattered electron is excluded from this study. While the reconstruction efficiency for the electron finder based on the Fisher Discriminant Method (FDM) with the discriminating variables described above as input is compatible to KALEP, the misidentification probability is a factor of 4.5 smaller. In figures 4.7 and 4.8 the dependence of the reconstruction efficiencies and the misidentification probabilities on the transverse momentum of the particle are shown. The reduction of the misidentification probability with respect to the KALEP electron finder allows for a lower cut on the transverse momentum in this analysis. This increases the statistics and gives access to a larger phase space.

So far, the estimators used to identify electrons and the efficiency of the electron finder were studied using Monte Carlo simulations. With the help of a very clean electron sample, which is obtained by selecting events with elastically produced J/ψ mesons, the Monte Carlo simulation is tested. The method and the results are discussed in the following.

4.1.5 Electron Identification Efficiency

In order to study the electron identification efficiency, events with elastically produced J/ψ mesons which decay into an electron and a positron are selected. The branching ratio for this decay channel is

$$\text{BR}(J/\psi \rightarrow e^+e^-) = (5.93 \pm 0.10) \%$$

In addition, there are contributions from radiative decays, i.e. next to leading order Feynman diagrams where a photon is emitted by one of the decay leptons: $J/\psi \rightarrow \gamma e^+e^-$. The branching

electron selection	ϵ_{rec} in %	misidentification probability in %
$p_t > 1.0 \text{ GeV}$ $20^\circ < \theta < 150^\circ$ track is fitted to the primary vertex		
calorimeter quality $Q = 3$ (KALEP)	73.9	8.1
$0.8 < E_{em}/p < 1.6$ (preselection)	82.5	13.7
Fisher discriminant method: $0.8 < E_{em}/p < 1.6$ (preselection) $t > -8.0$	69.7	1.8

Table 4.1: *The reconstruction efficiencies and the misidentification probabilities for different cut scenarios using electrons and hadrons from a beauty Monte Carlo.*

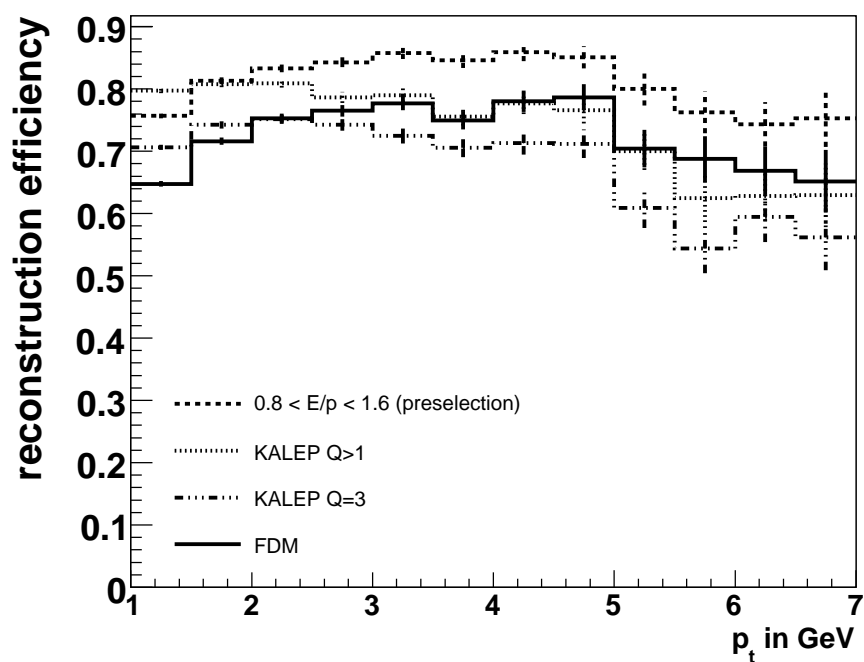


Figure 4.7: *Electron reconstruction efficiency as a function of p_t for different electron selection methods (PYTHIA beauty Monte Carlo).*

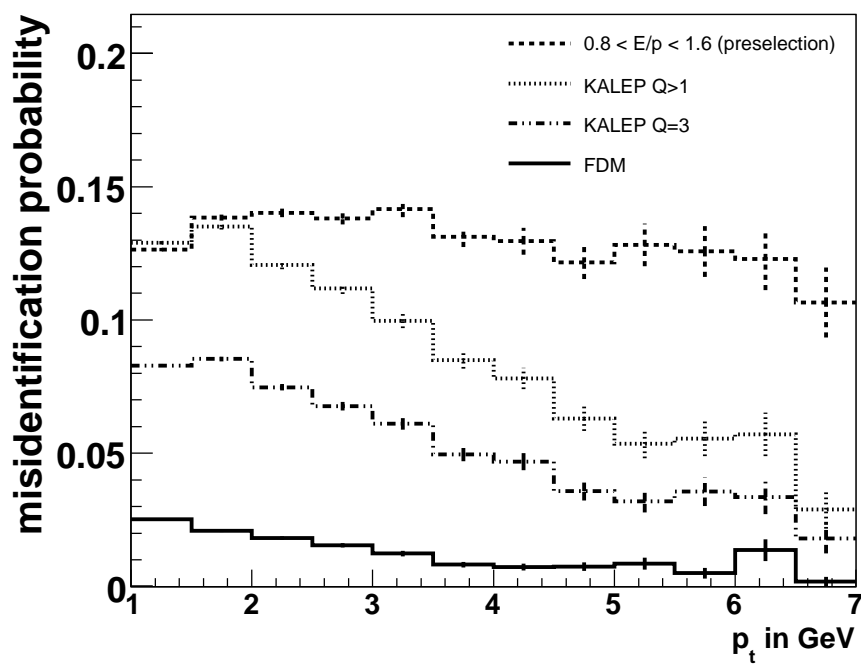


Figure 4.8: *Misidentification probability as a function of p_t for different electron selection methods (PYTHIA beauty Monte Carlo).*

Elastic J/ψ event selection cuts ($J/\psi \rightarrow e^+e^-$)	
Event properties	two primary vertex fitted central tracks unlike sign particles $2.0 \text{ GeV} < \text{invariant mass } m_{ee} < 4.0 \text{ GeV}$ $ z_{vtx} < 35 \text{ cm}$
Decay leptons	$20^\circ < \theta < 160^\circ$ $p_t > 0.8 \text{ GeV}$ one electron candidate with $0.8 < E/p < 1.6$ and $t_{FDM} > -8.0$

Table 4.2: Selection of events with elastically produced J/ψ mesons using the decay into an electron and a positron.

ratio for this radiative decay is about 1% and is therefore not negligible.

A complete list of all event selection cuts can be found in table 4.2. A cut on E/p and on the Fisher test statistic t_{FDM} is imposed on one of the electron candidates to suppress background. No such cuts are applied on the other lepton to allow for efficiency studies.

The invariant mass of all J/ψ candidates fulfilling the selection cuts are shown in figure 4.9. The distributions for HERA I (1999 and 2000) and HERA II (2004 and 2005) data are depicted separately. To extract the number of J/ψ mesons, a function consisting of a modified Gaussian to describe the signal and a linear function to describe the background is fitted to the data:

$$f(m) = \frac{N}{\sqrt{2\pi}\sigma} \cdot \exp \left[-\frac{1}{2} \left(\frac{m - \mu}{\sigma + d \cdot (|m - \xi| - (m - \xi))} \right)^2 \right] + a \cdot m + b \quad (4.10)$$

The Gaussian is modified to describe the radiative tail which can be seen in the invariant mass distributions. The Parameter ξ in the fit function specifies the invariant mass up to which the radiation correction is performed. It is set to 3.05 GeV. In 1999 and 2000 16100 and in 2004 and 2005 14700 J/ψ mesons are found. The number of J/ψ mesons is determined by integrating the signal function. The fit results are also shown in the figure. The width of the Gaussian is significantly larger in 2005 and also the tail is longer due to the worse momentum resolution and more material in the detector.

It is apparent that a very clean sample of electrons is obtained by this event selection. These electrons are used to check whether the discriminating variables exploited in this analysis to identify electrons are well described by the Monte Carlo simulation or not. The electron candidate, which is not required to be identified as an electron, is selected for this study. The distributions of the transverse momentum and the polar angle of these electrons are depicted in figure 4.10. The p_t distribution peaks at about 1.5 GeV and is steeply falling towards larger transverse momenta. Only a small fraction of electrons can be found at transverse momenta above 3.0 GeV. Therefore the identification efficiency in this energy regime cannot be studied. This is of course a drawback since the p_t distribution of electrons from beauty decays extends towards larger transverse momenta. However, it will turn out that the efficiency corrections which have to be applied to the simulation mainly depend on the polar angle but not on the transverse momentum.

In figure 4.11 a) the E/p distribution of electron candidates with a transverse momentum larger

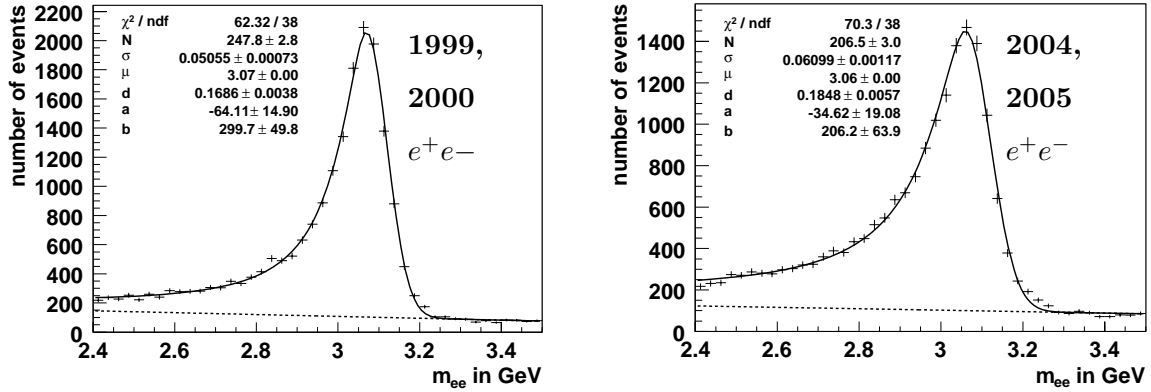


Figure 4.9: Invariant mass distribution of elastically produced J/ψ mesons for the years 1999 and 2000 (left) and 2004 and 2005 (right) separately. The J/ψ mesons are reconstructed via their decay into two electrons. A function consisting of a modified Gaussian and a linear function is fitted to the data (cf. equation 4.10). The results of the fits are shown.

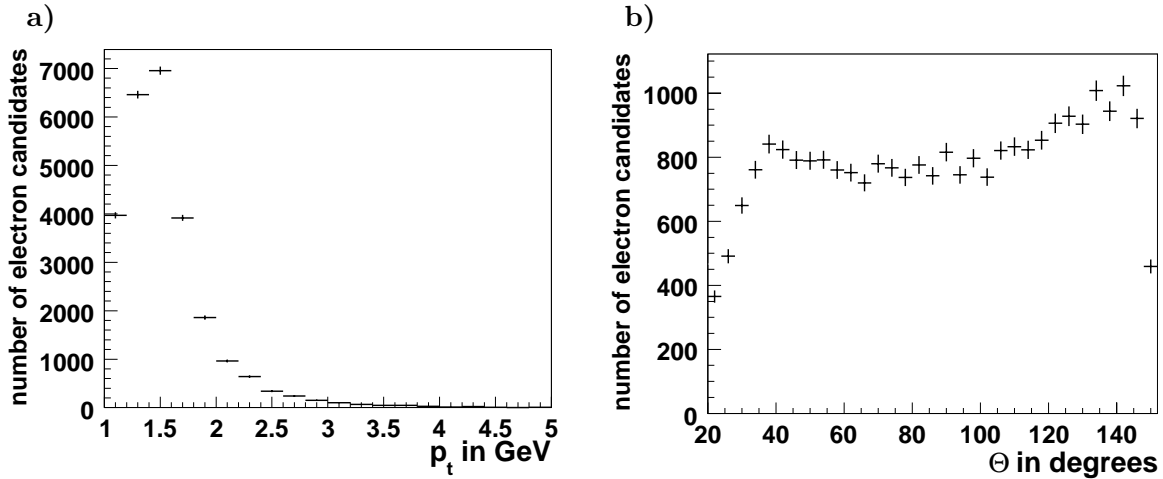


Figure 4.10: Transverse momentum p_t (a) and polar angle θ (b) distributions of the decay electrons of the selected J/ψ mesons.

than 1.0 GeV is shown for data and for the DIFFVM Monte Carlo simulation [64]. The simulation is normalised to the data to allow for a comparison of the shapes. Only events within the J/ψ mass region are considered. The simulation is slightly shifted towards larger values of E/p . This introduces a small bias in the efficiency to identify electrons in the Monte Carlo simulation. To check the influence of the background events on the shape of the E/p distribution which can be retrieved from data, the mass window was increased by a factor of two. It turned out that the effect is negligible. The simulation was also reweighted in the polar angle and in the transverse momentum to cancel any effects that may introduce any trivial bias. The ability of the simulation to describe the data strongly depends on the polar angle. Below 30 degrees the shift between the data and the Monte Carlo simulation is quite significant. This leads to a sizable overestimation of the efficiency in the forward region as will be shown later.

In the figures 4.11 b), c) and d) the other three variables, which are used to separate electrons from hadrons, are depicted. Only electron candidates fulfilling the preselection, i.e. a cut on E/p , are considered in these plots. While the amount of energy that is deposited in the hadronic part of the liquid argon calorimeter E_{had} and the lateral energy shower spread S_{long} are well described, a small shift towards smaller values of the simulation compared to the data can be seen in the distribution of the longitudinal shower spread S_{lat} . Since the Fisher test statistic is a linear function of all four estimators any shift in these variables is directly propagated to this quantity as can be seen in figure 4.11 e).

Both shifts observed in the E/p distribution and in the distribution of the Fisher discriminant variable t_{FDM} lead to an overestimation of the efficiency in the simulation when a cut on these quantities is performed. In particular in the forward region corrections to the Monte Carlo simulation are inevitable. In the following it will be explained how the efficiency is extracted from data. The results will then be compared to the simulation and correction factors as a function of the polar angle and the transverse momentum of the electrons will be derived.

One of the two electron candidates is required to be identified as an electron, i.e. it has to fulfil the cuts on E/p and on the Fisher test statistic t_{FDM} . To extract the efficiency to identify electrons in the calorimeter via the algorithm used in this analysis, it is tested whether the other electron is also identified as an electron or not. The efficiency is then given by the number of events where the other electron is identified divided by the total number of events. The number of electrons is extracted by a fit to the invariant mass distributions or, for low background, just by counting the events in the signal region. The electrons are distinguished by their charge. First the positive electron is required to fulfil the selection cut and the negative lepton is tested if it also fulfils the cuts. Then the procedure is repeated for the opposite case. This is done in bins of the polar angle θ and of the transverse momentum p_t to study the dependence of the efficiency on these quantities.

In a first step HERA I (1999 and 2000) and HERA II (2004 and 2005) data are compared. The p_t distributions in all θ bins agree well between the different data sets. Only in the data from the year 2004 some deviations in the p_t distributions due to the trigger setup are observed. These deviations have no significant impact on the efficiency and are neglected. The efficiency in the years 2004 and 2005 tends to be slightly smaller compared to HERA I data but these differences are not very significant and they are much smaller than the differences that are observed between data and the Monte Carlo simulation. To allow for a finer binning in the polar angle and in the transverse momentum, the data from all years is compared to the simulation. In figure 4.12 a) the efficiency to identify electrons with a transverse momentum larger than 1.0 GeV in the

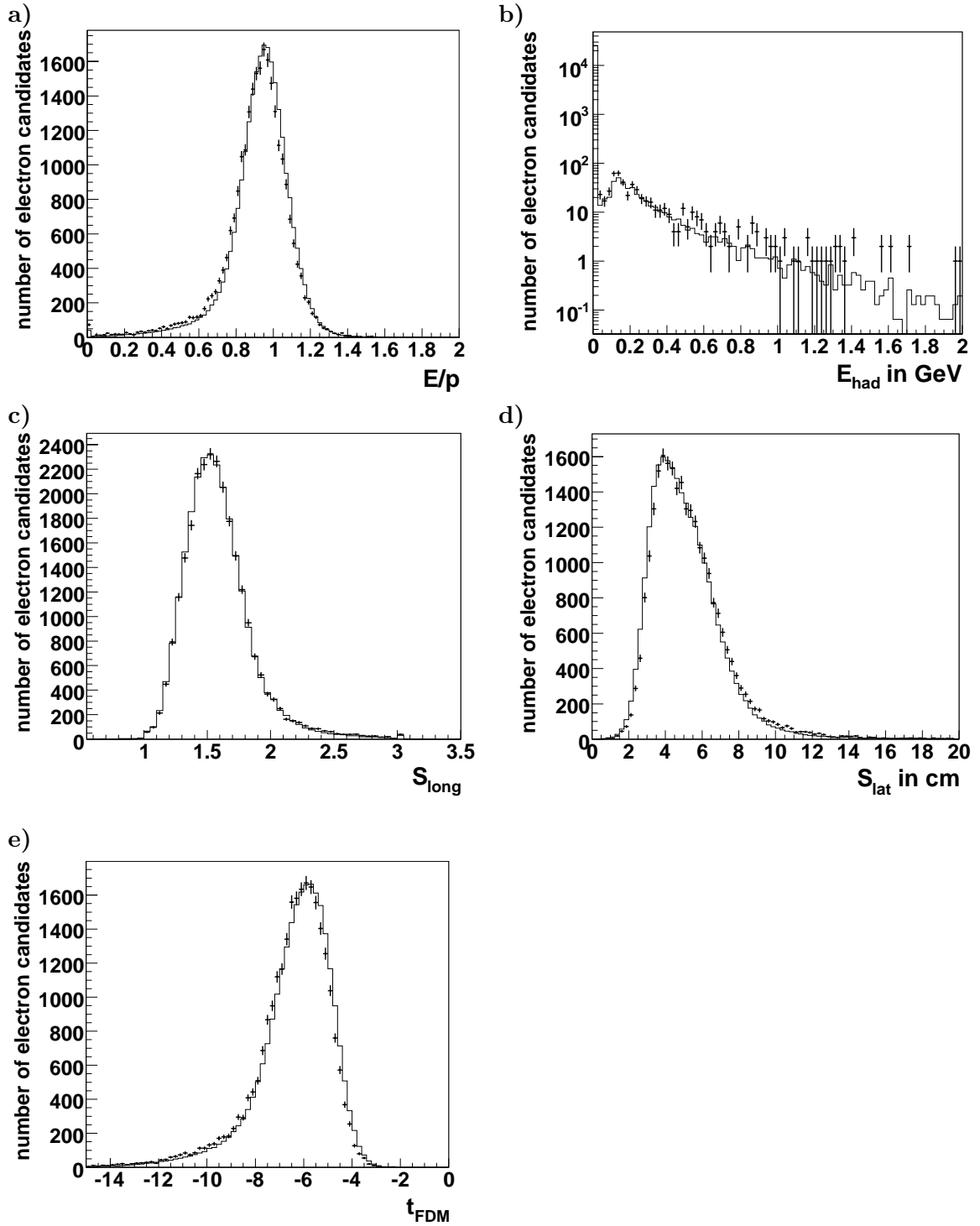


Figure 4.11: Description of the estimators which are used for the electron identification. Data ($J/\psi \rightarrow e^+e^-$) is compared to the DIFFVM Monte Carlo simulation (solid line). The simulation is normalised to the data. a) E/p , b) the energy deposited in the hadronic part of the liquid argon calorimeter E_{had} , c) the longitudinal energy deposition in the electromagnetic part of calorimeter S_{long} , d) the lateral energy deposition S_{lat} and e) the Fisher test statistic t_{FDM} .

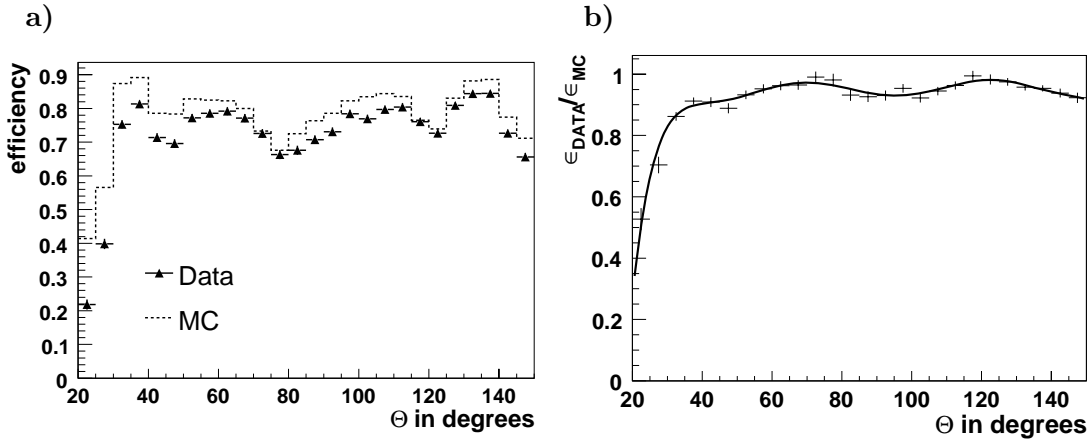


Figure 4.12: a) Efficiency to identify electrons in the calorimeter as a function of the polar angle θ for electron candidates with a transverse momentum larger than 1.0 GeV. The wheel structure of the calorimeter is clearly visible. The data (black triangles) is confronted with the Monte Carlo prediction (dashed line, DIFVM Monte Carlo). b) The efficiency extracted from data divided by the efficiency obtained from the simulation. A polynomial is fitted to the ratio of the efficiencies (full line). This function is used to correct the Monte Carlo.

liquid argon calorimeter is shown as a function of θ . The figure 4.12 b) shows the correction factors which have to be applied to the simulation in order to get a correct description. They are obtained by dividing the efficiency in data by the value from the Monte Carlo simulation. The wheel structure of the calorimeter is clearly visible. The efficiency in the two forward wheels is not well described by the simulation. Here the largest corrections have to be applied.

Figure 4.13 a) shows the efficiency to identify electrons in the liquid argon calorimeter as a function of the transverse momentum p_t for the polar angle region where the discrepancies between data and simulation are moderate ($55^\circ < \theta < 150^\circ$). In figure 4.13 b) the efficiency extracted from data is divided by the predicted efficiency. No dependence of the correction factors on the transverse momentum is observed. The same is true for the forward region ($20^\circ < \theta < 55^\circ$) where the description is, however, worse. The efficiencies obtained from the DIFVM Monte Carlo are compatible with the efficiencies extracted from a beauty Monte Carlo (cf. figure 4.7). This indicates that the results obtained here, using the well isolated decay electrons from elastically produced J/ψ mesons, can be transferred to events in which the electrons are accompanied by hadronic activity.

Since the dependence of the efficiency on the transverse momentum is negligible, corrections as a function of the polar angle are applied to the Monte Carlo simulation to get a better description of the data. The correction function is obtained by fitting a polynomial to the distribution of the correction factors which are determined in bins of the polar angle. The result is depicted in figure 4.12 b). In order to estimate the systematic error on the electron identification efficiency, correction functions are determined for each year separately. The largest deviations between the correction functions amount to about $\pm 3\%$. This value is used as a measure for the systematic uncertainty related to the electron identification efficiency.

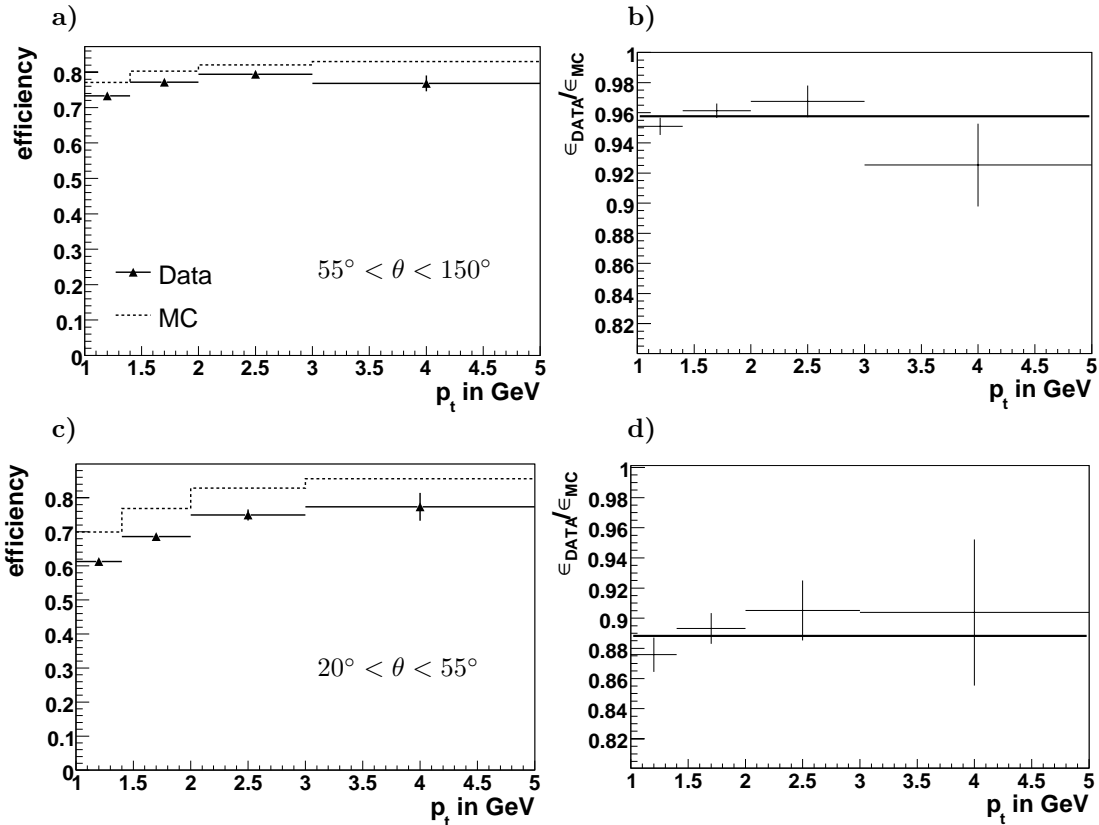


Figure 4.13: a) The efficiency to identify electrons in the liquid argon calorimeter as a function of the transverse momentum ($55^\circ < \theta < 150^\circ$). b) Efficiency in data divided by the predicted efficiency. No dependence of the corrections on the transverse momentum is observed. c) and d) The same distributions for the more forward region ($20^\circ < \theta < 55^\circ$).

4.2 Muon Identification

To identify muons, information from the muon system and from the liquid argon calorimeter is used. Depending on the distinctness of the muon signature from the background, different qualities are assigned to a muon candidate. The quality scheme, the reconstruction of muons in the instrumented iron and the algorithm that searches for muon signatures in the liquid argon calorimeter, the KALEP muon finder, will be briefly described in the beginning of this section. It will then be investigated if the detector simulation is able to describe the detector response to muons. This is done using muons from J/ψ meson decays. It will turn out that the muon system is reasonably well described. However, large discrepancies are observed for some of the KALEP estimators. For this reason, efficiency corrections to be applied to the simulation are derived.

4.2.1 Muons in the Instrumented Iron

At energies considered here, muons mainly lose energy in the detector material due to ionisation. They do not interact strongly and the energy loss due to radiation (Bremsstrahlung) becomes

important only at energies of a few hundred GeV and is therefore negligible here. According to the Bethe-Bloch equation muons are minimal ionising at energies of about 300 MeV. While electrons produce electromagnetic showers and are stopped in the first layers of the liquid argon calorimeter and hadrons generate showers due to strong interactions with both an electromagnetic and a hadronic component and are stopped also in the calorimeter muons lose only a small amount of their energy as they do not produce showers. Minimal ionising particles (MIPs) deposit on average about 10 MeV per traversed centimetre in lead. To reach the central muon system the muon momentum has to be greater than 1.5 GeV. In the instrumented iron muons lose about 90 MeV per iron plate. As described in section 3.2.3 they have to traverse several iron plates to allow the reconstruction of a track. As a consequence the energy of a muon has to be larger than about 2 GeV to be detected in the instrumented iron with an efficiency larger than 50 %.

Since the momentum and angle resolution of iron tracks, i.e. tracks that are reconstructed from hits in the instrumented iron, is not sufficient for this analysis only muon candidates with a link to an inner track are accepted. Tracks reconstructed using the central tracking system and the forward tracking device are denoted as inner tracks. The linking is performed by the standard H1 event reconstruction software H1REC. First, central tracks that match in the polar and in the azimuthal angle and that have a momentum larger than 1 GeV (for the barrel) are selected. These tracks are extrapolated to the muon system taking into account multiple scattering and energy loss due to ionisation assuming the muon hypothesis. Then a χ^2 value according to the following equation is calculated:

$$\chi^2 = (\vec{X}_E - \vec{X}_{Iron})^T V^{-1} (\vec{X}_E - \vec{X}_{Iron}) \quad (4.11)$$

\vec{X}_E contains the track parameters of the extrapolated inner track and \vec{X}_{Iron} the parameters of the iron track (also called outer track). The following three track parameters are used in the barrel: 1) The z -coordinate of the first point on the iron track. 2) The azimuthal angle ϕ_{iron} of the connection of the first measured point on the iron track to the event vertex. 3) The azimuthal angle ϕ_{dir} of the reconstructed iron track. V is the joint covariance matrix. Depending on the probability derived from the χ^2 value the linking hypothesis is accepted or rejected.

An iron quality $Q_{iron} = 10$ is assigned to a muon candidate in the central muon system with an inner track link if it fulfils the cuts listed in table 4.3. The cuts require that the iron track points to the event vertex and that a minimum number of layers is traversed to discriminate against pions.

4.2.2 Muon Identification in the Calorimeter

Muons can also be identified exploiting the typical pattern which they create traversing the liquid argon calorimeter. Since they are minimal ionising they deposit only a small amount of energy along their path through the calorimeter and they produce no showers like hadrons (pions and kaons for example). To search for lepton signatures, the KALEP program is executed during the event reconstruction. Tracks are extrapolated as a helix into the liquid argon calorimeter and four discriminating variables based on the energy depositions in the calorimeter cells within two cylinders of different radii around the extrapolated helix are evaluated. The following variables are calculated to identify muons:

$Q_{iron} = 10$
$\rho_0 < 100$ cm
$z_0 < 100$ cm
number of hit layers > 2
first layer hit ≤ 5
last layer hit ≥ 2
link probability $> 10^{-4}$

Table 4.3: *Standard selection cuts for muons in the instrumented iron. For simplification only the cuts for muons in the barrel are shown. ρ_0 and z_0 are the cylinder coordinates of the extrapolated iron track with respect to the event vertex at the point of closest approach.*

1. The sum of the cell energies in the electromagnetic part of the calorimeter within $R_a = 15$ cm around the extrapolated helix: E_{em} .
2. The sum of the cell energies in the calorimeter within $R_b = 30$ cm: E_{tot} .
3. The length of the extrapolated track from the calorimeter surface to the last assigned cell ($R_a = 15$ cm): L_{max} .
4. The sum of all track lengths from the calorimeter surface to all cells in the hadronic part of the calorimeter which are assigned to the track ($R_a = 15$ cm): L_{had} .

A lower as well as an upper cut is defined for E_{em} to discriminate against electrons or photons which deposit their whole energy in the electromagnetic part of the calorimeter, producing an electromagnetic shower that is fully contained in a cylinder with a radius of 15 cm resulting in a larger value for E_{em} than expected for muons. In the definition of E_{tot} also the energy depositions in the hadronic part of the calorimeter are taken into account. As hadronic showers tend to be much broader, a radius of 30 cm around the helix is chosen. By setting an upper limit for E_{tot} , hadrons are suppressed. Setting a lower limit on L_{max} and L_{had} one exploits that on average muons are able to penetrate the calorimeter much deeper than hadrons. No sharp cuts on the estimators are applied but deviations from the limits are calculated and summed up. The limits depend on the polar angle and on the momentum. According to the result a calorimeter quality is assigned to the muon candidate:

- no muon: $Q_{cal} = 0$
- weak quality: $Q_{cal} = 1$
- medium quality: $Q_{cal} = 2$
- good quality: $Q_{cal} = 3$

The total muon quality is then given by:

$$Q_{\mu} = Q_{iron} + Q_{cal}.$$

To investigate if the detector response to muons is well simulated, the same strategy as for electrons is followed. The procedure and the results are discussed in the following section.

Elastic J/ψ event selection cuts ($J/\psi \rightarrow \mu^+\mu^-$)	
Event properties	two primary vertex fitted central tracks unlike sign particles $2.0 \text{ GeV} < \text{invariant mass } m_{\mu\mu} < 4.0 \text{ GeV}$ no candidate for a cosmic ray muon $ z_{vtx} < 35 \text{ cm}$
Decay leptons	$20^\circ < \theta < 160^\circ$ $p_t > 0.8 \text{ GeV}$ one muon candidate with muon quality $Q_\mu \geq 2$

Table 4.4: Selection of events with elastically produced J/ψ mesons which decay into **two muons**. Details on the cuts against cosmic ray muons can be found in the text.

4.2.3 Muon Identification Efficiency

The efficiency to identify muons in the calorimeter and the instrumented iron is extracted from data using a sample of elastically produced J/ψ mesons. The efficiency depends on the polar angle θ and the transverse momentum p_t of the muon. Before the procedure is described in detail and the results are presented the event selection cuts will be briefly described.

First, events with two primary vertex fitted central tracks belonging to oppositely charged particles are selected. Then the muon mass is assigned to both particles and the invariant mass $m_{\mu\mu}$ is calculated. If the invariant mass is smaller than 2.0 GeV or larger than 4.0 GeV the event is rejected. Cuts on the decay leptons are applied to improve the signal to background ratio. The transverse momentum of both particles is required to be larger than 0.8 GeV and the polar angular range is restricted to $20^\circ \leq \theta \leq 160^\circ$. In addition, the tracks have to fulfil the selection cuts listed in table 5.2 and one muon candidate is required to have at least a medium muon quality to suppress background: $Q_\mu \geq 2$.

All events in which a candidate for a cosmic ray muon is found are rejected. Apart from non-resonant lepton pair production, cosmic ray muons are the main source of background. Cosmic ray muons are identified by the following criteria:

- When a cosmic ray muon traverses the central tracking chambers it may produce two tracks in opposite hemispheres of the detector. These two tracks show a typical back-to-back topology. To search for cosmic ray muons a straight line fit is performed. If the χ^2 of the fit is smaller than 10.0 then the hypothesis is accepted and the event is rejected.
- Tracks that originate from a cosmic ray muon do not necessarily point to the beam axis. This may lead to large distances of closest approach d_{ca} in the $r\phi$ -plane with respect to the fitted event vertex. Therefore events are rejected where both tracks have a d_{ca} larger than 0.1 cm.
- Tracks from an ep interaction show comparable track timings t_0 . The distribution of the difference of the two track timings Δt therefore peaks at zero for muons from a J/ψ decay. However, tracks from a cosmic ray muon have significantly different track timings. Thus all events with $|\Delta t| > 2.3 \text{ ns}$ (12 ticks, 500 ticks = 96 ns) are rejected.

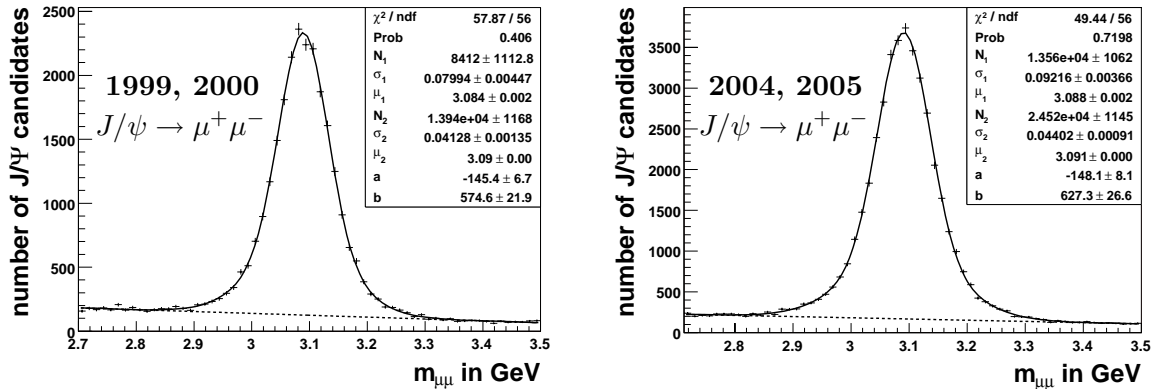


Figure 4.14: Invariant mass distribution of elastically produced J/ψ mesons for the years 1999 and 2000 (left) and 2004 and 2005 (right) separately. A function consisting of two Gaussians and a linear function is fitted to the data (cf. equation 4.12). The cuts listed in table 4.4 were applied.

- Cosmic ray background events outside the nominal interaction region along the beam axis are rejected by a cut on the z position of the reconstructed event vertex z_{vtx} .

All the event selection cuts are summarised in table 4.4. The invariant mass distributions of the J/ψ candidates passing the selection cuts for HERA I (1999 and 2000) and HERA II (2004 and 2005) data are shown in figure 4.14. To extract the number of J/ψ mesons a function that consists of two Gaussians and a linear function is fitted to the invariant mass distribution:

$$f(m) = \frac{N_1}{\sqrt{2\pi}\sigma_1} \cdot \exp\left[-\frac{1}{2}\left(\frac{m - \mu_1}{\sigma_1}\right)^2\right] + \frac{N_2}{\sqrt{2\pi}\sigma_2} \cdot \exp\left[-\frac{1}{2}\left(\frac{m - \mu_2}{\sigma_2}\right)^2\right] + a \cdot m + b \quad (4.12)$$

The signal is described by two Gaussians to take into account different mass resolutions in different phase space regions. N_1 and N_2 are the number of events, μ_1 and μ_2 the mean values and σ_1 and σ_2 the width of the Gaussians. The mean values agree with the nominal J/ψ mass. The linear function in formula 4.12 describes the background. The result of the fit is depicted in figure 4.14. The data is well described. In total about 14,000 J/ψ mesons are selected in 1999 and 2000. In the years 2004 and 2005 about 38,000 J/ψ mesons are found.

4.2.3.1 Muons in the Instrumented Iron

To investigate the efficiency to identify muons in the instrumented iron, the data is divided in bins of the transverse momentum p_t and the polar angle θ . In each bin the number of muons which are identified in the instrumented iron is divided by the total number of muons from J/ψ mesons which fall into that bin. Binominal errors are calculated. Both muons in an event are used since the muon identification in the iron is independent of the identification in the calorimeter. In order to avoid any bias, events are selected from the preselected data sample defined by the cuts listed in table 4.4 which contain at least one muon with medium or good calorimeter quality $Q_{cal} \geq 2$. The number of muons is determined by a fit to the invariant mass distributions in each bin. The distributions are fitted with a function which consists of a Gaussian

for the signal and an exponential, linear or constant function to describe the background. Which function is chosen depends on the size of the background contribution. In each bin the invariant mass distribution is well described by the fit. For low or medium background also a different approach to estimate the number of J/ψ mesons is used to check the results from the fit. The number of events in the signal region are counted and corrected for the number of background events. The number of background events is estimated using the sidebands of the invariant mass distribution. Consistent results are obtained for both methods. The latter method is preferred where applicable since it is faster and more stable in the case of low statistics.

In order to avoid any bias in the efficiency determination, events are selected which are triggered by subtriggers that do not contain any muon requirement on either trigger level. For the years 1999 and 2000 mainly the subtriggers S61 and S109 are used. The subtrigger S61 contains trigger elements delivered by the SpaCal and is designed to trigger events with a scattered electron at low and medium Q^2 . The subtrigger S109 contains trigger elements provided by the electron tagger at 33 meters downstream of the interaction point. In addition, tracks and a significant vertex are required.

In the year 2004 mainly the subtrigger S61 and in the year 2005 mainly the subtriggers S11 and S61 are used as monitor triggers. The subtrigger S11 contains mainly trigger elements from the CIP 2000 and is designed to trigger cosmic ray muons. A low track multiplicity and a back-to-back topology is required. Since the requirement on the back-to-back topology is quite loose this trigger has a very high efficiency to trigger elastically produced J/ψ mesons. In the HERA II running phase the subtrigger S61 is still used to trigger events at low and medium Q^2 but the energy threshold was raised. Furthermore the SpaCal acceptance corresponds to a slightly higher Q^2 as some of the inner cells were removed during the upgrade. In addition, the track and vertex conditions changed.

In a first step the iron efficiencies for the different years are compared with each other. To allow for a meaningful comparison of the muon efficiencies, it is inevitable that the muons have the same momentum distribution in each θ bin which is investigated since the efficiency to identify muons in the instrumented iron depends strongly on the momentum. To obtain comparable momentum distributions, the subtrigger S61 is required in each year for this investigation. To compare HERA I and HERA II data, a cut on Q^2 is applied in addition: $Q^2 > 4 \text{ GeV}^2$. This is done because the momentum distribution depends on Q^2 and because the acceptance in Q^2 is different for HERA I and HERA II data. The comparison shows that the efficiency is the same for all years within the statistical uncertainties.

For more detailed studies the data from all years are combined. The Monte Carlo simulation is reweighted in bins of the polar angle and transverse momentum to allow for comparisons with the data and to determine correction factors. Figure 4.15 shows the efficiency to identify muons in the instrumented iron as a function of the polar angle for different bins of the transverse momentum. Also shown is the ratio of the efficiencies between data and the simulation. In figure 4.16 the dependence of the iron efficiency on the transverse momentum is investigated for four different polar angular regions. The efficiency in the simulation is corrected in bins where the difference between data and the prediction is significant. The correction factors are known to a precision of $\pm 5 \%$. This number is used as systematic uncertainty on the muon identification efficiency.

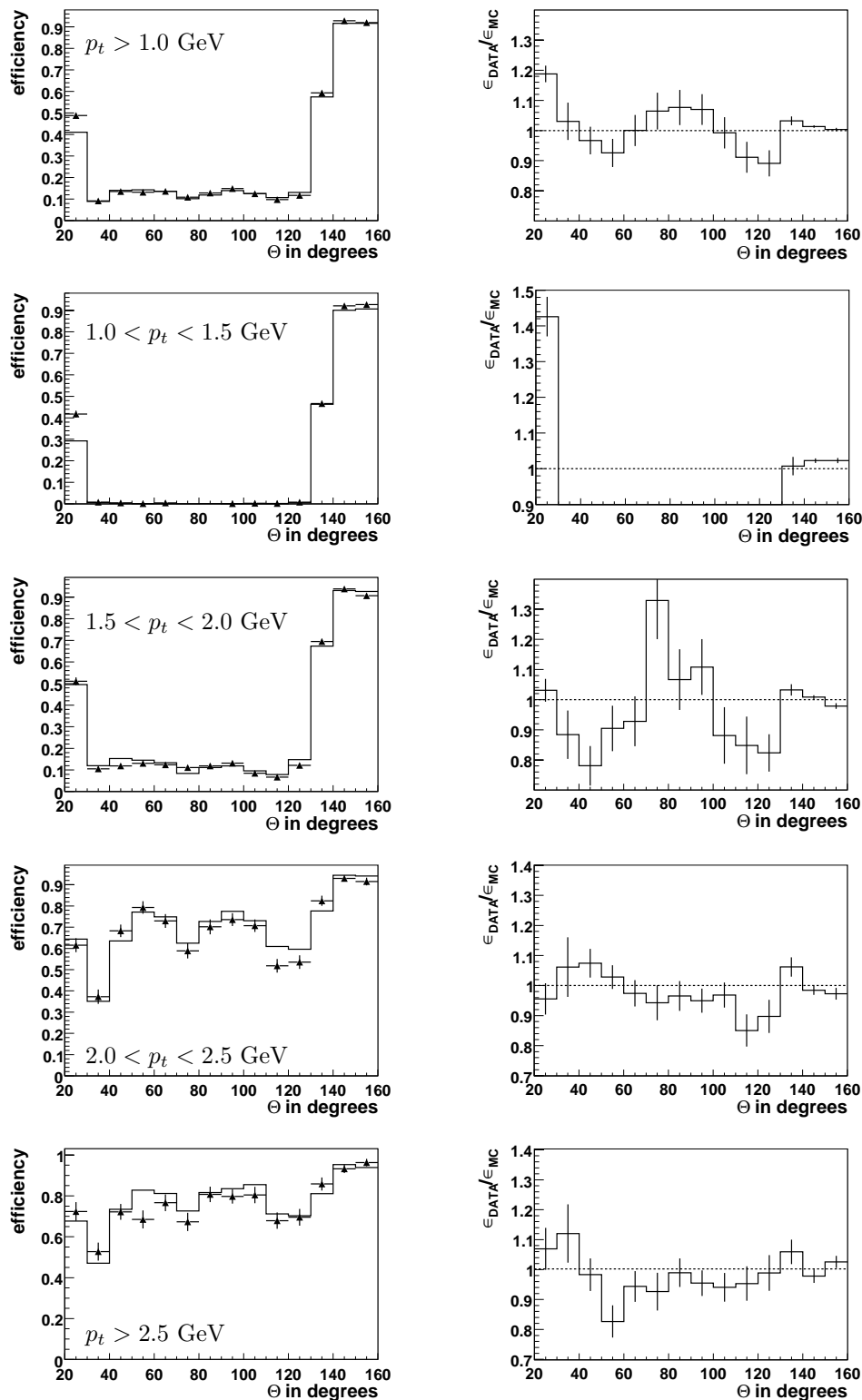


Figure 4.15: Efficiency to identify muons in the instrumented iron as a function of the polar angle θ for different bins of the transverse momentum p_t (left hand side). On the right hand side the ratios of the efficiencies between the data and the Monte Carlo simulation are shown.

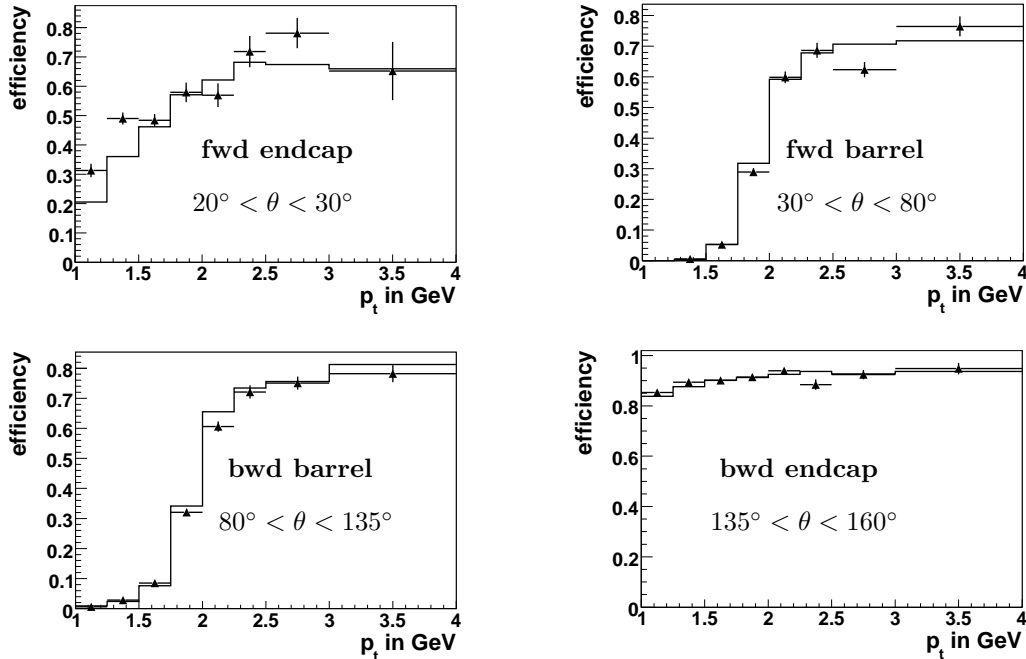


Figure 4.16: Efficiency to identify muons in the forward endcap, the forward and backward barrel and in the backward endcap as a function of the transverse momentum p_t . Data (black triangles, statistical errors are shown) is compared to the simulation (dashed line).

4.2.3.2 Muons in the Liquid Argon Calorimeter

The efficiency to identify muons in the liquid argon calorimeter is calculated in a similar way as it is done for iron muons but it has to be taken into account that already one muon candidate with at least a medium calorimeter quality ($Q_{cal} \geq 2$) is required in order to get a clean J/ψ sample. To avoid any bias in the efficiency determination, the data is divided into two samples. One sample consists of events where the positive lepton is required to have at least a medium calorimeter quality. It is then checked whether the negatively charged lepton fulfils the muon selection cuts ($Q_{cal} = 3$) or not. The procedure is repeated for the sample of negatively charged leptons which have at least a medium muon quality. The efficiencies for negative and positive leptons are different. For this reason the results cannot be combined to reduce the statistical uncertainty but the efficiencies have to be investigated separately for both cases.

Since the calorimeter efficiency is independent of the muon trigger in the instrumented iron, all events which fulfil the selection cuts are used for this study. It was carefully checked that no bias is introduced by this approach.

In figure 4.17 the distributions of the four KALEP estimators E_{em} , E_{tot} , L_{max} and L_{had} for the muons that enter the efficiency calculation are shown. Also shown is the hadronic energy E_{had} . The data is compared to the Monte Carlo simulation (DIFFVM). Only muons with a transverse momentum larger than 1.0 GeV are considered here and the invariant mass of the reconstructed J/ψ candidate has to be close to the nominal J/ψ mass, $|m_{\mu\mu} - m_{J/\psi}| < 0.1$ GeV. The electromagnetic energy E_{em} and the hadronic energy E_{had} are very poorly described. The simulation is shifted significantly towards larger values. The estimator L_{max} is reasonably well

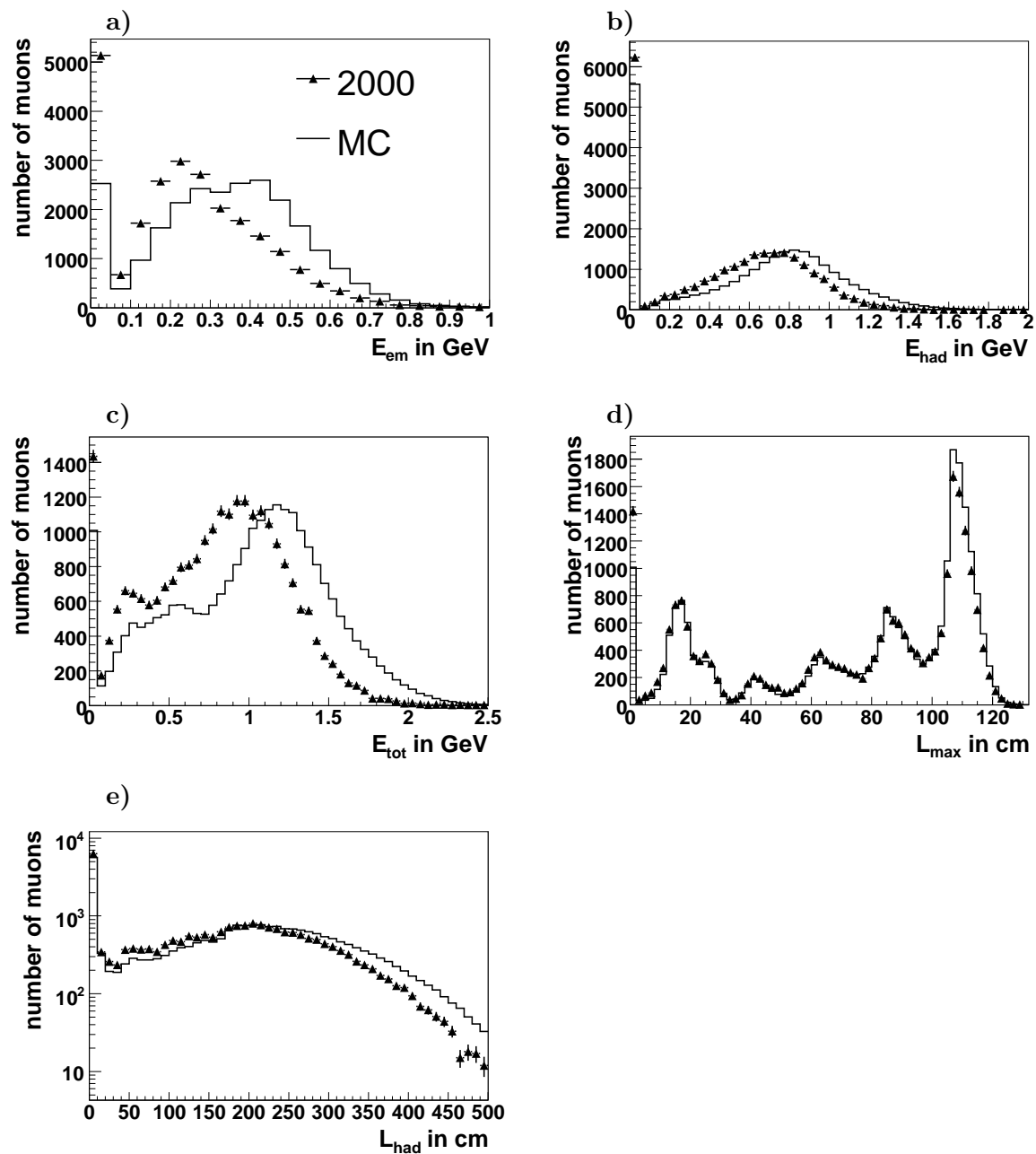


Figure 4.17: The description of the KALEP estimators for a sample of muons from J/ψ decays. The data (black triangles) is compared to the DIFFVM Monte Carlo (dashed line). a) The energy deposited in the electromagnetic part of the liquid argon calorimeter E_{em} , b) the energy deposited in the hadronic part of the LAr calorimeter E_{had} , c) the total energy in the calorimeter E_{tot} , d) the maximal track length in the calorimeter L_{max} and e) the hadronic track length L_{had} .

described. In contrast to electrons the description of the estimators is much worse. This results in larger corrections to be applied to the simulation as will be demonstrated in the following.

Figure 4.18 shows the efficiency to identify muons in the liquid argon calorimeter as a function of the polar angle θ . Muons and antimuons are investigated separately. The results for the different years are confronted with the Monte Carlo prediction. The efficiency in the year 2005 is smaller compared to 1999 and 2000 data. This effect is larger for antimuons than for muons. For the year 2004 the situation is even worse. The same tendency can be seen in figure 4.19 where the efficiency as a function of the transverse momentum for the forward region, $35^\circ < \theta < 80^\circ$, is shown. The efficiency for muons is higher than for antimuons and in general muons are better described by the simulation.

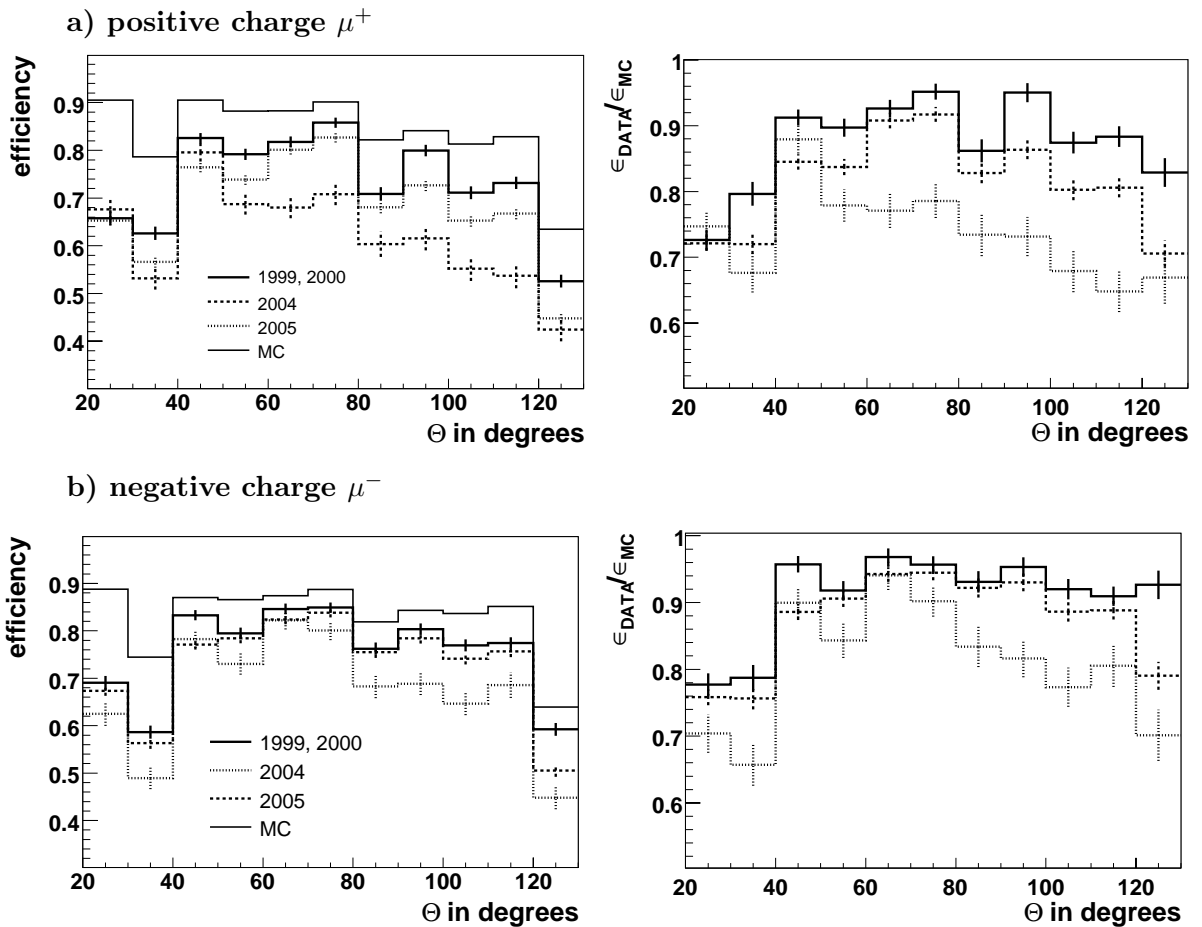


Figure 4.18: The muon identification efficiency in the calorimeter ($Q_{\text{cal}} = 3$) for muons with a transverse momentum larger than 1.0 GeV as a function of the polar angle for the different years considered in this analysis. The efficiency is investigated for antimuons (a) and for muons (b) separately.

In order to achieve a better description of the efficiency, the Monte Carlo simulation is corrected. The data is divided in bins of the polar angle and the transverse momentum. For each bin the efficiency is determined and the ratio between the data and the simulation $\epsilon_{\text{DATA}}/\epsilon_{\text{MC}}$ is calculated. Since the dependence of the efficiency on the polar angle θ is much stronger and

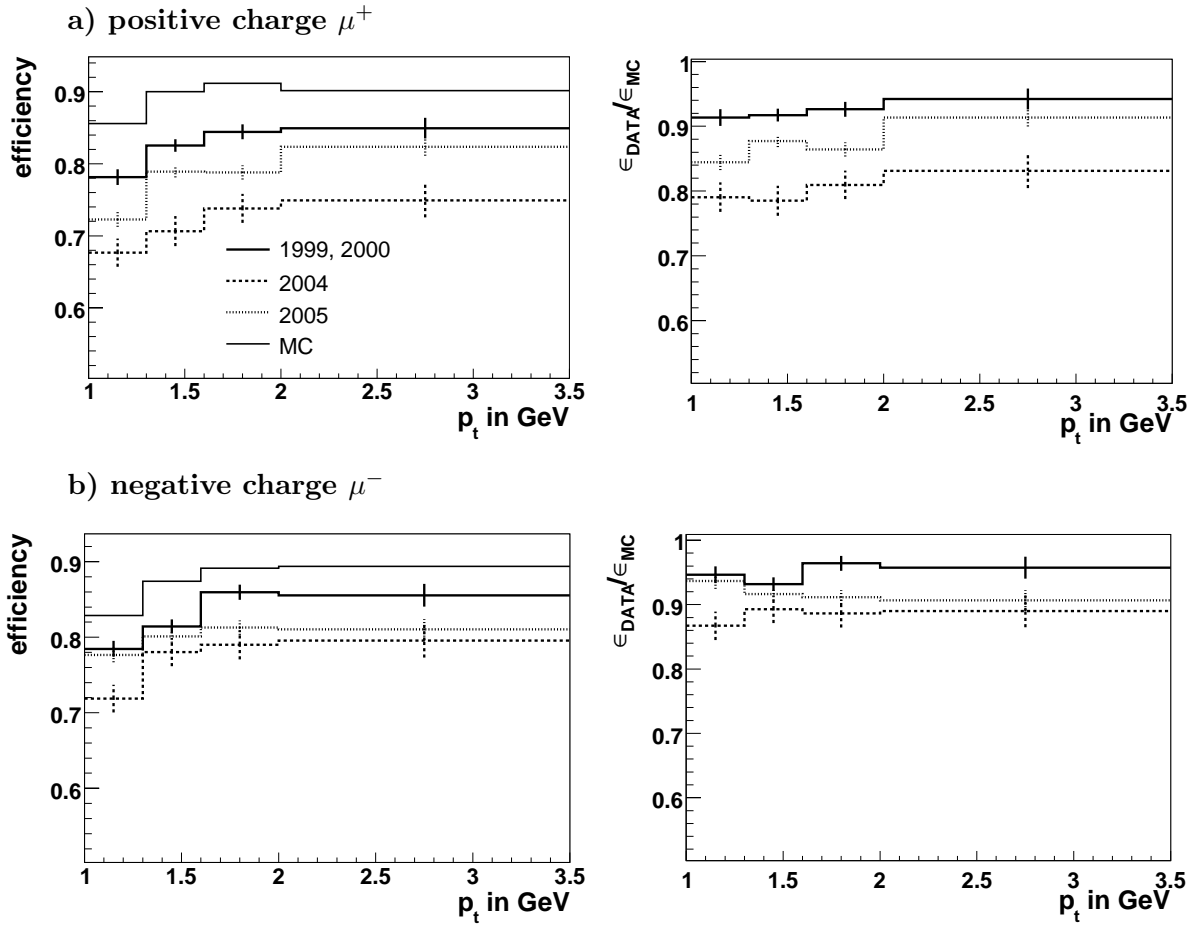


Figure 4.19: a) The efficiency to identify muons in the calorimeter ($Q_{\text{cal}} = 3$) as function of the transverse momentum p_t for $35^\circ < \theta < 80^\circ$. The efficiencies for antimuons (a) and muons (b) are shown separately.

less continuous compared to the p_t dependence the data is divided in eleven θ and just three p_t bins ($1.0 < p_t < 1.4$ GeV, $1.4 < p_t < 1.8$ GeV and $p_t > 1.8$ GeV). To obtain a continuous correction function the Delaunay triangulation technique [65] is used to interpolate the data set. Correction functions are determined for each year and for muon and antimuons separately.

Figure 4.20 shows the ratio of the efficiencies between data and the corrected Monte Carlo simulation for the different years. The efficiencies are reasonably well described. The remaining discrepancies are taken into account in the evaluation of the systematic uncertainty. The systematic uncertainty on the muon identification efficiency is estimated to amount to $\pm 3\%$.

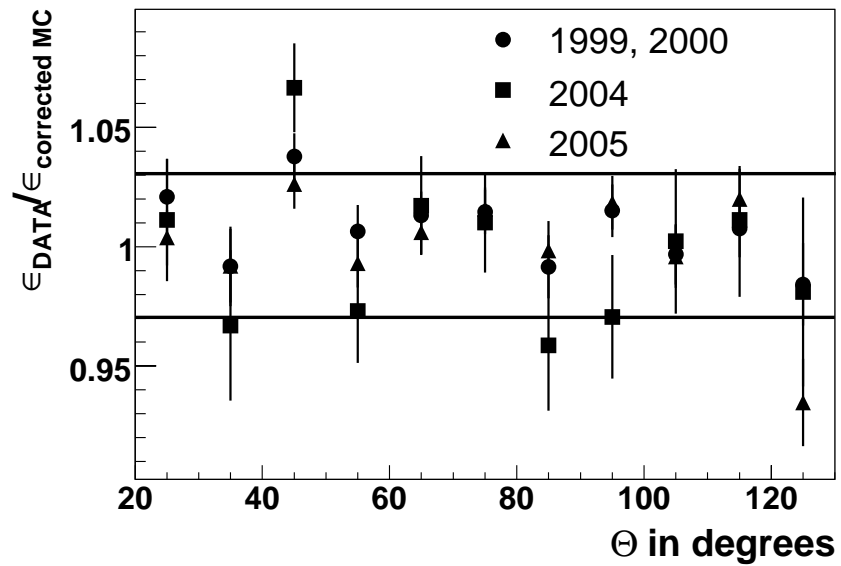


Figure 4.20: Ratio between the calorimeter efficiency ($Q_{\text{cal}} = 3$) in data and in the corrected Monte Carlo simulation.

CHAPTER 5

DATA SELECTION

In this chapter the selection of events with two leptons and two jets is described. The two leptons (two muons or a muon and an electron) are used to tag both heavy quarks (‘double tag’). Two jets in the final state are required to enrich the data sample with beauty events, to reconstruct the kinematics of the heavy quarks and to measure the beauty fraction via the transverse momentum of the leptons with respect to the jet axis p_t^{rel} . The charge and azimuthal angle correlation of the two leptons is also exploited to determine the beauty fraction. This allows to cross check the result obtained from a fit to the p_t^{rel} distributions and to combine both measurements to reduce the statistical uncertainty. The lepton correlation can also be used to determine the charm contribution.

In the first section the run selection is presented and the integrated luminosities \mathcal{L} for the different years and running periods are quoted. The total integrated luminosity amounts to $\mathcal{L} = 221.6 \text{ pb}^{-1}$.

In the subsequent section the jet selection is described. Jets are reconstructed in the laboratory frame using the inclusive k_t clustering algorithm. It will then be explained in detail how leptons are selected and which cuts are performed to enrich the data sample with heavy flavour events and to suppress background. Mainly because of trigger reasons one of the leptons is required to be a muon. The other lepton can either be a muon or an electron. This leads to two different data samples with different systematics that can be used to measure the same process. This allows for a number of cross checks and also increases the statistics and therefore the significance of the results.

The next important topic covered is the trigger used in this analysis. Most events have been triggered by the subtrigger S19 which requires a muon signature in the barrel part of the instrumented iron, a central vertex and track candidates in the jet chambers. The muon trigger element is only efficient for muons with a transverse momentum above 2 GeV. For dijet events containing heavy quarks the vertex and the track conditions are expected to be very efficient. Trigger efficiencies will be extracted from data and compared to the Monte Carlo predictions.

At the end of this chapter it will be described how photoproduction events are selected and the event yields for the different running periods are quoted to demonstrate the stability of the event selection.

Year	Lepton	First run	Last run	\mathcal{L} in pb^{-1}
1999 e^- (DST3)	e^-	231721	241649	10.4
1999 e^+ (DST3)	e^+	246159	259461	14.1
2000 (DST3)	e^+	262204	279006	46.4
2004 (DST2)	e^+	367284	391458	42.7
2005 (DST2)	e^-	399629	436893	108.0
Σ				221.6

Table 5.1: *Integrated luminosities for the different data taking periods.*

5.1 Run Selection

Data taken in the years 1999, 2000, 2004 and 2005 are used. Only events are considered where the detector components important for this analysis are fully operational. This includes both jet chambers (CJC1 and CJC2), the inner and outer proportional chamber (CIP and COP), the liquid argon calorimeter (LAr), the spaghetti calorimeter (SpaCal), the central muon system (CMD) and the time of flight (TOF), veto and luminosity systems. Runs have to be of good or medium quality and their luminosities have to be greater than 0.1 nb^{-1} to be accepted. Minimum bias and shifted vertex runs are not included. For the luminosity calculation satellite bunch corrections are performed. The ep interaction region is restricted in z to ± 35 cm around the nominal interaction point. The resulting integrated luminosities, including all mentioned corrections, are given in table 5.1. In total, an integrated luminosity of $\mathcal{L} = 221.6 \text{ pb}^{-1}$ is available.

5.2 Jet Selection

Jets are reconstructed in the laboratory frame using the inclusive k_t clustering algorithm as described in section 2.5. The input to this algorithm is the hadronic final state (HFS) that consists of all reconstructed particles from the ep interaction except for the scattered electron. The HFS particles are created out of track and cluster information such that double counting of energy is avoided. In the present analysis, the HADROO2 algorithm is used to build the HFS. Here just a brief overview will be given. More details can be found in [66].

5.2.1 The HFS algorithm

The HFS algorithm HADROO2 is implemented such that a loop over all vertex fitted tracks that fulfil the selection criteria listed in table 5.2 is performed and each track is extrapolated to the calorimeter and matched to clusters. The energy of all clusters in the calorimeter that lie within a cylinder around the extrapolated track is summed up. The radii are 25 cm for the electromagnetic and 50 cm for the hadronic part of the calorimeter, respectively. Depending on the errors of the energy measurements the track or the cluster information is preferred. For central tracks passing the mentioned selection criteria the track measurement is better than the calorimeter measurement up to energies of 25 GeV. If the track measurement is preferred, the corresponding cluster is locked. This means that the cluster is not taken into account by the

vertex fitted, prefer primary vertex fitted hypothesis
$p_t > 120 \text{ MeV}$
$20^\circ \leq \theta \leq 160^\circ$
$d'_{ca} \leq 2 \text{ cm}$
start radius $\leq 50 \text{ cm}$
radial track length $> 5 \text{ cm}$ for $\theta > 150^\circ$
radial track length $> 10 \text{ cm}$ for $\theta < 150^\circ$

Table 5.2: Selection criteria for vertex fitted tracks. For simplification and because they make up the biggest part of all tracks only the selection cuts for central fitted tracks are given. The d'_{ca} is the distance of closest approach of the non vertex fitted track hypothesis to the event vertex. The start radius is the distance of the first hit used for the track measurement from the beam line.

algorithm any further. If the cluster energy is significantly larger than the energy of the track, then the track energy is subtracted from the cluster energy. The remaining cluster energy can then be used as a seed for another particle candidate. If the calorimeter information is supposed to be more precise, a HFS particle is created out of the calorimeter measurement only. Neutral HFS particles are created out of the clusters that were not matched to tracks.

HADROO2 was developed to describe the energy flow and is not suitable for particle identification. One reason is that the HFS reconstructed by this algorithm obviously depends on the order in which the tracks are treated. If the cylinders of two extrapolated tracks overlap, a cluster may be matched to the track treated first, although the energy was deposited by the other track. Calorimeter based particle identification using the HFS reconstructed by this algorithm is therefore not sensible. In [67] an algorithm suitable for particle identification was developed. This algorithm in principle allows that several tracks may share the energy of the same clusters. Also a neural net for finding electrons was designed. It processes separation variables that exploit the differences in the shower shapes in the calorimeter between electrons and hadrons. Drawbacks of this method are for example that there is no jet calibration available for this algorithm and that muons are not treated at all. In this analysis a different approach is used. The HFS is not the basis for the particle identification but each track is extrapolated as a helix into the calorimeter and cells are matched to the track. These cells are input for the calorimeter based particle identification. As it was shown in chapter 4, an efficient electron identification is obtained by this method.

The HFS is not only the input to the jet algorithm, but it is also used to measure the inelasticity y via the hadron method as described in [68]:

$$y_h = \frac{1}{2 \cdot E_e} \sum_{\text{HFS}} (E - p_z) \quad (5.1)$$

In photoproduction, where the scattered electron escapes detection in the main part of the H1 detector, this method is chosen to reconstruct y . To calculate y via the electron method is only possible for a small subset where the scattered electron hits one of the electron taggers ('tagged photoproduction').

For an event to be accepted, two jets that fulfil the cuts listed in table 5.3 have to be reconstructed

Selection cuts for the first (second) jet
$p_t > 5(4) \text{ GeV}$ $20^\circ < \theta < 160^\circ$ number of tracks > 1

Table 5.3: *Jet selection cuts. The parentheses indicate the cut on the second jet.*

Iron muon selection
$p_t > 2.0 \text{ GeV}$ $30^\circ < \theta < 130^\circ$ muon quality $Q_\mu \geq 10$ linking probability $> 10^{-3}$ linked track is fitted to primary vertex muon is associated to one of the selected jets by the jet algorithm

Table 5.4: *Selection cuts for the iron muon that triggers the event. The cuts are the same for both dilepton samples.*

by the jet algorithm. The jet with the highest transverse momentum within the given θ range is referred to as the first or leading jet. The jet with the second highest transverse momentum is the second jet. The θ range is restricted to the acceptance of the jet chambers and the jets have to include more than one track. This is because both selected leptons are required to be associated to one of the selected jets by the jet algorithm and because a reasonable resolution of the jet axis has to be ensured.

The distributions of the most relevant jet quantities are shown in section 5.8 where a comparison with the Monte Carlo predictions is performed after the charm and beauty fractions from the fit were applied.

5.3 Lepton Selection

Mainly for trigger reasons, one of the selected leptons is always required to be a muon within the acceptance of the barrel part of the muon system. This restricts the kinematic range of the muon to

$$p_t > 2.0 \text{ GeV} \quad \text{and} \quad 30^\circ < \theta < 130^\circ$$

The requirement of a muon signature in the instrumented iron also drastically reduces the contribution from misidentified hadrons in the data samples. A muon candidate with a quality $Q_\mu \geq 10$ whose linking probability is greater than 10^{-3} is required for both event samples. All cuts are summarised in table 5.4.

5.3.1 Dimuon Selection

For the dimuon sample an additional muon is required that fulfils the selection cuts in table 5.5. The polar angle of the track is restricted to the acceptance of the jet chambers. The cut

Second muon
$p_t > 1.0 \text{ GeV}$ $20^\circ < \theta < 150^\circ$ muon quality $Q_\mu \geq 3$ central track that is fitted to the primary vertex

Table 5.5: *Selection cuts for the second muon.*

Electron
$p_t > 1.0 \text{ GeV}$ $20^\circ < \theta < 150^\circ$ $0.8 < E/p < 1.6$ electron identification: $t_{FDM} > -8.0$ central track that is fitted to the primary vertex

Table 5.6: *Electron selection cuts.*

on the transverse momentum is chosen such that the momentum is high enough for a muon to penetrate deeply into the calorimeter creating a typical muon signature allowing for a sufficient separation from hadrons. Due to the selection of events with two jets and two muons, with one muon being an iron muon, the event sample is enriched with beauty events. Therefore it is sufficient to ask for a muon quality $Q_\mu \geq 3$ in order to suppress background. The additional muon still provides separation power. When applying a lower cut on the transverse momentum or a smaller muon quality, the beauty fraction decreases drastically and the separation power of the second muon is lost.

Both muons are required to be associated to one of the two selected jets via the jet algorithm to ensure that for both muons a p_t^{rel} measurement is available.

5.3.2 Electron Selection

Electrons are identified by the algorithm presented in chapter 4. The algorithm is applied to electron candidates passing the preselection cuts, namely the track selection and the cut on E/p . All the selection cuts are listed in table 5.6.

In table 5.7 the event reconstruction efficiencies (cf. equation 7.2) according to the PYTHIA Monte Carlo, the beauty fractions derived from a simultaneous fit to both p_t^{rel} distributions and the number of events in data are quoted for different electron selection cuts. For this study, all the event selection cuts listed in table 5.11 which are not related to the electron are applied. The results for the different scenarios are compatible as within the errors the same visible cross sections are obtained. It is remarkable that the beauty fraction in the KALEP sample is similar to the beauty fraction in the sample where just a cut on E/p is imposed. The event reconstruction efficiency in the latter sample is even a bit higher. It can also be seen that the Fisher discriminant method allows to select a much purer muon-electron sample. The beauty fraction is increased by a factor of about three while at the same time the reconstruction efficiency only decreases by a few percent.

Electron Selection Cuts	ϵ_{rec} in %	$f_b(\mu e)$ in %	events in data
Track selection: $p_t > 1.0 \text{ GeV}$ $20^\circ < \theta < 150^\circ$ track is fitted to the primary vertex			
calorimeter quality $Q = 3$ (KALEP)	25.1	7 ± 1	6732
$0.8 < E_{em}/p < 1.6$ (preselection)	28.6	6 ± 1	10862
Fisher discriminant method: $t > -8$	20.9	29 ± 4	1254

Table 5.7: *The event reconstruction efficiencies for beauty events according to the Monte Carlo simulation, the fraction of beauty events derived from a simultaneous fit to both p_t^{rel} distributions and the number of events in the data are given for different cut scenarios. Only the statistical errors are quoted. The track selection is the same for all scenarios.*

Year	Definition of Subtrigger S19	mean prescale factor
1999 and 2000	$\text{DCRPh_Tc} \wedge \text{DCRPh_TNeg} \wedge \text{DCRPh_THig} \wedge \text{zVtx_sig} > 1 \wedge \text{Mu_Bar}$	1.03
2004	$\text{DCRPh_Tc} \wedge \text{DCRPh_TNeg} \wedge \text{DCRPh_THig} \wedge \text{Mu_Bar}$	1.01
2005	run 399629 to 401617: $\text{DCRPh_Tc} \wedge \text{DCRPh_TNeg} \wedge \text{DCRPh_THig} \wedge \text{Mu_Bar}$ run 401617 to 427872: $\text{FTT_mul_Tc} > 2 \wedge \text{FTT_mul_Td} > 0 \wedge \text{Mu_Bar}$ run 427872 to 429402: $\text{FTT_mul_Tc} > 2 \wedge \text{FTT_mul_Td} > 0 \wedge \text{CIP_sig} > 1 \wedge \text{Mu_Bar}$ since run 429402: $\text{FTT_mul_Tc} > 1 \wedge \text{FTT_mul_Td} > 0 \wedge \text{CIP_sig} > 1 \wedge \text{Mu_Bar}$	1.04

Table 5.8: *The definition of the subtrigger S19 for different run periods. Only the main trigger elements but not the veto conditions are listed. The mean prescale factors for each period are also given.*

5.4 Trigger Selection

As already discussed above, the majority of the events passing the event selection cuts are triggered by the subtrigger S19. This is true for all run periods considered here. In all run periods a muon pattern in the barrel part of the instrumented iron, central tracks above a certain momentum threshold and a significant vertex were required. In this respect, the definition of the subtrigger did not change over the years. The exact definitions of the subtrigger S19 for the different running periods are listed in table 5.8. The individual trigger elements are discussed in the following.

The trigger element `Mu_Bar` which is provided by the central muon trigger (cf. section 3.2.3) is part of the subtrigger S19 in all years. It fires if a muon signature in the barrel part of the muon system is found.

In the HERA I period the z-Vertex Trigger provided a first estimation of the z-coordinate of the primary interaction vertex (see section 3.2.1). In the years 1999 and 2000 $\text{zVtx_sig} > 1$ was required in the definition of subtrigger S19.

During the detector upgrade, the central inner z-chamber CIZ and the central inner proportional chamber CIP were replaced by the CIP 2000. Since then, the CIP 2000 delivers information about the ep interaction vertex (`CIP_sig`), the track multiplicity (`CIP_mul`) and the bunch crossing time (`CIP_T0`) to the central trigger logic (see section 3.2.1). To reject obvious background from beam-gas interactions, i.e. events with high track multiplicities and no significant vertex, the veto condition $\neg(\text{CIP_mul} > 7 \wedge \text{CIP_sig} == 0)$ is added to physics subtriggers. Since run

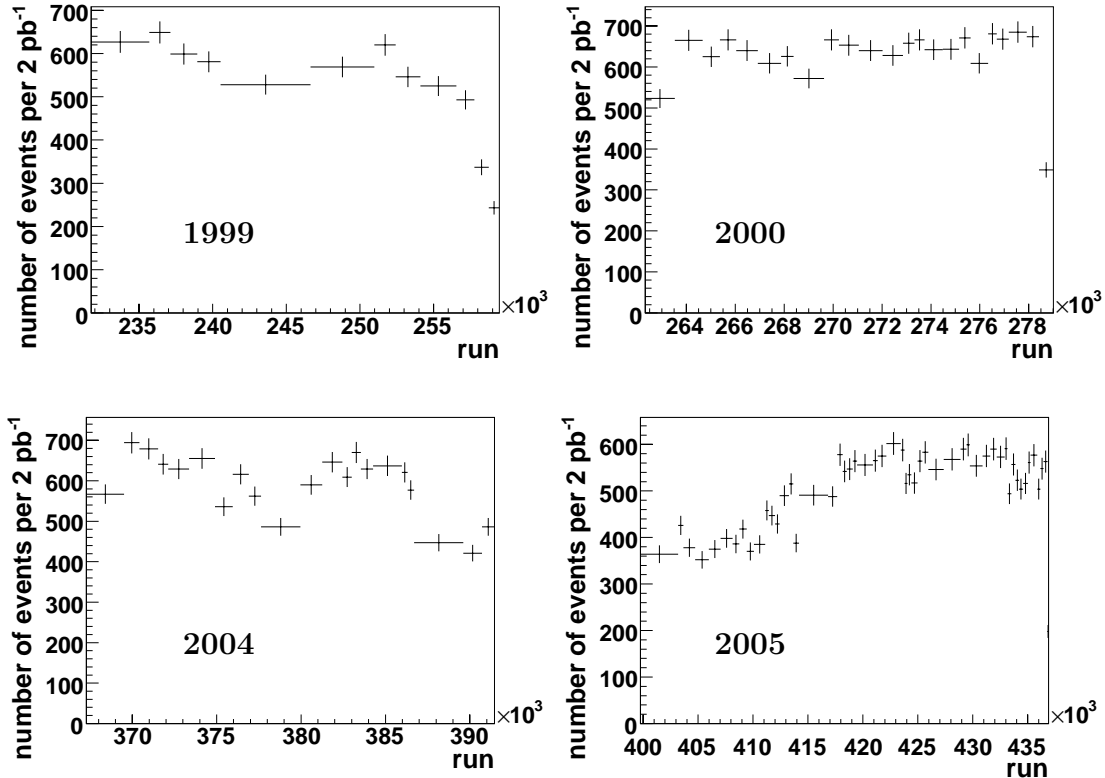


Figure 5.1: *The number of events triggered by S19 which contain one muon and two jets as a function of the run number, i.e. time. The event yields for the different years are presented separately. Each bin corresponds to an integrated luminosity of 2 pb^{-1} .*

427872 in the year 2005 the condition $\text{CIP_sig} > 1$ is added to the definition of the subtrigger S19. To get a homogeneous data sample this condition is imposed on analysis level to all HERA II runs.

In the beginning of 2005 the DCRPh Trigger was replaced by the Fast Track Trigger (FTT). Three different trigger elements provided by the DCRPh Trigger enter the definition of the subtrigger S19 before the FTT was implemented. The trigger element DCRPh_THig fires when at least one track with a transverse momentum above 0.8 GeV was found. DCRPh_TNeg is on when there is at least one negatively charged particle with a transverse momentum greater than 0.45 GeV in the event. DCRPh_Tc is fired when there are at least three tracks above the p_t threshold of 0.45 GeV.

In the definition of subtrigger S19 in the year 2005 at least 3 tracks with a transverse momentum greater than 400 MeV (FTT_mul_Tc) and at least one track with a transverse momentum greater than 900 MeV (FTT_mul_Td) are required.

In order to investigate the stability of the data taking, the number of photoproduction events with one iron muon and two jets that are triggered by subtrigger S19 as a function of the run number, i.e. time, for the different run periods are depicted in figure 5.1. Each bin corresponds to an integrated luminosity of 2 pb^{-1} . Prescales are taken into account. Only events are considered

where the relevant detector components were operational. As discussed above for all HERA II runs $CIP_sig > 1$ is required in addition. In the beginning of the year 2005, the event yield was much smaller compared to the previous years and to the second half of 2005. The reason was a hardware problem in the muon trigger electronics.

In order to study in detail if the efficiency of the subtrigger S19 is correctly described by the simulation, the efficiency for each individual trigger element is extracted from the data and compared to the Monte Carlo prediction. The study is performed using a sample of events containing at least four central tracks, two jets and a muon, where the muon is required to be identified in the central muon system. In addition to the muon track, another track with a transverse momentum larger than 1.0 GeV is required. Concerning the jet and the muon selection the analysis cuts were applied. The characteristics of this data sample are similar to the two lepton sample used in the present analysis.

The efficiency of the DCRPh Trigger, the FTT and the z-Vertex trigger is studied as a function of the number of central vertex fitted tracks N_{tracks} . In each bin the number of events in which the corresponding trigger element has fired is divided by the total number of events. To avoid any bias, only events are selected which were triggered by an independent subtrigger. This is for example the subtrigger S0 which only contains SpaCal trigger elements and no track or vertex conditions. The results are shown in figure 5.2. The DCRPh trigger elements and the relevant trigger element provided by the CIP 2000 ($CIP_sig > 1$) are well described by the simulation. For the FTT, no comparison to the simulation can be performed but for the data samples used in this analysis the relevant FTT trigger elements are fully efficient. In the case of the zVtx trigger element $zVtx_sig > 1$, the simulation overestimates the efficiency by about 5 %. The simulation is corrected accordingly.

In order to investigate the stability of the muon trigger the efficiency is shown as a function of the run number in figure 5.3. Each bin corresponds to 2 pb^{-1} . The subtrigger S61 is used as a monitor trigger. In the beginning of 2005, i.e. until run 415620, the efficiency is significantly lower compared to the previous years and to the rest of 2005. The reason was a problem with one of the low voltage power supply units which powered a trigger crate. This caused a bad trigger performance in the corresponding region of polar and azimuthal angle. The problem was solved by exchanging the power supply unit. In addition the high voltage in the barrel was increased leading to a higher trigger efficiency. The bad trigger performance in the beginning of 2005 is the reason for the lower event yield in that period (see figure 5.1).

The efficiency of the muon trigger, i.e. the trigger element Mu.Bar, depends on the transverse momentum, the polar and the azimuthal angle of the muon. Figure 5.4 shows the efficiency of the trigger element Mu.Bar as a function of these quantities. It can be seen that the efficiency varies significantly with time. For each single year, the efficiencies which are extracted from the data are compared to the prediction from the simulation. For this study events are selected which were triggered by a subtrigger that does not contain a muon requirement. Most of the subtriggers used here require a scattered electron in the SpaCal or the LAr calorimeter. This is the reason why no photoproduction cuts are applied for this study. The efficiencies for the years 1999 and 2000 are reasonably well described. The remaining discrepancies are on a few percent level and are observed mainly at transverse momenta just above 2.0 GeV. In 2004 the situation is worse. Significant inefficiencies are visible in some isolated regions of polar and azimuthal angle. In the beginning of 2005, the efficiency dropped to 40% in some regions of the detector. As can be seen in figure 5.4, these inefficiencies of the muon trigger are not yet incorporated into

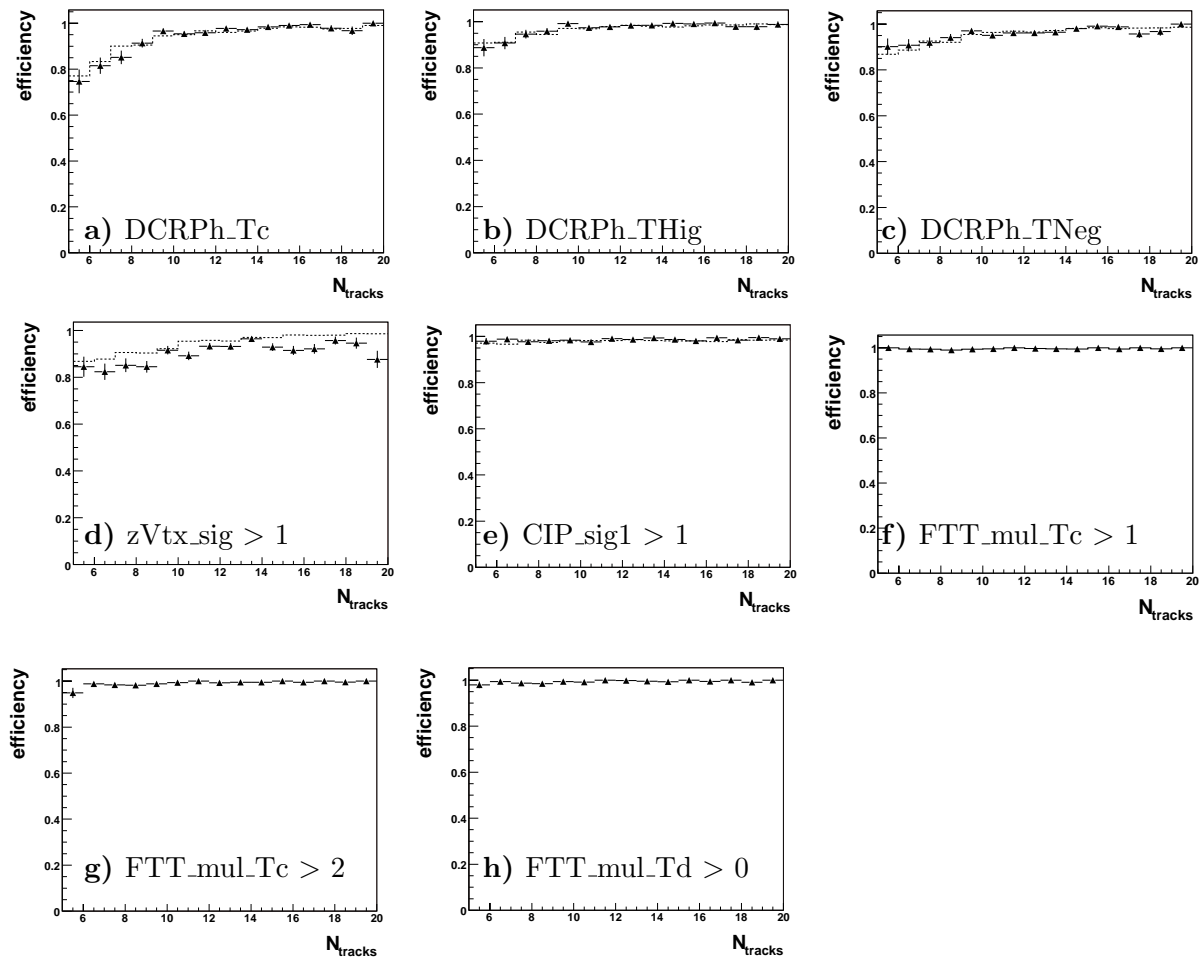


Figure 5.2: The efficiencies of the trigger elements used in the definition of subtrigger S19. Data (black triangles) is compared to the simulation (dashed line). The efficiencies are studied as a function of the number of central vertex fitted tracks.

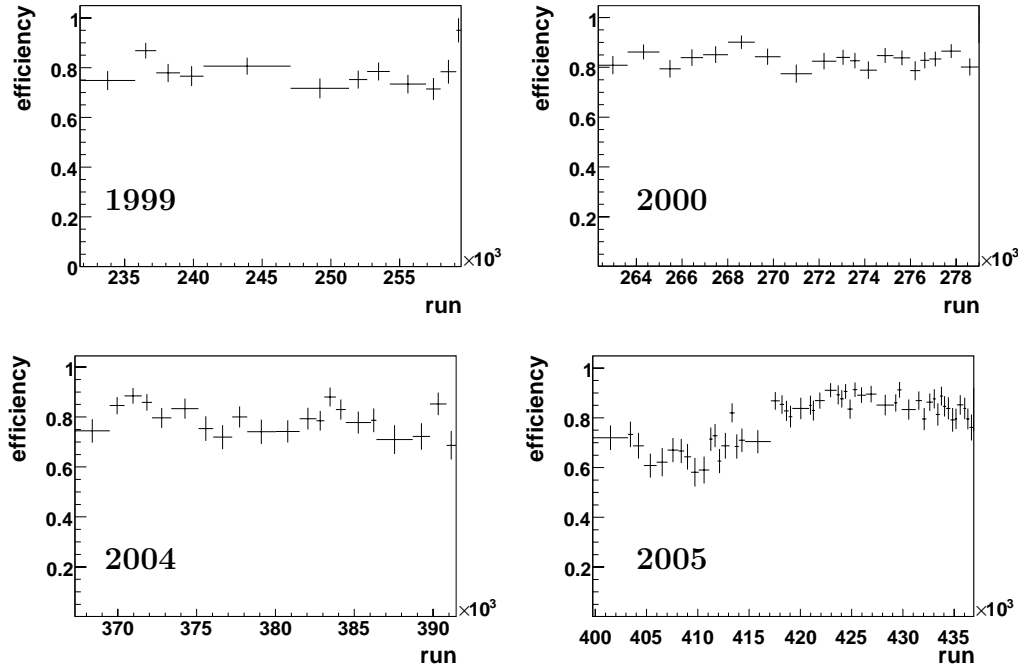


Figure 5.3: Efficiency of the central muon trigger (trigger element *Mu_Bar*) for the years 1999, 2000, 2004 and 2005. In 1999, 2000 and 2004 the efficiency is quite stable. In the beginning of the year 2005 the efficiency is significantly lower compared to the other periods.

the simulation. The simulation is therefore corrected by reducing the efficiency in the affected regions for the relevant run period. The correction is performed as a function of the polar and azimuthal angle. Figure 5.5 shows the correction factors obtained in the different angular regions. In order to get a continuous two dimensional correction function, the values between the bin centres are interpolated (Delaunay triangulation [65]). The results of this correction are shown in 5.4 (solid line) for the year 2004 and for the problematic run period in the year 2005. Applying the corrections, the data is well described. After the repair of the muon trigger system and the increase of the high voltage, the efficiency is even a bit higher in the data compared to the simulation.

As a summary, the efficiencies of the subtrigger S19 and the trigger element *Mu_Bar* are listed in table 5.9. The values obtained from the data are compared to the Monte Carlo prediction. For the years 2004 and 2005 the efficiencies of the corrected Monte Carlo are quoted. The binomial statistical errors according to the following formula are given:

$$\sigma = \sqrt{\frac{\epsilon \cdot (1 - \epsilon)}{N_1}} \quad \text{with} \quad \epsilon = \frac{N_2}{N_1} \quad (5.2)$$

Here, N_1 is the number of events in the total sample and N_2 is the number of events which fulfil the trigger requirement. The trigger efficiencies in the dimuon sample are larger compared to the efficiencies in the muon-electron sample since the second muon may also have reached the instrumented iron causing the muon trigger to fire. The efficiencies obtained from data are used in the calculation of the total visible cross sections.

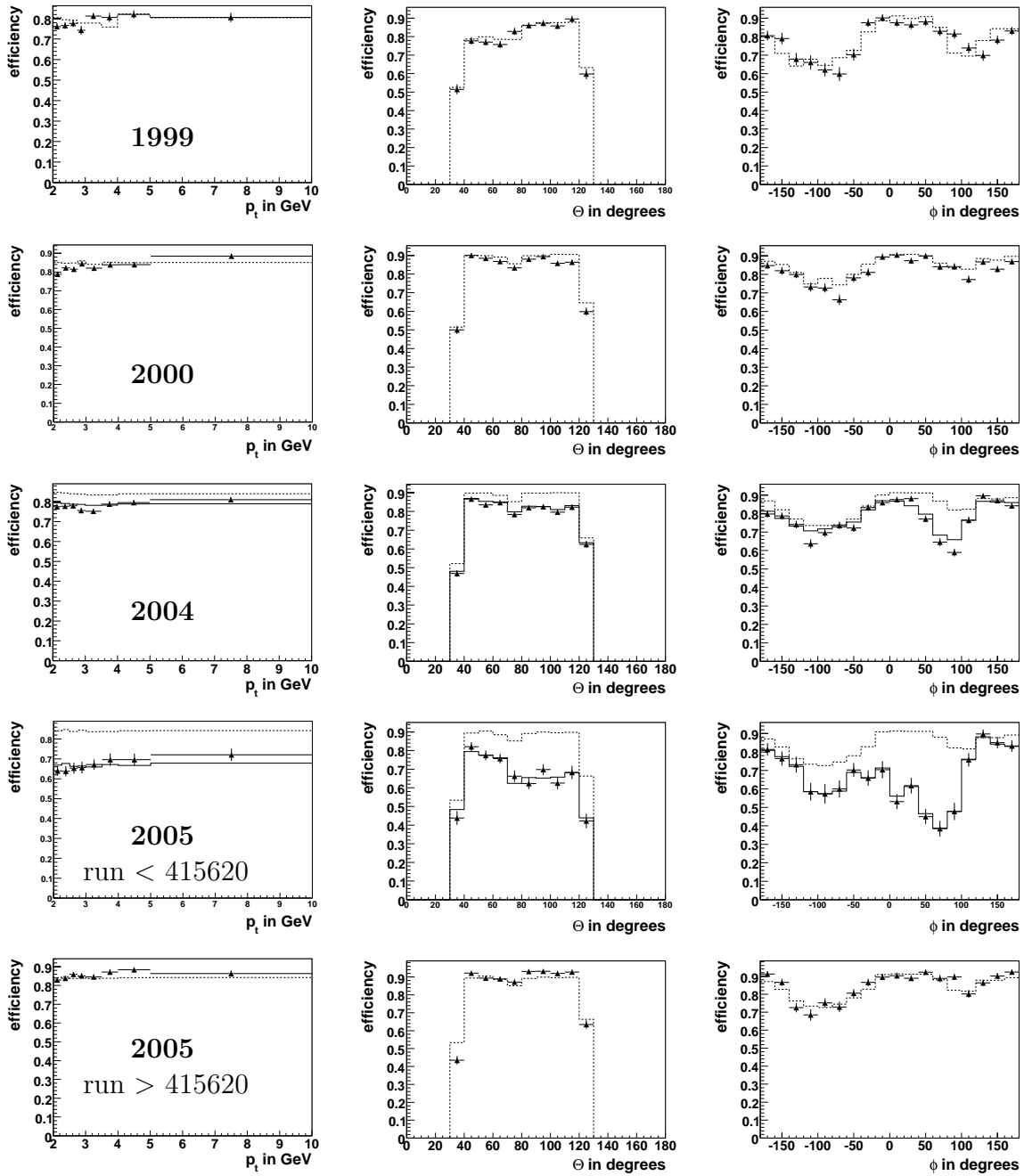


Figure 5.4: Efficiency of the central muon trigger (the trigger element Mu_Bar) as a function of the transverse momentum p_t , the polar angle θ and the azimuthal angle ϕ for the different years. Data (black triangles) is compared to the Monte Carlo prediction (dashed line). For 2004 and 2005 data (run < 415620) also the corrected Monte Carlo is shown (solid line).

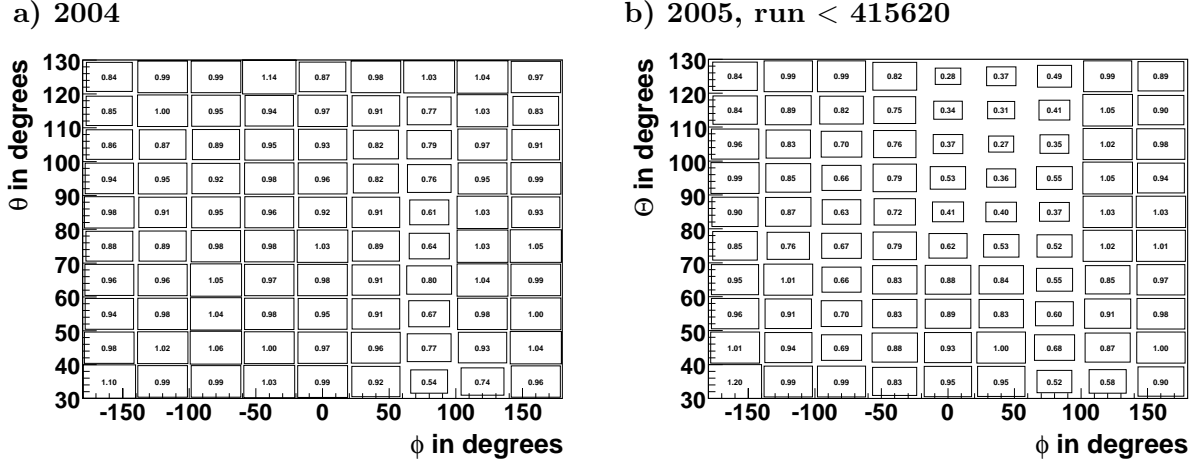


Figure 5.5: Correction factors ($\epsilon_{DATA}/\epsilon_{MC}$) applied to the Monte Carlo simulation to obtain a correct description of the muon trigger, i.e. the trigger element `Mu_Bar`, in the years 2004 (a) and 2005 (b).

		Trigger Efficiency ϵ_{trig} in %							
		1999/2000		2004		2005			
						run < 415620		run > 415620	
		DATA	MC	DATA	MC	DATA	MC	DATA	MC
$\mu\mu$	S19	76 ± 2	78 ± 1	80 ± 2	81	70 ± 3	70	86 ± 1	87
	Mu_Bar	84 ± 1	88 ± 1	83 ± 2	84	73 ± 2	75	89 ± 1	89
μe	S19	73 ± 1	74	74 ± 1	74	61 ± 1	62	82 ± 1	83
	Mu_Bar	81 ± 1	83	78 ± 1	79	66 ± 1	66	85 ± 1	85

Table 5.9: Efficiencies of the subtrigger `S19` and the trigger element `Mu_Bar` for the dimuon and the muon-electron sample. The efficiencies for the different running periods are listed. The binomial statistical errors are given. For the years 2004 and 2005 the efficiencies obtained from the corrected Monte Carlo simulation are shown.

5.5 Selection of Photoproduction Events

Photoproduction events are selected by demanding that there be no candidate for the scattered electron either in the SpaCal or in the liquid argon calorimeter with an energy of more than 8 GeV. This restricts the visible Q^2 range to $Q^2 < 1 \text{ GeV}^2$.

The algorithms used to identify the scattered electron in the LAr or in the SpaCal are both described in detail in [69]. The LAr electron finder requires a track with a transverse momentum larger than 3 GeV and an electron cluster with an energy larger than 5 GeV which consists of more than three cells. Three estimators, which exploit the characteristic properties of electromagnetic showers, are used to identify the scattered electron: 1) The fraction of the energy deposited in the electromagnetic part of the LAr calorimeter. 2) The transverse radius of the cluster. 3) The fraction of the energy deposited in the N most energetic neighbouring cells ('hot core fraction'). The cut values on the individual estimators depend on the polar angle θ to account for detector characteristics. In addition, the electron candidate has to be isolated in $\eta - \phi$. The candidate with the largest transverse momentum is chosen to be the scattered electron.

The SpaCal electron finder looks for electromagnetic clusters with an energy larger than 5 GeV and a radius of less than 4 cm. The position of the barycentre of the cluster in the $x - y$ -plane is calculated using logarithmic weighting. If the distance between an extrapolated BDC track and the SpaCal cluster is less than 3 cm, the BDC information is used to define the electron position.

5.6 Background Studies

The most important sources for background are investigated in this section: inelastically produced J/ψ mesons, electrons from photon conversion processes and the DIS background.

5.6.1 Unlike Sign Muons from J/ψ decays

Inelastically produced J/ψ mesons are source for unlike sign muon pairs. Although promptly produced J/ψ mesons are suppressed due to the event selection cuts, i.e. the relatively high momentum cuts on the leptons and the jet cuts, there is still a significant contribution from these events in the data sample. Contributions from promptly produced J/ψ affect the shape of the $|\Delta\phi| \times Q(\mu_1) \times Q(\mu_2)$ distribution. This of course would create problems when this distribution is used to extract the charm and beauty fraction. In order to suppress background from muonic decays of inelastically produced J/ψ mesons, it is required that both muons are accompanied by hadrons, i.e. that they are not isolated, if they are oppositely charged and the invariant mass $m_{\mu\mu}$ is close to the J/ψ mass ($m_{J/\psi} \approx 3.1 \text{ GeV}$):

$$2.8 \text{ GeV} < m_{\mu\mu} < 3.4 \text{ GeV} \quad (5.3)$$

The width of the mass window is chosen to be significantly larger than the J/ψ mass resolution which is about 50 MeV. As an estimator for the isolation, the transverse momenta of all HFS particles that are close to the muon in the $\eta - \phi$ plane

$$\Delta R = \sqrt{\Delta\eta^2 + \Delta\phi^2} < 1 \quad (5.4)$$

are summed up:

$$I_\mu = \sum_{\text{HFS}, \Delta R < 1} p_t. \quad (5.5)$$

For unlike sign muon pairs with an invariant mass compatible with the J/ψ mass according to equation 5.3

$$I_\mu > 2 \text{ GeV}$$

is required for both muons.

Figure 5.6 shows the distribution of the invariant mass $m_{\mu\mu}$ for events with unlike sign muons before the isolation cut. The data is compared to the PYTHIA Monte Carlo expectation. The fraction of b events is determined by a simultaneous fit to the p_t^{rel} distributions of both muons as will be described in detail in the next chapter. A significant excess of events in data at the position of the J/ψ mass region is observed. The excess amounts to about five standard deviations. Obviously, the Monte Carlo fails to describe the rate of promptly produced J/ψ mesons. Figure 5.8 shows the distributions of I_{μ_1} and I_{μ_2} for events with unlike sign muons. The excess which is observed in the lowest bins corresponds to the excess observed in the invariant mass distribution. In figure 5.7 the distribution of the invariant after applying the isolation cut is displayed. The data is now well described by the PYTHIA Monte Carlo.

5.6.2 Electrons from Photon Conversion Processes

When a photon interacts with the detector material it may convert into an electron and a positron. Leptons from this process are considered as background in this analysis. To suppress electrons and positrons from conversion processes, tracks which are fitted to a secondary vertex are rejected. Only primary vertex fitted tracks are used. In a second step, the distance ΔR (cf. equation 5.4) to the next neighbouring track which belongs to a particle with opposite charge is calculated for each electron candidate. If an electron from a conversion process is selected, one expects a second track at a very small distance since the opening angle between conversion electrons is quite small. In figure 5.9 a) the distance to the next neighbouring track is shown for electrons from beauty decays and for conversion electrons, respectively. For conversion electrons, the distance to the next track tends to be much smaller than for electrons from beauty decays. Large ΔR values for conversion electrons occur when the second track from the photon is not reconstructed. Figure 5.9 b) shows the invariant mass m_{ee} calculated from the four vectors of the two particles. As expected, the invariant mass is much smaller for conversion electrons. Figure 5.9 c) shows the distribution of the invariant mass for the muon-electron sample. In figure 5.9 d) the distributions of the quantity ΔR is depicted. Both distributions are compared to the Monte Carlo prediction. A significant excess at small ΔR and m_{ee} can be seen in data compared to the Monte Carlo simulation. This indicates that the rate of photon conversion processes is underestimated in the Monte Carlo simulation. In order to suppress the contribution from conversion electrons, the invariant mass m_{ee} is required to be larger than 0.1 GeV.

5.6.3 DIS Background

Due to inefficiencies of the electron finder, there is still a small contribution from DIS events in the photoproduction sample. In those events the electron is wrongly treated as a HFS particle.

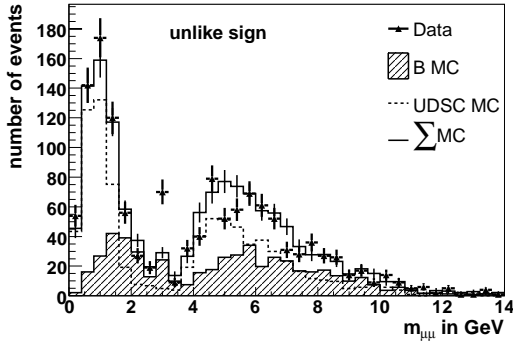


Figure 5.6: *Invariant mass of the unlike sign muon pairs without applying the isolation cut. The beauty fraction was determined by a simultaneous fit to both p_t^{rel} distributions. A significant excess at $m_{\mu\mu} \approx 3.1$ GeV is observed. Apart from this feature the distribution is described reasonably well.*

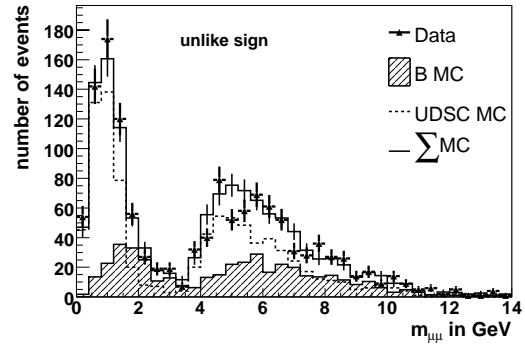


Figure 5.7: *Invariant mass of unlike sign muon pairs after applying the isolation cut. The distribution is well described. No excess in the J/ψ mass region is visible any more.*

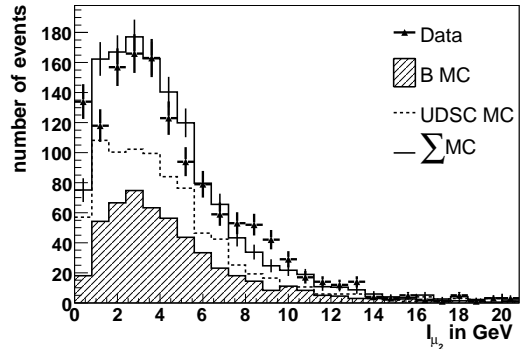
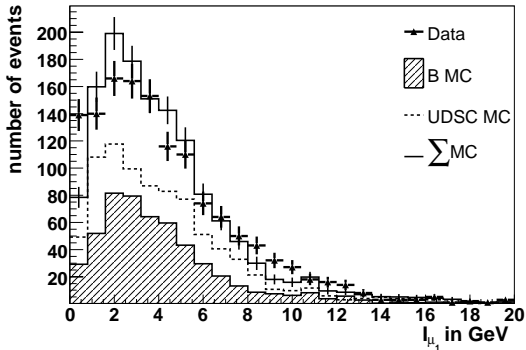


Figure 5.8: *Isolation as defined in formula 5.5. In both distributions a significant excess originating from prompt J/ψ production is observed in the first bin as this process is not correctly described by the Monte Carlo simulation.*

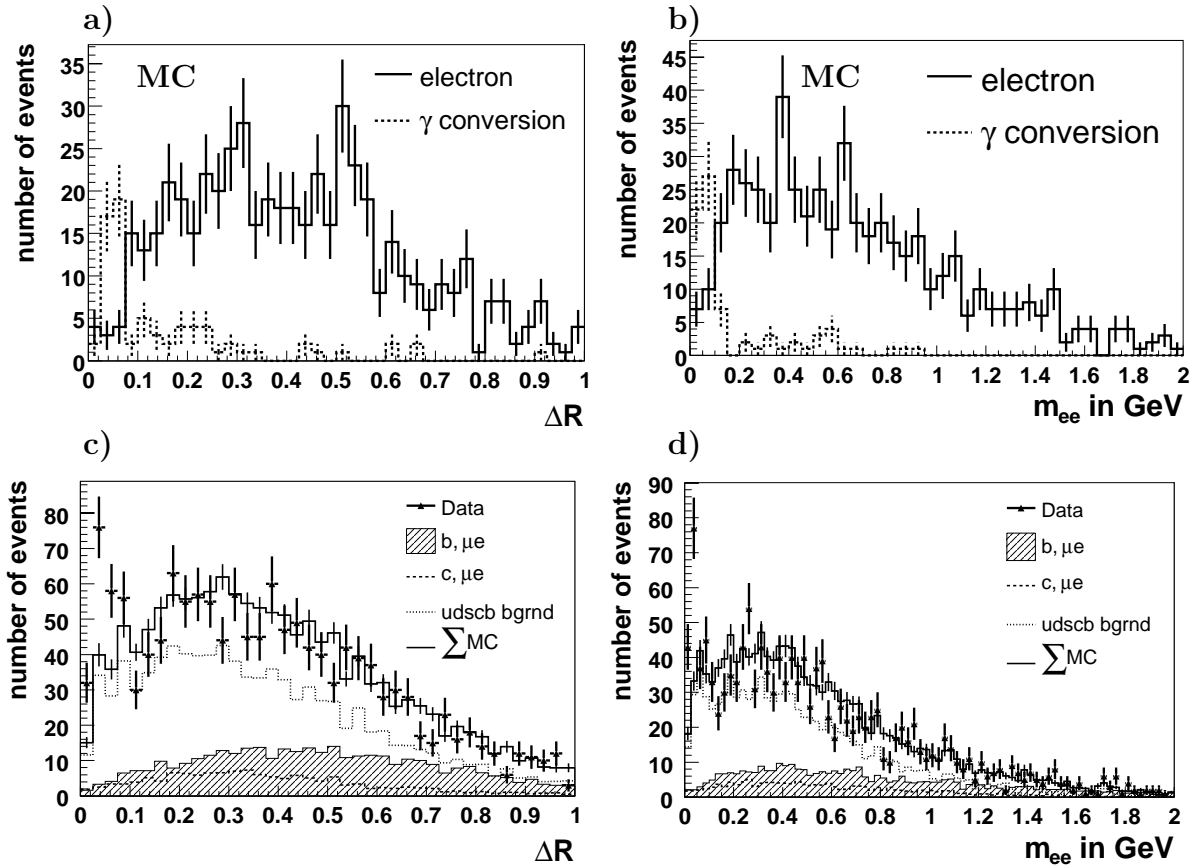


Figure 5.9: Contribution of electrons from photon conversion processes. a) Distance ΔR to the next neighbouring track (beauty Monte Carlo), b) Invariant mass m_{ee} (beauty Monte Carlo), c) and d) Comparison of the Monte Carlo prediction with the data. The different contributions from charm and beauty according to the fit are depicted.

Therefore kinematic quantities that use the HFS as input are wrong. In this analysis the inelasticity y is calculated via equation 5.1 where a sum over the HFS is performed. For DIS events, where the scattered electron is not identified and treated as part of the HFS, y_h is overestimated. From four-momentum conservation follows that the sum $\sum E_i - p_{z,i}$ over all particles is equal to $2 E_e$ for an ideal detector, where E_e is the electron beam energy. Since particles flying in the direction of the incident electron contribute most to the sum, the DIS background can be mainly found at large values of y_h . In photoproduction, the electron is scattered under a small angle and escapes detection in the main part of the H1 detector which leads to low values for y_h . Figure 5.10 shows the distribution of y_h for all selected events and for events with a generated Q^2 greater than 1.0 GeV^2 . It can be clearly seen that DIS events tend to have a large y_h . To suppress the contribution from DIS events to the sample, an upper limit on y_h is imposed: $y_h < 0.7$.

In the course of the luminosity upgrade, a new super-conducting focusing magnet was installed close to the interaction region. Also the beam pipe within the H1 experiment was replaced by a larger one. As a consequence some of the inner SpaCal cells had to be removed [40]. This

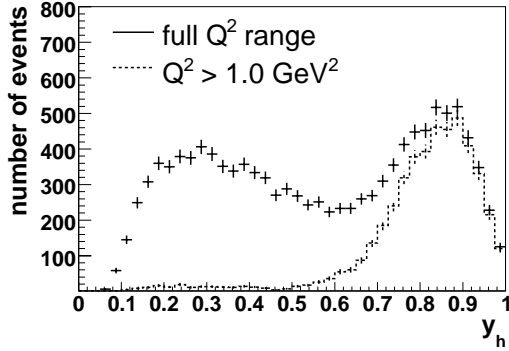


Figure 5.10: The inelasticity calculated via the hadron method y_h for muon-electron events according to HERA II Monte Carlo. Also shown is the distribution for DIS events ($Q^2 > 1 \text{ GeV}^2$). Events at large y_h are dominated by DIS events.

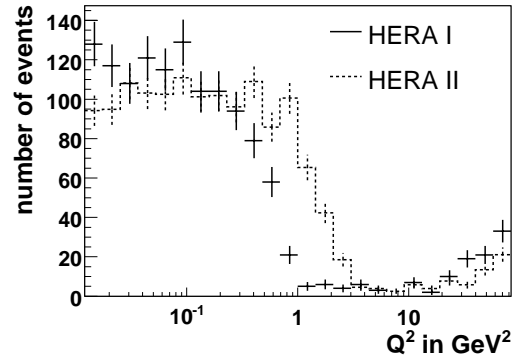


Figure 5.11: The generated Q^2 for muon-electron events. HERA I Monte Carlo is compared to HERA II Monte Carlo. The difference is due to a different detector configuration.

	Dimuon		Muon-electron	
	HERA I	HERA II	HERA I	HERA II
DIS contribution	1%	4%	3%	8%
mean Q^2 [GeV^2]	0.04	0.06	0.04	0.06

Table 5.10: The DIS contributions to the dilepton samples as obtained from HERA I and HERA II beauty Monte Carlo. Also listed is the mean Q^2 for photoproduction events.

of course has an influence on the accessible polar angle range for the detection of the scattered electron and therefore also on the Q^2 range. This is illustrated in figure 5.11 where the generated Q^2 is depicted for HERA I and HERA II Monte Carlo separately. The cut on y_h was applied. In HERA II the electron finder starts to be efficient at a higher Q^2 value than in HERA I. Therefore the contribution of DIS events to the photoproduction sample is larger in HERA II than in HERA I. In table 5.10 the DIS contributions to the different photoproduction samples are given for HERA I and HERA II. For both event samples the DIS contribution in HERA II is expected to be much larger than in HERA I. Also the average Q^2 for photoproduction events are listed. Different acceptances in Q^2 lead to different migration corrections to the reconstruction efficiency in both run periods.

5.7 Summary of the Selection Cuts

All event selection cuts are summarised in table 5.11. In addition to the selection cuts discussed above, the inelasticity y_h is required to be larger than 0.1 to ensure that a significant part of the HFS is in the acceptance of the central tracking system where measurements are most precise. Furthermore, a cut on the position of the event vertex along the z -axis z_{vtx} is applied: $|z_{vtx}| < 35$ cm. This cut ensures the event vertex to lie within the nominal interaction region and helps to reduce non ep background.

The number of events which pass the selection cuts are quoted in table 5.12 for both data samples.

5.8 Comparison of Data and Simulation

The PYTHIA Monte Carlo simulation is used to extract the reconstruction efficiency, to correct for migration effects and to determine the charm and beauty fractions. For reliable results it is necessary that the simulation describes the data well. In order to check this and to study the properties of the selected data samples, the relevant distributions are compared to the Monte Carlo prediction. The charm and beauty fractions obtained from a fit to the data are applied. The fit procedure is described in the next chapter. The fitted charm and beauty fractions, as summarised in table 6.4, are applied to the Monte Carlo predictions presented here. The distributions for the muon-electron sample are considered first, then the relevant distributions for the dimuon sample are displayed.

First the distributions of the relevant kinematic quantities are investigated, i.e. y_h and x_γ^{obs} according to the equations 5.1 and 2.31, respectively. In figure 5.12, both distributions are compared with the Monte Carlo predictions. A good description of the data is obtained.

In the following it is investigated if the selected leptons are described by the Monte Carlo simulation. The most relevant control distributions for the iron muon in the muon-electron sample are compiled in figure 5.13. Except for the muon quality, all the distributions are well described. The reason for the muon quality to be described poorly is that there are problems with the description of the KALEP estimators used to identify muons in the calorimeter. This was shown in detail in section 4.2.3.2. As a consequence of this poor description of the KALEP estimators, the efficiencies to identify muons in the calorimeter have to be corrected in Monte Carlo. This is done in bins of the transverse momentum and of the polar angle. As no calorimeter

	Event Selection	
	Dimuon sample	Muon-electron sample
Data	1999, 2000, 2004, 2005 ($\mathcal{L} = 221.6 \text{ pb}^{-1}$)	
Trigger	subtrigger 19 ($\mathcal{L} = 214.9 \text{ pb}^{-1}$)	
γp ($Q^2 < 1 \text{ GeV}^2$)	no scattered electron in the SpaCal or the LAr calorimeter $y_h < 0.7$	
First lepton (muon)	$p_t > 2.0 \text{ GeV}$ $30^\circ < \theta < 130^\circ$ primary vertex fitted central track muon quality ≥ 10 link probability > 0.001	
Second lepton	primary vertex fitted central track	
	$p_t > 1.0 \text{ GeV}$ $20^\circ < \theta < 150^\circ$ KALEP muon quality ≥ 3	$p_t > 1.0 \text{ GeV}$ $20^\circ < \theta < 150^\circ$ $0.8 < E/p < 1.6$ $t_{FDM} > -8.0$
Jets	$p_t > 5(4) \text{ GeV}$ $20^\circ < \theta < 160^\circ$ jets contain at least two central tracks	
Background cuts	isolation cut: $I_{\mu_{1/2}} > 2 \text{ GeV}$ (cf. equation 5.5) for unlike sign muons with $2.8 \text{ GeV} < m_{\mu\mu} < 3.4 \text{ GeV}$	suppress photon conversions: $m_{ee} > 0.1 \text{ GeV}$ for unlike sign electrons
Additional cuts	$ z_{vtx} < 35 \text{ cm}$ $y_h > 0.1$ number of central tracks > 4 both leptons are associated to one of the selected jets	

Table 5.11: Summary of all event selection cuts for both dilepton and dijet samples.

Year	Luminosity in pb ⁻¹ (S19)	Dilepton sample			
		μe		$\mu\mu$	
		number of events	yield per pb ⁻¹	number of events	yield per pb ⁻¹
1999	23.4	137	5.8 ± 0.5	288	12.3 ± 0.7
2000	45.1	292	6.5 ± 0.4	703	15.6 ± 0.6
2004	42.3	279	6.6 ± 0.4	567	13.4 ± 0.6
2005	103.8	546	5.3 ± 0.2	1288	12.4 ± 0.3
1999-2005	214.6	1254	5.8	2846	13.3
HERA I MC	239.5	1617	6.8	2011	8.4

Table 5.12: Event yields for the different years considered in this analysis for both dilepton and dijet samples.

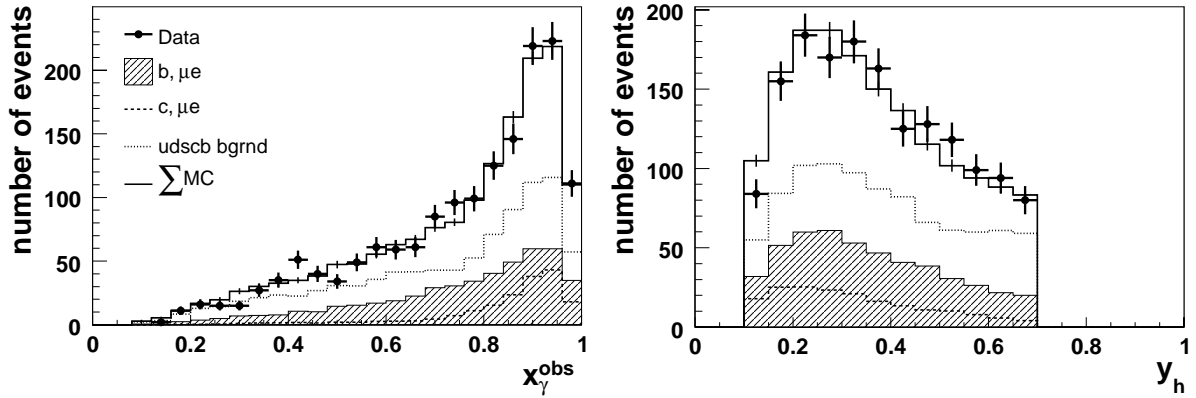


Figure 5.12: The x_γ (left) and y_h (right) distributions for the **muon-electron** sample are confronted with the PYTHIA Monte Carlo prediction. The fitted charm and beauty fractions are applied. The data is described well.

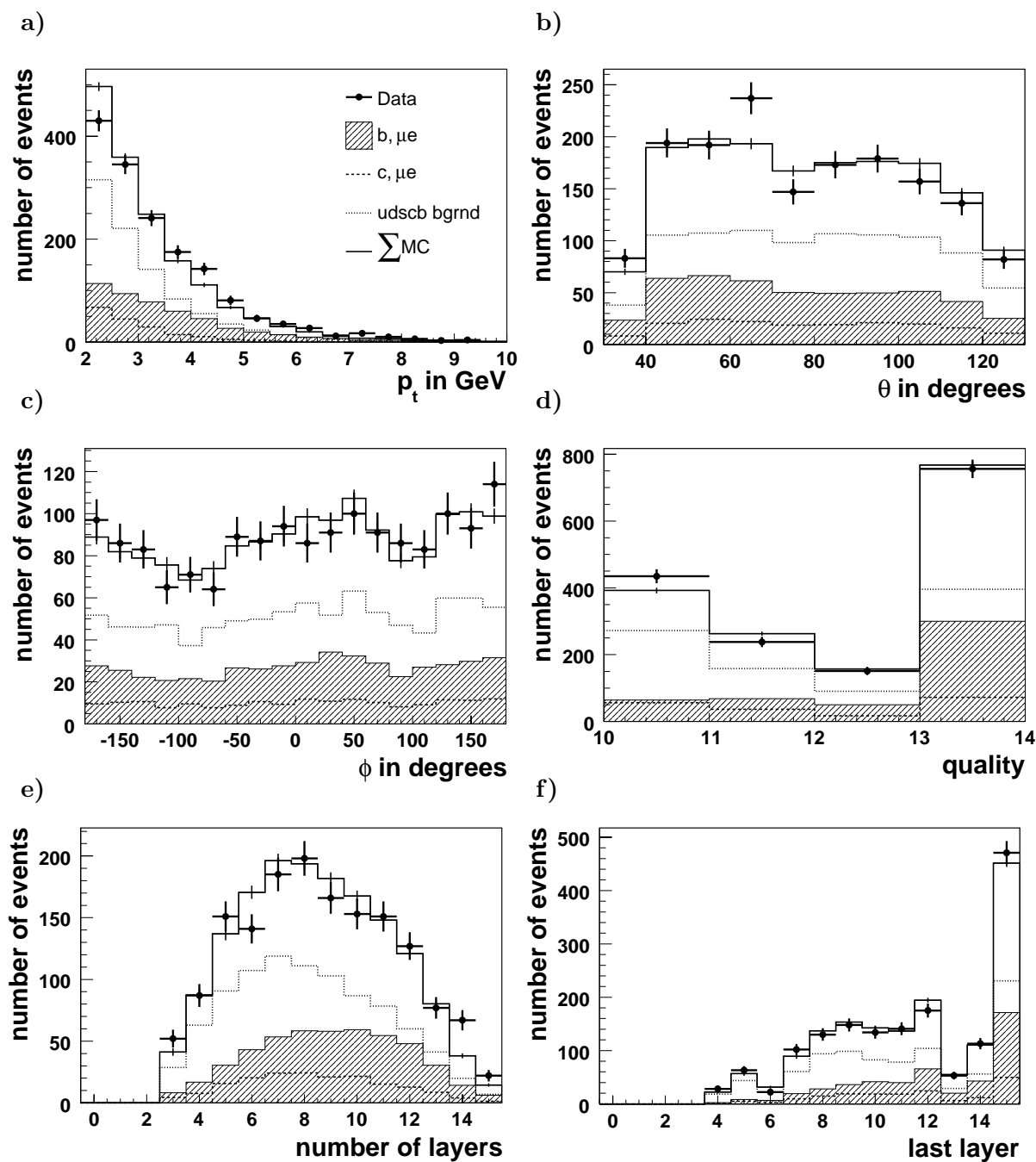


Figure 5.13: Comparison of the data with the PYTHIA Monte Carlo expectation. The most relevant quantities of the **muon** identified in the instrumented iron are shown: a) the transverse momentum p_t , b) the polar angle θ , c) the azimuthal angle ϕ , d) the muon quality Q_μ , e) the number of hit layers in the muon detector, f) the last layer hit. The data is reasonably well described by the Monte Carlo simulation.

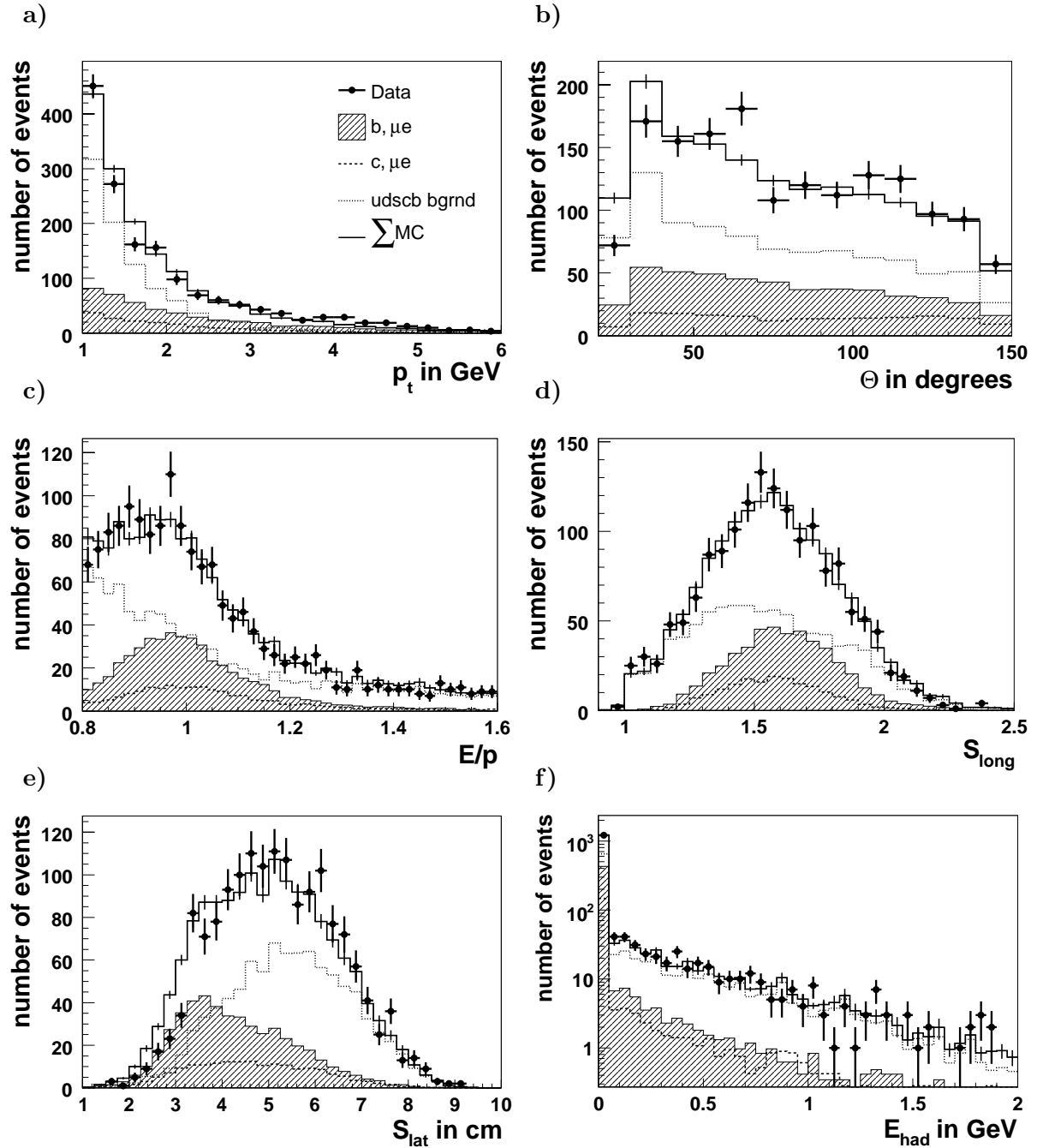


Figure 5.14: Control distributions for the electron. The following quantities are shown: a) the transverse momentum p_t , b) the polar angle θ , c) E/p , d) the longitudinal energy deposition, e) the lateral energy deposition, f) the hadronic energy. The data is well described by the PYTHIA Monte Carlo simulation. In the case of the lateral energy deposition some minor deviations between the data and the Monte Carlo simulation are observed.

quality is required for the iron muon and the response of the iron system to muons is well described within this kinematic range, no correction for the iron muon is applied.

In figure 5.14 the relevant control distributions for the electron are depicted. The kinematic quantities as well as the discriminators used to identify electrons in the calorimeter are well described. The distributions of the discriminating variables are quite sensitive to the beauty fraction since the shapes from muon-electron events differ considerably from the background. From this point of view the results are consistent.

The control distributions for the first (leading) and the second jet are shown in the figures 5.15, 5.16, 5.17 and 5.18. In general the jets are described reasonably well. In the case of the leading jet the prediction slightly overshoots the data at low transverse momenta (cf. 5.15 a)) and there are discrepancies in the description of the jet size (cf. 5.15 c)), which is defined as the energy weighted mean distance of the HFS particles from jet axis:

$$\langle \Delta R \rangle = \frac{\sum_{HFS \in Jet} E_{HFS} \sqrt{\Delta\phi^2 + \Delta\eta^2}}{E_{Jet}} \quad (5.6)$$

The data is shifted towards lower values. Jets from beauty quarks are much broader than jets from light flavours. The shape of this distribution is therefore sensitive to the beauty fraction.

In order to study the jet structure and the source of the deviations in more detail, jet profiles are investigated as well. For each HFS object, the distances to the jet axis in $\Delta\phi$, $\Delta\eta$ and $\Delta R = \sqrt{\Delta\phi^2 + \Delta\eta^2}$ are calculated. It is observed that in data more particles are closer to the jet axis than in the simulation. The corresponding distributions of the second jet are described much better (cf. figures 5.17 and 5.18).

The number of HFS particles and tracks in the jets is well simulated for both jets (cf. figures 5.15 e) and 5.17 e)). The same is true for the invariant jet mass m_{jet} (see figures 5.15 d) and 5.17 d)) which is defined according to the following formula:

$$m_{jet} = \sqrt{\left(\sum_j p_j \right)^2} \quad (5.7)$$

The sum contains the four-momenta p_j of all particles which are associated to the jet via the jet algorithm.

In the following, the correlations between the leptons are studied. Therefore the beauty fraction is obtained from a two-dimensional fit to both p_t^{rel} distributions alone (cf. section 6.4.2). The charge and the azimuthal angle correlation of the leptons is not used. The charm fraction is fixed according to the expectation from the PYTHIA Monte Carlo simulation. The distribution of the invariant mass of the dilepton system $m_{\mu e}$ is shown in figure 5.19 a). The charge and azimuthal angle correlations of the dilepton system are depicted in figure 5.19 b), c) and d). In figure 5.19 e) and f) the transverse momentum and the polar angle distributions of the dilepton system are displayed. All distributions are reasonably well described.

Figure 5.20 shows the distance ΔR of the muon (left) and the electron (right) to the jets. These distributions are sensitive to the beauty fraction since leptons from a beauty decay tend to have a larger distance to the jet axis than leptons from charm or light flavour decays due to the higher relative transverse momenta. The peaks in the distributions are therefore much broader for

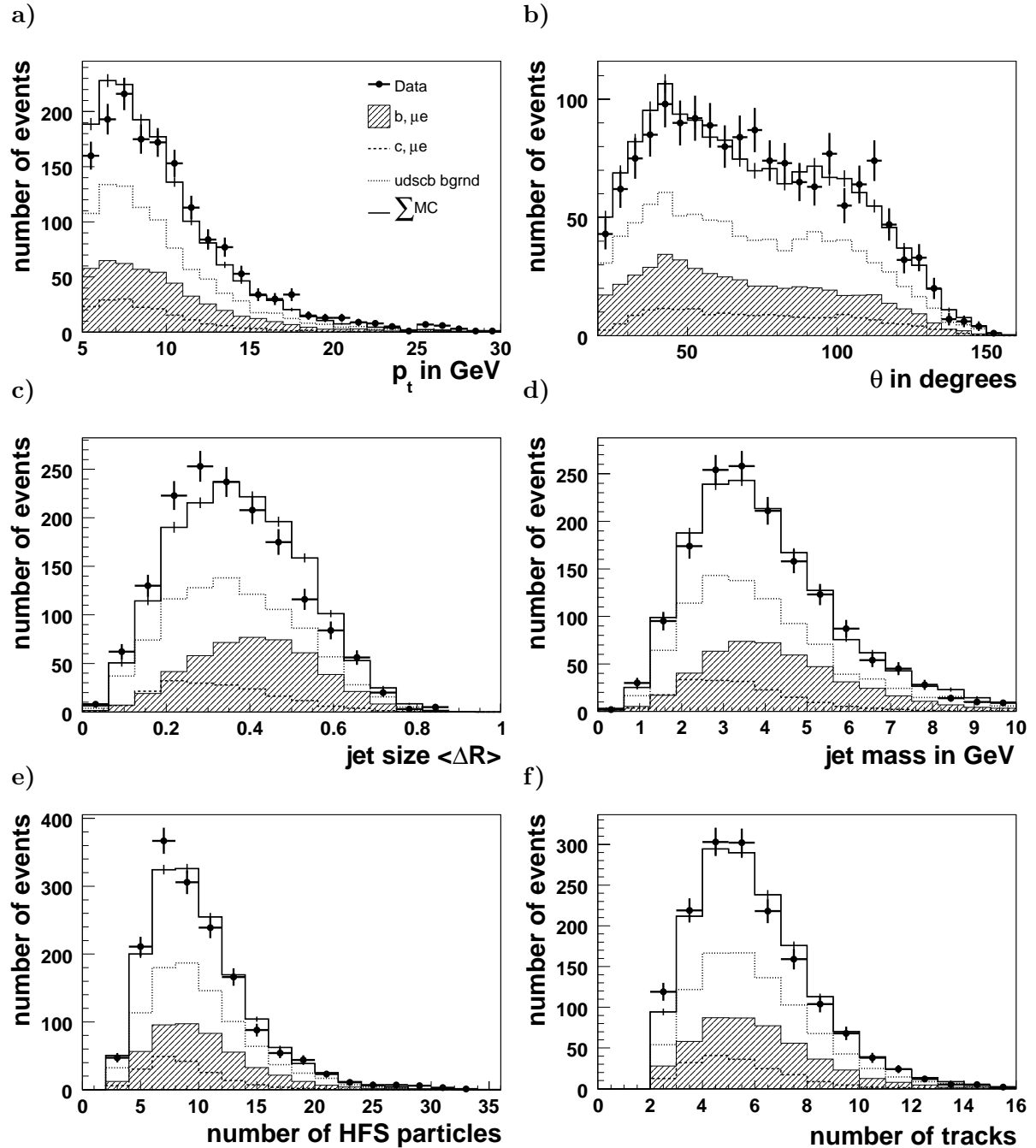


Figure 5.15: Control distributions for the leading jet (muon-electron sample). The following quantities are shown: a) the transverse momentum p_t , b) the polar angle θ , c) the jet size, d) the jet mass, e) the number of HFS particles in the jet, f) the number of tracks in the jet. Deviations of the PYTHIA Monte Carlo prediction from the data are observed at small transverse momenta. Also the jet size is not well described. The data is shifted towards smaller values.

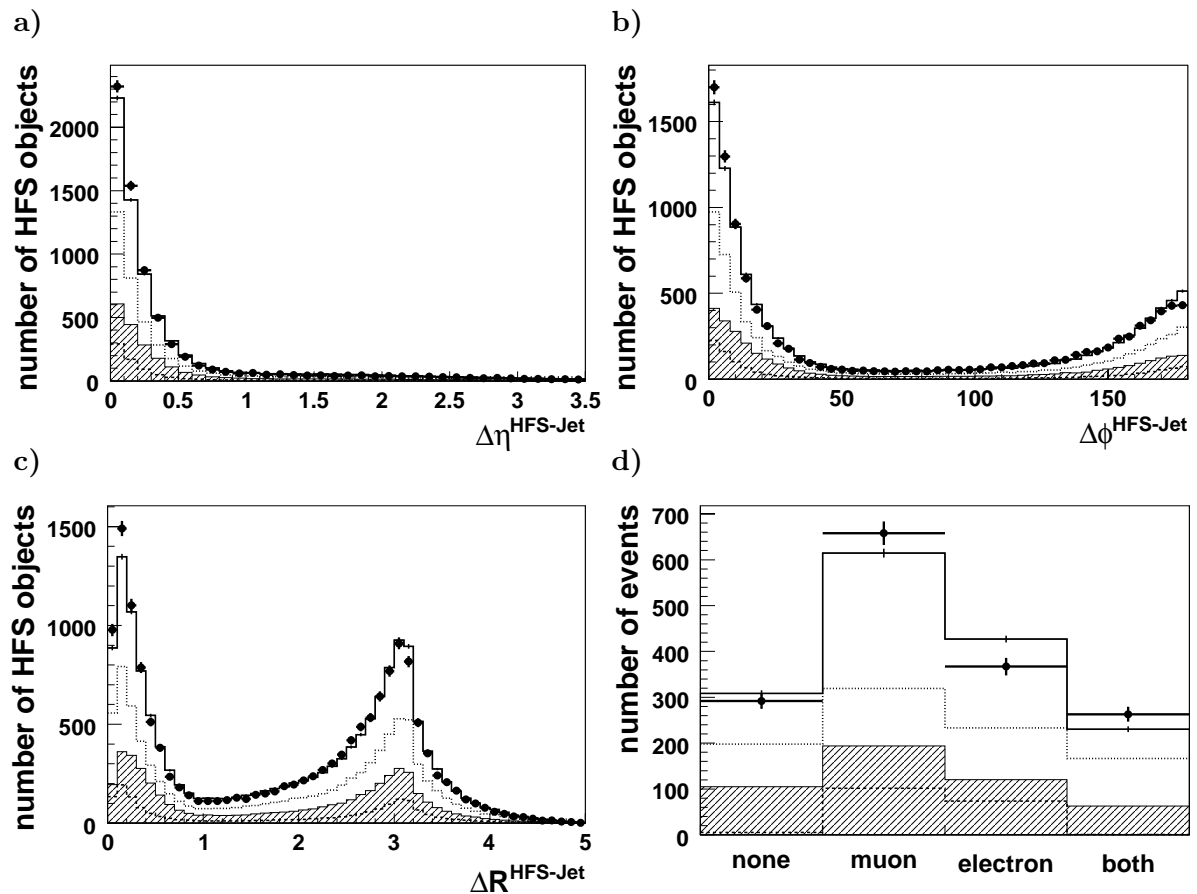


Figure 5.16: Control distributions for the leading jet (muon-electron sample). The following distributions are shown: a) the jet profile in $\Delta\eta$, b) the jet profile in $\Delta\phi$, c) the jet profile in ΔR , d) leptons associated to the jet via the jet algorithm.

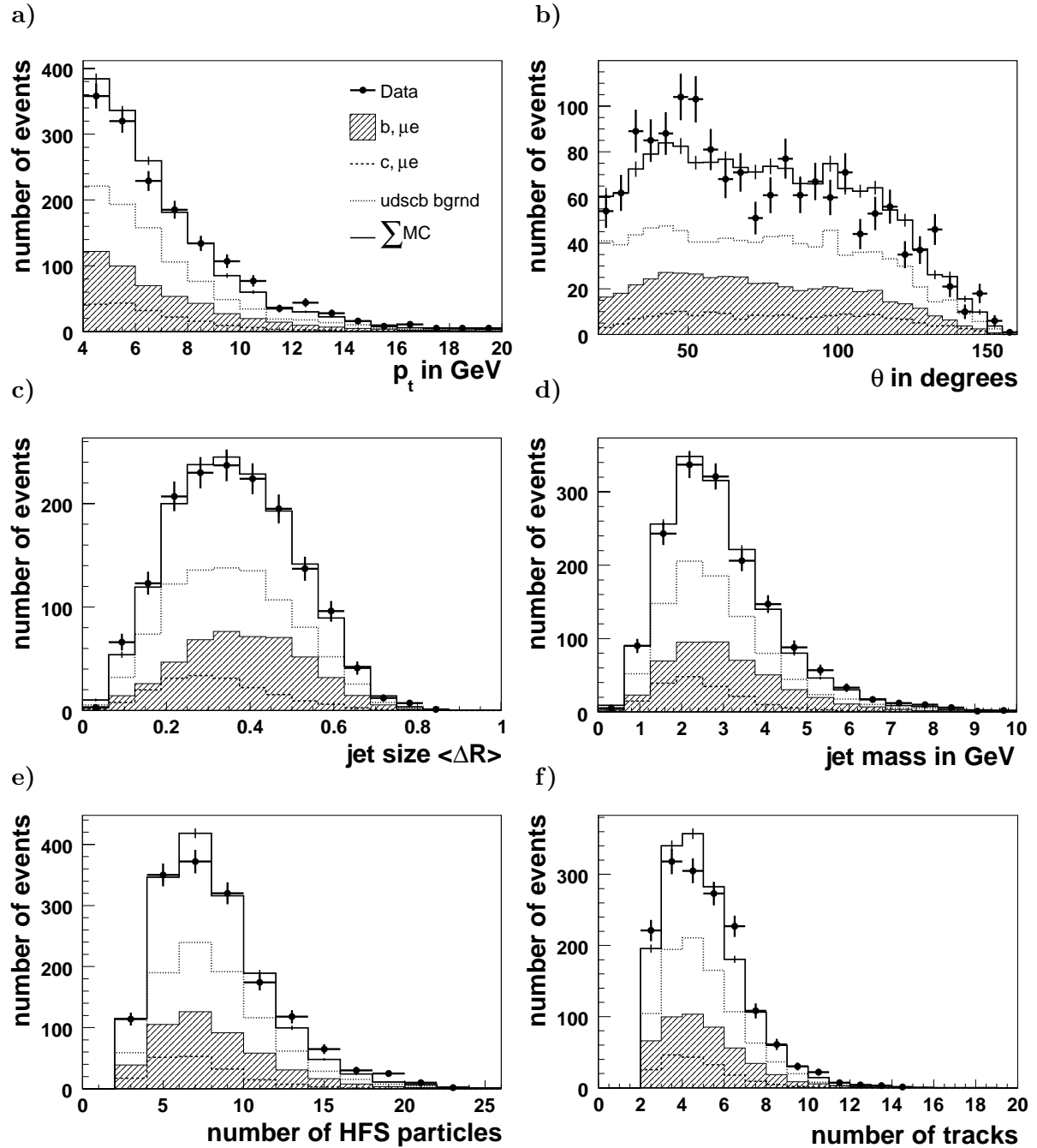


Figure 5.17: Control distributions for the second jet (muon-electron sample). The following quantities are shown: a) the transverse momentum p_t , b) the polar angle θ , c) the jet size, d) the jet mass, e) the number of HFS particles in the jet, f) the number of tracks in the jet. The jet quantities are well described by the PYTHIA Monte Carlo.

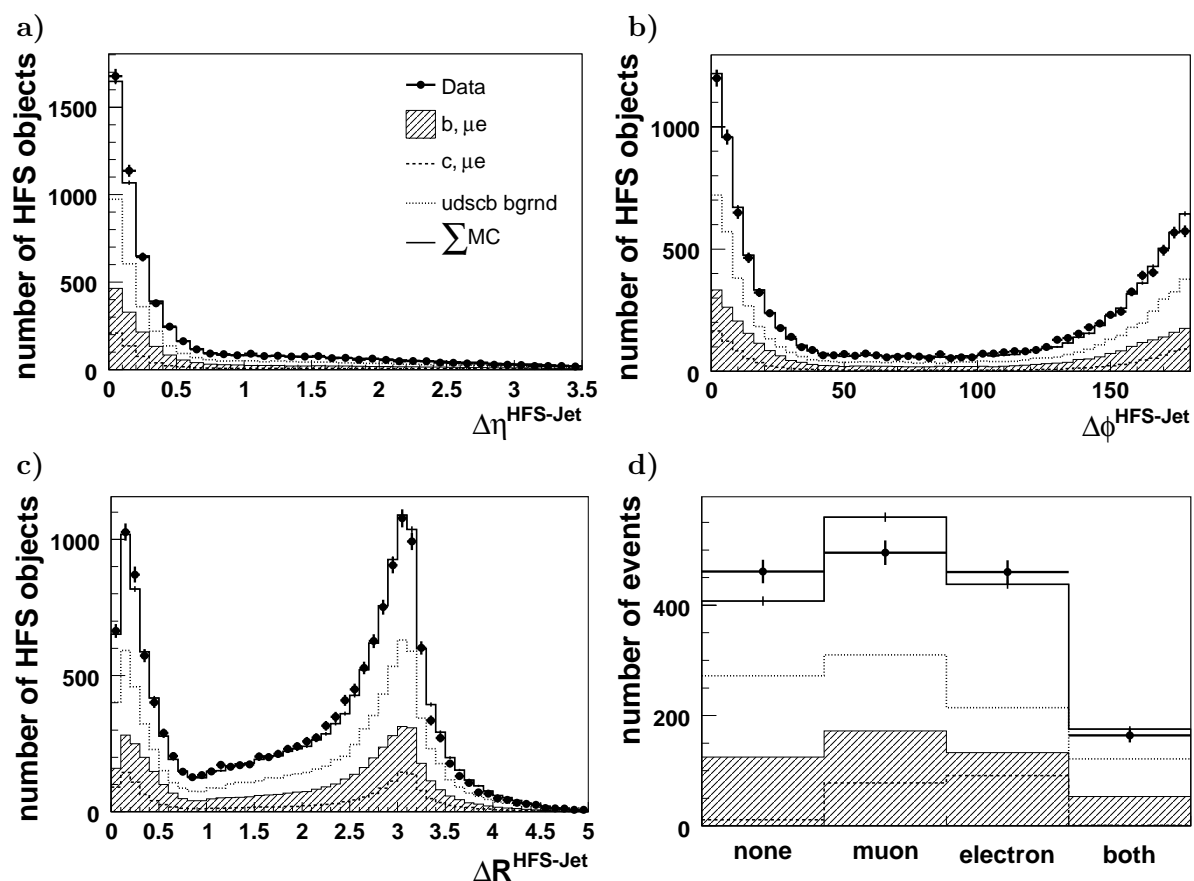


Figure 5.18: Control distributions for the second jet (muon-electron sample). The following distributions are shown: a) the jet profile in $\Delta\eta$, b) the jet profile in $\Delta\phi$, c) the jet profile in ΔR , d) leptons associated to the jet via the jet algorithm.

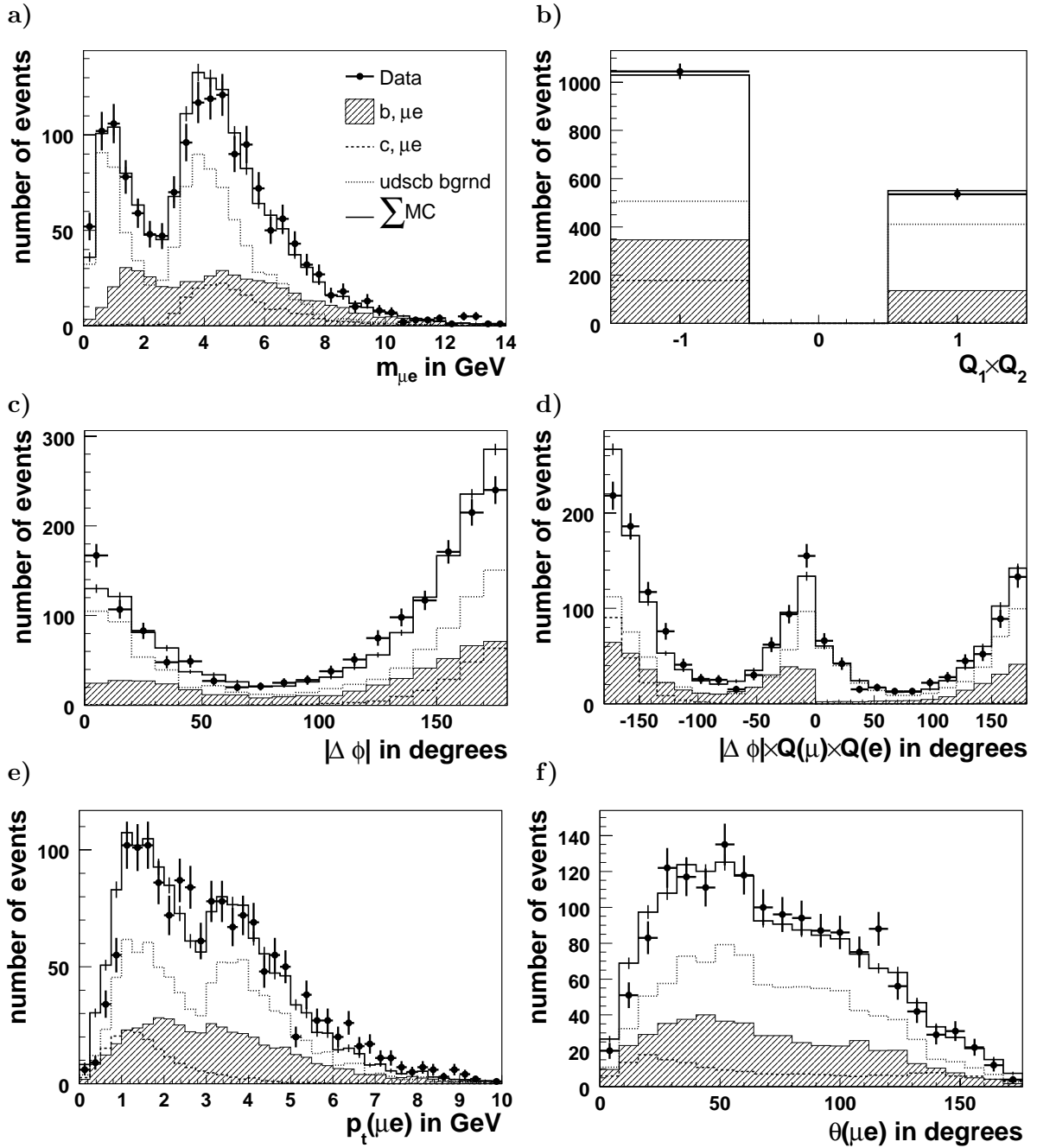


Figure 5.19: Muon-electron correlations. The following quantities are depicted: a) the invariant mass of the dilepton system $m_{\mu e}$, b) the product of the charges in units of the electron charge $Q(\mu_1) \times Q(e)$, c) $|\Delta\phi|$ of both leptons, d) $|\Delta\phi| \times Q(\mu) \times Q(e)$ of both leptons, e) the transverse momentum of the dilepton system, f) η of the dilepton system. The data and the PYTHIA Monte Carlo simulation agree well.

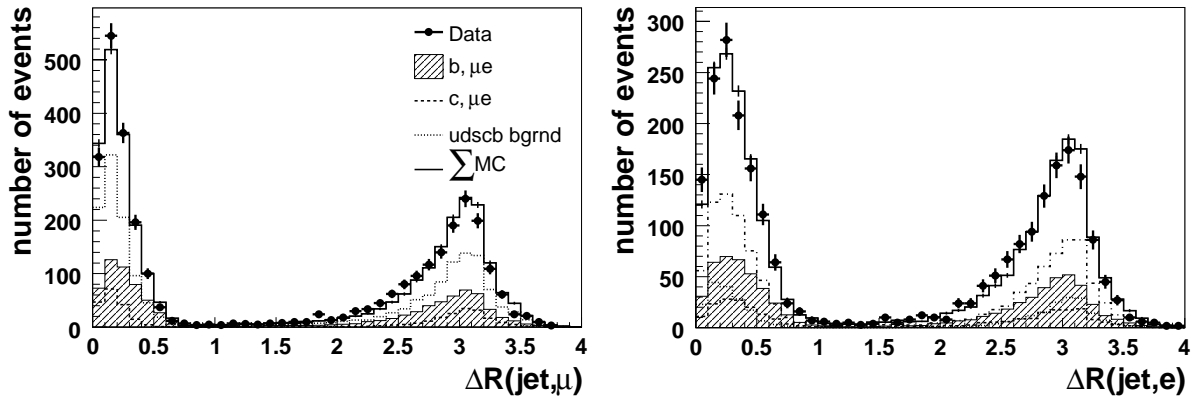


Figure 5.20: The distance ΔR of the muon (left) and the electron (right) to the selected jets.

beauty events than for charm events. Both distributions are reasonably well described. A clear double peak structure is visible due to the fact that both leptons are required to be associated to one of the selected jets.

Finally, the most relevant control distributions for the second muon in the dimuon sample are shown. First the kinematic variables and the muon quality are investigated. Then the KALEP estimators used to identify muons in the calorimeter are displayed. While all other distributions are well described, there are large discrepancies between the data and the PYTHIA Monte Carlo simulation in the distribution of E_{em} , the electromagnetic energy that is assigned to the muon candidate. Discrepancies in the description of the KALEP estimators would lead to incorrect efficiencies for finding muons. For this reason, corrections are applied to the simulation as described in section 4.2.3.2. The control distributions for the event kinematics, the iron muon and the selected jets are not shown for the dimuon sample since they are similar to the muon-electron sample.

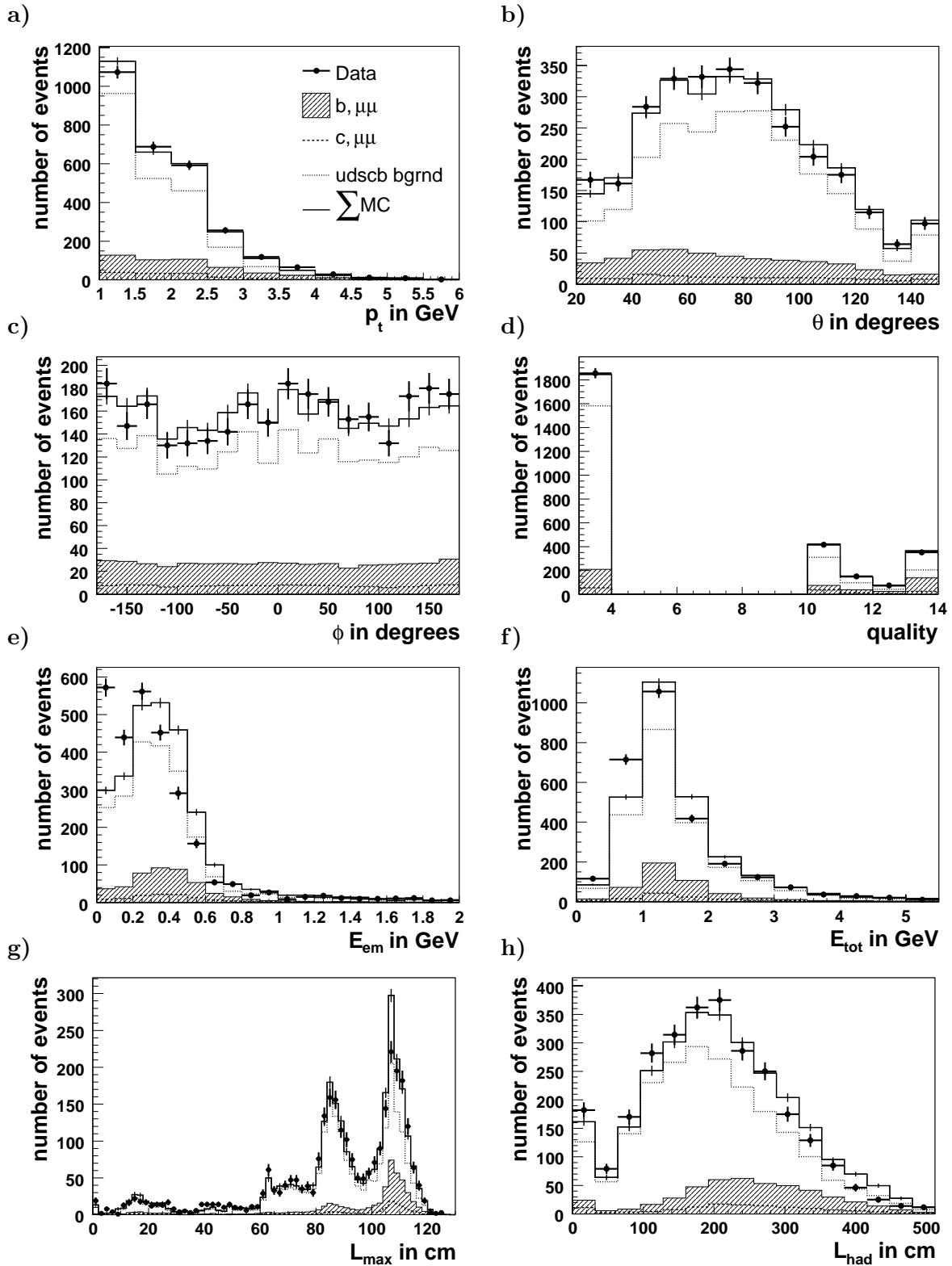


Figure 5.21: Control distributions for the second muon in the dimuon sample. The following quantities are shown: a) the transverse momentum p_t , b) the polar angle θ , c) the azimuthal angle ϕ , d) the muon quality, e) E_{em} , f) E_{tot} , g) L_{max} and h) L_{had} . The data is reasonably well described by the Monte Carlo simulation. The only exceptions are the distribution of E_{em} and E_{tot} (cf. section 4.2.2) where large discrepancies are observed.

CHAPTER 6

DETERMINATION OF THE CHARM AND BEAUTY FRACTIONS

In this chapter it is described in detail how the fractions of dilepton events from charm and from beauty are determined. The same method is applied to the dimuon ($\mu\mu jj$) and the muon-electron ($\mu e jj$) samples. The data collected by the H1 detector in the years 1999, 2000, 2004 and 2005 are considered and the cuts listed in table 5.11 are applied to select the dilepton and dijet samples. First the observables which are used to distinguish between beauty, charm and light quark events are summarised. Then the different contributions to the event samples are discussed and it is studied how the contributions from charm and beauty events with two leptons can be distinguished from background events. After that the fit procedure and the fit algorithm are described. In the last two sections of this chapter the results for the muon-electron and the dimuon sample are presented.

6.1 Discriminating Variables

Three observables are used to extract the charm and beauty fractions (cf. section 2.6). In order to separate beauty events from charm and light quark (u , d and s) events, the comparatively high mass of the beauty quark ($m_b \approx 4.75$ GeV), which gives rise to large transverse momenta of leptons from semileptonic b decays with respect to the directions of flight of the incident B hadron, is exploited. The momentum of the B hadron is in good approximation given by the momentum of the jet. The observable p_t^{rel} , i.e. the transverse momentum of the lepton with respect to the jet axis, is used to tag beauty quarks:

$$p_t^{rel} = \frac{|\vec{p}_{lep} \times (\vec{p}_{jet} - \vec{p}_{lep})|}{|\vec{p}_{jet} - \vec{p}_{lep}|} \quad (6.1)$$

This quantity is well described by the Monte Carlo simulation and widely used in high energy physics experiments. In a recent H1 publication, p_t^{rel} was used together with the signed impact parameter δ to study beauty production from events with one muon and two jets [58]. It was shown that consistent results are obtained when both observables p_t^{rel} and δ are used independently. This can be regarded as a proof that the p_t^{rel} method gives reliable results. In the present analysis, events with two leptons and two jets are selected and two p_t^{rel} distributions are

Contributions in %	Selected Lepton Candidates								
	beauty				charm				uds
	$\mu_1 l_2$	$\mu_1 f$	$f l_2$	ff	$\mu_1 l_2$	$\mu_1 f$	$f l_2$	ff	ff
μe (MC)	15	9	1	1	9	27	6	11	21
$\mu\mu$ (MC)	11	10	1	1	9	29	9	10	20

Table 6.1: Contributions to the muon-electron and dimuon samples according to the Monte Carlo prediction. μ_1 denotes the (first) muon and l_2 the second lepton originating from the decay of a beauty or charm quark. f denotes a fake lepton.

available, which can be used to extract the beauty fraction and to distinguish between signal and background events from beauty. The charm fraction cannot be determined using the observable p_t^{rel} since the shapes of the p_t^{rel} distributions are almost identical for charm and light quark events.

To measure both the charm and the beauty fraction, the charge and azimuthal angle correlation of the selected leptons is exploited. In this analysis, the difference in the azimuthal angle of the two leptons is multiplied with the charges of the two leptons in units of the proton charge to study the dilepton correlation:

$$|\Delta\phi(\mu_1, l_2)| \times Q(\mu_1) \times Q(l_2) \quad (6.2)$$

Here μ_1 denotes the (first) muon. In the dimuon sample, μ_1 is the muon with the larger transverse momentum. l_2 denotes the second lepton. This can either be a muon or an electron.

6.2 Contributions to the Event Samples and Fit Strategies

The selected data samples are composed of signal events, i.e. events where both selected leptons originate from beauty or charm decays, and background events in which either one or both selected leptons are fake, i.e. originate from light flavour decays or misidentified hadrons. This background contains contributions from beauty, charm and light quark events. The contributions to the muon-electron and the dimuon sample are listed in table 6.1. The fractions according to the simulation are quoted. The largest contribution arises from charm events where a muon from a charm quark decay and a fake lepton is selected. The beauty contribution to the muon-electron sample is dominated by events in which the muon originates from a b quark decay. In only 8 % of the beauty events the muon is fake. The same is true for the dimuon sample. Here, the first muon is defined as the muon with the larger transverse momentum.

Table 6.1 shows how often the selected lepton candidates originate from a heavy quark decay and how often they are fake. Now it will be investigated if the correct leptons are actually selected on the reconstruction level or if a fake lepton is picked up instead. Figure 6.1 a) shows the situation for the muon-electron sample. Here, two leptons, a muon and an electron, within the kinematic range are required on the generator level. In 96% of all events the selected leptons correspond to the leptons from the heavy quark decays. Figure 6.1 b) shows if the selected muon in events without an electron on generator level originates from a beauty quark decay or not. In 99% of the events the correct muon is selected. There are also a few events in which an electron

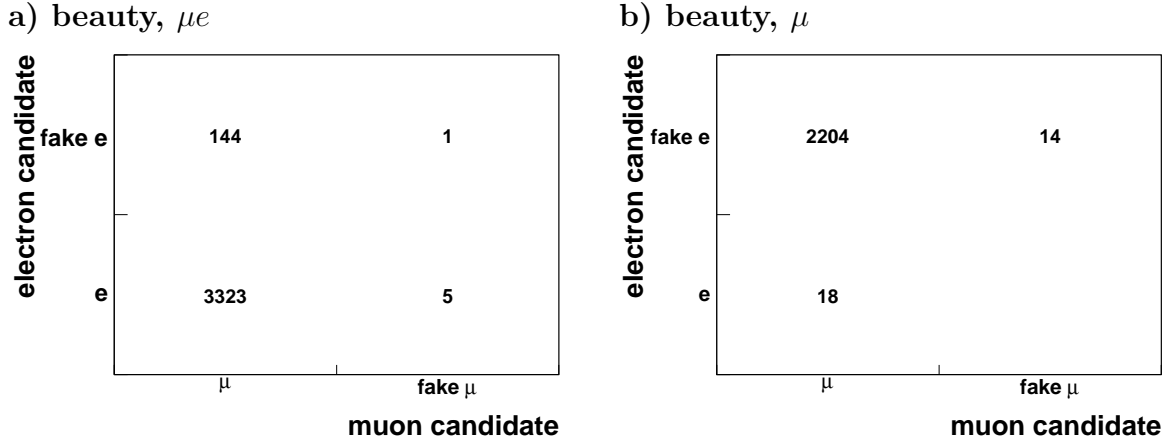


Figure 6.1: Fake contribution in events with two leptons, a muon and an electron, from a beauty quark decay (a) and in events with one muon from beauty only (b). In both cases the selected muon is hardly ever fake. Only in 4% of the events the selected electron candidate is fake when there is an electron from a beauty quark decay in the event.

from a heavy quark decay is selected although there is no electron in the kinematic range on generator level. This can be attributed to migration effects which are also taken into account in the reconstruction efficiency.

One can conclude that the p_t^{rel} distribution of the muon is mainly sensitive to the total beauty fraction, while the p_t^{rel} distribution of the electron is sensitive to the fraction of beauty signal events, i.e. beauty events with a muon and an electron. This is also reflected in figure 6.2, where the muon and electron p_t^{rel} distributions for the light quark plus charm quark, the beauty signal and the beauty background contribution are shown. While for muons the shapes of the p_t^{rel} distributions are almost identical for the beauty signal and the beauty background contributions, the corresponding p_t^{rel} distributions for the electron differ significantly. Here the p_t^{rel} distribution of the beauty background is similar to that of the charm and the light flavour contribution. The slight tendency to larger p_t^{rel} values in the beauty background distribution for the electron arises from beauty background events where an electron from a beauty decay and a fake muon is selected.

Of course information on the correlation of both p_t^{rel} values is lost when both p_t^{rel} distributions are considered separately. This correlation is important if one wants to separate the beauty signal and beauty fake contributions since in beauty signal events both p_t^{rel} values tend to be large which is not the case for beauty background. Although in the case of the muon-electron sample both beauty contributions can be separated by fitting both p_t^{rel} distributions separately, fitting the two-dimensional distribution of $p_t^{rel}(\mu)$ versus $p_t^{rel}(e)$ leads to smaller errors since the ambiguities are smaller. If the total beauty fraction, i.e. signal plus background, is fitted to the data, both approaches lead to the same result and the errors are compatible.

For the dimuon sample, a two dimensional fit is even more advisable. The reason can be seen in figure 6.3, where the p_t^{rel} distributions for the first and the second muon are depicted. The p_t^{rel} distributions of the beauty background contribution deviates significantly from the light quark and charm contribution in the case of the second muon candidate. This leads to ambiguities

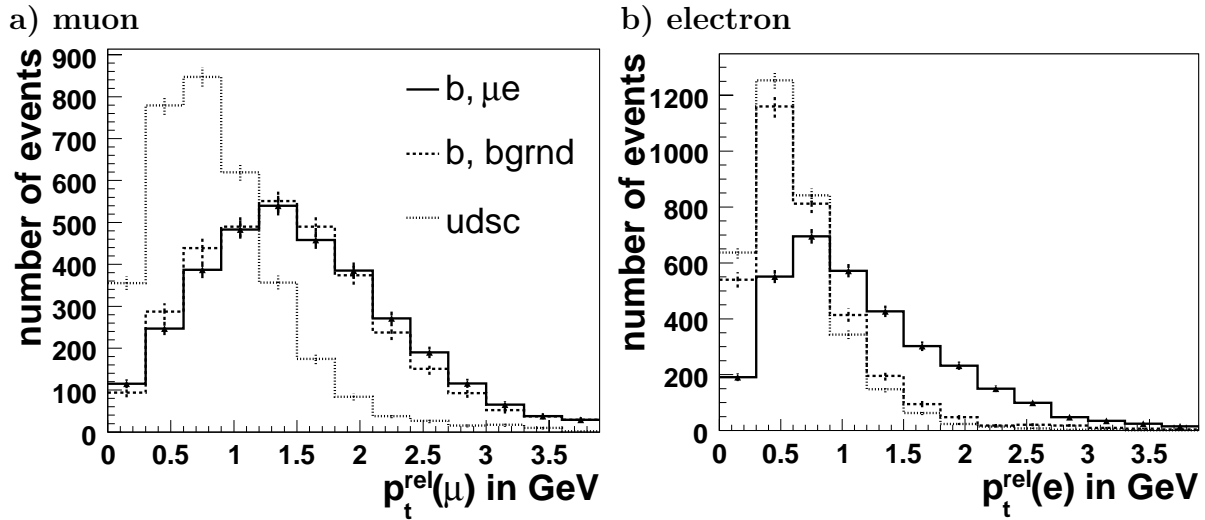


Figure 6.2: The p_t^{rel} distributions for the muons (a) and the electrons (b) in the muon-electron sample. The distributions are normalised to the same number of events to allow for shape comparisons. The signal and the background contributions from beauty can only be distinguished in the electron p_t^{rel} distribution.

which can be resolved better with a two-dimensional fit.

Additional separation power is obtained when the charge and azimuthal angle correlation of the leptons is taken into account. Figure 6.4 a) shows the lepton correlation $|\Delta\phi| \times Q(\mu) \times Q(e)$ for the charm and for the beauty signal contribution. As expected the distribution for charm is strongly peaked for events that are back-to-back and have unlike sign lepton pairs. In this respect the charm signal contribution differs significantly from all the other contributions. The beauty signal contribution also differs significantly from the background which is depicted in figure 6.4 b). In contrast to the background, almost no like sign lepton pairs with a small opening angle are observed for beauty signal events. The three background contributions, i.e. the light flavour, the charm and beauty background contributions, differ only slightly in shape. The best separation power, i.e. the smallest errors on the fitted fractions, is obtained when the two p_t^{rel} and the $|\Delta\phi| \times Q(\mu) \times Q(e)$ distributions are fitted simultaneously. The p_t^{rel} distributions constrain the beauty component while the $|\Delta\phi| \times Q(\mu) \times Q(e)$ distribution provides separation power to distinguish between charm and beauty signal events and the background.

6.3 The Fit Procedure

The shapes of the p_t^{rel} and $|\Delta\phi| \times Q(\mu) \times Q(e)$ distributions for charm, beauty and light quark events are taken from the Monte Carlo simulation (PYTHIA) and the normalisations of each contribution are determined by a binned maximum likelihood fit to the data. Since the light quark and charm background contributions cannot be separated by any of the used observables, the relative fraction of both contributions is fixed to the Monte Carlo prediction. The algorithm used in this analysis will be described in the following.

The input distributions are divided into n bins. The total number of events in the data is

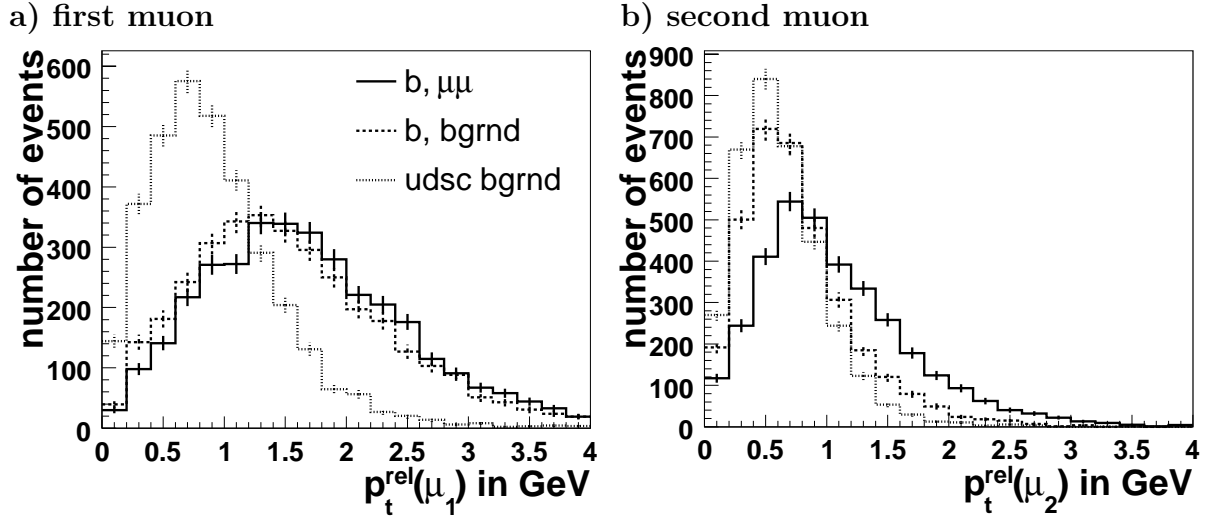


Figure 6.3: The p_t^{rel} distributions for the first (a) and the second muon (b) in the dilepton sample according to the Monte Carlo simulation. The distributions are normalised to the same number of events to allow for shape comparisons.

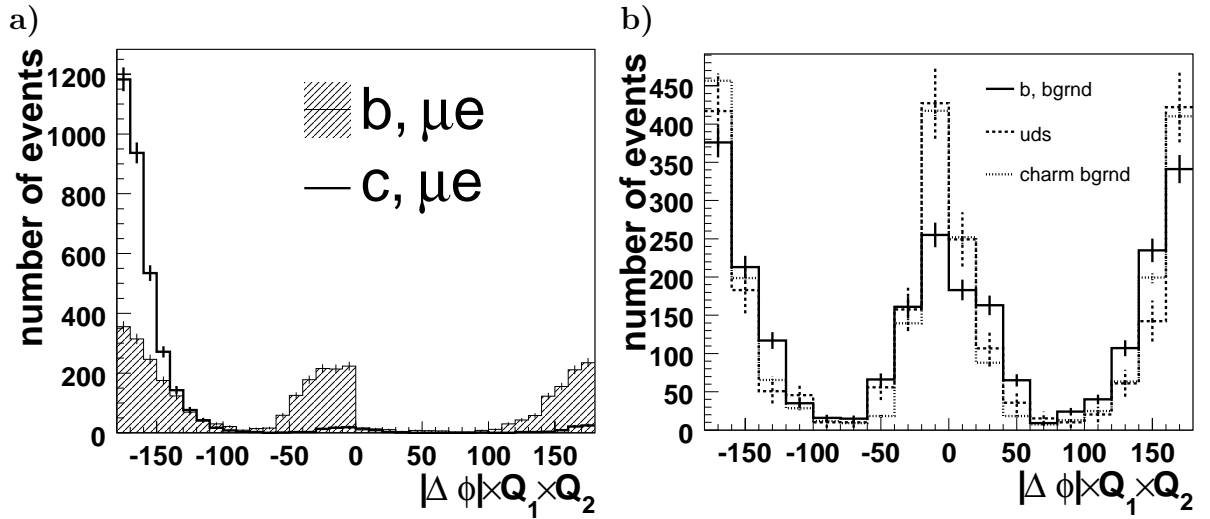


Figure 6.4: The lepton correlation $|\Delta\phi| \times Q(\mu) \times Q(e)$ for charm and beauty muon-electron events (a) and for the different background contributions from charm, beauty and light flavours (b). The distributions are normalised to the same number of events to allow for shape comparisons. The corresponding distributions for the dimuon sample show a similar behaviour.

$N = \sum_{i=1}^n d_i$, where d_i is the number of events in bin i . In the case of m Monte Carlo sources, the predicted number of events in each bin p_i is given by

$$p_i = N \sum_{j=1}^m \frac{f_j a_{ji}}{N_j} \quad (6.3)$$

N_j is the total number of events in Monte Carlo source j and a_{ji} are the number of events that fall into bin i . The coefficients f_j are the fractions which are determined by a fit. Since the number of events in some bins is small, a χ^2 minimisation assuming Gaussian errors is inappropriate. The Gaussian is only a good approximation to the Poisson distribution for large numbers of events. Instead a binned likelihood fit using Poisson statistics is performed. The following likelihood \mathcal{L} has to be maximised:

$$\ln \mathcal{L} = \sum_{i=1}^n d_i \ln p_i - p_i \quad (6.4)$$

As usual, the logarithm of the likelihood is considered since this simplifies the calculations.

So far, uncertainties arising from limited Monte Carlo statistics, i.e. bin-by-bin fluctuations in the a_{ji} , are not taken into account. This is however important and implemented as follows. The observed a_{ji} follow a Poisson distribution with the expected number of events A_{ji} . The probabilities to observe the a_{ji} have to be included in the likelihood. The logarithm of the likelihood to be maximised is then given by the following equation which now contains $m \times (n+1)$ unknowns:

$$\ln \mathcal{L} = \sum_{i=1}^n d_i \ln p_i - p_i + \sum_{i=1}^n \sum_{j=1}^m a_{ji} \ln A_{ji} - A_{ji} \quad (6.5)$$

To calculate the maximum, this equation has to be differentiated and set to zero. This leads to a system of $m \times (n+1)$ nonlinear and coupled equations that has to be solved [70].

It is obvious that different contributions can only be separated from each other if their shapes differ significantly. The variable used for the separation should be well described by the Monte Carlo simulation, including both the description of the underlying physics process and the detector simulation. Ideally the variable is independent of the details of the physics model and insensitive to a certain extent to imperfections of the detector description.

6.4 Charm and Beauty Fractions from Muon-Electron Events

In a first step, the beauty fraction is determined from fits to the p_t^{rel} distributions alone without using the charge and azimuthal angle correlation of the selected muon and electron candidates. The total beauty fraction and the fractions of the signal and background contribution from beauty are determined. It will turn out that the results are compatible with each other. Fits will be performed in one and in two dimensions. In both cases consistent results are obtained. Then the charge and angle correlation is used to extract the beauty fraction in a completely independent way. Since the results agree, a simultaneous fit to the two p_t^{rel} and the $|\Delta\phi| \times Q(\mu) \times Q(e)$ distribution is performed. The fraction of charm and beauty signal events, from the beauty background and from the charm plus light flavour background are obtained.

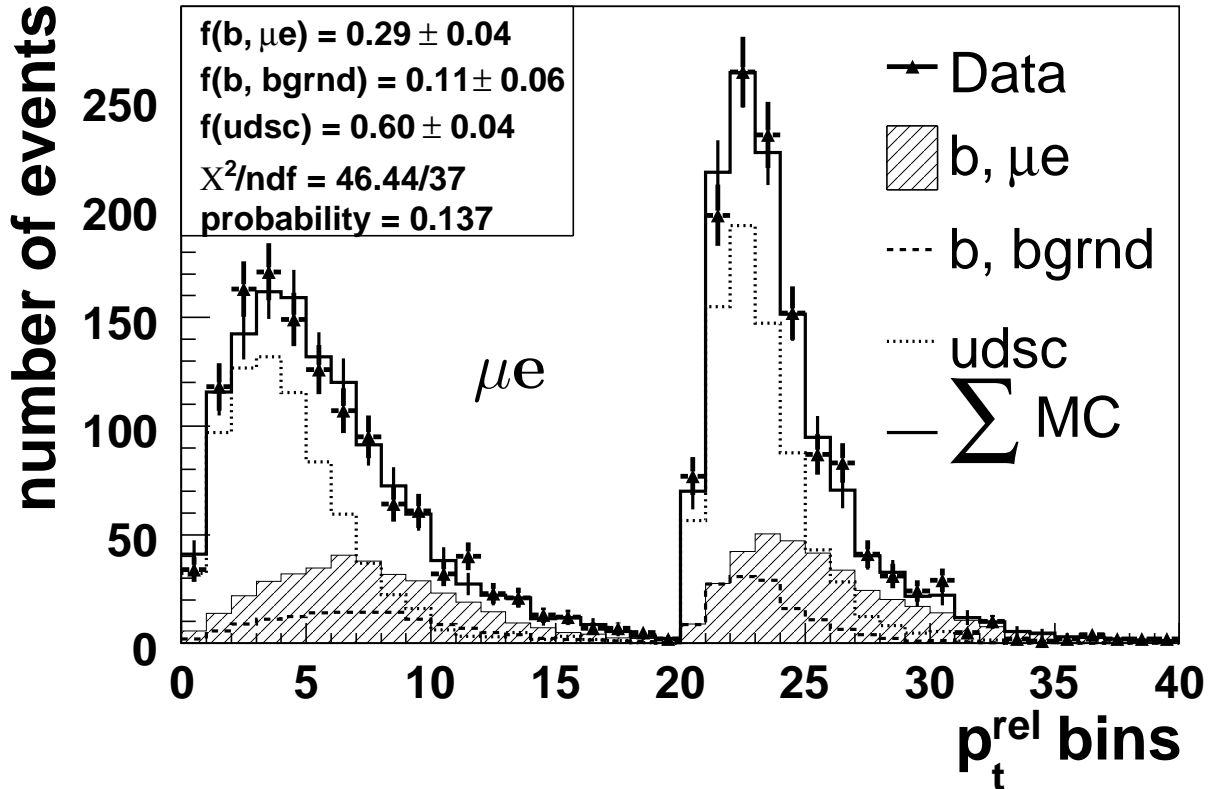


Figure 6.5: Result of a simultaneous fit to both p_t^{rel} distributions for the **muon-electron** sample. Both p_t^{rel} distributions are plotted subsequently in one histogram. One bin in the histogram corresponds to 0.2 GeV. The solid line is the overall Monte Carlo prediction obtained from the fit. A very good agreement with the data is observed. The numbers for the fitted fractions are quoted.

6.4.1 One-Dimensional Fit

Figure 6.5 shows the result of a simultaneous fit to both p_t^{rel} distributions for the muon-electron sample. The contributions from beauty signal, beauty background and charm plus light quarks are fitted to the data sample. For practical reasons and for better understanding, both p_t^{rel} distributions are plotted subsequently in one histogram. The p_t^{rel} distribution of the muon comes first, then follows the electron distribution with an offset of 4.0 GeV. One bin in the histogram corresponds to 0.2 GeV. The overall Monte Carlo prediction obtained by the fit as well as the different contributions according to their fitted fractions are depicted. The data is well described by the Monte Carlo prediction. This is reflected in a very good χ^2 value as can be read off, together with all the numbers for the individual fractions, from the text box in the figure. The fitted fractions are quoted in table 6.2 as well. As previously explained, the contributions from beauty signal and beauty background events look very similar and cannot be disentangled in the case of the muon p_t^{rel} distribution. This is due to the fact that for beauty events the selected muon originates predominantly from a b quark. This is not the case for the electron candidate as can be seen when looking at the electron p_t^{rel} distribution. In this case the

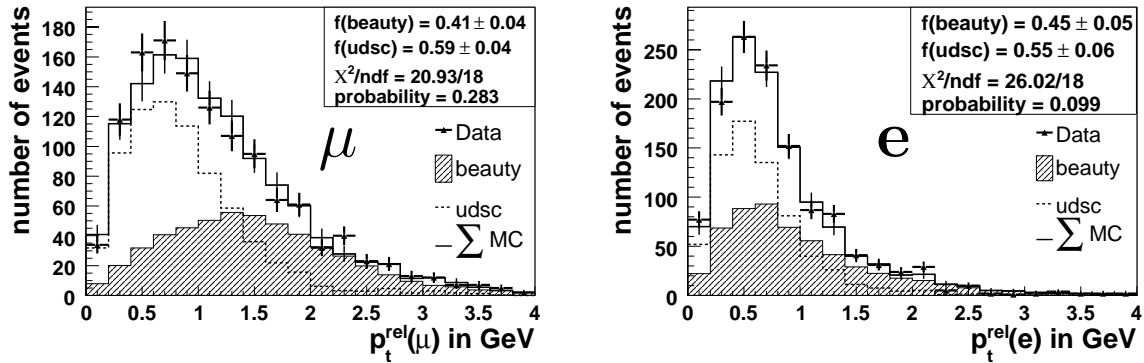


Figure 6.6: Results of the fit to the **muon** (left) and to the **electron** (right) p_t^{rel} distributions separately. Here, the beauty signal and beauty background contributions are combined. The fractions extracted from both distributions are compatible.

	Fitted fractions for the muon-electron sample in %					
	$p_t^{rel}(\mu)$ and $p_t^{rel}(e)$	$p_t^{rel}(\mu)$	$p_t^{rel}(e)$	$p_t^{rel}(\mu)$ vs. $p_t^{rel}(e)$	$ \Delta\phi \times Q(\mu) \times Q(e)$	$ \Delta\phi \times Q(\mu) \times Q(e)$ and $p_t^{rel}(\mu)$ and $p_t^{rel}(e)$
$b, \mu e$	29 ± 4	41 ± 4	45 ± 5	28 ± 4	46 ± 8	29 ± 4
b bgrnd	11 ± 6			12 ± 5		11 ± 5
$c, \mu e$	60 ± 4	59 ± 4	55 ± 6	59 ± 4	11 ± 3	13 ± 3
$udsc$ bgrnd					42 ± 7	47 ± 5

Table 6.2: Compilation of the fit results for the **muon-electron** sample.

background and the signal contributions from beauty look very different and the contribution from fake beauty events looks like the contribution from charm and light quark events. The fake electron can either be a misidentified hadron or an electron that does not originate from a b quark decay. Possible sources are for example electrons from photon conversion processes or light flavour decays. The contributions from beauty events where both leptons are fake (b, ff) and events with an electron and a fake muon (b, fe) are negligible.

In a next step, the overall beauty contribution and the contribution from charm plus light quarks are fitted to the p_t^{rel} distributions. Both distributions are fitted separately to investigate if compatible fractions are obtained from each p_t^{rel} distribution. The results are shown in figure 6.6. Both p_t^{rel} distributions are well described by the Monte Carlo prediction as can be deduced from the χ^2 values of the fit. In addition, both fit results agree with each other and also with the result from the simultaneous fit to both p_t^{rel} distributions (cf. table 6.2).

Additional cross checks have been performed. It was checked that changing the binning within reasonable values does not influence the outcome of the fit. Also, instead of data, a Monte Carlo sample containing all flavours was fitted. With the fit procedure described above the correct result for the beauty fraction was obtained.

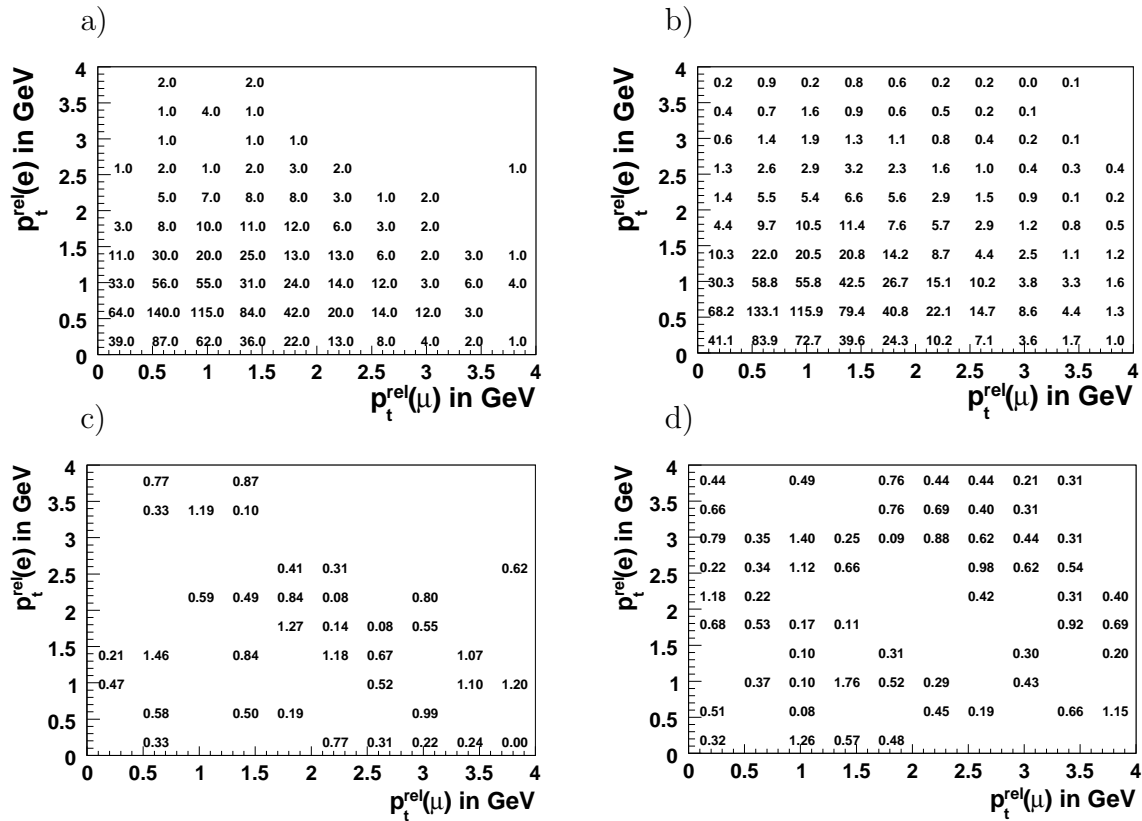


Figure 6.7: Result of a fit to the two-dimensional distribution of $p_t^{\text{rel}}(\mu)$ and $p_t^{\text{rel}}(e)$. a) The number of events per bin in the data. b) The number of events per bin as predicted by the Monte Carlo. c) Relative deviations in units of one standard deviation σ of the prediction from the data for events where the data is above the predictions. d) Relative deviations for events where the data is below the predictions.

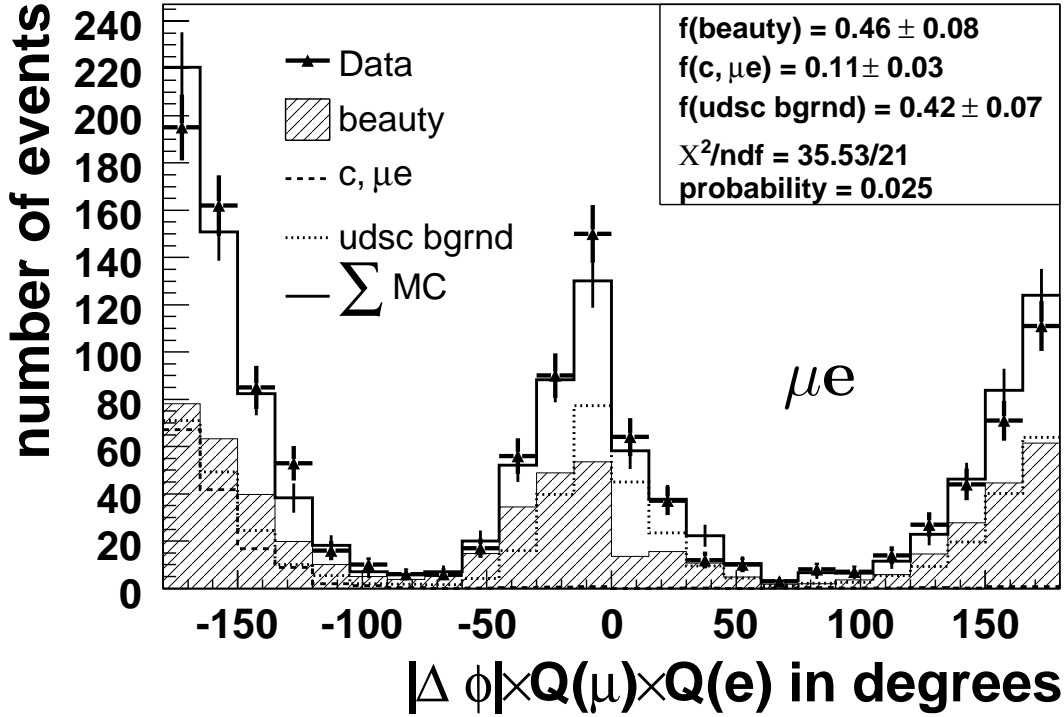


Figure 6.8: Result of a fit to the $|\Delta\phi| \times Q(\mu) \times Q(e)$ distribution for the **muon-electron** sample. The solid line is the overall Monte Carlo prediction obtained from the fit. The data is reasonably well described by the Monte Carlo prediction. The numbers for the different fractions are quoted.

6.4.2 The Two-Dimensional Fit

The result of a binned likelihood fit to the two-dimensional distribution of $p_t^{rel}(\mu)$ and $p_t^{rel}(e)$ is shown in figure 6.7. Contributions from beauty signal (μe), from beauty fake and from $udsc$ events are fitted to the data. In figure 6.7 a) the number of events per bin in data is shown. Figure 6.7 b) shows the number of events per bin according to the MC prediction. The Monte Carlo prediction is the sum of the three different contributions which are considered here. In figure 6.7 c) and d) the relative deviations of the prediction from the data are shown. Figure 6.7 c) shows the relative deviations in units of one standard deviation σ for bins where the prediction is below the measurement and 6.7 d) shows the deviations for the opposite case. No systematic effects like large deviation which are clustered in some region of phase space are observed. Instead, a good description of the data is obtained in two dimensions. The fitted fractions are also given in table 6.2. Furthermore, the results of the fit are fully compatible with results from the one-dimensional fit. Within the precision of this measurement, the relative fraction of the beauty signal ($b, \mu e$) and the beauty background ($b, \mu f$) contribution is compatible with that of the Monte Carlo prediction (cf. table 6.1).

	Fitted fractions for the dimuon sample in %					
	$p_t^{rel}(\mu_1)$ and $p_t^{rel}(\mu_2)$	$p_t^{rel}(\mu_1)$	$p_t^{rel}(\mu_2)$	$p_t^{rel}(\mu_1)$ vs. $p_t^{rel}(\mu_2)$	$ \Delta\phi $ $\times Q(\mu_1)$ $\times Q(\mu_2)$	$ \Delta\phi \times Q(\mu_1) \times Q(\mu_2)$ and $p_t^{rel}(\mu_1)$ and $p_t^{rel}(\mu_2)$
$b, \mu\mu$	19 ± 4	33 ± 2	35 ± 4	16 ± 3	27 ± 5	17 ± 2
b bgrnd	14 ± 6			17 ± 4		16 ± 4
$c, \mu\mu$	67 ± 3	67 ± 3	65 ± 4	67 ± 3	5 ± 2	5 ± 1
$udsc$ bgrnd					68 ± 5	62 ± 3

Table 6.3: *Compilation of the fit results for the dimuon sample.*

6.4.3 Charm Fraction from Muon-Electron Events

In the previous section, the beauty fraction was derived from the p_t^{rel} distributions. Now the beauty fraction is derived from the charge and azimuthal angle correlation of the leptons, yielding a second, independent result. In addition, the fraction of charm signal events ($c, \mu e$) is determined. Figure 6.8 shows the results of a fit to the $|\Delta\phi| \times Q(\mu) \times Q(e)$ distribution. The contributions from beauty (signal plus background), charm signal and from light flavour plus charm background are considered. The two independent results for the beauty signal fraction agree with each other (cf. table 6.2).

To reduce the errors and to obtain more stable results, the two p_t^{rel} and the $|\Delta\phi| \times Q(\mu) \times Q(e)$ distributions are fitted simultaneously. The p_t^{rel} distributions constrain the beauty component while the $|\Delta\phi| \times Q(\mu) \times Q(e)$ distribution provides separation power to distinguish between charm signal, beauty signal and the light flavour plus charm background component. Figure 6.9 shows the result of the fit. The $|\Delta\phi| \times Q(\mu) \times Q(e)$ and the p_t^{rel} distributions are plotted in one histogram. The beauty fraction obtained by this fit is in very good agreement with the result presented in the previous section. The charm fraction extracted from the fit is

$$f(c, \mu e) = (13 \pm 3)\%$$

and the fraction of beauty signal events amounts to

$$f(b, \mu e) = (29 \pm 4)\%.$$

6.5 Charm and Beauty Fractions from Dimuon Events

For the dimuon sample, the same strategy is used to extract the fraction of charm and beauty signal events. All cross checks and fits performed for the muon-electron sample were also done for the dimuon sample and consistent results are obtained. The fit results are listed in table 6.3. Only the fits to the p_t^{rel} distributions and the result of the simultaneous fit to the $|\Delta\phi| \times Q(\mu_1) \times Q(\mu_2)$ and the p_t^{rel} distribution are shown.

Figure 6.10 shows the results of the fits to the muon p_t^{rel} distributions. Both distributions are described well by the Monte Carlo prediction and both fits give compatible results for the beauty (signal plus background) fraction.

In figure 6.11, the result of a simultaneous fit to the $|\Delta\phi| \times Q(\mu_1) \times Q(\mu_2)$ and to both p_t^{rel} distributions is shown. The data is well described by the Monte Carlo prediction. This is reflected in a good χ^2 value. Also shown are the different contributions which are fitted to the data. As it was done for the muon-electron sample, four different contributions are considered. The first contribution is from beauty signal events, i.e. beauty events with two muons from a b quark decay. The second contribution is from beauty background events. The third contribution consists of charm signal events, while the fourth contribution is from charm and light flavour background events. A charm fraction of

$$f(c, \mu\mu) = (5 \pm 1)\%$$

is obtained by the fit. The beauty fraction amounts to

$$f(b, \mu\mu) = (17 \pm 2)\%.$$

Considerably smaller errors on the fitted charm and beauty fractions are obtained when the $|\Delta\phi| \times Q(\mu_1) \times Q(\mu_2)$ and both p_t^{rel} distributions are fitted simultaneously (cf. table 6.3).

The final results for the fitted charm and beauty fractions are summarised in table 6.4. The fractions obtained for the muon-electron and the dimuon sample are compared to the expected fractions according to the PYTHIA Monte Carlo.

	Fractions in %			
	μe		$\mu\mu$	
	Data	MC	Data	MC
$b, \mu_1 l_2$	29 ± 4	15	17 ± 2	11
b bgrnd	11 ± 5	11	16 ± 4	12
$c, \mu_1 l_2$	13 ± 3	9	5 ± 1	9
$udsc$ bgrnd	47 ± 5	65	62 ± 3	68

Table 6.4: Summary of the final fit results for the **muon-electron** and the **dimuon** samples. The fractions extracted from the data are compared to the expected fractions according to the PYTHIA Monte Carlo.

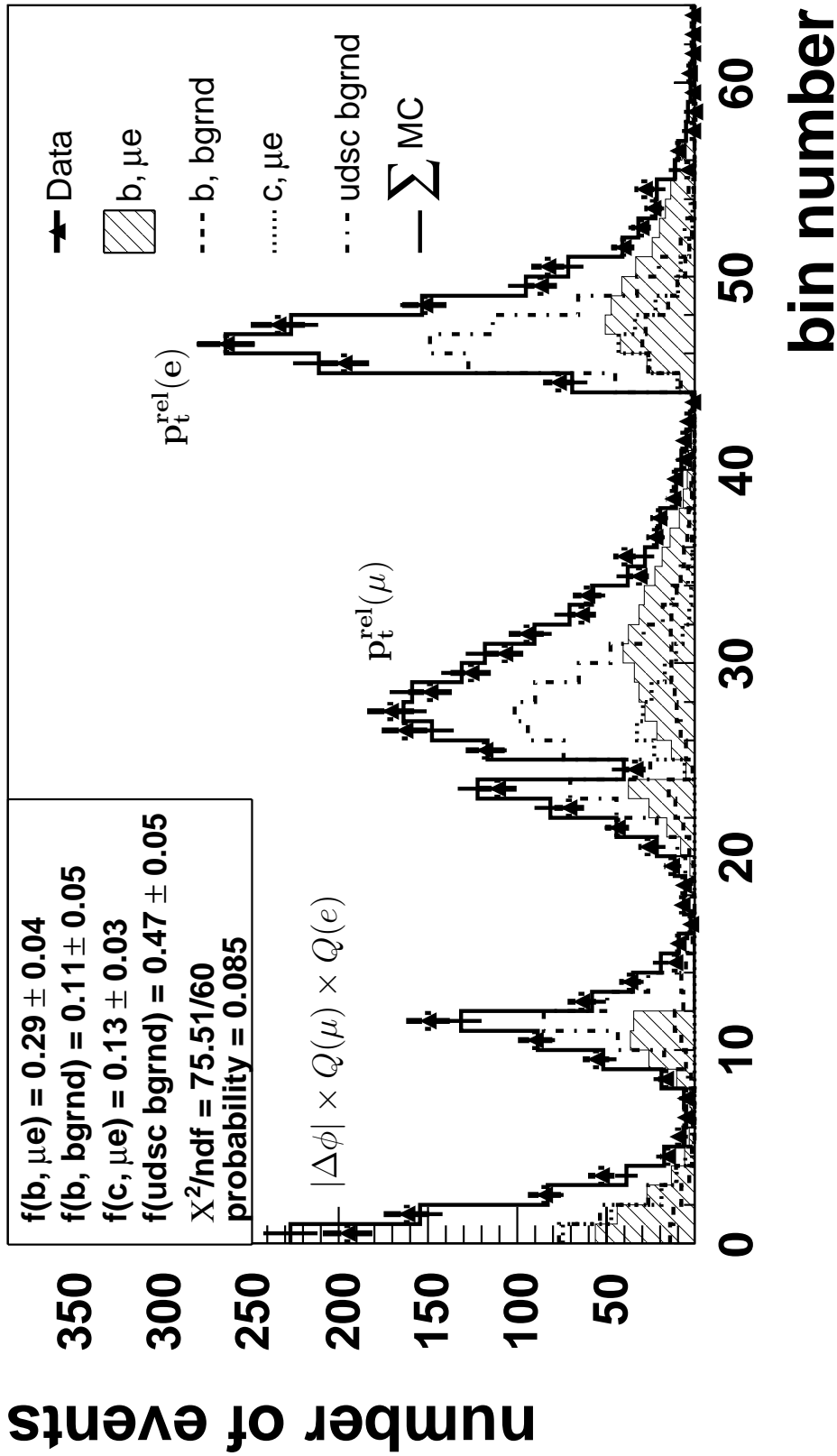


Figure 6.9: Result of a simultaneous fit to the $|\Delta\phi| \times Q(\mu) \times Q(e)$ and the two p_t^{rel} distributions for the muon-electron sample. The distributions are plotted subsequently in one histogram. The solid line is the overall Monte Carlo prediction obtained from the fit. The data is well described by the Monte Carlo prediction. The numbers for the different fractions are quoted.

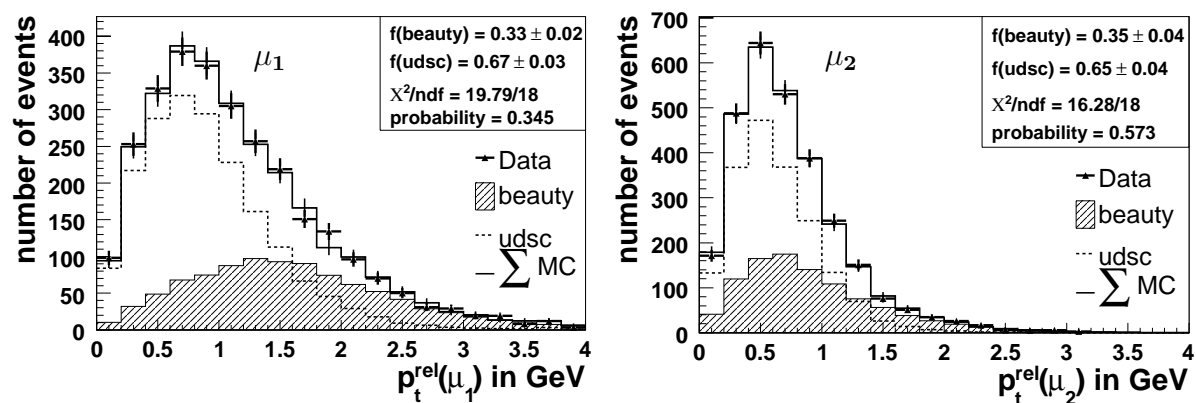


Figure 6.10: Results of a fit to the p_t^{rel} distributions of the iron muon (left) and the second muon (right). Here, the contributions from beauty signal and beauty background are combined. The fractions extracted from both distributions are compatible.

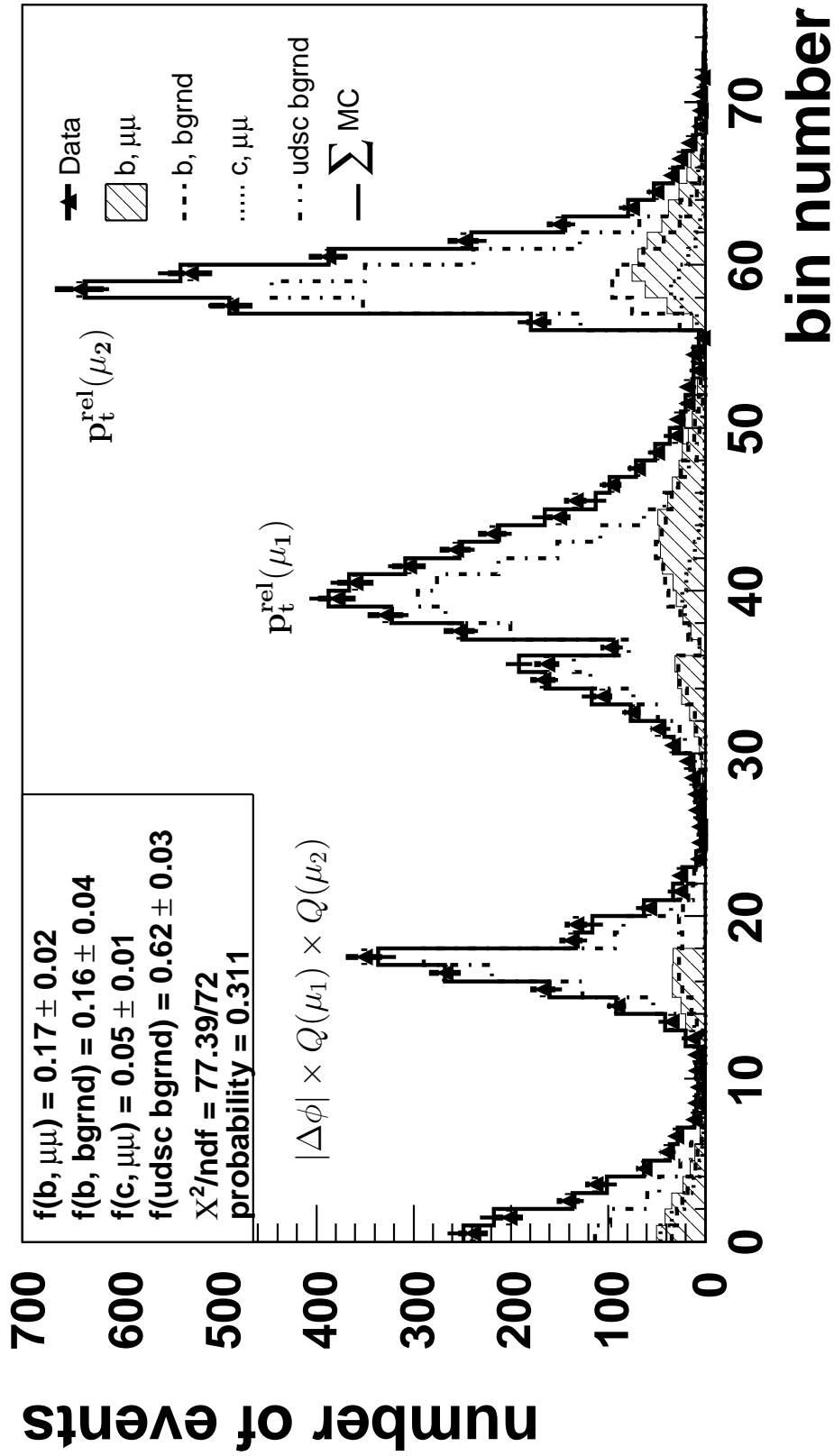


Figure 6.11: Result of a simultaneous fit to the $|\Delta\phi| \times Q(\mu_1) \times Q(\mu_2)$ and the two p_t^{rel} distributions for the dimuon sample. The distributions are plotted subsequently in one histogram. The solid line is the overall Monte Carlo prediction obtained from the fit. The data is well described by the Monte Carlo prediction. The results for the different fractions are quoted.

CHAPTER 7

TOTAL CROSS SECTIONS

In this chapter the measured charm and beauty cross sections for the photoproduction of events with two leptons and two jets in the final state are presented. First a definition of the cross section is given and then the different quantities that enter the cross section formula are discussed. No event-wise identification of heavy quarks is performed but the fractions of charm and beauty events in the dilepton samples are determined by statistical means (see chapter 6). Before the cross sections are presented and discussed, the main systematic uncertainties are investigated. The muon-electron and the dimuon sample are treated in parallel to allow for comparisons at each single step of the analysis.

7.1 Cross Section Definition

The cross section for a given process is defined as the number of events divided by the luminosity \mathcal{L} . In order to retrieve the number of events originating from the process under investigation, several corrections for detector effects have to be applied. Taking into account all correction factors, the cross section is given by the following expression:

$$\sigma_{vis} = \frac{N \cdot f_q}{\epsilon_{rec} \cdot \epsilon_{trig} \cdot \mathcal{L}} \quad \text{with } q = c, b \quad (7.1)$$

N is the number of selected events in data, ϵ_{rec} the reconstruction efficiency, ϵ_{trig} the trigger efficiency and f_q the fraction of c and b events, respectively. In the following, these quantities are discussed in detail.

It has to be taken into account that not all events within the visible range are reconstructed. For example there is only a finite probability for the leptons or the jets to be reconstructed. The visible range is given by the acceptance of the detector. Since detectors in high energy physics are quite complex, the reconstruction efficiency is usually extracted from Monte Carlo simulations according to the following formula:

$$\epsilon_{rec} = \left. \frac{N_{rec}}{N_{gen}} \right|_{vis} \quad (7.2)$$

N_{gen} is the number of generated events within the visible range. N_{rec} denotes the number of reconstructed events within the visible range according to the measurement regardless if the

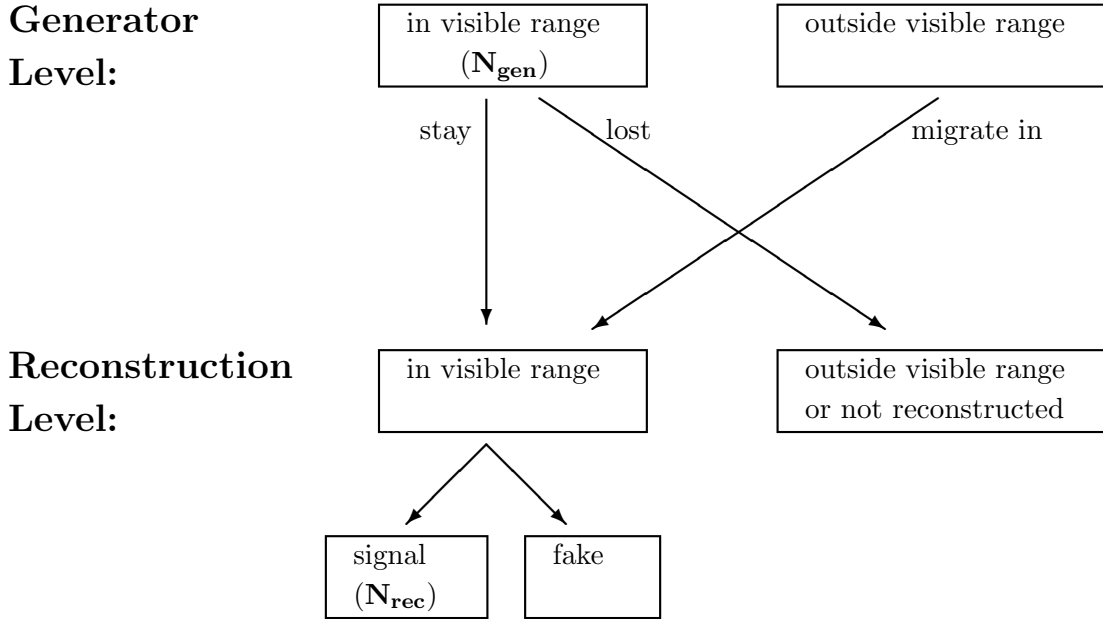


Figure 7.1: *Definition of the reconstruction efficiency.*

event actually is in the kinematic range on generator level or not. Therefore, the reconstruction efficiency defined in this way also incorporates migration effects. Only events are counted in which leptons from a heavy flavour decay are actually selected. Therefore, the reconstruction efficiency also contains corrections for the case in which fake leptons¹ are selected although there are leptons from heavy flavour decays within the kinematic range. It turns out that the latter effect amounts only to a few percent. The definition of the reconstruction efficiency and the different corrections which are incorporated are depicted in figure 7.1.

It has to be carefully checked that the reconstruction efficiency in the data is well described by the simulation in order to avoid that the cross section measurement is biased. Any deviations between data and simulation have to be corrected or have to be taken into account in the systematic uncertainty. In the present analysis, for example, the lepton identification efficiency in the Monte Carlo simulation is corrected (see chapter 4).

Another detector effect one has to take into account is the finite trigger efficiency ϵ_{trig} . The trigger efficiency is defined as the number of reconstructed and triggered events $N_{rec,trig}$ divided by the number of reconstructed events:

$$\epsilon_{trig} = \frac{N_{rec,trig}}{N_{rec}} \Big|_{vis} \quad (7.3)$$

This quantity can be extracted from Monte Carlo simulations or from data using independent triggers. In the present analysis the events are triggered by the subtrigger S19 which requires

¹Leptons that do not originate from the decay of a heavy quark or misidentified hadrons are referred to as fake leptons.

a muon signature in the instrumented iron, an event vertex and several central tracks above a certain momentum threshold as described in section 5.4. This subtrigger can therefore be cross checked with a subtrigger which only contains calorimeter or electron tagger information. The subtrigger S19 has no level two (L2) condition. In addition, the events in the selected data samples have no L4 weights. So inefficiencies which could originate from those two sources don't play a role in this analysis. In addition to the trigger efficiency on level one (L1), only the efficiency for the verification of the L1 trigger decision on L4 has to be studied. As the verification is always performed when a subtrigger has fired on L1, there is plenty of statistics to study this contribution to the trigger efficiency.

Not all events in the selected data samples are actually dilepton events with the leptons originating both from heavy quarks. There are also contributions from background events coming from different sources. The fractions of charm and beauty events f_q were determined in the previous chapter.

7.2 Systematic Uncertainties

In addition to the statistical errors, there are systematic effects which lead to uncertainties of the measured cross sections. In order to determine these uncertainties, relevant parameters are varied within a reasonable range and the influence on the result is evaluated using the Monte Carlo simulation. Some of the uncertainties considered here arise from imperfections of the detector simulation. Examples are the error on the trigger efficiency or the error due to the imperfect description of the lepton identification efficiency. Other errors are related to uncertainties of the physics model. There are also detector effects like the energy calibration of the calorimeter or the error on the luminosity measurement which have to be taken into account. The main systematic uncertainties which are considered here are listed in table 7.1. Assuming uncorrelated uncertainties, the total systematic uncertainty is obtained by adding all contributions in quadrature. In the following each contribution to the error will be discussed in detail.

- ▷ The systematic uncertainty on the measurement of the **integrated luminosity** amounts to 1.5 % [71].
- ▷ The **trigger efficiency** is extracted from data. The uncertainty related to the method which is used is estimated to amount to 3 %.
- ▷ The total **systematic uncertainty on the lepton reconstruction** is composed of the error on the **track reconstruction efficiency** and the error on the **lepton identification efficiency**. The relative systematic uncertainty on the track reconstruction efficiency amounts to 2 % for high p_t tracks [72].

In chapter 4 the efficiencies to identify leptons as a function of the polar angle θ and the transverse momentum p_t were extracted from data. The results were compared to the Monte Carlo prediction and correction functions to obtain a better description of the data were derived. In addition, the systematic uncertainty on the lepton identification efficiency was estimated. For muons with a transverse momentum larger than 2.0 GeV within the polar angle range $30^\circ < \theta < 130^\circ$ which are identified in the central muon detector, the

systematic uncertainty amounts to 5 % (cf. section 4.2.3.1). For muons which are identified in the calorimeter only, significant corrections to the simulation have to be applied. Due to the detailed study, the systematic uncertainty connected to the lepton identification efficiency is reduced. A systematic uncertainty of 3 % was estimated (cf. section 4.2.3.2). The uncertainty on the electron identification efficiency was estimated to amount to 3 % (see section 4.1.5).

For both dilepton samples the systematic uncertainty related to the lepton reconstruction is 6 %. This value is obtained by adding all contributions in quadrature.

- ▷ The contributions from **light flavour and charm background** cannot be separated from each other in this analysis. Therefore the relative fraction of both contributions are obtained from the Monte Carlo simulation and fixed to that value during the fit. To study the sensitivity of the charm and beauty cross sections to variations of the light flavour and charm background, the ratio predicted by the Monte Carlo simulation is varied by 50 %. While the p_t^{rel} distributions is not affected, the $|\Delta\phi(\mu_1, l_2)| \times Q(\mu_1) \times Q(l_2)$ distribution changes slightly. Since the beauty fraction is predominantly constrained by the p_t^{rel} distributions, the measured beauty cross section does not change. The effect on the measured charm cross section amounts to 6 % for both dilepton analyses.
- ▷ The systematic uncertainty on the **hadronic energy scale in the LAr calorimeter** amounts to $\pm 4\%$ and the **electromagnetic energy scale in the LAr calorimeter** is known to an accuracy of $\pm 2\%$. To evaluate the uncertainty on the cross section measurement due to these uncertainties, the cell energies were varied accordingly. Then the HFS and the jet finder were run and the analysis was repeated. The changes to the energy scales mainly have an influence on the jet energies and on the kinematic variables which are calculated from the HFS, in particular the inelasticity computed via the hadron method y_h which is used in this analysis to select photoproduction events. The discussed variations lead to cross section changes of about 5 %.

The **SpaCal energy scale** was varied by $\pm 4\%$. Mainly the efficiency of the SpaCal electron finder close to the energy threshold and the y_h measurement are affected by this variation. A systematic effect which amounts to about 2 % was determined.

- ▷ The polar and the azimuthal angles of the **jet axes** are varied by $\pm 2.5^\circ$, according to the resolution of the jet axis measurement. The effect on the measured cross section amounts to 3 %.
- ▷ The dependence of the cross section measurement on the **physics model** is studied comparing the predictions from the two Monte Carlo generators CASCADE and PYTHIA. No differences in the shapes of the p_t^{rel} distributions is observed. Also the charge and angle correlation of the two leptons is the same for both event generators as shown in section 2.6. Furthermore both Monte Carlo samples give the same result for the reconstruction efficiency.

The sensitivity of the cross section measurement on the fragmentation model is tested using the Lund [15] fragmentation model instead of the Peterson fragmentation function [16]. No systematic effect is observed.

Source	Dimuon events		Muon-electron events	
	$\Delta\sigma/\sigma$ in %		$\Delta\sigma/\sigma$ in %	
	beauty	charm	beauty	charm
Luminosity \mathcal{L}	1.5			
Trigger efficiency	3			
Lepton reconstruction	6		6	
LAr energy scales	5			
SpaCal energy scale	2			
Jet axis	3			
Charm and uds background	negligible	6	negligible	6
MC model dependence: CASCADE vs. PYTHIA MC Fragmentation (Peterson vs. Lund)	negligible negligible			
Total	10	12	10	12

Table 7.1: *Compilation of the systematic uncertainties on the charm and beauty cross sections for both dilepton samples.*

The total systematic uncertainty on the measured beauty cross section is estimated to amount to 10 % for both dilepton samples. The systematic uncertainty on the charm cross section is slightly larger and amounts to 12 %.

7.3 Visible Charm and Beauty Cross Sections

In this section the visible cross sections for the production of lepton pairs originating from heavy quarks are presented. The **visible range** is defined as follows:

$$Q^2 < 1 \text{ GeV}^2 \quad \text{and} \quad 0.1 < y < 0.7$$

Jets:

$$p_t > 5(4) \text{ GeV} \quad \text{and} \quad 20^\circ < \theta < 160^\circ$$

Muon:

$$p_t > 2.0 \text{ GeV} \quad \text{and} \quad 30^\circ < \theta < 130^\circ$$

Second lepton:

$$p_t > 1.0 \text{ GeV} \quad \text{and} \quad 20^\circ < \theta < 150^\circ$$

In table 7.2 the number of events that pass the selection criteria (cf. table 5.11) are given. In addition, the charm and beauty fractions derived from the fits as discussed in the previous section are listed for both dilepton samples.

Dilepton sample	No. of events	beauty fraction	No. of b events	charm fraction	No. of c events
μe	1254	$(29.3 \pm 3.8) \%$	367 ± 48	$(13.2 \pm 2.9)\%$	166 ± 36
$\mu\mu$	2846	$(16.9 \pm 2.4) \%$	481 ± 68	$(4.6 \pm 1.5)\%$	131 ± 42

Table 7.2: Number of events passing the selection criteria in table 5.11, the charm and beauty fractions and the calculated number of charm and beauty events in both dilepton samples.

beauty	reconstruction efficiency ϵ_{rec} in %		
	HERA I	HERA II	mean value
muon-electron sample	20.9 (1)	26.2 (2)	24.5
dimuon sample	23.1 (1)	29.1 (1)	27.2

Table 7.3: The reconstruction efficiencies for **beauty** events derived from the Monte Carlo simulation for both dilepton samples. The value in parentheses denotes the contribution due to migration effects.

charm	reconstruction efficiency ϵ_{rec} in %		
	HERA I	HERA II	mean value
muon-electron sample	19.9 (1)	23.7 (2)	22.5
dimuon sample	25.1 (1)	30.5 (1)	28.8

Table 7.4: The reconstruction efficiencies for **charm** events derived from the Monte Carlo simulation for both dilepton samples. The value in parentheses denotes the contribution due to migration effects.

In the tables 7.3 and 7.4 the event reconstruction efficiencies for beauty and charm events are given. The efficiencies are determined using Monte Carlo simulations. The reconstruction efficiencies in the HERA II running period are about 5 % higher than in HERA I. The main reason for the higher efficiencies is that during the upgrade broken wires in the CJC were replaced. Another reason is that some of the inner SpaCal cells were removed. This led to a smaller Q^2 acceptance and therefore to different migration effects. The luminosity weighted mean value of the reconstruction efficiencies are used to determined the cross section.

The trigger efficiencies of subtrigger S19 for different run periods are listed in table 7.5. The efficiencies are derived from data using the independent subtrigger S0. The luminosity weighted mean values are also given. The trigger efficiencies for the dimuon sample are slightly larger than the trigger efficiencies for the muon-electron sample since the second muon, depending on its transverse momentum and polar angle, may also trigger the event. The trigger efficiencies in the years 1999 and 2000 are expected to be similar as there were no significant changes in the trigger definition in this period. In 2004 the trigger definition changed as the the old z-Vertex trigger was not operational any more and trigger elements provided by the CIP 2000 entered the veto conditions of subtrigger S19. In 2005 new trigger elements provided by the FTT were incorporated. Therefore the years 2004 and 2005 are treated separately. At the end of 2004

and in the beginning of 2005 problems with the efficiency of the muon system occurred. This is not described by the Monte Carlo simulation but taken into account in the efficiencies extracted from data. Therefore the trigger efficiencies extracted from data are used.

beauty / charm	trigger efficiency ϵ_{trig} S19 in %				
	1999	2000	2004	2005	mean value
μe	64.2 ± 4.1	73.7 ± 2.9	73.7 ± 2.8	77.4 ± 1.9	74.4 ± 1.3
$\mu\mu$	75.8 ± 3.1	76.4 ± 2.3	81.1 ± 2.2	80.6 ± 1.3	79.3 ± 1.0

Table 7.5: The trigger efficiencies of the subtrigger S19 for different data taking periods. The trigger efficiencies extracted from the data are given.

Using the fitted charm and beauty fractions and the efficiencies, the following visible cross sections for the photoproduction of lepton pairs are obtained:

Visible charm cross sections

Muon-electron analysis:

$$\sigma(ep \rightarrow ec\bar{c}X \rightarrow ejj\mu eX') = 4.6 \pm 1.0(stat.) \pm 0.5(sys.) \text{ pb}$$

$$\frac{\sigma_{meas}}{\sigma_{MC}} = 1.2 \pm 0.3 \quad \text{with } \sigma_{MC} = 4.1 \text{ pb}$$

Dimuon analysis:

$$\sigma(ep \rightarrow ec\bar{c}X \rightarrow ejj\mu\mu X') = 2.7 \pm 0.9(stat.) \pm 0.3(sys.) \text{ pb}$$

$$\frac{\sigma_{meas}}{\sigma_{MC}} = 0.8 \pm 0.3 \quad \text{with } \sigma_{MC} = 3.3 \text{ pb}$$

Visible beauty cross sections

Muon-electron analysis:

$$\sigma(ep \rightarrow eb\bar{b}X \rightarrow ejj\mu eX') = 9.4 \pm 1.2(stat.) \pm 0.9(sys.) \text{ pb}$$

$$\frac{\sigma_{meas}}{\sigma_{MC}} = 1.5 \pm 0.2 \quad \text{with } \sigma_{MC} = 6.3 \text{ pb}$$

Dimuon analysis:

$$\sigma(ep \rightarrow eb\bar{b}X \rightarrow ejj\mu\mu X') = 10.4 \pm 1.5(stat.) \pm 1.0(sys.) \text{ pb}$$

$$\frac{\sigma_{meas}}{\sigma_{MC}} = 1.9 \pm 0.3 \quad \text{with } \sigma_{MC} = 5.6 \text{ pb}$$

Visible Cross Sections in pb	Beauty		Charm	
	μe	$\mu\mu$	μe	$\mu\mu$
Data	9.4 ± 1.5	10.4 ± 1.8	4.6 ± 1.1	2.7 ± 0.9
Pythia	6.3	5.6	4.1	3.3
Cascade	8.9	7.7	6.7	6.1

Table 7.6: *Compilation of the visible charm and beauty cross sections for both dilepton samples. The data is compared to QCD calculations in leading order with parton showers. The LO+PS events generators PYTHIA and CASCADE are considered. The statistical and systematic errors are added in quadrature.*

The statistical and the systematic errors (cf. section 7.2) are given. The predicted cross sections according to the PYTHIA Monte Carlo and the ratios between the measured cross sections and the predictions $\sigma_{meas}/\sigma_{MC}$ are quoted as well. The errors on the ratios consist of the statistical and the systematic uncertainties added in quadrature. The photon and the proton parton density functions, the fragmentation functions and the heavy quark masses, which are used by the PYTHIA event generator, are listed in table A.1 in appendix A.

The charm and beauty cross sections obtained from the dimuon and muon-electron analyses are compatible, since within the errors the ratios between the data and the prediction from the PYTHIA LO+PS event generator agree well.

Within the errors, the charm cross sections agree well with the Monte Carlo prediction while the measured beauty cross sections are significantly larger for both dilepton samples. All results are summarised in table 7.6. In addition, the predicted cross sections from the CASCADE event generator are listed. CASCADE predicts considerably larger cross sections than PYTHIA. The predicted beauty cross sections are somewhat below the data, while the charm cross sections are considerably above the measurements.

In the following the results obtained in the present analysis are compared to recent measurements by H1 and ZEUS which were discussed in section 3.3. The figures 7.2 and 7.3 show a compilation of the measured visible cross sections for charm and beauty photoproduction. The data is compared to the predictions from the PYTHIA LO+PS event generator. The ratios between the measurements and the predictions are depicted as well. According to figure 7.2, the visible charm cross sections obtained in the present analysis ($jj\mu e$ and $jj\mu\mu$) are in agreement with the other recent measurements from H1, since the ratios between the data and the predictions are the same. Furthermore, all charm results are in agreement with the predictions. In figure 7.3 recent measurements of visible beauty cross sections in photoproduction performed by H1 and ZEUS are compared to the results of the present analysis. While the measurements are in agreement with each other, they all lie above the prediction by a factor of about two.

Note that the expected cross section for muon-electron production is slightly larger than the cross section for dimuon production. When the same kinematic cuts on the first and the second lepton are applied, the cross section for muon-electron production is expected to be about a factor two larger than the dimuon cross section, since there are twice more muon-electron than dimuon final states possible. The factor between the muon-electron and the dimuon cross section is slightly smaller than two. This is due to different branching fractions. B hadrons can decay into a J/ψ meson which further decays into two muons. A muon-electron final state is not

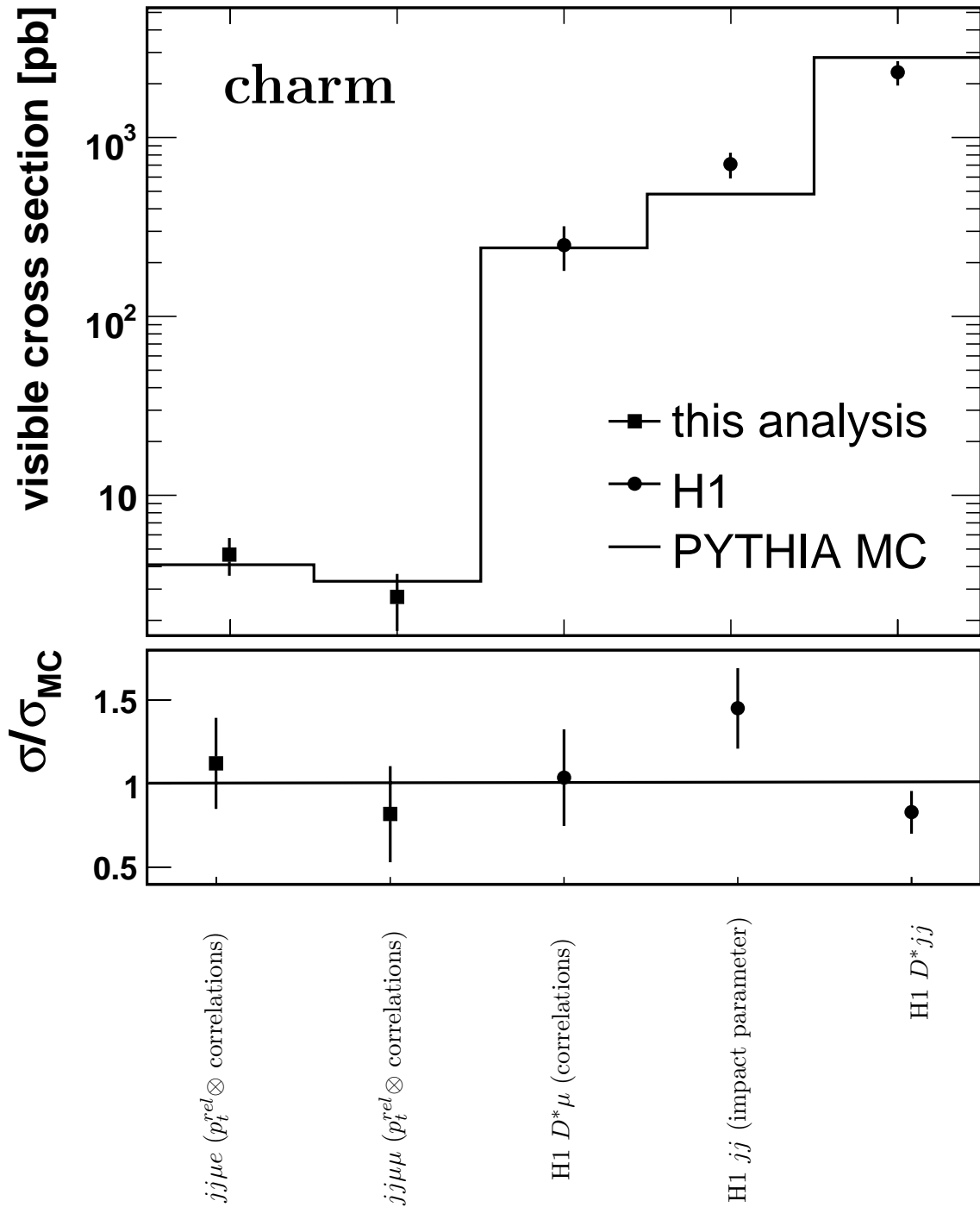


Figure 7.2: The visible cross sections for charm photoproduction obtained in the present analysis in comparison to recent results from H1 and to LO+PS QCD predictions according to the PYTHIA event generator. The errors on the measurements consist of the statistical and the systematic uncertainty added in quadrature. Shown are the visible cross sections (upper plot) and the ratios between the data and the predictions (lower plot).

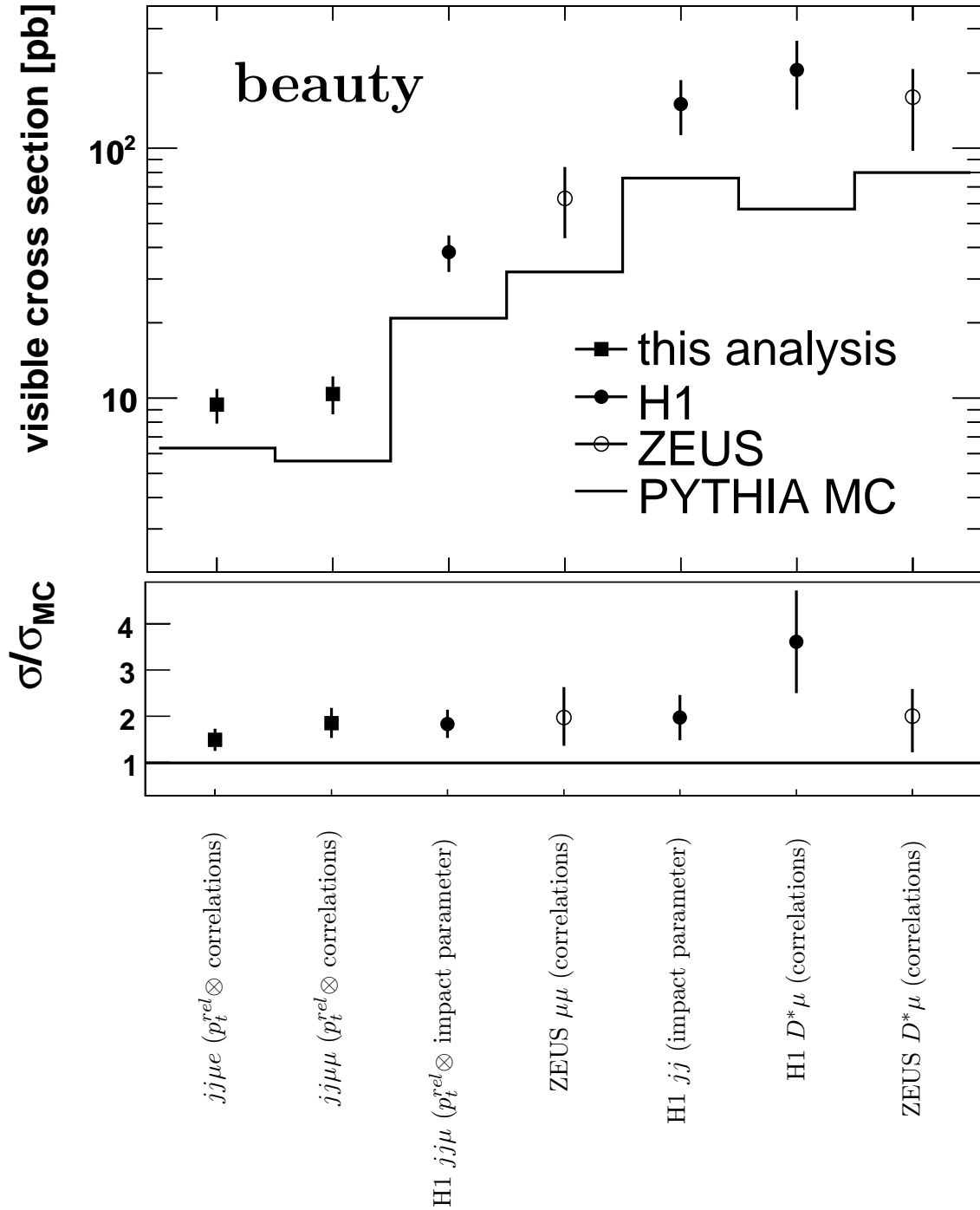


Figure 7.3: The visible cross sections for beauty photoproduction obtained in the present analysis in comparison to recent results from H1 and ZEUS and to LO+PS QCD predictions according to the PYTHIA event generator. The errors on the measurements consist of the statistical and the systematic uncertainty added in quadrature. Shown are the visible cross sections (upper plot) and the ratios between the data and the predictions (lower plot).

possible for this decay. For asymmetric cuts on the leptons, the effect becomes smaller, but is still there.

CHAPTER 8

DIFFERENTIAL CROSS-SECTIONS

In order to study the production of dilepton pairs in more detail differential cross sections are investigated. The emphasis is on lepton-lepton and jet-jet correlations but also differential cross sections as a function of the transverse momentum and the polar angle of the jets are shown. Both dilepton samples are studied in parallel to allow for comparisons and cross checks at each step of the calculations. Before the results are presented and compared to the MC prediction the procedure used to extract differential cross sections from data will be briefly discussed. Differential cross sections are only investigated for beauty production, since the number of charm events does not allow a meaningful differential analysis (cf. table 7.2).

8.1 Determination of Differential Cross Sections

To evaluate differential cross sections the data is divided into bins of the quantity which is investigated. The binning has to be chosen such that the statistics in each bin allows for a reliable determination of the beauty fraction via a simultaneous fit to both p_t^{rel} distributions and that migrations effects are not too large. To monitor the migrations effects two quantities, the purity \mathcal{P} and the stability \mathcal{S} , are defined.

The purity is defined as the number of events which are generated and reconstructed in the examined bin, N_{Stay} , divided by the number of reconstructed events in that bin, N_{Rec} :

$$\mathcal{P} = \frac{N_{Stay}}{N_{Rec}} \quad (8.1)$$

The number of reconstructed events, N_{Rec} , is given by the number of events which were generated and reconstructed in that bin, N_{Stay} , and the number of events which were generated in a different bin but which were reconstructed in that bin, $N_{SmearIn}$:

$$N_{Rec} = N_{Stay} + N_{SmearIn} \quad (8.2)$$

The purity is a measure for the fraction of events in a given bin which actually belong there.

The stability is defined as follows:

$$\mathcal{S} = \frac{N_{Stay}}{N_{Stay} + N_{SmearOut}} \quad (8.3)$$

In this equation $N_{SmearOut}$ indicates the number of events which were generated but not reconstructed in that bin. As can be read of from the definition, the stability specifies the fraction of events which remain in a given bin.

In order to calculate the cross section in each bin migrations have to be taken into account. In this analysis the corrections for migration effects are incorporated in the reconstruction efficiency. This leads to the following definition of the reconstruction efficiency:

$$\epsilon_{rec} = \frac{N_{Stay} + N_{SmearIn}}{N_{Gen}} = \frac{N_{Rec}}{N_{Gen}} \quad (8.4)$$

N_{Gen} is the number of events which were generated in that bin. This equation shows explicitly that migrations have a direct influence on the measurement. Since migration corrections can only be extracted from the simulation it is important to keep them as small as possible to reduce the sensitivity to the correct modelling of the events. Thus the bins are chosen such that the purity and stability are larger than 40 % in each bin.

The fraction of beauty signal events in each bin is determined by a simultaneous fit to both p_t^{rel} distributions and the $|\Delta\phi(\mu_1, l_2)| \times Q(\mu_1) \times Q(l_2)$ distribution.

The beauty fraction f_b , the reconstruction efficiency ϵ_{rec} and the trigger efficiency ϵ_{trig} determined in each bin enter the formula for the bin averaged differential cross section in a given quantity x :

$$\frac{d\sigma_{vis}}{dx} = \frac{N \cdot f_b}{\mathcal{L} \cdot \epsilon_{rec} \cdot \epsilon_{trig} \cdot \Delta x} \quad (8.5)$$

N denotes the number of selected events which fall into the bin and Δx is the width of the considered bin.

The differential cross sections extracted from the data are shown for both dilepton samples and can thus be directly compared to each other. The results are compared to the predicted differential cross sections from the two event generators PYTHIA and CASCADE, which incorporate leading order matrix elements supplemented with parton showers. The ratio between the measured visible beauty cross section and the prediction from PYTHIA, as derived in the previous chapter, is used to scale the Monte distributions to allow for shape comparisons. Combining the ratios determined for the dimuon and the muon-electron analysis a scaling factor of 1.7 is obtained. For CASCADE the scaling factor is 1.2.

8.2 Single Lepton, Dilepton and Jet Cross Sections

The figures 8.1 and 8.2 show the differential cross section measurements as a function of the transverse momentum and the polar angle of the selected leptons for the dimuon and the muon-electron sample, respectively. The trigger efficiencies are extracted from data. Only the statistical errors of the differential cross sections are given since they are dominant. The shapes of the differential distributions are well described by both Monte Carlo event generators. Within the errors no indication for an excess at low transverse momenta can be seen as observed in a recent H1 publication [58] (cf. section 3.3).

In order to pursue the comparison with the results from the mentioned H1 publication, differential jet cross sections are investigated. Figure 8.3 shows the bin averaged differential beauty cross sections in bins of the transverse momentum, the polar angle and the angle correlation of the two

selected jets. Again the shapes of the distributions are well described by the PYTHIA Monte Carlo and there is no indication for an excess at low jet transverse momenta. The CASCADE Monte Carlo predicts a momentum spectrum which is somewhat harder than the data.

In figure 8.3 the azimuthal angle correlation $|\Delta\phi_{jj}|$ of the jets is studied as well. This quantity is of interest since it relates to the azimuthal angle correlation of the two outgoing partons from the hard subprocess and since it is sensitive to higher order QCD effects. In the leading order picture the two outgoing parton are back-to-back in the transverse plane. Due to the limited detector resolution and higher order effects, such as gluon emissions, the peak at $|\Delta\phi_{jj}| = 180^\circ$ is smeared to lower values. Within the errors of this measurement the distributions for the dimuon and the muon-electron sample are well described.

In order to study the production of lepton pairs in more detail, figure 8.4 shows differential photoproduction cross sections in bins of the invariant mass $m_{\mu_1 l_2}$, the polar angle $\theta(\mu_1 l_2)$, the transverse momentum $p_t(\mu_1 l_2)$ and the charge and azimuthal angle correlation of the dilepton system $|\Delta\phi(\mu_1, l_2)| \times Q(\mu_1) \times Q(l_2)$ ($l_2 = \mu_2, e$) are displayed. Note that for the charge and azimuthal angle correlation the fraction of beauty signal events is determined by a fit to the p_t^{rel} distributions only. The properties of the dilepton system are reasonably well described.

All results are summarised in the tables B.1, B.3, B.4 and B.6 in appendix B where the binwise fitted beauty fractions, the trigger efficiencies, the reconstruction efficiencies and the bin averaged differential cross sections are quoted.

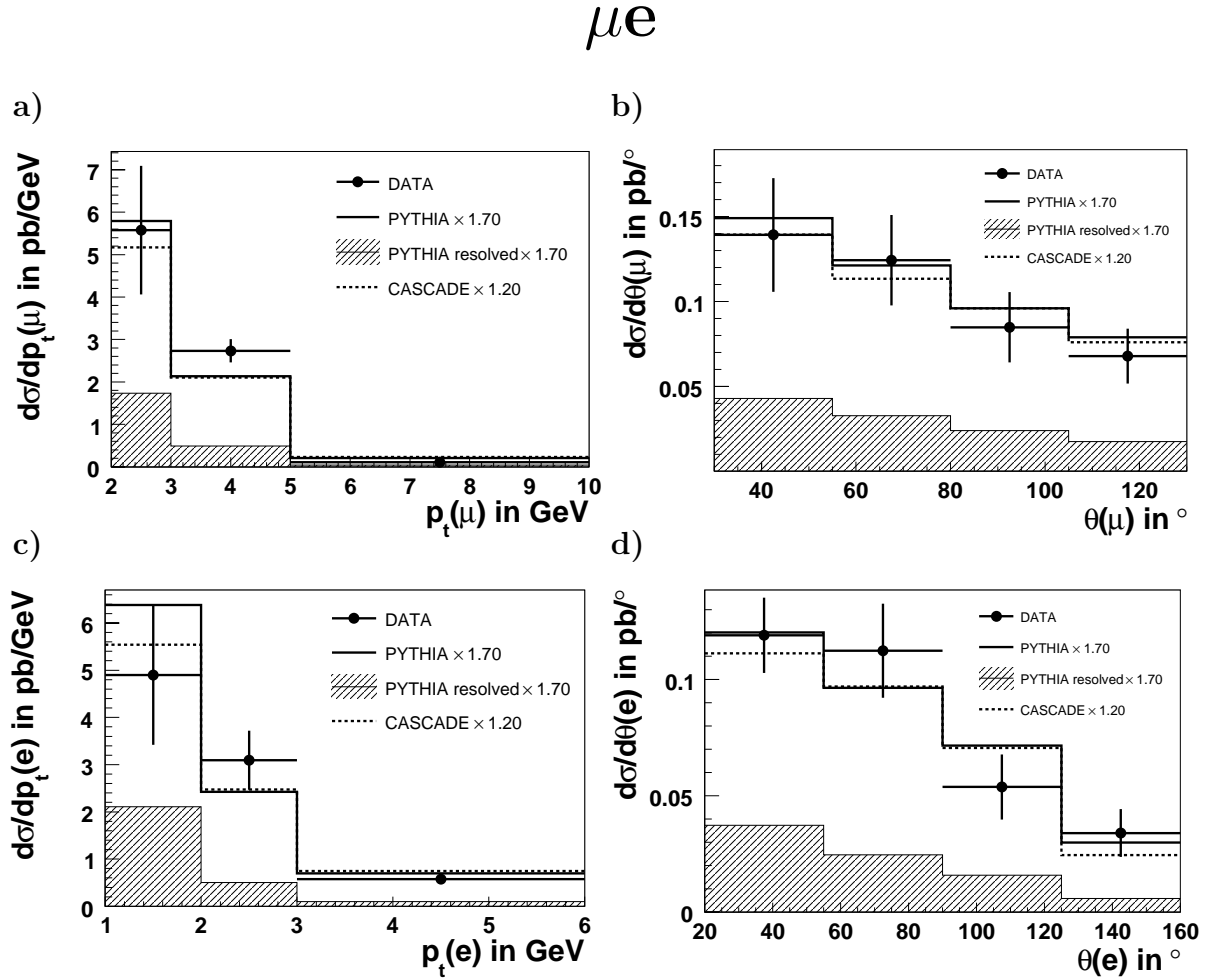


Figure 8.1: Differential beauty photoproduction cross sections in bins of the transverse momentum p_t and the polar angle θ of the **muon** (a and b) and the **electron** (c and d). Only the statistical errors are shown. The data is compared with the scaled predictions by the LO+PS event generators *PYTHIA* and *CASCADE*.

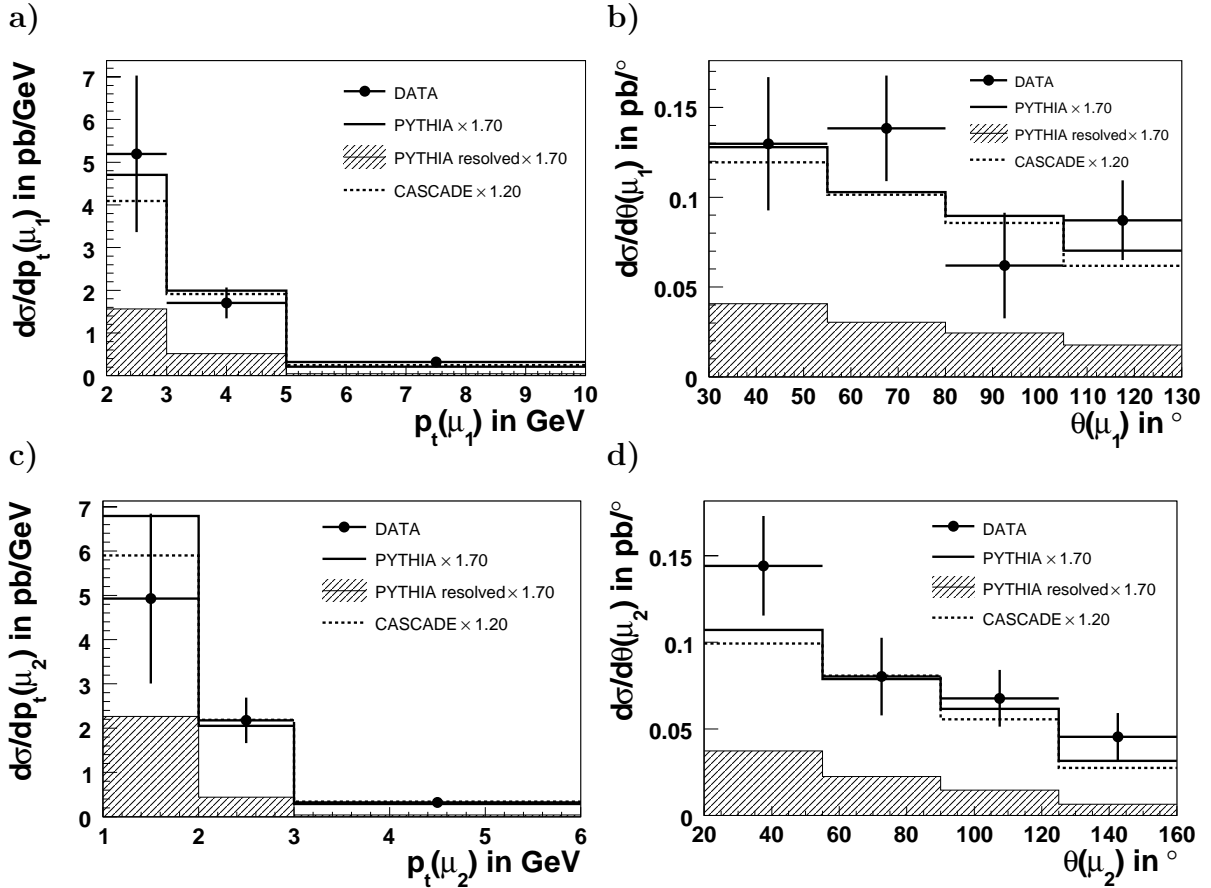
$\mu\mu$ 

Figure 8.2: Differential beauty photoproduction cross sections in bins of the transverse momentum p_t and the polar angle θ of the **first muon** (a and b) and the **second muon** (c and d). Only the statistical errors are shown. The data is compared with the scaled predictions by the LO+PS event generators *PYTHIA* and *CASCADE*.

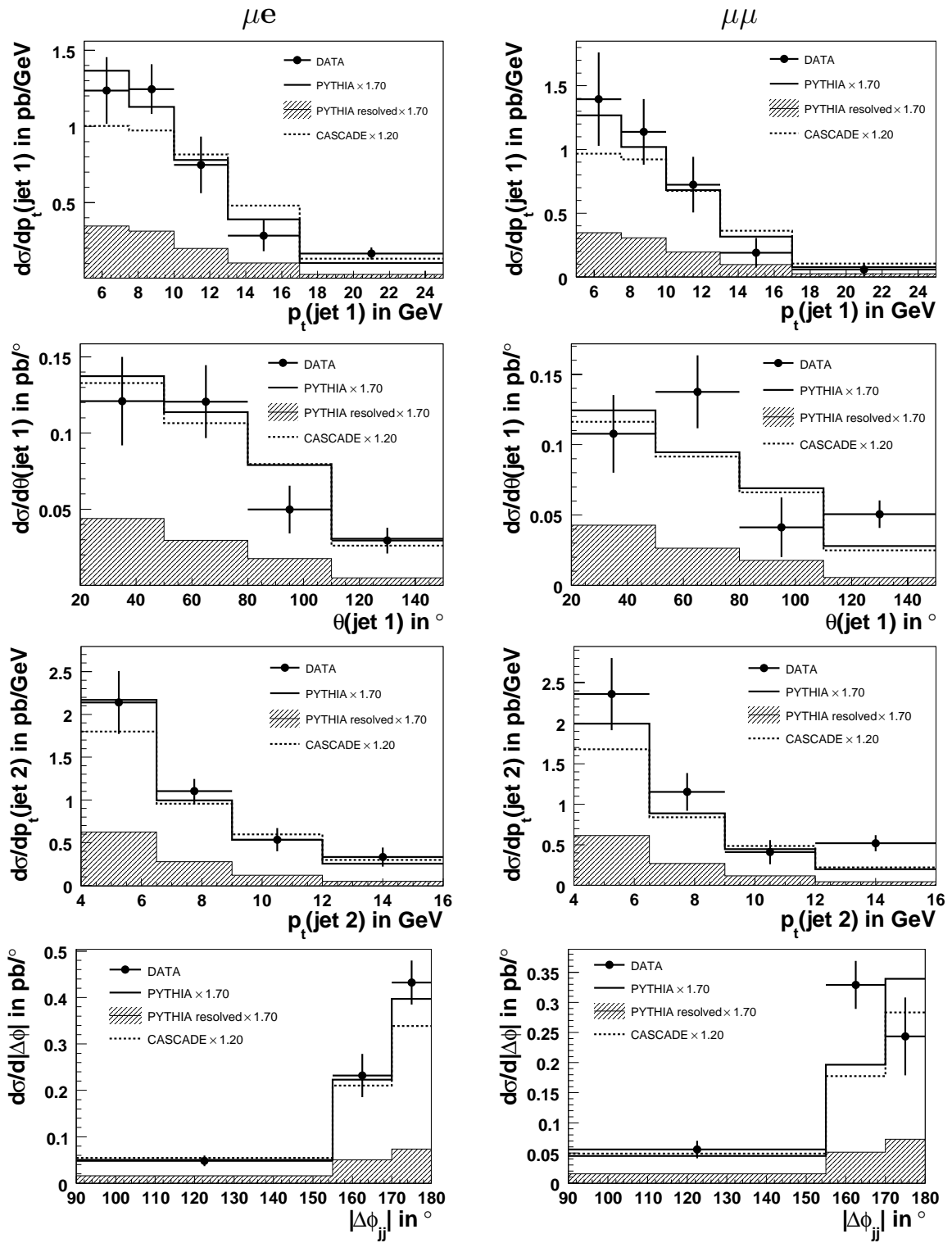


Figure 8.3: Differential cross sections for the production of lepton pairs from b quark decays in bins of the transverse momentum and polar angle of the first jet, the transverse momentum of the second jet and angle correlation of the two selected jets $|\Delta\phi_{jj}|$. The results obtained for the muon-electron (left) and the dimuon analysis (right) are shown.

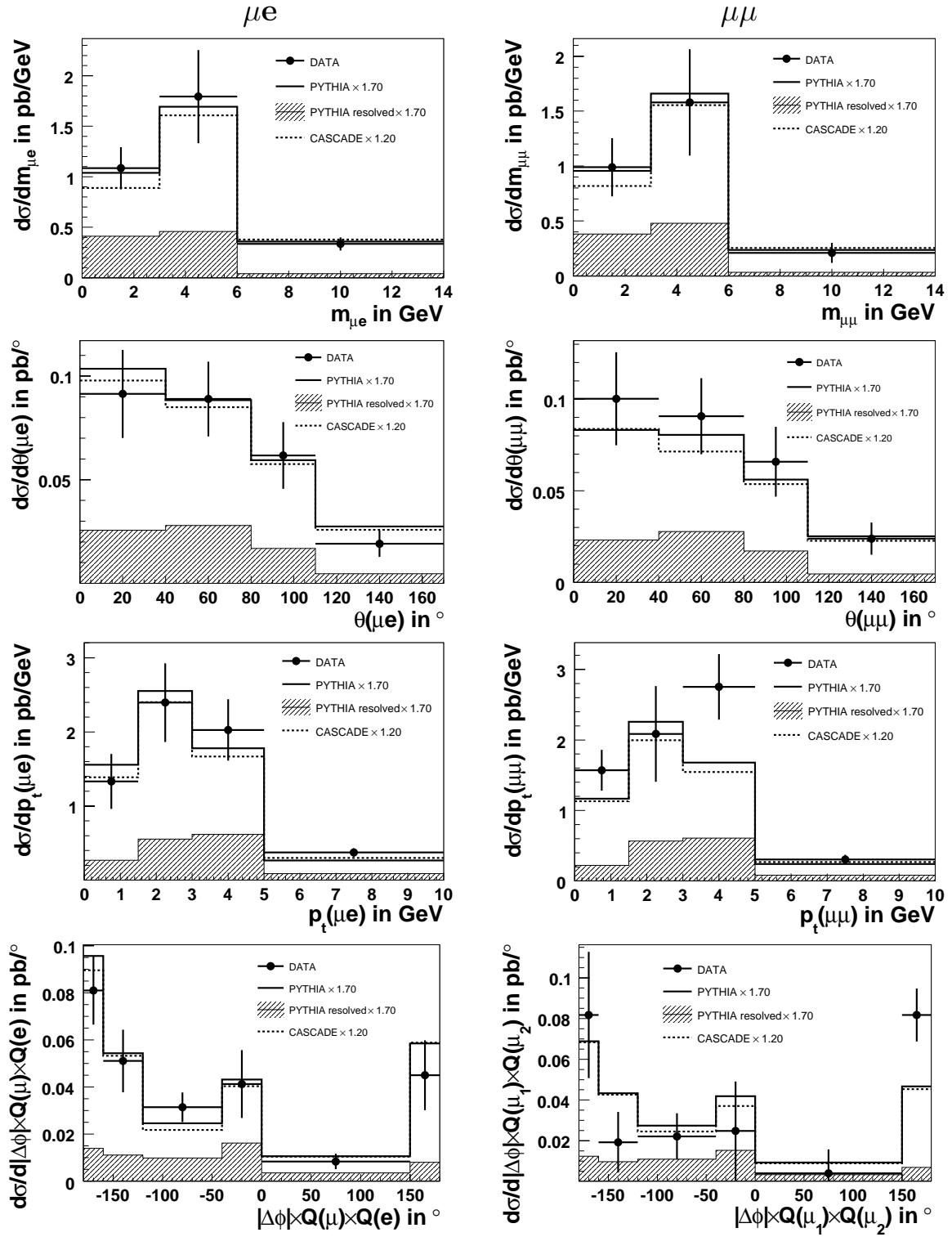


Figure 8.4: Differential cross sections for the production of lepton pairs from b quark decays in bins of the invariant mass $m_{\mu_1 l_2}$, the polar angle $\theta(\mu_1 l_2)$, the transverse momentum $p_t(\mu_1 l_2)$ and the charge and angle correlation $|\Delta\phi(\mu_1, l_2)| \times Q(\mu_1) \times Q(l_2)$ of the dilepton system ($l_2 = \mu_2, e$). On the left hand side the results for the muon-electron analysis are shown. On the right hand side the results obtained in the dimuon analysis are depicted.

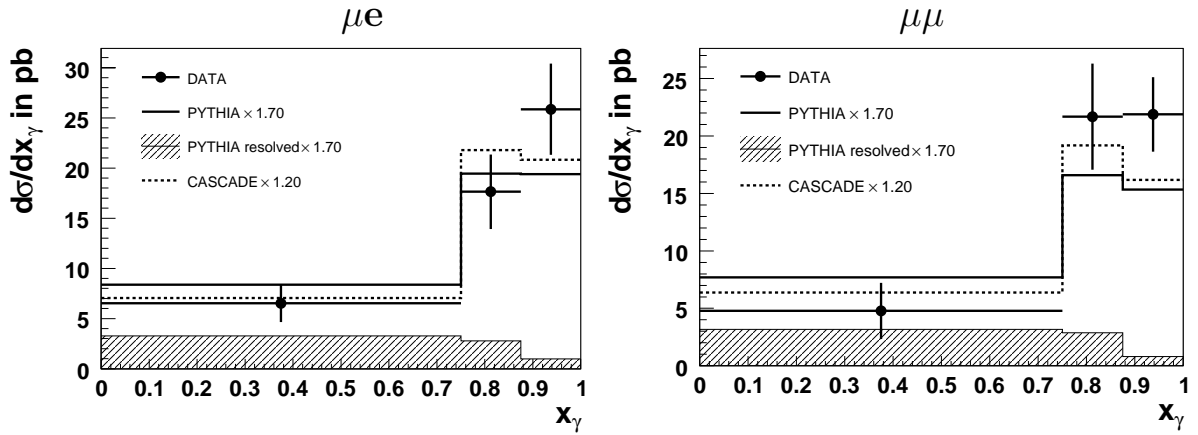


Figure 8.5: *Differential dilepton production cross sections in bins of x_γ^{obs} for both dilepton samples. Only the statistical errors are shown.*

8.3 Differential Cross Sections in x_γ^{obs}

The bin averaged differential cross sections as a function of the observable x_γ^{obs} (cf. equation 2.31) are shown in figure 8.5. For resolved processes, this observable is related to the momentum fraction of the photon participating in the hard interaction. In the leading order picture, x_γ^{obs} approaches unity for the direct process. For resolved processes x_γ^{obs} tends to be smaller. The distributions are reasonably well described in shape. The beauty fractions, the efficiencies and the bin averaged cross sections for each bin are listed in tables B.2 and B.5 in appendix B.

Both the PYTHIA and the CASCADE Monte Carlo event generators are able to describe the data. Furthermore, the results from the two different dilepton analyses agree with each other. The differences in the predicted cross sections for the two dilepton analyses are small compared to the errors of the measurement.

CHAPTER 9

SUMMARY, CONCLUSIONS AND OUTLOOK

Measurements of the charm and beauty cross sections for the photoproduction of two jets and two leptons in ep collisions at HERA are presented here. Data collected by the H1 detector in the years 1999 and 2000 (before the luminosity upgrade) and in the years 2004 and 2005 (HERA II) are considered. The collected data correspond to an integrated luminosity of 221.6 pb^{-1} . This is the first measurement of charm and beauty cross sections using HERA II data.

Two different data samples, a dimuon and a muon-electron sample, are investigated. Events with two or more jets of transverse momentum $p_t > 5(4) \text{ GeV}$ in the polar angular range $20^\circ < \theta < 160^\circ$ together with two leptons of transverse momentum $p_t > 2(1) \text{ GeV}$ in the polar angular ranges $30^\circ < \theta_1 < 130^\circ$ and $20^\circ < \theta_2 < 150^\circ$, respectively, are selected. The first lepton is a muon, the second either a muon or an electron. Cross sections are measured in photoproduction, i.e. at photon virtualities $Q^2 < 1 \text{ GeV}^2$, and for inelasticities $0.1 < y < 0.7$.

The relative transverse momentum p_t^{rel} of the leptons with respect to the jet they are associated to and the charge and azimuthal angle correlation of the leptons are exploited to determine the fractions of charm and beauty events in the data samples. While the charm fraction can only be determined using the charge and azimuthal angle correlation of the leptons, the beauty fraction can be extracted using either the observable p_t^{rel} or the dilepton correlation, thus providing two independent means to extract the beauty fraction. Consistent beauty fractions are obtained for both methods. Using both observables simultaneously, the statistical and the systematic errors are reduced. The following charm and beauty fractions for the muon-electron sample are obtained:

$$f(c, \mu e) = (13 \pm 3) \%$$

$$f(b, \mu e) = (29 \pm 4) \%$$

The fitted charm and beauty fractions for the dimuon sample are:

$$f(c, \mu\mu) = (5 \pm 1) \%$$

$$f(b, \mu\mu) = (17 \pm 2) \%$$

The fitted fractions are used to determine the visible charm and beauty cross sections for dilepton and dijet photoproduction:

$$\begin{aligned}\sigma(ep \rightarrow ec\bar{c}X \rightarrow ejj\mu eX') &= 4.6 \pm 1.0(stat.) \pm 0.5(sys.) \text{ pb} \\ \sigma(ep \rightarrow ec\bar{c}X \rightarrow ejj\mu\mu X') &= 2.7 \pm 0.9(stat.) \pm 0.3(sys.) \text{ pb} \\ \sigma(ep \rightarrow eb\bar{b}X \rightarrow ejj\mu eX') &= 9.4 \pm 1.2(stat.) \pm 0.9(sys.) \text{ pb} \\ \sigma(ep \rightarrow eb\bar{b}X \rightarrow ejj\mu\mu X') &= 10.4 \pm 1.5(stat.) \pm 1.0(sys.) \text{ pb}\end{aligned}$$

While the measured charm cross sections are within the errors in good agreement with the predictions from the PYTHIA LO+PS event generator, the beauty cross sections are somewhat higher. In order to compare the results obtained from the muon-electron and the dimuon samples to previous measurements at HERA, for all measurements the ratio between the measured cross sections and the PYTHIA predictions are calculated. The results of the present analysis are in good agreement with previous measurements.

Bin averaged differential jet and single lepton beauty cross sections as a function of the transverse momentum p_t and the polar angle θ are determined. In addition, the azimuthal angle correlation of the selected jets and the properties of the dilepton system are studied. The invariant mass $m(\mu l)$, the transverse momentum $p_t(\mu l)$, the polar angle $\theta(\mu l)$ and the charge and angle correlation $|\Delta\phi(\mu_1, l_2)| \times Q(\mu_1) \times Q(l_2)$ of the dilepton system are investigated. The dilepton charge and azimuthal angle correlation is studied using the observable p_t^{rel} alone to determine the beauty fraction. In order to study if the contributions from direct and resolved processes to the event sample are well modelled, differential cross sections as a function of the observable x_γ^{obs} are determined. The differential measurements are compared to the PYTHIA Monte Carlo prediction. The prediction is normalised to the measured visible cross sections. The shape of the distributions is well described by LO+PS QCD calculations. There are no indications for an excess in any isolated region of phase space.

The standard H1 electron finder, as implemented in the program package KALEP, is not used in the present analysis, since the probability for hadrons to be misidentified as electrons is too large for a meaningful dilepton analysis. Therefore, a new electron finder is developed, providing a misidentification probability which is about a factor of 4.5 smaller, while the electron reconstruction efficiencies are compatible. The decisive difference between the two electron finders is that a discriminating variable related to the lateral shower spread in the electromagnetic calorimeter is used in the new finder, which provides a good separation power.

Outlook

The statistical precision of the present measurement will be considerably improved by incorporating the data collected in the years 2006 and 2007. The data taken in the year 2006 correspond to an integrated luminosity of about 130 pb^{-1} , yielding a factor of about 1.6 more statistics. The statistical precision can be further improved by combining both dilepton samples.

Towards a publication, several improvements and extensions of the present analysis are planned. It will be studied if it is feasible to perform a binned likelihood fit to the three-dimensional

distribution of $p_t^{rel}(\mu_1)$, $p_t^{rel}(l_2)$ and $|\Delta\phi(\mu_1, l_2)| \times Q(\mu_1) \times Q(l_2)$, using the full HERA I and HERA II statistics. The possibility to perform an unbinned likelihood fit will be addressed as well. The aim is to reduce both the statistical and the systematic uncertainties.

The next important tasks are to study if the misidentification probability for hadrons is well described by the detector simulation and if the charm and the light flavour background are well modelled. These studies will help to reduce the systematic uncertainties of the charm cross section measurement. The improvement of the lepton identification algorithm as well as the effects of lowering the cut on the transverse momenta of the second lepton will also be studied. One possibility is to use dE/dx measurements, which would help to reject hadrons at low momenta. Using a larger data sample would allow the muon identification efficiency to be studied in more detail, thus reducing the corresponding systematic uncertainty.

It is promising to study if the description of the calorimeter response to muons gets better for a calorimeter simulated with finer granularity. Concerning the muon identification it can be studied if an approach based on the Fisher discriminant technique leads to a lower misidentification probability. The discriminating variables should also be revised. For the electron identification, it can be investigated if the definition of the lateral shower spread can be improved in such a way that the tails of the distribution become smaller.

The next important step is to compare the measurements to NLO calculations, which are performed in a massive scheme (FMNR), in a massless scheme (ZMVFNS) or in a matched approach (GMVFNS). A promising new development is the MC@NLO event generator, which matches parton showers to NLO matrix elements. MC@NLO will be available for ep collisions in the near future. The main advantage of this approach is that the output is in form of events which can be passed through a detailed detector simulation and event reconstruction. Comparisons between the measurements and NLO predictions can then be carried out much easier. In addition, more elaborate hadronisation models compared to the approach of independent fragmentation can be easily used.

APPENDIX A

MONTE CARLO DATA SETS

Flavour	Generator	Year	\mathcal{L} [pb^{-1}]	PDF p/γ	$m_{c/b}$ [GeV]	Fragmentation	Main Cuts
b	PYTHIA 6.1	99/00	1078.2	CTEQ 5L LO GRV-G LO	1.5/4.75	Lund-Bowler	$\hat{p}_t > 4 \text{ GeV}$, $p_t(\mu) > 1.9 \text{ GeV}$, $20^\circ < \theta(\mu) < 150^\circ$
b	PYTHIA 6.1	99/00	2293.5	CTEQ 5L LO GRV-G LO	1.5/4.75	Peterson $\epsilon_b = 0.0069$ $\epsilon_c = 0.058$	$\hat{p}_t > 4 \text{ GeV}$, $p_t(\mu) > 1.9 \text{ GeV}$, $20^\circ < \theta(\mu) < 150^\circ$
b	PYTHIA 6.2	04/05	1342.9	CTEQ6L1 SAS 1D	1.5/4.75	Lund-Bowler	$\hat{p}_t > 4 \text{ GeV}$, $p_t(\mu) > 1.9 \text{ GeV}$, $20^\circ < \theta(\mu) < 150^\circ$
b	CASCADE 1.0	99/00	1129.0	JS2001	1.5/4.75	Peterson	$p_t(\mu) > 1.9 \text{ GeV}$, $20^\circ < \theta(\mu) < 150^\circ$
c	PYTHIA 6.1	99/00	753.6	CTEQ 5L LO GRV-G LO	1.5/4.75	Lund-Bowler	$\hat{p}_t > 4 \text{ GeV}$, $p_t(\mu) > 1.9 \text{ GeV}$, $20^\circ < \theta(\mu) < 150^\circ$
c	PYTHIA 6.1	99/00	2163.8	CTEQ 5L LO GRV-G LO	1.5/4.75	Peterson	$\hat{p}_t > 4 \text{ GeV}$, $p_t(\mu) > 1.9 \text{ GeV}$, $20^\circ < \theta(\mu) < 150^\circ$
c	PYTHIA 6.2	04/05	1684.5	CTEQ6L1 SAS 1D	1.5/4.75	Lund-Bowler	$\hat{p}_t > 4 \text{ GeV}$, $p_t(\mu) > 1.9 \text{ GeV}$, $20^\circ < \theta(\mu) < 150^\circ$
c	CASCADE 1.0	99/00	924.9	JS2001	1.5/4.75	Peterson	$p_t(\mu) > 1.9 \text{ GeV}$, $20^\circ < \theta(\mu) < 150^\circ$
$udscb$	PYTHIA 6.1	99/00	239.5	CTEQ 5L LO GRV-G LO	1.5/4.75	Peterson	$\hat{p}_t > 4 \text{ GeV}$, at least one track with: $p_t > 1.9 \text{ GeV}$, $20^\circ < \theta < 150^\circ$
$udscb$	PYTHIA 6.2	04/05	84.21	CTEQ6L1 SAS 1D	1.5/4.75	Lund-Bowler	$\hat{p}_t > 4 \text{ GeV}$, at least one track with: $p_t > 1.9 \text{ GeV}$, $20^\circ < \theta < 150^\circ$

Table A.1: Monte Carlo data sets used in the present analysis. The main parameters and selection cuts are given.

APPENDIX B

MEASURED DIFFERENTIAL CROSS SECTIONS

B.1 Muon-Electron Events

Quantity	Range	f_b in %	ϵ_{rec} in %	ϵ_{trig} in %	$d\sigma$ in pb
$p_t(\mu)$	2.00 - 3.00 GeV	27.51 ± 7.33	18.95	73.55 ± 1.93	5.57 ± 1.51
	3.00 - 5.00 GeV	45.14 ± 3.73	26.46	74.47 ± 2.13	2.73 ± 0.27
$\theta(\mu)$	30.00 - 55.00°	34.26 ± 7.80	20.04	66.63 ± 2.66	0.14 ± 0.03
	55.00 - 80.00°	32.40 ± 6.60	25.13	75.01 ± 2.50	0.12 ± 0.03
	80.00 - 105.00°	27.46 ± 6.44	25.57	82.13 ± 2.21	0.08 ± 0.02
	105.00 - 130.00°	30.93 ± 6.90	25.90	74.49 ± 2.98	0.07 ± 0.02
$p_t(e)$	1.00 - 2.00 GeV	18.36 ± 5.48	18.43	74.48 ± 1.98	4.90 ± 1.48
	2.00 - 3.00 GeV	53.69 ± 9.90	26.77	72.21 ± 2.98	3.09 ± 0.62
	3.00 - 6.00 GeV	45.78 ± 6.23	33.69	76.35 ± 2.57	0.58 ± 0.09
$\theta(e)$	20.00 - 55.00°	35.80 ± 4.28	19.92	77.43 ± 2.32	0.12 ± 0.02
	55.00 - 90.00°	37.81 ± 6.33	25.39	71.45 ± 2.58	0.11 ± 0.02
	90.00 - 125.00°	23.26 ± 5.81	26.47	73.52 ± 2.77	0.05 ± 0.01
	125.00 - 160.00°	39.93 ± 11.34	26.21	75.19 ± 3.00	0.03 ± 0.01

Table B.1: Measured differential beauty photoproduction cross sections, beauty fractions and efficiencies for the **muon-electron** sample. The differential cross sections in bins of the transverse momentum p_t and the polar angle θ of the muon and the electron are quoted.

Quantity	Range	f_b in %	ϵ_{rec} in %	ϵ_{trig} in %	$d\sigma$ in pb
x_γ^{obs}	0.00 - 0.75	26.19 ± 7.36	12.92	76.94 ± 2.37	6.53 ± 1.88
	0.75 - 0.88	36.78 ± 7.28	31.17	76.59 ± 2.61	17.63 ± 3.71
	0.88 - 1.00	40.15 ± 6.71	44.03	72.04 ± 1.96	25.86 ± 4.54

Table B.2: Measured differential cross sections, beauty fractions and efficiencies as a function of x_γ^{obs} for the **muon-electron** sample.

Quantity	Range	f_b in %	ϵ_{rec} in %	ϵ_{trig} in %	$d\sigma$ in pb
$m_{\mu e}$	0.00 - 3.00 GeV	30.94 ± 5.10	25.93	75.94 ± 2.15	1.12 ± 0.20
	3.00 - 6.00 GeV	22.00 ± 6.67	16.95	72.29 ± 2.47	1.48 ± 0.46
	6.00 - 14.00 GeV	54.45 ± 9.15	32.65	74.81 ± 2.34	0.34 ± 0.06
$\theta_{\mu e}$	0.00 - 40.00°	35.16 ± 7.76	21.35	68.43 ± 2.71	0.09 ± 0.02
	40.00 - 80.00°	31.45 ± 6.08	23.36	77.63 ± 2.24	0.09 ± 0.02
	80.00 - 110.00°	29.49 ± 7.33	24.38	79.18 ± 2.84	0.06 ± 0.02
	110.00 - 170.00°	23.45 ± 7.49	29.24	72.95 ± 2.76	0.02 ± 0.01
$p_t(\mu e)$	0.00 - 1.50 GeV	25.55 ± 6.76	22.83	67.83 ± 3.25	1.33 ± 0.37
	1.50 - 3.00 GeV	33.59 ± 7.08	20.94	75.69 ± 2.71	2.40 ± 0.53
	3.00 - 5.00 GeV	35.97 ± 6.98	22.02	74.92 ± 2.40	2.03 ± 0.41
	5.00 - 10.00 GeV	50.56 ± 6.33	36.22	77.56 ± 2.43	0.37 ± 0.06
$ \Delta\phi $ $\times Q(\mu)$ $\times Q(e)$	-180.00 - -160.00°	26.99 ± 4.33	27.35	73.75 ± 3.00	0.08 ± 0.01
	-160.00 - -120.00°	30.62 ± 7.52	22.95	71.46 ± 3.21	0.05 ± 0.01
	-120.00 - -40.00°	67.85 ± 9.54	12.28	77.88 ± 5.19	0.03 ± 0.01
	-40.00 - 0.00°	34.80 ± 11.87	36.26	74.54 ± 2.77	0.04 ± 0.01
	0.00 - 150.00°	15.49 ± 5.91	17.05	76.14 ± 2.94	0.01 ± 0.00
	150.00 - 180.00°	31.93 ± 10.09	26.92	74.43 ± 3.29	0.05 ± 0.01
$p_t(\text{jet } 1)$	5.00 - 7.50 GeV	31.03 ± 4.93	21.39	77.48 ± 3.76	1.24 ± 0.22
	7.50 - 10.00 GeV	38.31 ± 4.23	27.68	76.08 ± 3.05	1.24 ± 0.16
	10.00 - 13.00 GeV	32.45 ± 7.66	25.63	72.57 ± 2.75	0.75 ± 0.19
	13.00 - 17.00 GeV	23.09 ± 7.99	21.63	70.28 ± 2.87	0.28 ± 0.10
	17.00 - 25.00 GeV	52.88 ± 10.42	19.43	76.37 ± 3.03	0.17 ± 0.04
$\theta(\text{jet } 1)$	20.00 - 50.00°	35.31 ± 8.10	21.16	71.77 ± 2.55	0.12 ± 0.03
	50.00 - 80.00°	33.87 ± 6.36	23.66	76.49 ± 2.48	0.12 ± 0.02
	80.00 - 110.00°	20.08 ± 6.16	26.06	78.07 ± 2.54	0.05 ± 0.02
	110.00 - 150.00°	27.50 ± 7.50	27.46	71.00 ± 3.03	0.03 ± 0.01
$p_t(\text{jet } 2)$	4.00 - 6.50 GeV	17.99 ± 3.31	25.77	76.20 ± 1.85	2.36 ± 0.45
	6.50 - 9.00 GeV	18.78 ± 3.67	32.04	77.60 ± 2.07	1.15 ± 0.23
	9.00 - 12.00 GeV	14.71 ± 5.25	28.56	82.20 ± 1.99	0.41 ± 0.15
	12.00 - 16.00 GeV	40.38 ± 6.29	17.12	77.74 ± 2.69	0.52 ± 0.10
$\theta(\text{jet } 2)$	20.00 - 50.00°	38.03 ± 6.53	19.76	72.55 ± 2.44	0.15 ± 0.03
	50.00 - 80.00°	38.65 ± 6.89	25.90	74.20 ± 2.57	0.11 ± 0.02
	80.00 - 110.00°	24.36 ± 6.68	24.64	76.00 ± 2.64	0.06 ± 0.02
	110.00 - 150.00°	29.52 ± 9.38	26.70	75.79 ± 2.94	0.04 ± 0.01
$ \Delta\phi $ jets	90.00 - 155.00°	29.71 ± 6.76	20.20	77.22 ± 2.34	0.05 ± 0.01
	155.00 - 170.00°	34.59 ± 6.53	25.31	72.49 ± 2.62	0.23 ± 0.05
	170.00 - 180.00°	38.98 ± 3.62	26.75	73.35 ± 2.16	0.43 ± 0.05

Table B.3: Measured differential cross sections, beauty fractions and efficiencies for the muon-electron sample. Dilepton and jet cross sections are shown.

B.2 Dimuon Events

Quantity	Range	f_b in %	ϵ_{rec} in %	ϵ_{trig} in %	$d\sigma$ in pb
$p_t(\mu_1)$	2.00 - 3.00 GeV	10.85 ± 3.79	16.13	75.12 ± 1.72	5.20 ± 1.83
	3.00 - 5.00 GeV	16.39 ± 3.41	32.91	81.99 ± 1.45	1.71 ± 0.36
	5.00 - 10.00 GeV	35.00 ± 6.02	46.98	79.83 ± 2.23	0.32 ± 0.06
$\theta(\mu_1)$	30.00 - 55.00°	16.59 ± 4.66	22.28	75.94 ± 2.06	0.13 ± 0.04
	55.00 - 80.00°	19.78 ± 4.09	26.55	81.94 ± 1.76	0.14 ± 0.03
	80.00 - 105.00°	9.46 ± 4.46	26.53	85.45 ± 1.63	0.06 ± 0.03
	105.00 - 130.00°	18.85 ± 4.63	25.24	72.49 ± 2.57	0.09 ± 0.02
$p_t(\mu_2)$	1.00 - 2.00 GeV	8.76 ± 3.40	18.67	78.15 ± 1.27	4.93 ± 1.92
	2.00 - 3.00 GeV	19.42 ± 4.50	43.41	81.31 ± 1.78	2.17 ± 0.51
	3.00 - 6.00 GeV	34.01 ± 7.23	47.28	80.87 ± 2.95	0.32 ± 0.07
$\theta(\mu_2)$	20.00 - 55.00°	25.15 ± 4.86	23.83	77.78 ± 1.86	0.14 ± 0.03
	55.00 - 90.00°	12.71 ± 3.51	29.48	81.66 ± 1.51	0.08 ± 0.02
	90.00 - 125.00°	17.09 ± 4.02	29.54	79.09 ± 1.93	0.07 ± 0.02
	125.00 - 160.00°	25.49 ± 7.19	21.58	73.25 ± 3.93	0.05 ± 0.01

Table B.4: Measured differential beauty photoproduction cross sections, beauty fractions and efficiencies for the **dimuon** sample. The differential cross sections in bins of the transverse momentum p_t and the polar angle θ of the first and the second muon are quoted.

Quantity	Range	f_b in %	ϵ_{rec} in %	ϵ_{trig} in %	$d\sigma$ in pb
x_γ^{obs}	0.00 - 0.75	9.43 ± 4.81	14.49	78.64 ± 1.85	4.78 ± 2.45
	0.75 - 0.88	21.38 ± 4.43	34.85	81.19 ± 1.92	21.68 ± 4.62
	0.88 - 1.00	21.58 ± 3.08	53.19	79.23 ± 1.40	21.87 ± 3.24

Table B.5: Measured differential cross sections, beauty fractions and efficiencies as a function of x_γ^{obs} for the dimuon sample.

Quantity	Range	f_b in %	ϵ_{rec} in %	ϵ_{trig} in %	$d\sigma$ in pb
$m_{\mu\mu}$	0.00 - 3.00 GeV	10.98 ± 2.83	28.83	80.89 ± 1.31	0.97 ± 0.25
	3.00 - 6.00 GeV	16.69 ± 5.01	17.74	76.46 ± 1.87	1.92 ± 0.58
	6.00 - 14.00 GeV	23.90 ± 10.65	44.61	80.28 ± 2.30	0.19 ± 0.09
$\theta_{\mu\mu}$	0.00 - 40.00°	24.28 ± 6.00	25.78	71.58 ± 2.33	0.10 ± 0.03
	40.00 - 80.00°	15.41 ± 3.46	25.41	83.90 ± 1.42	0.09 ± 0.02
	80.00 - 110.00°	14.30 ± 4.06	26.28	83.24 ± 1.82	0.07 ± 0.02
	110.00 - 170.00°	14.61 ± 5.25	29.41	72.50 ± 2.71	0.02 ± 0.01
$p_t(\mu\mu)$	0.00 - 1.50 GeV	20.30 ± 3.49	29.00	73.15 ± 2.96	1.57 ± 0.29
	1.50 - 3.00 GeV	18.60 ± 5.97	22.91	78.57 ± 2.21	2.09 ± 0.68
	3.00 - 5.00 GeV	20.66 ± 3.36	22.34	78.79 ± 1.66	2.75 ± 0.47
	5.00 - 10.00 GeV	18.65 ± 3.93	42.81	83.00 ± 1.70	0.31 ± 0.07
$ \Delta\phi $ $\times Q(\mu_1)$ $\times Q(\mu_2)$	-180.00 - -160.00°	20.67 ± 7.71	35.08	74.08 ± 3.09	0.08 ± 0.03
	-160.00 - -120.00°	9.45 ± 7.26	26.23	77.77 ± 2.92	0.02 ± 0.01
	-120.00 - -40.00°	27.73 ± 13.86	12.11	75.94 ± 3.73	0.02 ± 0.01
	-40.00 - 0.00°	7.63 ± 7.45	39.42	79.69 ± 1.70	0.02 ± 0.02
	0.00 - 150.00°	3.14 ± 9.15	17.61	83.54 ± 1.79	0.00 ± 0.01
	150.00 - 180.00°	32.00 ± 4.61	33.64	78.77 ± 2.80	0.08 ± 0.01
$p_t(\text{jet } 1)$	5.00 - 7.50 GeV	19.89 ± 5.03	23.14	76.46 ± 2.90	1.70 ± 0.44
	7.50 - 10.00 GeV	18.97 ± 3.85	31.46	77.24 ± 2.42	1.23 ± 0.26
	10.00 - 13.00 GeV	13.32 ± 4.21	27.00	76.68 ± 2.11	0.65 ± 0.21
	13.00 - 17.00 GeV	9.36 ± 5.79	25.19	79.93 ± 2.06	0.19 ± 0.12
	17.00 - 25.00 GeV	20.67 ± 21.50	24.83	83.50 ± 2.10	0.08 ± 0.09
$\theta(\text{jet } 1)$	20.00 - 50.00°	16.29 ± 4.10	24.83	77.99 ± 1.80	0.11 ± 0.03
	50.00 - 80.00°	20.50 ± 3.74	25.92	82.06 ± 1.68	0.14 ± 0.03
	80.00 - 110.00°	7.97 ± 4.07	27.56	81.30 ± 1.87	0.04 ± 0.02
	110.00 - 150.00°	27.44 ± 4.84	30.95	71.65 ± 3.00	0.05 ± 0.01
$p_t(\text{jet } 2)$	4.00 - 6.50 GeV	17.99 ± 3.31	25.77	76.20 ± 1.85	2.36 ± 0.45
	6.50 - 9.00 GeV	18.78 ± 3.67	32.04	77.60 ± 2.07	1.15 ± 0.23
	9.00 - 12.00 GeV	14.71 ± 5.25	28.56	82.20 ± 1.99	0.41 ± 0.15
	12.00 - 16.00 GeV	40.38 ± 6.29	17.12	77.74 ± 2.69	0.52 ± 0.10
	16.00 - 25.00 GeV	12.08 ± 10.01	15.87	91.24 ± 2.21	0.03 ± 0.03
$\theta(\text{jet } 2)$	20.00 - 50.00°	24.37 ± 4.54	23.28	78.29 ± 1.77	0.17 ± 0.03
	50.00 - 80.00°	19.30 ± 4.05	27.30	82.73 ± 1.71	0.11 ± 0.02
	80.00 - 110.00°	9.45 ± 4.48	27.74	79.31 ± 2.03	0.05 ± 0.02
	110.00 - 150.00°	10.97 ± 4.13	29.34	74.88 ± 2.59	0.03 ± 0.01
$ \Delta\phi $ jets	90.00 - 155.00°	17.27 ± 4.39	21.97	81.70 ± 1.65	0.06 ± 0.01
	155.00 - 170.00°	25.15 ± 2.78	28.28	74.88 ± 1.97	0.33 ± 0.04
	170.00 - 180.00°	12.48 ± 3.27	30.72	80.47 ± 1.68	0.24 ± 0.06

Table B.6: Measured differential cross sections, beauty fractions and efficiencies for the dimuon sample. Dilepton and jet cross sections are shown.

List of Tables

1.1	The fundamental fermions of the Standard Model.	2
2.1	Summary of the event selection cuts (generator level).	16
2.2	Possible dilepton charge and angle correlations in open charm and beauty production.	18
4.1	The reconstruction efficiencies and the misidentification probabilities for the electron for different cut scenarios.	47
4.2	$J/\psi \rightarrow e^+e^-$ selection cuts.	49
4.3	Standard selection cuts for iron muons.	56
4.4	J/ψ selection cuts.	57
5.1	Integrated luminosities for the different data taking periods.	67
5.2	Track selection	68
5.3	Jet selection	69
5.4	Selection of the iron muon.	69
5.5	Selection of the additional muon	70
5.6	Electron selection cuts.	70
5.7	Comparison of different cut scenarios for the electron.	71
5.8	Definition of the subtrigger S19.	72
5.9	Trigger efficiencies.	78
5.10	DIS contribution to the photoproduction sample.	83
5.11	Summary of all event selection cuts.	85
5.12	Event yields.	86
6.1	Contributions to the muon-electron and dimuon samples according to the Monte Carlo simulation.	98
6.2	Compilation of the fit results (μe).	104
6.3	Compilation of the fit results ($\mu\mu$).	107
6.4	Summary of the final fit results.	108

7.1	Systematic uncertainties.	116
7.2	Number of selected events and beauty fraction.	117
7.3	Reconstruction efficiencies for beauty events.	117
7.4	Reconstruction efficiencies for charm events.	117
7.5	Efficiency of the subtrigger S19.	118
7.6	Visible charm and beauty cross sections.	119
A.1	Monte Carlo data sets used in the present analysis.	135
B.1	Single lepton differential cross sections (μe).	136
B.2	Differential cross sections as a function of x_γ^{obs} (μe).	137
B.3	Differential cross sections (μe): Dilepton system and jets.	138
B.4	Single lepton differential cross sections ($\mu\mu$).	139
B.5	Differential cross sections as a function of x_γ^{obs} ($\mu\mu$).	139
B.6	Differential cross sections ($\mu\mu$): dilepton system and jets.	140

List of Figures

2.1	Electron proton scattering (neutral and charged current).	3
2.2	The QCDC and BGF processes in leading order.	6
2.3	General gluon ladder.	7
2.4	The proton structure function F_2 .	8
2.5	Principle of factorisation in QCD.	9
2.6	Boson-gluon fusion.	10
2.7	The Lund string fragmentation model.	11
2.8	Peterson fragmentation functions for charm and beauty.	12
2.9	Principle layout of an event generator.	13
2.10	The decay $B^+ \rightarrow \bar{D}^0 \mu^+ \nu_\mu$ in the spectator model.	16
2.11	Production of a unlike sign muon pair in PGF.	17
2.12	Cascade decay of a beauty quark.	17
2.13	Feynman diagrams for $B^0 - \bar{B}^0$ mixing.	18
2.14	Charge and angle correlation (generator level).	19
2.15	Invariant mass of the dilepton system.	19
2.16	p_t^{rel} definition.	20
2.17	p_t^{rel} distributions for the muon and the electron on generator level.	20
2.18	x_γ^{obs} for charm and beauty events.	21
2.19	Contributions from subprocesses to the muon-electron sample (PYTHIA Monte Carlo).	21
2.20	Charge and angle correlation of leptons from direct processes (beauty).	22
2.21	Charmonium decay.	22
2.22	Photon-photon fusion and Drell-Yan processes.	23
3.1	The electron proton storage ring HERA.	25
3.2	The H1 detector.	26
3.3	The central tracking system.	27
3.4	Principle of operation of the Fast Track Trigger (FTT).	28
3.5	Principle of the z-Vertex Trigger.	29

3.6	Track segment reconstruction in the CIP 2000.	30
3.7	The liquid argon calorimeter (rz -view).	31
3.8	The calorimeter wheel CB2 ($r - \phi$ -view).	32
3.9	The four parts of the central muon detector.	32
3.10	Cross section view of an instrumented iron module.	33
3.11	Summary of beauty measurements at HERA.	37
4.1	E/p for electrons and hadrons (beauty Monte Carlo).	43
4.2	Energy in the hadronic part of the liquid argon calorimeter (beauty Monte Carlo).	43
4.3	Longitudinal shower spread (beauty Monte Carlo).	43
4.4	Lateral shower spread (beauty Monte Carlo).	43
4.5	Distribution of the Fisher test variable.	46
4.6	Efficiency and fake suppression depending on the Fisher test variable.	46
4.7	Electron reconstruction efficiency as a function of p_t	48
4.8	Misidentification probability as a function of p_t	48
4.9	Elastic J/ψ	50
4.10	Transverse momentum and polar angle distributions of the decay electrons.	50
4.11	Description of the electron estimators in events with elastically produced J/ψ mesons.	52
4.12	Electron efficiency as a function of the polar angle.	53
4.13	Electron efficiency as a function of the transverse momentum.	54
4.14	Elastic J/ψ	58
4.15	Muon-efficiency in the instrumented iron as a function of the polar angle.	60
4.16	Muon-efficiency in the instrumented iron as a function of the transverse momentum.	61
4.17	Description of the KALEP estimators for the muon identification.	62
4.18	Muon efficiency in the calorimeter as a function of the polar angle.	63
4.19	Muon efficiency in the calorimeter as a function of the transverse momentum.	64
4.20	Ratio between the calorimeter efficiency in data and in the corrected MC simulation.	65
5.1	Event yields (subtrigger S19).	73
5.2	The efficiencies of the trigger elements used in the definition of subtrigger S19	75
5.3	Efficiency of the muon trigger.	76
5.4	Efficiency of the central muon trigger as a function of p_t , θ and ϕ	77
5.5	Corrections applied to the Monte Carlo simulation for a better description of the muon trigger.	78
5.6	Invariant mass of unlike sign muon pairs (no isolation cut).	81
5.7	Invariant mass of unlike sign muon pairs (isolation cut applied).	81
5.8	Isolation.	81
5.9	Photon conversion.	82

5.10	The inelasticity for y_h according to the Monte Carlo simulation (HERA II). . . .	83
5.11	The generated Q^2 for muon-electron events according to the Monte Carlo simulation.	83
5.12	y_h and x_γ distributions for the muon-electron sample	86
5.13	Description of the iron muon (muon-electron sample).	87
5.14	Description of the electron (muon-electron sample).	88
5.15	Description of the leading jet (muon-electron sample) I.	90
5.16	Description of the leading jet (muon-electron sample) II.	91
5.17	Description of the second jet (muon-electron sample) I.	92
5.18	Description of the second jet (muon-electron sample) II.	93
5.19	Lepton correlations (muon-electron sample)	94
5.20	The distance ΔR of the leptons to the selected jets.	95
5.21	Description of the second muon (dimuon sample).	96
6.1	Fake contribution in muon-electron events.	99
6.2	The p_t^{rel} distributions for the muon and the electron.	100
6.3	The p_t^{rel} distributions of the muons in the dimuon sample.	101
6.4	$ \Delta\phi \times Q(\mu) \times Q(e)$ distributions for charm, beauty and light flavour events. . . .	101
6.5	Simultaneous fit to both p_t^{rel} distributions (μe).	103
6.6	Fit to both p_t^{rel} distributions separately.	104
6.7	Two-dimensional fit (muon-electron sample).	105
6.8	Fit to the $ \Delta\phi \times Q(\mu) \times Q(e)$ distribution (μe sample).	106
6.9	Simultaneous fit to the $ \Delta\phi \times Q(\mu) \times Q(e)$ and the two p_t^{rel} distributions (μe). .	109
6.10	Fit to both p_t^{rel} distributions separately.	110
6.11	Simultaneous fit to the $ \Delta\phi \times Q(\mu_1) \times Q(\mu_2)$ and the two p_t^{rel} distributions (μe). .	111
7.1	Definition of the reconstruction efficiency.	113
7.2	The visible cross sections for charm photoproduction obtained in the present analysis in comparison to recent results from H1 and ZEUS.	120
7.3	The visible cross sections for beauty photoproduction obtained in the present analysis in comparison to recent results from H1 and ZEUS.	121
8.1	Differential cross sections: Single leptons(μe).	126
8.2	Differential cross sections: Single leptons($\mu\mu$).	127
8.3	Differential cross sections: selected jets.	128
8.4	Differential cross sections: dilepton system.	129
8.5	Differential cross sections: x_γ^{obs}	130

References

- [1] F. Halzen and A. D. Martin, *Quarks and Leptons: An Introductory Course in Modern Particle Physics*. New York, USA: Wiley (1984) 396p.
- [2] V. N. Gribov and L. N. Lipatov, “Deep inelastic ep scattering in perturbation theory”, *Sov. J. Nucl. Phys.* **15** (1972) 438–450.
- [3] L. Lipatov, “The parton model and perturbation theory.”, *Sov. J. Nucl. Phys.* **20** (1975) 94.
- [4] G. Altarelli and G. Parisi, “Asymptotic freedom in parton language.”, *Nucl. Phys.* **B 126** (1977) 298.
- [5] Y. Dokshitzer, “Calculation of the structure functions for deep inelastic scattering and e^+e^- annihilation by perturbation theory in quantum chromodynamics.”, *Sov. Phys. JETP* **46** (1977) 641.
- [6] M. Ciafaloni, “Coherence effects in initial jets at small Q^2/s ”, *Nucl. Phys.* **B 296** (1988) 49.
- [7] S. Catani, F. Fiorani and G. Marchesini, “QCD coherence in initial state radiation”, *Phys. Lett.* **B 234** (1990) 339.
- [8] S. Catani, F. Fiorani and G. Marchesini, “Small x behaviour of initial state radiation in perturbative QCD”, *Nucl. Phys.* **B 336** (1990) 18.
- [9] G. Marchesini, “QCD coherence in the structure function and associated distributions at small x ”, *Nucl. Phys.* **B 445** (1995) 49.
- [10] E. Kuraev, L. Lipatov and V. Fadin, “Multi - reggeon processes in the yang-mills theory”, *Sov. Phys. JETP* **44** (1976) 443.
- [11] E. Kuraev, L. Lipatov and V. Fadin, “The pomeranchuk singularity in nonabelian gauge theories.”, *Sov. Phys. JETP* **45** (1977) 199.
- [12] Y. Balitsky and L. Lipatov, “The pomeranchuk singularity in quantum chromodynamics.”, *Sov. J. Nucl. Phys.* **28** (1978) 822.
- [13] **CTEQ** Collaboration, R. Brock *et al.*, “Handbook of perturbative QCD: Version 1.0”, *Rev. Mod. Phys.* **67** (1995) 157–248.

- [14] L. M. Jones and H. W. Wyld, “Charmed particle production by photon gluon fusion”, *Phys. Rev.* **D17** (1978) 759.
- [15] B. Andersson, G. Gustafson, G. Ingelman and T. Sjostrand, “Parton fragmentation and string dynamics”, *Phys. Rept.* **97** (1983) 31.
- [16] C. Peterson, D. Schlatter, I. Schmitt and P. M. Zerwas, “Scaling violations in inclusive e^+e^- annihilation spectra”, *Phys. Rev.* **D27** (1983) 105.
- [17] P. Nason and C. Oleari, “A phenomenological study of heavy-quark fragmentation functions in e^+e^- annihilation”, *Nucl. Phys.* **B565** (2000) 245–266, [hep-ph/9903541](#).
- [18] V. G. Kartvelishvili, A. K. Likhoded and V. A. Petrov, “On the fragmentation functions of heavy quarks into hadrons”, *Phys. Lett.* **B78** (1978) 615.
- [19] C. F. von Weizsacker, “Radiation emitted in collisions of very fast electrons”, *Z. Phys.* **88** (1934) 612–625.
- [20] E. J. Williams, “Nature of the high-energy particles of penetrating radiation and status of ionization and radiation formulae”, *Phys. Rev.* **45** (1934) 729–730.
- [21] T. Sjostrand, L. Lonnblad and S. Mrenna, “Pythia 6.2: Physics and manual”, [hep-ph/0108264](#).
- [22] H. Jung and G. Salam, “Hadronic final state predictions from CCFM: The hadron-level Monte Carlo generator CASCADE”, *Eur. Phys. J.* **C 19** (2001) 351. [hep-ph/0012143](#).
- [23] H. Jung, “The CCFM Monte Carlo generator CASCADE for lepton - proton and proton - proton collisions”, *Comp. Phys. Comm.* **143** (2002) 100.
<http://www.quark.lu.se/~hannes/cascade/>.
- [24] R. Brun, F. Bruyant, M. Maire, A. C. McPherson and P. Zancarini, “GEANT3”, CERN-DD/EE/84-1.
- [25] S. D. Ellis and D. E. Soper, “Successive combination jet algorithm for hadron collisions”, *Phys. Rev.* **D48** (1993) 3160–3166, [hep-ph/9305266](#).
- [26] S. Catani, Y. Dokshitzer, M. Seymour and B. Webber, “Longitudinally invariant k_t clustering algorithms for hadron collisions”, *Nucl. Phys.* **B 406** (1993) 187.
- [27] J. M. Butterworth, J. P. Couchman, B. E. Cox and B. M. Waugh, “Ktjet: A C++ implementation of the k_t clustering algorithm”, *Comput. Phys. Commun.* **153** (2003) 85–96, [hep-ph/0210022](#).
- [28] **Particle Data Group** Collaboration, W. M. Yao *et al.*, “Review of particle physics”, *J. Phys.* **G33** (2006) 1–1232.
- [29] I. A. et al. (H1 Collaboration), “The H1 Detector at HERA”, *Nucl. Instr. Meth.* **A386** (1997) 310–347.
- [30] I. A. et al. (H1 Collaboration), “The Tracking, Calorimeter and Muon Detectors of the H1 Experiment at HERA”, *Nucl. Instr. Meth.* **A386** (1997) 348–396.

- [31] T. Wolff *et al.*, “A drift chamber track finder for the first level trigger of the H1 experiment”, *Nucl. Instrum. Meth.* **A323** (1992) 537–541.
- [32] A. Baird *et al.*, “A fast high resolution track trigger for the H1 experiment”, *IEEE Trans. Nucl. Sci.* **48** (2001) 1276–1285, [hep-ex/0104010](#).
- [33] S. Eichenberger *et al.*, “A fast pipelined trigger for the H1 experiment based on multiwire proportional chamber signals”, *Nucl. Instrum. Meth.* **A323** (1992) 532–536.
- [34] H. Beck, “Principles and Operation of the z-Vertex Trigger”, *H1 internal note* (1996). H1-05/96-479.
- [35] J. Becker *et al.*, “A vertex trigger based on cylindrical multiwire proportional chambers”, [physics/0701002](#).
- [36] D. P. et al., “The H1 silicon vertex detector”, *Nucl. Instrum. Meth.* **A454** (2000) 334–349, [hep-ex/0002044](#).
- [37] B. List, “The H1 silicon tracker”, *Nucl. Instrum. Meth.* **A549** (2005) 33–36.
- [38] **H1 Calorimeter Group** Collaboration, B. Andrieu *et al.*, “The H1 liquid argon calorimeter system”, *Nucl. Instrum. Meth.* **A336** (1993) 460–498.
- [39] **H1 SPACAL Group** Collaboration, R. D. Appuhn *et al.*, “The H1 lead/scintillating-fibre calorimeter”, *Nucl. Instrum. Meth.* **A386** (1997) 397–408.
- [40] D. Reyna, “Modifications to SpaCal for H1 High Luminosity Operation and the Effect on the Acceptance”, *H1 internal note* (1998). H1-11/98-555.
- [41] **E598** Collaboration, J. J. Aubert *et al.*, “Experimental observation of a heavy particle J”, *Phys. Rev. Lett.* **33** (1974) 1404–1406.
- [42] **SLAC-SP-017** Collaboration, J. E. Augustin *et al.*, “Discovery of a narrow resonance in e^+e^- annihilation”, *Phys. Rev. Lett.* **33** (1974) 1406–1408.
- [43] O. Behnke, *Production of Charm and Beauty Quarks at HERA*. Habilitationsschrift, Ruprecht-Karls Universität Heidelberg, 2005.
- [44] A. B. Meyer, *Heavy Quark Production at HERA*. Habilitationsschrift, Universität Hamburg, 2005.
- [45] **H1** Collaboration, A. Aktas *et al.*, “Inclusive $D^{*\pm}$ meson cross sections and $D^{*\pm}$ jet correlations in photoproduction at HERA”, [hep-ex/0608042](#).
- [46] S. Frixione, M. L. Mangano, P. Nason and G. Ridolfi, “Total cross-sections for heavy flavor production at HERA”, *Phys. Lett.* **B348** (1995) 633–645, [hep-ph/9412348](#).
- [47] S. Frixione, P. Nason and G. Ridolfi, “Differential distributions for heavy flavor production at HERA”, *Nucl. Phys.* **B454** (1995) 3–24, [hep-ph/9506226](#).
- [48] B. A. Kniehl, “Hadron production in hadron hadron and lepton hadron collisions.”, [hep-ph/0211008](#).

- [49] G. Heinrich and B. A. Kniehl, “Next-to-leading-order predictions for $D^{*\pm}$ plus jet photoproduction at DESY HERA”, *Phys. Rev.* **D70** (2004) 094035, hep-ph/0409303.
- [50] B. A. Kniehl, G. Kramer, I. Schienbein and H. Spiesberger, “Inclusive $D^{*\pm}$ production in $p\bar{p}$ collisions with massive charm quarks”, *Phys. Rev.* **D71** (2005) 014018, hep-ph/0410289.
- [51] B. A. Kniehl, G. Kramer, I. Schienbein and H. Spiesberger, “Collinear subtractions in hadroproduction of heavy quarks”, *Eur. Phys. J.* **C41** (2005) 199–212, hep-ph/0502194.
- [52] **H1** Collaboration, A. Aktas *et al.*, “Inclusive production of D^+ , D^0 , D_s^+ and D^{*+} mesons in deep inelastic scattering at HERA”, *Eur. Phys. J.* **C38** (2005) 447–459, hep-ex/0408149.
- [53] S. W. Herb *et al.*, “Observation of a dimuon resonance at 9.5 GeV in 400 GeV proton - nucleus collisions”, *Phys. Rev. Lett.* **39** (1977) 252–255.
- [54] **H1** Collaboration, A. Aktas *et al.*, “Measurement of charm and beauty photoproduction at HERA using $D^* \mu$ correlations”, *Phys. Lett.* **B621** (2005) 56–71, hep-ex/0503038.
- [55] **CDF** Collaboration, M. D’Onofrio, “Beauty production cross section measurements at $E_{cm} = 1.96$ TeV”, hep-ex/0505036.
- [56] **CDF** Collaboration, D. Acosta *et al.*, “Measurement of the J/ψ meson and B -hadron production cross sections in $p\bar{p}$ collisions at $\sqrt{s} = 1960$ GeV”, *Phys. Rev.* **D71** (2005) 032001, hep-ex/0412071.
- [57] S. Frixione and M. L. Mangano, “Heavy-quark jets in hadronic collisions”, *Nucl. Phys.* **B483** (1997) 321–338, hep-ph/9605270.
- [58] A. A. et al (H1 Collaboration), “Measurement of beauty production at HERA using events with muons and jets”, *Eur. Phys. J.* **C41** (2005) 453–467, hep-ex/0502010.
- [59] **ZEUS** Collaboration, S. Chekanov *et al.*, “Bottom photoproduction measured using decays into muons in dijet events in ep collisions at $\sqrt{s} = 318$ GeV”, *Phys. Rev.* **D70** (2004) 012008, hep-ex/0312057.
- [60] **ZEUS** Collaboration, S. Chekanov, “Measurement of open beauty production at HERA in the $D^* \mu$ final state”, hep-ex/0609050.
- [61] I. Bloch, “Measurement of beauty production from dimuon events at HERA/ZEUS”, DESY-THESIS-2005-034.
- [62] B. Naroska, S. Schiek and G. Schmidt, “Lepton identification in the H1 detector at low momenta”, *H1 internal note* (1997). H1-05/97-518.
- [63] G. Cowan, *Statistical Data Analysis*. Oxford, UK: Clarendon (1998) 197 p.
- [64] B. List and A. Mastroberardino, “DIFFVM: A Monte Carlo generator for diffractive processes in ep scattering”, *DESY-PROC-1999-02* (1999).
- [65] B. Delaunay, *Sur la sphere vide*. Bulletin of Academy of Sciences of the USSR, 1934.

-
- [66] M. Peetz, B. Portheault and E. Sauvan, “An energy flow algorithm for hadronic reconstruction in OO: HADROO2”, *H1 internal note* (2005). H1-01/05-616.
- [67] B. Wessling, *Measurement of the beauty cross section using the semileptonic decay into electrons at HERA*. Ph.D. thesis, Universität Hamburg, 2005.
- [68] F. Jacquet and A. Blondel, “Detection and study of the charged current event”,. U. Amaldi (Hg.) *Study of an ep-Facility for Europe*, DESY, August 1979, 391-396.
- [69] The H1 OO Group, *The H1 Physics Analysis Project*. H1 internal documentation.
- [70] R. J. Barlow and C. Beeston, “Fitting using finite Monte Carlo samples”, *Comput. Phys. Commun.* **77** (1993) 219–228.
- [71] N. G. et al., “An offline luminosity determination for the 1995 e^+p data”, *H1 internal note* (1996). H1-02/96-472.
- [72] W. Erdmann, *Untersuchung der Photoproduktion von D^* -Mesonen am ep-Speicherring HERA*. Ph.D. thesis, ETH Zürich IPP, 1996.

Danksagung

Mein Dank richtet sich an alle, die direkt oder indirekt zum Zustandekommen dieser Arbeit beigetragen haben.

Zunächst möchte ich Frau Prof. Dr. Beate Naroska für die Betreuung meiner Arbeit und ihr großes Engagement danken.

Bei Herrn Dr. A. Geiser bedanke ich mich für die Übernahme des Zweitgutachtens.

Herrn Dr. Andreas Meyer danke ich für das Lesen meines Manuskriptes und die hilfreichen Bemerkungen.

Ganz herzlich bedanken möchte ich mich besonders bei meinen Kollegen Axel Cholewa, Dr. Gero Flucke, Dr. Hannes Jung, Angela-Isabela Lucaci-Timoce, Lluís Martí, Svetlana Vinokurova, Dr. Jeannine Wagner und Dr. Bengt Wessling für die vielen anregenden Gespräche, die angenehme Atmosphäre und die hilfreichen Bemerkungen zu meiner Arbeit.

Großen Dank für ihr Verständnis und ihre Unterstützung schulde ich meiner lieben Familie.